FABRICATION OF GRAPHENE BASED APTASENSORS FOR EARLY DETECTION OF PROSTATE CANCER BY EXPERIMENTAL AND COMPUTATIONAL TECHNIQUES

By

Athika Darumas Putri

(Reg. No: 21557639)

Submitted in fulfilment of the requirements of the degree of Master of Applied Science in Chemistry in the Faculty of Applied Sciences at the Durban University of Technology

June 2017

DECLARATION

I **Athika Darumas Putri** declare that the thesis submitted for the degree of Masters of Applied Science (M.App.Sci.): Chemistry at the Durban University of Technology is the result of my own investigation and has not already been accepted in substance for any degree, and is not being concurrently submitted for any other degree. All the work was done by the Author.

Student Name: Athika Darumas Putri

Student Signature: [redacted] Date: 24/8/2017

Supervisor Name: Professor K. Bisetty

Signature: [redacted] Date: 24/8/17

Co-Supervisor Name: Assoc. Prof. Ashutosh Tiwari, Linköping University (Sweden)

Signature: [redacted] Date: 24/8/2017

ACKNOWLEDGEMENTS

All praise is to Almighty Allah Swt., Most beneficent, Most merciful, on whom everything depends for guidance and sustenance. These opportunity, perseverance, and patience do not but belong to Him.

My gratitude and faithful regards to my supervisor, Prof. K. Bisetty, Head of Department of Chemistry, for his great supervision as Masters student. His compassionate direction, time-discipline, and full-support of assistance in every talk and discussion have inspired me to grow and improve my own-capabilities, skills, and thoughtful approach in accomplishing the computational research. My deep gratefulness for allowing me to be involved in the computational conference which was a precious moment for me to be surrounded by computational experts. The synergy between the experimental and computational works have therefore been possible to be conducted successfully at DUT.

My sincere appreciation goes to my co-supervisor, Prof. Ashutosh Tiwari, Research Group Leader of Smart Materials and Biodevices, IFM, Linkoping University, who has given me this avenue to see the world-wide-research and introduced me to Prof. K. Bisetty at the beginning. His astonishing passion shaped me to be a better scientist. I'd like to thank him for this wonderful learning-experience given, entire motivations, his truthful supports during the tenure, beneficial discussions, and invaluable assistance chairing my Masters studies.

I would like to express my thankfulness to the Centre for High Performance Computing (CHPC) of South Africa, for providing a genuine computational base, which has enabled me to make up my entire computational studies.

I'm also indebted for expressing my special gratitude to the senior researchers in Computational Modeling and Bio-Analytical Chemistry (CMBAC) group members (Dr.

Kanchi, Myalo, Dr. Shahbaaz, Dr. Deepali). Thank you for all irreplaceable discussion and having supported me to finish the thesis. Special thanks to the peers: Bayu, Nosipho, Kwanele, Keval, and Shemica. You guys are too amazing! Thank you for listening, laughing, debating, offering me moral advice, and any incredible support. We have finally succeeded going through these entire processes!

To my mother, sisters, and my whole families, who always supported me through their pious duaa (prayers), love, and intense caring through communication during the time core. They are the real role models for me to keep moving forward reaching the ultimate goals in my life. May Allah grant and always shower His blessings to you all.

I am particularly grateful to all friends: Mrs. Aminah Yousouf, Vawda's families, Fathima Sheikh, Adhilla-Waseem, Suhaifa, Nausheina, Mrs. Zubaidah, Poonam Singh, Faiz Ansari, Dr. Abhiseek, Dr. Anand, Dr. Raam, Muthu, Fitsum, Khanyi, Mrs. Tola, Vasant, Bibuthi, Dennies Ochieng, Kunle, and all those who their names do not appear. Thank you for your support and sincere friendship during my study in Durban.

I would like to thank all our Indonesia family in South Africa, Mrs. Suki Muller, Mr and Mrs Reza, Ripani, Maryam's family, and Mr. Ambassador. It is great to have you all family here!

Athika Darumas Putri

ABSTRACT

High prevalence and mortality cases of prostate cancer (PCa) have increased around the world, particularly in developing countries. Several forthcoming factors have been revealed nowadays, one of them is due to the incapability of the diagnostic methods to produce reliable results, which impacts negatively on cancer-treatment. However, a sensitive diagnosis of PCa cells remains a challenge in the field of biosensors. Emerging whole-cell detection as biosensing targets has opened up avenues for successful cancer diagnostics, due to high selectivity among other cells. A switchable and flexible surface-based graphene material is one of the techniques that revolutionized smart biodevice platforms in biosensor technology. In this present study, a covalently linked poly-(*N*-isopropylacrylamide) (PNIPAM) to graphene oxide surface has been employed as "on/off"-switchable aptamer-based sensor for the detection of PC3 whole-cancer cell. The constructed surface has benefitted from PNIPAM, as the thermal-stimulus agent, which allows the coil-to-globule transitions by triggering temperature changes. When the system is above its lower critical solution temperature (LCST) of 32^{o}C, PNIPAM will exist as hydrophobic -globular state providing an "on" binding region for the whole-cell, reaching the interactions on the biosurface. The "off" binding systems is only possibly when the PNIPAM turns into extended-state by lowering its temperature below LCST. The first principle studies have successfully characterized the electronic behavior with particular emphasis of PNIPAM monomer functions along with the description of the structural energetics of complex through density functional theory (DFT). Docking studies have further been performed to predict a plausible binding aptamer toward the protein-representative PCa cell. To better understand the prospect of an aptamer-based tunable biosensor, molecular dynamics (MD) highlighted the behavior

of PNIPAM-grafted GO in exhibiting a globular and extended conformations at above and below LCST, permitting the biomolecules to interact with each other as well as to avoid interactions, respectively. Experimental studies have been included to validate the theoretical predictions by fabricating real-biosensor systems using electrochemical impedance technique, resulting a low-detection limit down to 14 cells/mL. Engagement between theoretical and experimental studies delivered an enhanced tunable-biosensor performance for the detection of whole cell prostate cancer.

LIST OF CONFERENCE PRESENTATIONS AND PUBLICATIONS

Poster Presentations

10th Center for High Performance Computing (CHPC) National Meeting held at ICC, East London, South Africa. 5th to 9th December **2016**. "A DFT Study of The Interaction of Functionalized Graphene Oxide with DNA/RNA nucleobases".

10th Center for High Performance Computing (CHPC) National Meeting held at ICC, East London, South Africa. 5th to 9th December **2016**. "Computational Study of The Regioselective Dopamine Adsorption onto Multilayer Surface of FTO/TiO_2".

Publications

Athika Darumas Putri, Bayu Tri Murti, Suvardhan Kanchi, Krishna Bisetty, and Myalowenkosi I. Sabela. **2017**. Nanopolymer Chitosan in Cancer and Alzheimer Biomedical Application. *In:* Shakeel Ahmed & Saiqa Ikram (eds.) *Chitosan: Derivatives, Composites and Applications.* USA: John Wiley & Sons-Scrivener Publishing LLC (ISBN: 1119363500, 9781119363507).

Athika Darumas Putri, Ashutosh Tiwari, and Krishna Bisetty. Fabrication of Graphene Based Aptasensors for Early Detection of Prostate Cancer Using Computational and Experimental Techniques (in preparation).

Athika Darumas Putri, Bayu Tri Murti, Krishna Bisetty, and Ashutosh Tiwari. Review: Advancements in Whole-Cell Biosensors for Detection of Cancer (in preparation).

Athika Darumas Putri, Bayu Tri Murti, Krishna Bisetty, and Ashutosh Tiwari. Computational Studies of MK-8931-Carbon Nanotube Complex in Inhibiting β-Secretase Activity (in preparation).

Bayu Tri Murti, **Athika Darumas Putri**, Krishna Bisetty, and Ashutosh Tiwari. Density Functional and Molecular Docking Studies of Drug Loaded Pegylated-Prospective Nanomaterials onto Active Site of BACE1 Protein: A Comparative Study for Alzheimer's Drug Nanocarrier (in preparation).

TABLE OF CONTENT

LIST OF FIGURES

LIST OF TABLES

LIST OF ACRONYMS AND SYMBOLS

PCa	Prostate cancer
PSA	Prostate specific antigen
PSMA	Prostate specific membrane antigen
BPH	Benign prostatic hyperplasia
SELEX	Systematic evolution of ligands exponential enrichment
GO	Graphene oxide
PNIPAM	Poly-(*N*-isopropylacrylamide)
LCST	Lower critical solution temperature
DFT	Density functional theory
MD	Molecular dynamic
PIN	Prostatic intraepithelial neoplasia
FDA	Food and Drug Administrations
IHC	Immunohistochemistry
ELISA	Enzyme-Linked Immunosorbent Assay
KLK2	Human kallikrein-2
PSCA	Prostate stem-cell antigen
EPCA	Early prostate cancer antigen
AMACR	Alpha-methylacyl-CoA racemase
PAP	Prostatic acid phosphatase
uPA	Urokinase plasminogen activation
uPAR	uPA receptor
PAI-1	Plasminogen activator inhibitor type-1
HPLC	High performance liquid chromatography
LC-MS	Liquid chromatography-mass spectroscopy
DNA	Deoxyribonucleic acid
ssDNA	Single-stranded DNA
dsDNA	Double-stranded DNA
RNA	Ribonucleic acid
ssRNA	Single-stranded RNA
PCR	Polymerase chain reaction
NAATs	Nucleic acid amplification
SPR	Surface plasmon resonance
HTMSU	Modified-high throughput micro sampling unit
Ep-CAM	Anti-epithelial cell adhesion molecule
CTC	Circulating tumor cell
ECL	Electrochemiluminescence
EIS	Electro impedance spectroscopy
R_{et}	Electronic transfer resistance
GC	Glassy carbon
WGA	Wheat germ agglutinin
EC-ELISA	Electrochemical-ELISA
ALP	Alkaline phosphatase
p-APP	p-aminophenyl phosphate
DPV	Differential pulse voltammetry
CNT	Carbon nanotube
Rgo	Reduced graphene oxide

NMR	Nuclear magnetic resonance
XRD	X-ray diffraction spectroscopy
ATP	Adenosine triphosphate
POC	Point-of-care
PNIPAM-AAc	PNIPAM-co acrylic acid
$5CB_{PNIPAM}$	b-poly(4-cyanobiphenyl-4'-oxyundecylacrylate)
SDS	Sodium dodecyl sulfate
R-B	Radial-to-bipolar
QM	Quantum mechanics
MM	Molecular mechanics
SCF	Self-consistent field
KS	Kohn-Sham
XC	Exchange correlation
LDA	Local density approximation
GGA	Generalized gradient approximation
GTO	Gaussian type orbitals
STO	Slater type orbitals
3G	Three Gaussian peaks
DZ	Double-zeta
VDZ	Valence double-zeta
AO	Atomic orbital
MIN	Minimal basis set
DNP	Double polarized numerical basis set
DIIS	Direct inversion of the iterative subspace
FFT	Fast fourier transform
PSC	Pairwise shape complementary
UB	Urey-Bradley
COMPASS	Condensed-phase Optimized Molecular Potentials for Atomistic Simulation Studies
CFF	Consistent force field
UFF	Universal force field
NVT	Number of atoms, volume, temperature
NVE	Number of atoms, volume, energy
NPH	Number of atoms, pressure, enthalpy
NPT	Number of atoms, pressue, temperature
NHL	Nosé-Hoover-Langevin
PBC	Periodic boundary condition
DFT-D	DFT-dispersion
TS	Tkatchenko and Scheffler
A	Adenine
G	Guanine
T	Thymine
C	Cytosine
HOMO	Highest-occupied molecular orbital
LUMO	lowest-unoccupied molecular orbital
RNA FRABASE	RNA Fragment Base Search Engine
PDB	Protein data base
RCSB	Research Collaboratory for Structural Bioinformatics
ACE	Atomic contact energy
MW	molecular weight
ABNR	Adjusted basis set Newton-Raphson

PPPM	Particle-Particle Particle-Mesh Ewald
ALA	Alanine
CYS	Cysteine
ASP	Aspartic acid
GLU	Glutamic acid
PHE	Phenylalanine
GLY	Glycine
HIS	Histidine
ILE	Isoleucine
LYS	Lysine
LEU	Leucine
MET	Methionine
ASN	Asparagine
PRO	Proline
GLN	Glutamine
ARG	Arginine
SER	Serine
THR	Threonine
VAL	Valine
TRP	Tryptophan
TYR	Tyrosine
GCE	Glassy carbon electrode
PBS	phosphate buffer saline
EDC	1-ethyl-3-(3-dimethylaminopropyl) carbodiimidehydrochloride
NHS	*N*-hydroxysuccinimide
TEMED	N, N, N, N-tetramethylethylenediamine
RPMI	Roswell Park Memorial Institute
DPBS	Dulbecco's phosphate buffered saline
APT	Wy5a aptamer
MTT	Methylthiazoletetrazolium
NIPAM	*N*-isopropylacrymide
ESP	Electrostatic potential
TDOS	Total density of states
CV	Cyclic voltammetry

CHAPTER 1

INTRODUCTION

This chapter provide details about prostate cancer (PCa) as being one of the foremost causes of cancer deaths worldwide. The causes of PCa and the current progress of the therapy are included in this section. This chapter also provides an overview of biomarkers with particular emphasis on aptamer based biosensors, a recent development in the field of clinical diagnostics. The need for reliable diagnostic methods, and aptasensor techniques for diagnostics are also presented here. Furthermore, the synergies between computational chemistry tools in relation to biosensor systems are presented in this section. This is followed by the aims and objectives and a brief outline of the thesis.

1.1 Prostate Cancer

Cancer is the most threatening and deadly disease for human beings worldwide (Kunii et al., 2011). For men in many industrialized nations, prostate cancer (PCa) is one of the leading causes of death with over 26, 000 cases reported in 2016 (Jemal et al., 2006, Tai et al., 2011, American Cancer Society, 2016). However, the incidence and fatalities have increased dramatically in developing countries. Nearly three-quarters of all fatalities is attributed to PCa (Delongchamps et al., 2007). The highest rate of mortality in the world is in the Caribbean region of African descent, with the rate of incidence for the accumulated standardized-age is 15 times higher than in the Middle East and Eastern Asia and 4 times much higher than in the US (American Cancer Society, 2011). The PCa incidence is generally caused by internal matter, such as the mutation of genetic heredity itself. However, the non-genetic factor is more likely responsible for an unpredictable growth of PCa.

Instead of environmental exposure, a poor-result of diagnosis may also lead to untimely prognosis and therapy (Zeigler-Johnson et al., 2008). In several cases, a high PCa prevalence is also influenced by the reliability of a diagnostic method (Haas et al., 2008). Common methods for PCa diagnostics are prostate specific antigen (PSA) or prostate specific membrane antigen (PSMA) level measurements in blood serum. However, PSA blood serum has a low specificity since it still could be detected in other cases of disease, such as benign prostatic hyperplasia (BPH) and prostatitis (Hessels and Schalken, 2013). Meanwhile, the PSMA detection mostly does not belong to the aggressiveness of PCa itself and in regard to malignant stages, the PSMA fails to interpret the advanced status of cancer as somehow, the level can decline (Douglas et al., 1997, Tricoli et al., 2004).

On the other hand, the number of biomarkers to clearly detect earlier cases of PCa which has been identified and validated till now are very few. Furthermore, an artificial oligonucleotide selected from *in vitro* iteration, so-called aptamer has been found to be able to bind with various target types with robust sensitivity and selectivity. Aptamer based biosensors has been recently developed in clinical diagnostics and several vital technologies. The metastatic PC3 cell is a model of a particularly pernicious PCa, which is hormone-insensitive and does not express PSA on the surface, making it suitable to construe the existence of PCa. However, it is difficult to target PSA by only using standard antigen–antibody mechanism. Furthermore, Wang and co-workers have successfully synthesized and investigated the model of aptamers which specifically binds to PC3 cell-line, known as Wy5a and Wy5b aptamers (Wang et al., 2014). The authors reported the whole-cells in systematic evolution of ligands exponential enrichment (cell-SELEX) process which was taken into account in order to produce a selective aptamer candidate toward the PC3 cells. During the cell-SELEX

process, the native biological conformation of target cells are ignored without any preceding knowledge since the entire SELEX process recognizes the whole cell body as the target (Djordjevic, 2007). As an output, the produced aptamer has the ability in determining the target cells through its overall properties without missing any important part, such as important surface proteins. Accordingly, this reinforces the fact that the inclusion of aptamers are such promising strategies in the recognition of target cells amongst normal type of cancer cells.

Additionally, biosensor-based electrochemical offers tremendous advantages due to its high sensitivity, small size sample, easy-to-handle, real time analysis, and cost-effectiveness among other biosensor methods. The performance of electrochemical biosensors has already been proven in numerous critical fields, particularly in healthcare and biotechnology industry (Pohanka and Skladai, 2008, Ding et al., 2010b, Liu et al., 2012, Kaur et al., 2015, Bai et al., 2016). Graphene oxide (GO) has been known as one of excellent nanomaterial commodities which is fitting with the biosensors fabrication by virtue of its outstanding conductivity, feasibility for microfabrication, high definition of surface area, great optical transparency, and surface biocompatibility (Lightcap and Kamat, 2013, Rodríguez-Pérez et al., 2013, Gupta et al., 2013, Vashist and Luong, 2015). The presence of the oxygen-functional groups spread on the honeycomb plane is useful as preliminary sites for deposition of organic biomolecules, which excavates an advanced multifunctional nanoscaled optoelectronic materials (Sun et al., 2014). Due to its specific platform, GO induces the hydrophilicity, thus increases a good dispersion feature in water as well as alcohol which is particularly useful in biological application (Lee et al., 2016).

Poly-(*N*-isopropylacrylamide) (PNIPAM) is the greatest extensively studied of thermal responsive polymers in biosensor system. Its lower critical solution temperature (LCST) of 32^0C enables PNIPAM to possibly control the interactions evidenced in *in vivo* studies (Islam et al., 2014). PNIPAM exists as coil state and hydrophilic at below LCST and will be a desolvated globule at above LCST temperature. Taking PNIPAM's behavior into account in this experimental study will open up a switchable interaction between aptamer and the target cells, which is eventuated at above LCST to mimic the normal temperature of human body. Emerging from the thermo-responsive polymer to carbon nanomaterials is believed to generate a hybrid and tunable biosensor systems underlying a stimuli responsive function, where it may not be obtainable in individual components (Zhou et al., 2016). Integrating PNIPAM through surface modification on GO will possibly facilitate a modest advance to accomplish an effective detection induced by external stimuli.

Computational chemistry methods have been widely applied to better understand the nature behind experimental technique (Almeida et al., 2014). Computational biology also count on the integrated purpose of biological mechanism within a cell that is potential to transfigure further biological and medicinal aspects by understanding and designing their biological systems (Di Ventura et al., 2006). In the field of science and engineering, density functional theory (DFT) method has become very successful technique in order to produce correlation between the activity of compounds and their various physicochemical parameters. This method transforms electronic and structural properties from a simple three-dimensional system to a many-body system in functional forms of electron density as well as single-particle orbitals. In agreement with the DFT performance, one can obtain the fundamental state of electronic energy of the system through the total electronic density with comparable

precision to other methods in efficient computational cost (Kohn et al., 1996, Chtita et al., 2013).

Molecular docking is a key tool to understand the interaction between biomolecules in maintaining complex regulatory and metabolic networks, especially for cell signaling. Most approaches to the protein-protein docking are generated from rigid-body assumption with the goal to predict the reasonable binding modes through three-dimensional simplistic models. Successful docking approaches discover high-dimensional spaces including scoring function to rank the candidate models of dockings properly (Lengauer and Rarey, 1996b, Morris and Lim-Wilby, 2008, Pierce et al., 2014). Molecular dynamics (MD) simulation explores the motion of biophysical systems within a time frame, whereas the atoms are subjected to forces of intermolecular interactions. It investigates the self-assembling mechanisms as well as their structural energetics during dynamics interactions. Some important features applied under experimental circumstances could be involved in this computational techniques, such as temperature, aqueous environment, and pressure (Kalé et al., 1999, Johnson et al., 2008).

With the aim of discovering the first principal mechanism between PNIPAM-grafted GO and Wy5a aptamer, the geometry and electronic calculations of each basic element have been discovered through DFT. Along with the calculation, the molecular docking and MD simulations have been successfully performed to validate the experimental results in understanding the behavior of the system under particular environment of temperatures. Due to the collaborative nature of this project, all experimental works were carried out in Linköping University, Sweden, while all the computational works were accomplished at Durban University of Technology (DUT). The scheme of the computational works is

presented in **Figure 1.1** with the scheme of the methods work in **Figure 1.2**. By employing the electrochemical technique in GO based aptamer biosensor system integrated with the computational studies, the biosensor system was expected to give more reliable performance for early detection of PCa.

1.2 Aims and Objectives

This study is aimed at fabricating and validating an aptamer-based biosensor for the early detection of prostate cancer using experimental and computational techniques.

Objectives:

- ✓ Fabricate and optimize the electrochemical biosensor properties using aptamers for the detection of PC3 cells for prostate cancer.
- ✓ Analyze the sensing ability of electrochemical biosensor based PNIPAM-modified GO immobilized with Wy5a aptamers in biological samples.
- ✓ Analyze the first principal studies of each compartment of PNIPAM-modified GO toward Wy5a aptamers using Density Functional Theory (DFT).
- ✓ Perform the interaction mechanisms between the Wy5a aptamers and protein of PC3 cells through molecular docking studies.
- ✓ Validate the binding energies of protein corresponded PC3 cells using computer-aided simulations of PNIPAM-modified GO immobilized with Wy5a aptamers.

1.3 Thesis Outline

Following the Introduction, further chapters in this thesis are expanded as follows:

1.3.1 **Chapter 2:** In this section, general reviews associated with the prostate cancer evidence, prevalence, carcinogenesis, recent diagnostic methods, biosensors

fundamentals, particularly the biorecognition use of aptamer, SELEX process, and recent biosensors studies of PCa using several methods are explained. Likewise, the focus in application of nanomaterial of graphene oxide and assembly of thermal responsive polymer in biosensor architecture is also described here.

1.3.2 **Chapter 3:** In this chapter, the rigorous concepts behind DFT, molecular docking, molecular mechanics, and molecular dynamics simulation are described. DFT methods include Schrödinger and Hartree Fock approximations, exchange-correlation term, and self-consistent field. In particular, molecular docking partly discusses the ZDOCK-ZRANK backgrounds, while the main force fields and simulation properties (i.e. ensemble, thermostat) are explained under molecular mechanics and molecular dynamics simulation. Special attention will be given to the DMol3 and Forcite packages as implemented within the computational methods.

1.3.3 **Chapter 4:** The methodologies and work-protocols of computational studies including DFT, molecular docking, and molecular dynamics simulation are presented in detail. In a separate sub-section, the experimental works of electrochemical aptasensor design including the preparation of cancer cells, synthesis of the PNIPAM functionalized GO, characterization studies, and the evaluation of the aptasensor in biological samples are also thoroughly described here.

1.3.4 **Chapter 5:** The results of the computational and experimental works are discussed here.

1.3.5 **Chapter 6:** A summary of the main results of each methodology of computational and experimental works of PCa aptasensor are described. The results are also correlated and associated with each other in order to obtain concluding remarks and highlights of these works. Future work and recommendations are also briefly proposed to improve

significant and interrelated works for the advancement of early PCa detection using computational and biosensor experimental techniques.

1.3.6 **References:** The references used within this thesis are enclosed.

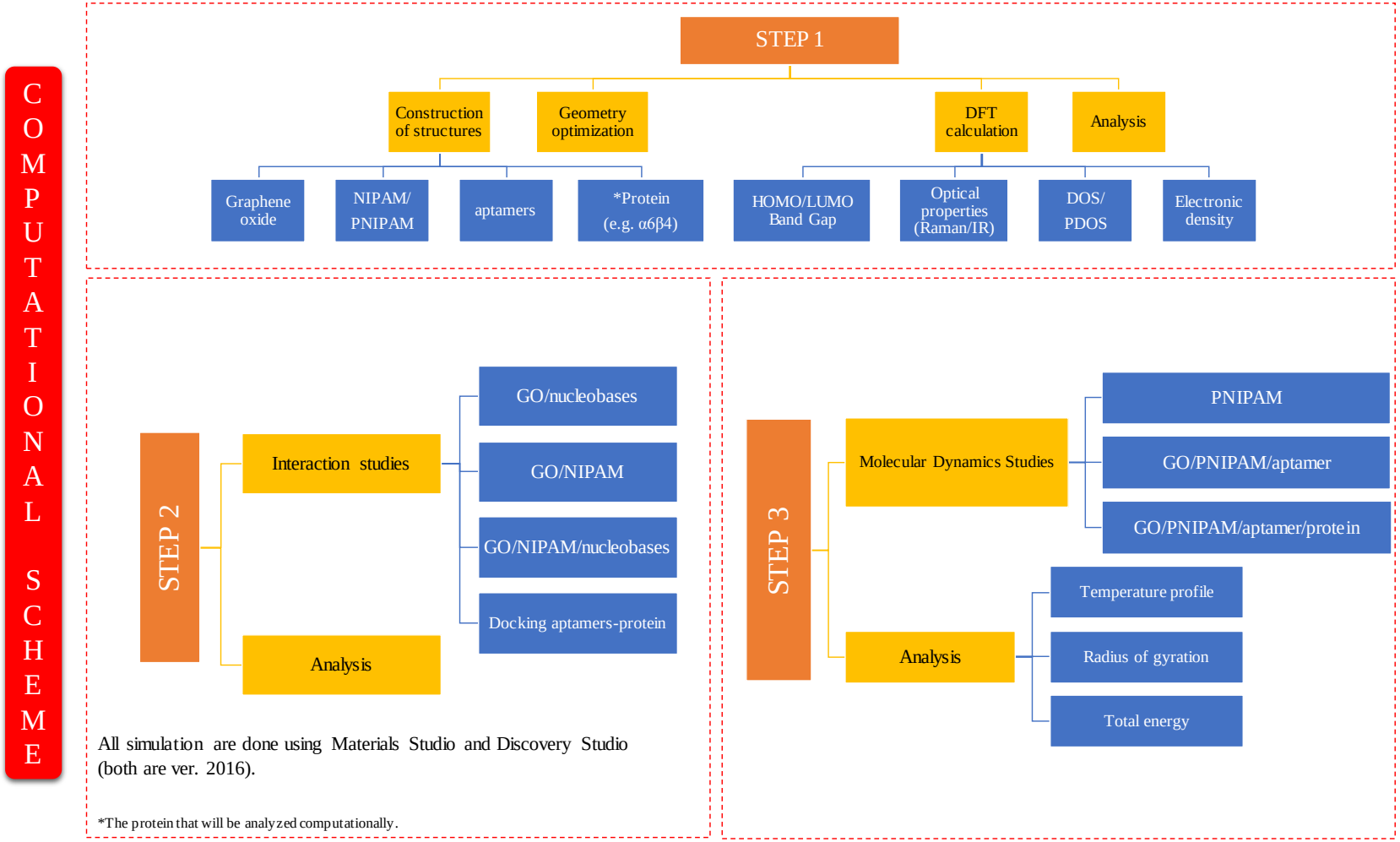

Figure 1.1 The workflow of computational research methodology.

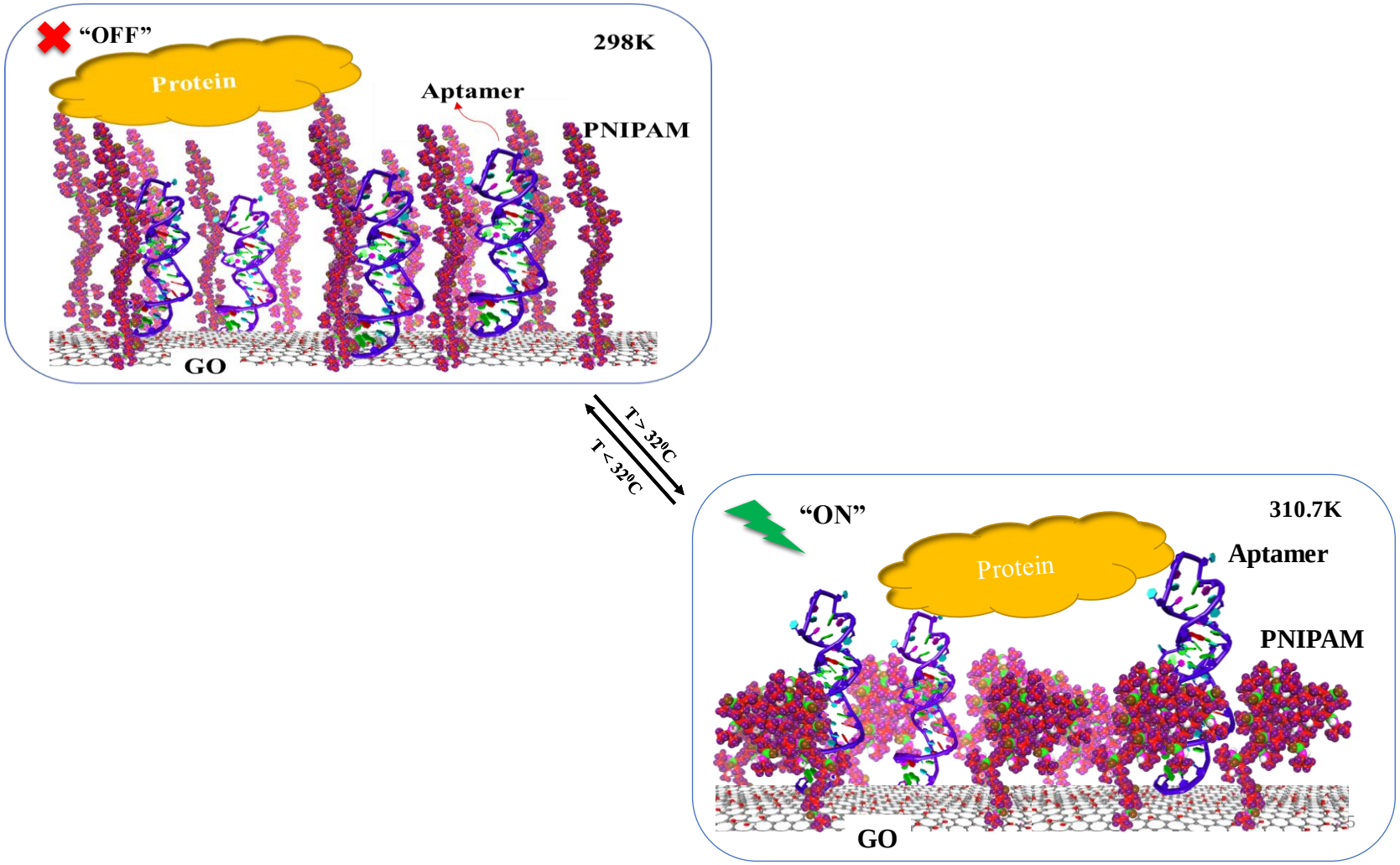

Figure 1.2 The computational illustration of PNIPAM functionalized GO for aptamer and protein interaction under LCST control.

CHAPTER 2

LITERATURE REVIEW

This chapter highlights the historical aspects of cancer and general reviews associated with the prostate cancer evidence, prevalence and carcinogenesis. A review of recent diagnostic methods including biosensor applications particularly aimed at the biorecognition use of aptamers is also presented. The SELEX processes leading to recent biosensor studies of PCa using optical and electrochemical methods are highlighted. The focus of this review is aimed at novel applications of nanomaterials such as graphene oxide and assembly of thermal responsive polymers in the application of biosensor architecture in PCa detection.

2.1 Prostate Cancer

2.1.1 Prostate Cancer Incidence

Incidences of cancer has risen to about 8.2 million cases of mortality, 32.6 million patients living with cancer, and 14.1 million new cases reported, with the less developing countries experiencing more evidences in the last five years (Ferlay et al., 2015). In the US, men have the highest incidences such as prostate, lung-bronchus and colorectal cancer (**Figure 2.1**). Meanwhile, the breast, lung-bronchus and colorectal cancer are highly prevalent amongst women in the US (Siegel et al., 2015).

Among the men, prostate cancer (PCa) is one of utmost threatening cancers with an approximated 26,120 deaths in 2016 (American Cancer Society, 2016). In developing countries, PCa is the most frequently diagnosed cancer where almost two-thirds of all PCa cases are found in 17 % of the men population (American Cancer Society, 2011). The

incidences vary based on the geographic area where the highest prevalence is found in Australia and New Zealand and the rarest one is in Asian regions (**Figure 2.2**). Meanwhile, the highest mortality rates occurred in the Caribbean and Africa countries followed by America, Europe, and Asia (Torre et al., 2015).

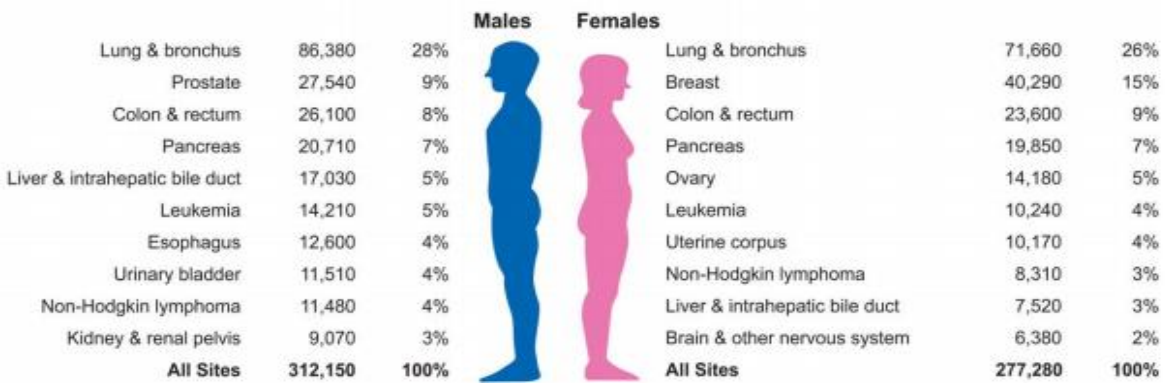

Males			Females		
Lung & bronchus	86,380	28%	Lung & bronchus	71,660	26%
Prostate	27,540	9%	Breast	40,290	15%
Colon & rectum	26,100	8%	Colon & rectum	23,600	9%
Pancreas	20,710	7%	Pancreas	19,850	7%
Liver & intrahepatic bile duct	17,030	5%	Ovary	14,180	5%
Leukemia	14,210	5%	Leukemia	10,240	4%
Esophagus	12,600	4%	Uterine corpus	10,170	4%
Urinary bladder	11,510	4%	Non-Hodgkin lymphoma	8,310	3%
Non-Hodgkin lymphoma	11,480	4%	Liver & intrahepatic bile duct	7,520	3%
Kidney & renal pelvis	9,070	3%	Brain & other nervous system	6,380	2%
All Sites	**312,150**	**100%**	**All Sites**	**277,280**	**100%**

Figure 2.1 The rates of new leading cancer-caused mortality in US are figured out by sex group among 2015 (Siegel et al., 2015).

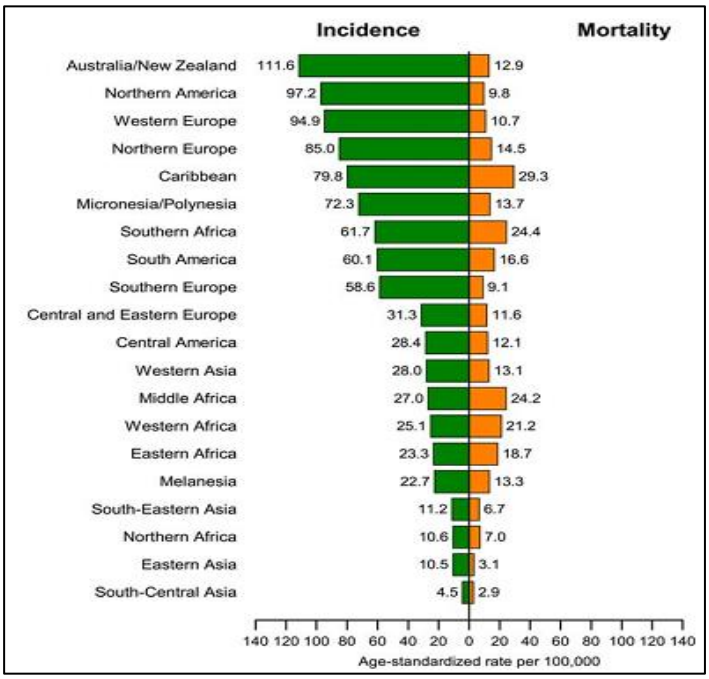

Figure 2.2 The rates of incidence (green group) and mortality (yellow group) of PCa disease among men worldwide per year of 2012 (Torre et al., 2015).

Regarding mortality rates, the male population of African descent in the Caribbean region has the highest risk of PCa in the world, where the incidence is four times higher as compared to those in the US, and 15 times higher than those in the Eastern Asia and Middle-Eastern countries, with the same age-standardized rates of men (American Cancer Society, 2011). These phenomena have been significantly contributed either by non-genetic or genetic factors which creates the PCa discrepancies among different nations. However, the combination of both factors and unreliable diagnostic results may clarify the poorer outcomes experienced in men of African descent (Zeigler-Johnson et al., 2008, Baade et al., 2009, Center et al., 2012).

2.1.2 Carcinogenesis of PCa

Generally, there are many causes of cancer, such as unhealthy lifestyle which includes the use of preservatives in food, excessive alcohol consumption and inhalation of tobacco (smoking) which affects the immune system by causing damage and modulating the multistage of carcinogenesis. The carcinogenesis is divided into four stages (**Figure 2.3**) as explained below. Each of the following stages is defined by modifications in morphology and biochemical genetic and epigenetic changes (Kaur et al., 2014).

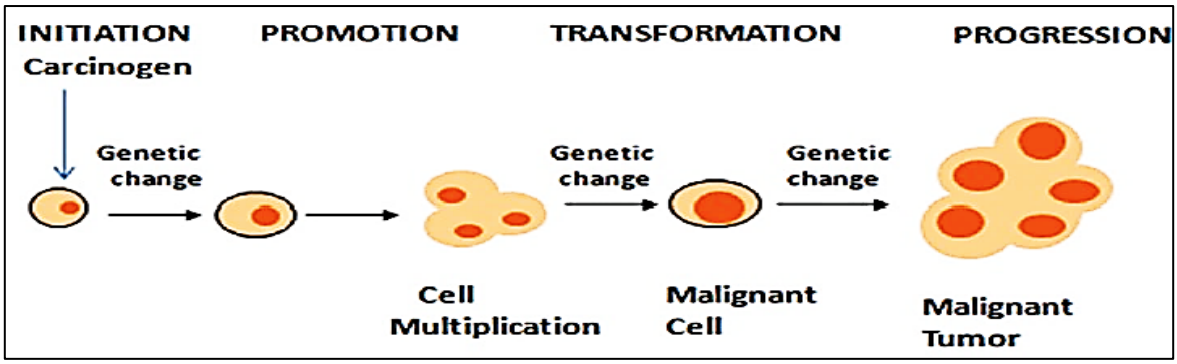

Figure 2.3 The multistage of carcinogenesis (Kaur et al., 2014).

The carcinogenesis starts from a repetitive exposure to one of the factors above or potential chemical compounds, which alters the metabolism of normal cells thereby initiating the cancer growth. This **initiation** progress completely occurs when the nucleic acid arrangement of normal cells is genetically altered. Subsequently, the affected cells secrete carcinogenic metabolites, leading to the mutation in nucleic acids of other neighboring cells causing them to become cancerous. At the expansion stage, **promotion** induces the accumulation of the affected cells; the amount of clonal expansion and the change of basic circumstances of the next round of target cells, in order to provide a specific environment for the affected cells to grow as malignant and immortalized cells (Jones and Baylin, 2002, Weston and Harris, 2003).

The **malignant** stage may not be induced by tumor promoters since the cancer cells themselves already have self-promoter potency. Interestingly, this hallmark allows for the expansion of malignant cells to be broader, reversible and comprehensive with anti-programmed death cells which can impact to the physiological alteration at the tissue level (Weston and Harris, 2003, Anisimov, 2007, Hanahan and Weinberg, 2011). However, the expression of aggressive malignant cells, called tumor **progression**, have unstable genomic and uncontrolled growth characters. The malignant phenotype of cells is physiologically heterogeneous, and has the ability to metastasize as well as assist with their own expansion as the primary tumors. In the metastatic stage, any genetic information of cancer metabolism, invasiveness and progression characters are derived for the next round of the malignancy progress (Yokota, 2000, Anisimov, 2007).

In PCa, the progress starts in the periphery side of a glandular tissue as adenocarcinoma which leads to the congealing and collapsing of the epithelial primary and secretory layers. In this stage, the so-called prostatic intra-epithelial neoplasia (PIN) (**Figure 2.4**), the secretion of prostate specific antigen (PSA) and other biological markers are more released during the cancer proliferation. The less control of the cells apoptosis during expansion process increases the growth of the abundant PCa cells with its varied phenotypes. In addition, these heterogeneities are commonly investigated under histological sampling with Gleason scoring to interpret the prostate tissue-status. This matter is more likely to be an end-main method after several PCa detections have failed (Gleason, 1966, Schulz et al., 2003).

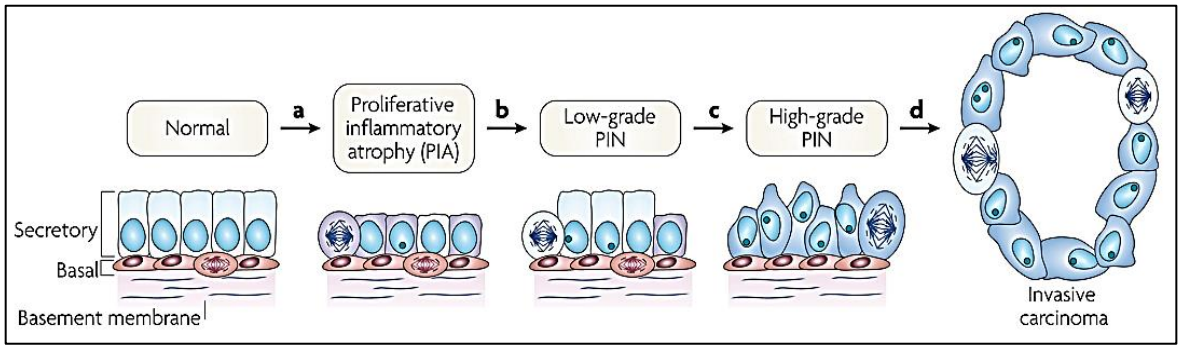

Figure 2.4 The PCa progress. Adapted from De Marzo et al. (2007).

2.1.3 Recent Diagnostics of PCa

PSA screening is the most widely used detection of early diagnosis of PCa among other methods to date, since the diagnosis is fast and easy to process. Although the results have already shown reduction of the death rates (relative reduction, 20%), this most popular diagnostic test contributes to the poor results which are far from accurate (Roobol and Carlsson, 2013). In special test cases, PSA results are always neglected as it is not that capable to distinguish the increased levels in non-cancerous statuses, e.g. prostatitis, benign prostate hyperplasia (BPH), or other chronic inflammations. Therefore, the progress in

development of PCa detection with respect to non-invasive methods are certainly encouraged since the unspecific and insensitive results are inaccurate in other conventional methods (Ramirez et al., 2008, Shariat et al., 2011).

Recently, a plethora of diagnostics has been established using biomarkers as the foremost strategy. The biomarker itself defines an explicit substance secreted or is present in certain biological systems (i.e. cell), which responds to the status of its particular condition. Therefore, it harnesses to reveal any pathological symptoms and may lead to better prognosis, such as monitoring the progression of disease, envisaging further appropriate therapies as well as survival after medical remedy. In regards to cancer treatment, biomarkers can either contribute in improving safety and efficacy or become a target of the cancer-drug's application (Madu and Lu, 2010). New biomarkers are discovered by using such advanced technologies, micro-array or parallel-assays leading *down to*-gene level. Understanding *what* currently happens at the gene-level is beneficial to the interpretation of the health status of corresponding cells in biological systems (Negm et al., 2002).

Nowadays, there are several types of PCa biomarkers that have been established. The characteristics of biomarkers vary depending on their signature origin. In order to attain higher performances and synergic outcomes, biomarkers are commonly combined with each other. Instead of PSA, the other well-known biomarkers of PCa are PSMA, KLK2, PSCA, EPCA, AMACR, and uPA (Bradford et al., 2006, Shariat et al., 2011, Dimakakos et al., 2014). Each role in the PCa detection is described below.

2.1.3.1 PSA

PSA is one of Kallikrein subtypes secreted in the prostatic epithelium of prostate gland by replacing the damaged prostatic acid phosphatase (PAP). To accomplish the preliminary need, US Food and Drug Administration (FDA) approved PSA as a standard method for early screening of PCa (Stamey et al., 1987). PSA has proteolytic activity which involves the degradation of the proteins associated with seminal vesicles to release active sperms (Rittenhouse et al., 1998). Several studies have been conducted with PSA, a promising strategy for PCa detection (Papsidero et al., 1980, Lowe and Trauzzi, 1993, Wang et al., 2002, Tosoian and Loeb, 2010).

2.1.3.2 PSMA

Prostate-specific membrane antigen (PSMA) is one of the folate hydrolase type II membrane proteins which are composed of internal and transmembrane amino acids represented by 7E11-C5.3 murine monoclonal antibodies. PSMA is expressed by prostate tissues in any condition, either normal or cancerous. Regarding detection purpose, PSMA can be collected or detected from prostate tissues, blood circulation and serum by using immunohistochemistry (IHC), Western-blot, or enzyme-linked immunosorbent assays (ELISA) (Horoszewicz et al., 1987, Ross et al., 2003, Chang, 2004). A study of using Western technique showed that PSMA scores were raised in hormone refractory tumors of post-prostatectomy patients, revealing that PSMA level may correspond to deprived clinical outcomes (Murphy et al., 1998, Tricoli et al., 2004). PSMA serum level was elevated along with age and was significantly increased in men over fifty years old. However, further study indicated that an increase of PSMA in serum levels did not associate with disease

aggressiveness. On another hand, due to the tumor differentiation status, some studies have discovered that the levels decrease in chronic diseases (Tricoli et al., 2004).

2.1.3.3 KLK2

Human kallikrein 2 (KLK2) are similar in structure to PSA, due to the same origin cluster of Kallikrein family. As compared to PSA, KLK2 has an auto-activation for itself and plays an important role in the activation of PSA in prostate gland (Rittenhouse et al., 1998). Further, it also contributes in PCa invasiveness (Yousef and Diamandis, 2001). Several studies revealed the potency of KLK2 in combination with other biomarkers. KLK2 leveled higher in cancerous prostate patients as opposed to BPH's patients. When KLK2 combined with PSA in a serial test by IHC staining, the performance of PSA detection was improved to be more accurate to the patients who had total of PSA between 4 and 10 ng/mL (normal is ~ 4 ng/mL) and even problems with lower urinary duct. These studies found better results, when KLK2 was employed altogether with total PSA and free PSA measurements, than using %free PSA alone (Becker et al., 2000). Combination of KLK2 with alpha globulin glycoprotein, macroglobulin, and protease inhibitor which bound to PSA increases specificity and sensitivity results (Karazanashvili and Abrahamsson, 2003). In another study, KLK2 combined with total PSA gained more reliable results as compared to either of KLK2 or total PSA test, in stand-alone measurements (Martin et al., 2004).

2.1.3.4 PSCA

Prostate stem cell antigen (PSCA) is mainly recognized on prostate gland and its mRNA is also detected in placenta, bladder, stomach, colon, kidney, and small intestine (Reiter et al., 1998, Gu et al., 2000, Cunha et al., 2006). In prostate tissue, PSCA is expressed in the basal

and secretory epithelial cells as well as in neuroendocrine cells (Gu et al., 2000). Even though it is commonly obtained from blood stream or body fluids as serum biomarker, it has abundant substandard sensitivities with no significant capability to distinguish between the malignant and the benign diseases. To compromise, several attempts revealed that PSCA was recognized to be able to exhibit disease sensitivity, specificity, and prognostic values (Hara et al., 2002).

2.1.3.5 EPCA

The early prostate cancer antigen (EPCA) is a marker associated with nuclear structural proteins, expressed by the tissue and other precursor lesions of PCa, typically around the proliferative inflammatory atrophy and PIN (Dhir et al., 2004). The study of Uetsuki and co-workers correlated the EPCA with the initial carcinogenesis and found that EPCA is not associated with the disease stage or Gleason score after sampling radical prostatectomy (Uetsuki et al., 2005). This protein has also been recognized in patients who had preliminary negative biopsies. However, the early biopsy with ambiguous predictions are not recommended until the indication of PCa is clearly defined (Dhir et al., 2004).

2.1.3.6 AMACR

Alpha-methylacyl-CoA racemase (AMACR) is one of the isomerases family, which is a branch of peroxisomal beta-oxidation and has a role in metabolism cycle (Brawer et al., 1992, Catalona et al., 1997, Qu et al., 2014). The genomic studies showed that AMACR chromosomes contain genes which are responsible in PCa regulation and associated to increase risks of PCa in family who derived PCa hereditary (DiGiuseppe et al., 1997). It has been noted that over-expression of AMACR contributes to development of PCa stage in PIN

(Brawer et al., 1992, Catalona et al., 1997). Due to its high expression level, AMACR has been detectable in biological fluids, for example in blood serum, and commonly exists in urine of men after having prostate biopsy (Cooperberg et al., 2003, Jemal et al., 2005, Lin et al., 2012). However, determination of AMACR concentration along with the prostate biopsy bargains a classical issue of soreness since the biopsy tends to injure and generates a worse implication (Sreekumar et al., 2004). In addition, the over-expression of AMACR can induce the humoral immune activity which may lower the AMACR serum detection rate (Tricoli et al., 2004).

2.1.3.7 uPA

The urokinase plasminogen activation (uPA) is related with the multistage of PCa. Through binding to the uPA receptor (uPAR), the serum protease of uPA plays a role in several phases of tumor development as well as progression by converting plasminogen to plasmin, then activating the proteases and starting the extracellular matrix degradation (Duffy, 2002). Gupta and co-workers mentioned that overexpression of both uPA and plasminogen activator inhibitor type-1, another inhibitor of uPAR, associates with the adverse pathological effect and increases the risk of entire and aggressiveness of PCa in patients who are in radical prostatectomy treatment (Gupta et al., 2009). Moreover, the present of uPA along with elevation of uPAR as well as prostatic tumor-load and its significant decrease levels after prostate removal indicate high level production of circulating markers (Shariat et al., 2007).

2.1.3.8 Immunohistochemistry

Immunohistochemical (IHC) analysis is a common technique performed after biopsy. It is an essential pathological examination in the case of poor results of PCa determination if the type

of the cells is difficult to assign decisively under biopsy. To perform IHC, the tumor tissues are sampled and treated in frozen packs or engrained in liquid paraffin and partitioned onto slides containing monoclonal antibodies to be stained with chromogenic substances. The stained cells are subsequently investigated under microscope. However, this method is known as an invasive method which can leave inconvenience adverse effects, requiring laborious equipment as well as trained people to assess the staining and produces qualitative results that may vary depending on the subjectivity (Erdile et al., 2001). This missing prognostic evidence has initiated a substantial "over-treatment" for patients who apparently only need conventional management.

Finally, although most biomarkers have shown quite promising results, they are produced and expressed normally by the prostate gland, but any fluctuating conditions, such as inflammatory disease, can reduce their adequate status for giving a reliable result in PCa screening. For instance, the raised serum concentrations of biomarkers induced by local release from the prostate gland, can be possibly due to the BPH or prostate infection. An insufficient diagnosis of PCa is such a major clinical issue till now which is exposed by the incapability of the current techniques to readily distinguish the aggressiveness from indolent tumors in PCa patients with low Gleason score upon biopsy. Therefore, it is valuable to use the advanced methodologies which can fulfill reasonable expectations of the correct PCa diagnostic quantitatively and accurately without severity of the side effects, such as using biosensors platform (Sartor et al., 2008, Shen and Abate-Shen, 2010).

2.2 Biosensors

A biosensor is a simplified and integrated version of a complex analytical instrument compiled into one compartment of a sensing system. Its work format contains three important components to respond to the specific biological substances or analytes as target, *viz.*, the biological receptor (bioreceptor/biorecognition), as the sensing function; the transducer, as a signal converter and quantifier; and a signal reader, as signal processor and interpreter (**Figure 2.5**). A biorecognition element is commonly extracted either from biological (e.g. antibody, antigen, cells, and enzyme) or environmental (e.g. glucose, lactate, any other organic compounds) resources. As opposed to the conventional methods (e.g. HPLC, LC-MS, spectrophotometry), biosensor embraces the biorecognition as a detector agent to identify the nature of the analyte as the target based on its selectivity properties (Vilarino et al., 2009). The application of biosensors have been used broadly in many fields, such as pharmaceutical drug discovery, medical diagnosis, food safety, environmental waste control, and military defense (Turner, 2013).

Emerging biosensor for the early cancer detection are beneficial to turn the complicated cancer screening procedures into a simplified and reliable one. In terms of early detection, biosensors usually target the cancer biomarker as they represent the existence of particular substance produced by cancerous cells and correspond to the dynamical changes of physiology of cancer cells (Strimbu and Tavel, 2010). The attention of cancer biomarkers is thereby predominated by DNA, RNA, proteins, enzymes, and metabolites which are mostly detected in blood serum, blood plasma, urine, and cerebrospinal fluids (Tothill, 2009, Bohunicky and Mousa, 2010). Further, biomarkers are also essential in monitoring the drug

delivery in cancer therapy as well as the progression of cancer (Anonym, 1996, Basil et al., 2006).

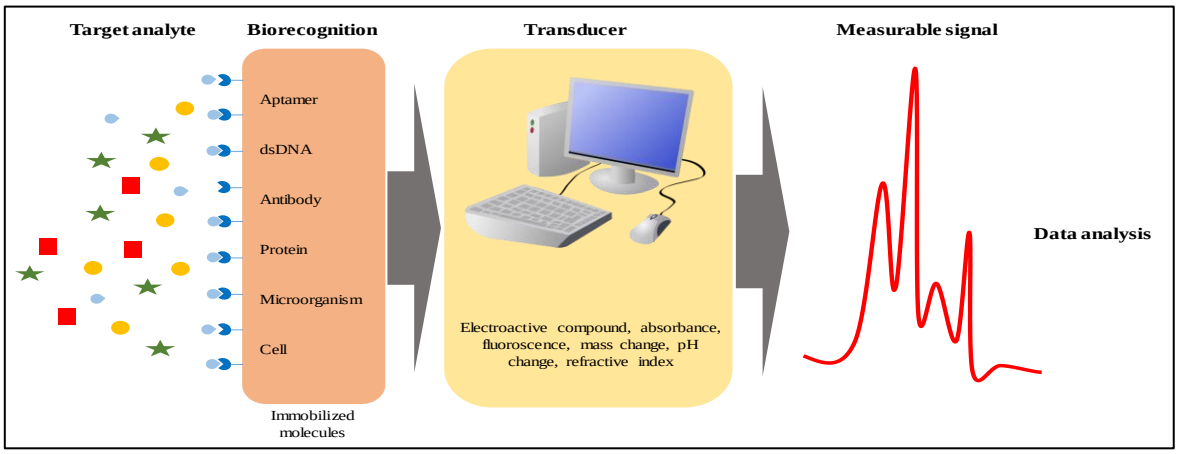

Figure 2.5 Scheme of biosensor workflow.

2.2.1 Molecular Targets

Protein is normally available in any biological origins at various concentrations. In cancer research, most cases of carcinogenesis are evident in the protein structure alteration and modification, that may potentially be mutated. Targeting proteins are more likely to be well-noticed due to their large structure with numerous binding sites allowing it to be easily determined by biorecognition. In biosensor, the detected protein molecules are accessed as a measurable signal representing its concentration. Nucleic acid (e.g. DNA) consists of nucleobases connected in a chain carrying numerous slices of genetic information as hereditary characters in the current living cells. DNA has its own unique property in each living organism which also supports the recognition of any cellular disruption due to unpredictable diseases (Liu et al., 2012, Sohrabi et al., 2016). For example, mutations in particular DNA could initiate severe diseases, such as cancer, which is inheritable due to the single mutation in the nucleobases structure leading to the epigenetic impact for the dynamics

of physiological properties (Laubenbacher et al., 2009). Therefore, its importance now points toward on how one distinguish the cancerous and the normal cells appropriately based on the pathways of gene regulation, cell metabolism, signaling, or other biological changes.

2.2.2 Biorecognition

2.2.2.1 Antibody and Biomolecule

Molecular targeting in cancer detection is commonly associated with the recognition trend of biomolecules toward the cell surface properties, e.g. protein, enzyme, metabolite (Sinha et al., 2006). Antibody is one of the most extensively used biorecognitions in several biomedical fields nowadays, especially for detection and escorting the anti-cancer agent therapies to the sick cells to promote the induction of anti-tumor immune responses (Weiner et al., 2010). Generally, the principle of antibodies on the way to targeting the sick cells is through the binding of the identifiable sites of the molecular signatures over-expressed on the cell surface, which is known as *antibody-antigen* interaction (Scott et al., 2012). By targeting the specific cell signatures, antibody is able to recognize its target selectively (Yang et al., 2015). Similarly, some biomolecules are selected to define a high-affinity binding in targeting receptors, i.e. folic acids for folate receptor (Kukowska-Latallo et al., 2005). They are involved in recognition of the target cells for diagnostics purposes as well as the drug delivery to particular molecules. For example, the folate receptors on the target cell surfaces will be immediately induced to initiate self-receptor endocytosis after activation by folic acids (Kukowska-Latallo et al., 2005, Yang et al., 2013). However, there are only few antibodies and molecules which are well-represented for the cancer cells targeting. The comparison between aptamers and other biomolecules is presented in **Table 2.1** below.

Table 2.1 Comparison of the biorecognitions in whole-cell detection.

	Aptamers	**Other Biomolecules**
Stable in various temperature	√	-
Resistant to nuclease degradation	-	√
Resistant to immunologic defense	√	-
Ease to produce	√	√
Production cost-savings	√	√
Low toxicity	√	-

2.2.2.2 Nucleic Acids

Nowadays, the strategy of cancer diagnostics has been merged into the analysis of DNA sequences (genomic), such a molecular level determination suggesting a highly sensitive method to identify genetic variation. Harnessing the double Witson-Crick idea, hybridization of nucleic acids can be employed for the biosensor design of a probe tool for detection of gene mutation or type of the diseases. The duplex formation performed between the capture probe and the target oligonucleotides can be recognized through an appropriate hybridization process or other related changes initialized from the binding evidence. The hybridized state indicating the target oligonucleotides will then appear as a readable signal (Lucarelli et al., 2004, Sohrabi et al., 2016).

The capture probe is commonly generated from various chemical materials that has been designed to recognize the conformational body of the target. However, there are limitations in the length of oligonucleotides used as a probe. Generally, to obtain a higher specificity, the capture probe length is only from 18 up to 25 nucleotides. Extremely long probes can potentially disturb the analysis reading with unexpected hybridization yields (Lucarelli et al., 2008). Further, a biosensor platform which is based on the labelling approach, so-called

microarray, has taken into account the hybridization mechanism of short nucleic acid strands as a new therapeutic agent in the design of sequencing libraries, genome screening, and pathogen detection (Mascini et al., 2005).

2.2.2.3 Aptamers

Cell membrane has critical purpose in regulating cellular life as well as the functions of growing, proliferating, signaling, metabolism processing, and apoptosis (Revankar et al., 2005, Blobel, 2005). With respect to the cancer, one of the specific reasons explaining how mutations lead to cancer with physiological disorders, is due to the unnatural habits of expression levels and/or malfunction of cell membrane receptors (Downward, 2003, Hollingsworth and Swanson, 2004). Several studies have explored the cell membrane receptors as biomarkers by giving reliable results for a specific cancer investigation, such as diagnosis and further therapy. However, most of biomarkers contempt tedious results, showing the failure of selectivity tested among type of cancers (Luo et al., 2003, Chen et al., 2006, Nishizuka, 2006, Omenn, 2006).

Furthermore, in order to reveal the specific detection, one should address how to distinguish between normal and abnormal cells by using proper methodology with good validation to ensure the next step taken in clinical practice. By doing so, the conventional study practically begins from the molecular stage to classify the disease into genomic or proteomic level. Even though this will provide quite significant outcome, this method is still time consuming and quite tedious due to its correlation with abundant track-record data from patient (Shangguan et al., 2006, Tothill, 2009, Fang and Tan, 2010). On the other hand, polymerase chain reaction (PCR) and nucleic acid amplifications (NAATs) are two commonly used techniques to

sequence the gene of interest as well as to sort the genetic and molecular information of the target gene. However, the complex steps starting from RNA's expression stage, long isolation control, and PCR's variability handling remain less effective (Ghossein and Bhattacharya, 2000, Iinuma et al., 2000, Yin and Grimwade, 2002, Caliendo et al., 2013).

Aptamer has been introduced as synthetic oligonucleotides (either RNA or DNA) populated from several iterative sequencings processes of systematic evolution of ligands by exponential enrichment (SELEX) against specific targets involving control of biomolecules to retain selectivity of the oligonucleotides. Aptamers cover a large number of biological target types, from the small to large molecules, for instance toxins, proteins, and cells (Djordjevic, 2007). Further, the most common targets of aptamer to detect cancer are proteins present on the cancerous surface. Unfortunately, not all the proteins have readily been purified thus allowing to be recognized. The proteins in complex membranes are more likely to be shielded or difficult to be accessed. To overcome this, the target proteins are usually exposed to an extended purification before involved in SELEX processes. However, some pressurized processes may break the nature of protein conformations, and affects to lower protein expressions with bulk of hydrophobic tendencies (Cerchia and de Franciscis, 2010).

Cell-based SELEX (or cell-SELEX) is a technique used to generate aptamers that has specific binding interactions to whole-cells as the target. This is an alternative solution to maintain the aptamer selectivity as compared to the conventional SELEX in targeting the cell proteins. Cell-SELEX principally works with the introduced cell-body or whole-cell which naturally contains the main targets, such as important proteins or other biomarkers. Therefore, this

method can deal with any cell signatures without any prior knowledge of unknown protein conformations on the cell surface (Cerchia and de Franciscis, 2010).

The first process of cell-SELEX involves synthesizing the nucleotides of single-strand DNA/RNA (ssDNA/RNA) (10^{15} - 10^{16}) sequences from random oligonucleotides which consists of the primary combination of nucleic acids. Under selected environments, the nucleotide library is incubated with the target cells until the sequences are bound to the target cells. The unbound sequences are removed, and the restricted sequences are eluted from the target binding to get into the next process. The selected oligonucleotides are then introduced to the target and control cells in an event, to interrogate if there is still a binding possibility present toward the control cells. Subsequently, the enriched selected sequences are separated from the unrestricted cells. The enriched aptamers will be incriminated to the next round of counter as well as further selection processes, until the most enriched sequences are collected. The resulting aptamers in final stage are ready for use in selectively binding toward the target cells (**Figure 2.6**) (Tombelli et al., 2005, Djordjevic, 2007).

All iterative processes are controlled by flow cytometry processes investigating the fluorophore-labeled primers to show the binding affinity (Sefah et al., 2010). Once the high affinity aptamers are obtained, the cloning and sequencing clones will vindicate the specific sequences and conformation of selected aptamers (Luzi et al., 2003). To better achieve the recognition capability of the aptamer to target cells, the selected aptamers are tested to distinguish the real cells among other *look-alike-target cells*, by incubating the aptamers into the complex cells (Marshall and Ellington, 2000).

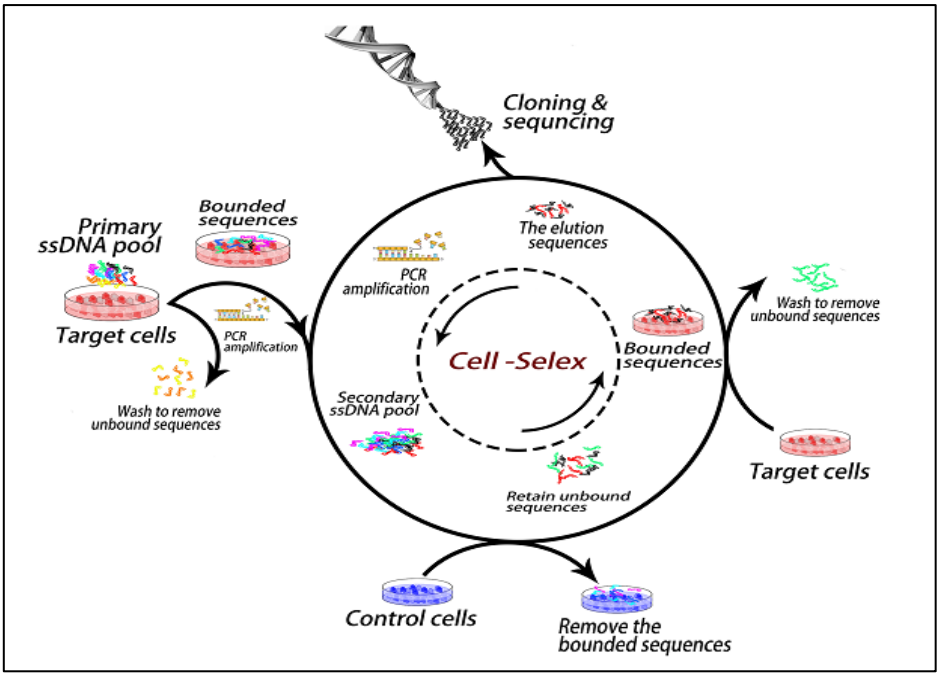

Figure 2.6 Cell-SELEX Procedure. Adapted from Wang et al. (2014).

Since the cell-SELEX process only involves the capability of oligonucleotides in binding the target cells directly, the information of the target cell's morphology, conformation, and appearance, are not further required at the prior stage. However, this is in order to manage and retain the natural conformation of biomolecules composed on the target cells from an ineffective protein cell purification. By doing so, several processes of molecular probe development and elucidation of biological mechanisms can be significantly simplified by approaching the cell-SELEX (Tang et al., 2007, Ye et al., 2012).

2.2.3 Transducers

2.2.3.1 Optical

The development of optical biosensors enhances the performance of biosensors, especially for label-free detection. This technique benefits the light power by transmitting it to the wavelength which is in response with the changes of biological properties occurred between

molecular recognition and the analyte. With the real-time processing, these types of biosensors are widely used for numerous analytes detection simultaneously in chemical and biological substance (Soldatkin et al., 2003, Dey and Goswami, 2011). The most commonly used methods for optical biosensors are fluorescence and surface plasmon resonance. Relying on the excellent fundamentals of signal binding quenching and intensity and no radioactive used, fluorescence offers tremendous advantages. This type of method leads itself to be exciting in terms of monitoring the frequency change between the analyte and fluoro-probe (Tatiana Duque et al., 2013).

Surface plasmon resonance (SPR) is one of the frequently used optical techniques employing a specific surface that can be integrated with any biosensors fabrication, such as microfluidics or lab on chip designs. Currently, it is commercially available for cancer detection (Joon-Yong et al., 2006, Wang, 2011, Dey and Goswami, 2011). The SPR processing is characterized by interrogating the wave signals from the resonance alterations in different refractive indexes assisted with the presence of the light of first resonances occurred at the recognition surface where the analyte is adsorbed (Chien and Chen, 2004, Fan et al., 2008, Gupta and Verma, 2009, Bhatia and Gupta, 2011). Several advantages of SPR sensors include easy handling to perform, inexpensive, high sensitivity, and label-free (Fan et al., 2008). As opposed to SPR, the resonance reading of micro cantilever is performed by shifting the induced stress on its surface, which is available whilst the target analyte binds to its specific recognition and the electromagnetic wave is given. Meanwhile, the other sides of the surfaces are retained not to be interactive with the sample. The advantages offered by this method are label free, miniaturizable, and small volume needed in operation (Fritz, 2008, Alvarez and Lechuga, 2010).

Several PCa biosensors studies have been reported by using optical methods and most studies showed excellent results in selectivity as well as sensitivity. Dharmasiri and co-workers reported microfluidic technique using a modified-high throughput micro sampling unit (HTMSU) bead to observe the prostate cancer circulating tumor cells (Dharmasiri et al., 2009). A10 RNA aptamers and anti-EpCAM antibodies were immobilized on the modified-HTMSU to compare the cells binding efficiency (**Figure 2.7 (a)**). The recognition performance was investigated by means of linear velocity method, where about 90% of ± 250 LNCaP cells had been successfully captured in 1 mL of whole blood in optimized velocity of 2.5 mm/s (optimized time was at 29 s) (**Figure 2.7 (b)**). This velocity was faster than that of anti-EpCaM antibodies results (2.0 mm/s). In addition to establish an appropriate therapy, this research currently needs to perform molecular profiling assay (Dharmasiri et al., 2009).

In the purpose of cell-count, microfluidics offers an integrated simple design of biosensors for responding the electricity signal of down to single cell detection, such as in circulating cancer cells (CTC) detection (Etayash et al., 2015). Etayash and co-workers applied the *antibody-antigen interaction* to observe the captured CTC of MCF7 cancer cells using micro cantilever. The modified peptide was employed to distinguish the cancerous from the normal cells, resulting in a detection limit down to 50-100 cells/mL and with a successfully real-sample application as high as 80% of the captured cells. As explained above, the results were enhanced by utilizing other biosensor techniques which are based on surface power inherence, such as SPR and micro cantilever and with respect of fulfillment of other biosensors requirements thus presenting rapid and favorable biosensors (Etayash et al., 2015).

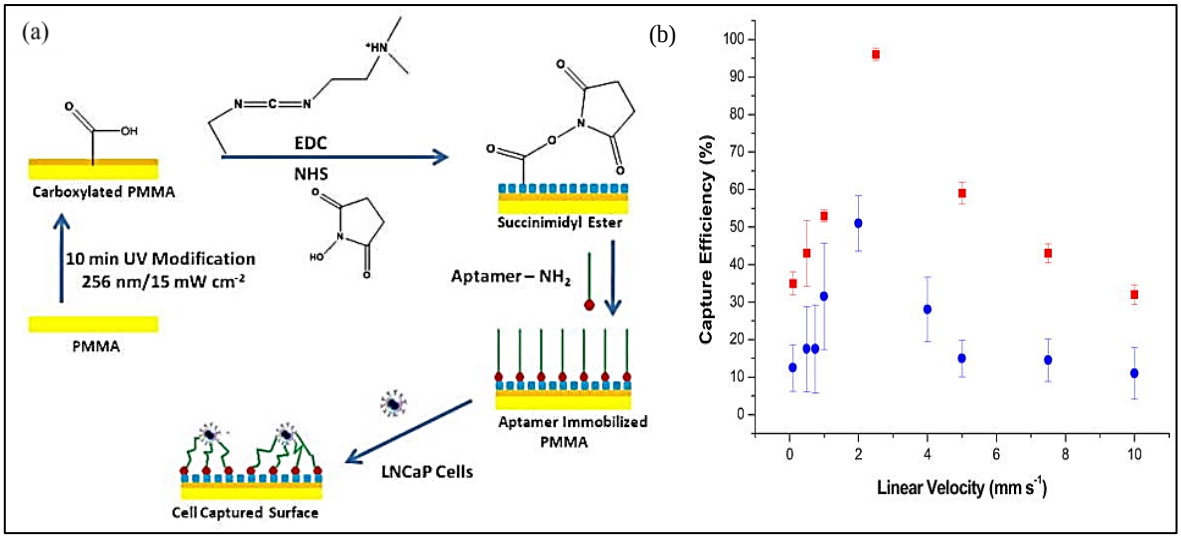

Figure 2.7 (a) Schematic process of fabrication and biorecognitions immobilization on the HTMSU; (b) Capture efficiency differences between A10 RNA aptamers (red squares) and anti-EpCAM antibodies (blue dots) toward LNCaP cells. Adapted from Dharmasiri et al. (2009).

Wang and co-workers investigated aptamers which specifically binds to PC3 cells (Wang et al., 2014). The Wy5a aptamers, which had been observed and chosen from cell-SELEX, showed high binding affinity toward the target cells, and also selective among other PCa cells types as well as different tumor cells. The aptamers selection was carried out by flow cytometry imaging to point out the best aptamers binding toward PC3 cells. To figure out the sensitivity and selectivity of the selected aptamers, the fluorescent technique was used to distinguish PC3 cells among control cancer cells. The fluorescence intensity showed that only Wy5a aptamers bound to the PC3 cells for more than 85% (> 1.7 x 10^5) cells (K_d = 73.59 ± 11.01 nM); whereas no binding appeared with other cancer cells (Wang et al., 2014).

2.2.3.2 Electrochemical

Electrochemical techniques have been known as an advanced method in generalizing a prompt and reliable compliance results for biological and clinical analysis purposes.

Additionally, this prevents unexpected drawbacks which may be resourced from diverge therapeutic decision. Taking into account its advantages, electrochemical biosensors offer various benefits for the user, e.g. low cost, ease of handling, portable, and simple for sensors fabrication (Pohanka and Skladai, 2008, Grieshaber et al., 2008, Ronkainen et al., 2010). These techniques have already been applied in either non-biological or biological analyte analysis, down to tissue and cell levels (Drummond et al., 2003, Xiao et al., 2006, Doerr, 2011, Wang, 2011, Arya and Bhansali, 2011, Pheeney et al., 2012, Wen et al., 2012, Das et al., 2012). Selecting the platforms for constructing the biosensors encourages the specific knowledge about (bio) material recognition used to interact with the target of interest, the native information of the target, proper boundaries which will provide the electrochemical signal enhancement, and a comfy data interpretation (Grieshaber et al., 2008, Ronkainen et al., 2010).

Electrochemical biosensors are clustered to amperometric, potentiometric, impedance, and voltammetric methods. Briefly, the amperometric method determines the electronic differences of electroactive substrates which are occurred due to reduction-oxidation mechanism at constant potential. Each current measured is linear to each concentration of the substrate applied. Whereas, the potentiometric technique is the method to examine the potential difference behavior of the bulk concentrations toward reference electrode at zero current condition. In comparison with the amperometric technique, the voltages recorded will define the amount of substrate concentrations (Grieshaber et al., 2008). Similarly, impedimetric method permits the conductivity interactions toward the target biomolecules on the electrode surface. During the measurements, the redox active agent is commonly employed in order to notify any circumstance change of electrical properties upon the

complex formation between recognition agent and analyte. The alteration detected then will be transformed into electronic transfer resistance (R_{et}) signal with respect to the impedance behavior (Lisdat and Schäfer, 2008). Another most popular electrochemical technique is voltammetry which occupies the benefits of amperometric and potentiometric methods in single type measurement. In other words, this technique involves the currents alteration in measurement, while controlling the changes in potential (Grieshaber et al., 2008, Ronkainen et al., 2010).

Another method is electrochemiluminescence (ECL), a blended method between electrochemical and chemiluminescence techniques, which is usually used for a wider analyte detection. As this method is of combination, the substrate actual reading will be done first electrochemically with monitoring the potential until the electron leaps are produced. Subsequently, in the presence of light and the support of additional precursor, the current will be converted into reactive species with releasing the measurable light (Zheng et al., 2001, Chovin et al., 2004, Richter, 2004).

Emerging aptamer in biosensor systems has been developed by Min and co-workers for PSMA-expressed PCa cells detection (Min et al., 2010). Through streptavidin-coated quantum dots nanoparticles as a linker and biotin functionalization, the authors combined dual aptamers which have different targets to enhance the binding complex in targeting PSMA-expressed PCa cells (LNCaP and PC3 cells), in which A10 RNA aptamer was used to recognize the PSMA (+) PCa cells and DUP-1 aptamer was as the PSMA (-) PCa cells. Several preparations were being concerned toward the aptamers on the electrode surface before they were evaluated with electrochemical impedance spectroscopy (EIS) technique.

The interesting part of these stages is to determine the mixing ratio of both aptamers which is one of very influencing steps since it affects the sensitivity and selectivity in targeting the cells. The increasing signal was noticed once the PCa cells were introduced on to the gold electrode surface indicating a higher resistance of electron transfer (R_{et}). The presence of the biological elements blocked the working electrode, thereby hindering the redox probe to access the surface. Consequently, this biosensor satisfied with the detection limit as low as 100 cells/mL for both LNCaP and PC3 cells (Min et al., 2010).

Moscovici and co-workers reported electrochemical biosensor using enzyme-modified gold electrode array to simplify and eliminate the use of invasive sampling method (Moscovici et al., 2013). The microfabricated chip arrays were constructed using photolithographic technique and some glass materials as a substrate (**Figure 2.8 (i)**). The unique and tunable gold surface electrodes consisted of two active sites that can be performed in the same moment. One electrode site is used to apply the samples and another electrode site is for the blank or normal cells as control. The DU145 cells samples were detected by anti-epithelial cell adhesion molecule (EpCAM) antibody electrodeposited on a gold surface. The electrochemical signal decreased by the time DU145 cells were applied, suggesting blocking currents occurred during the cells measurement. The area size of working electrode influences the detection limit obtained for biosensors. Among three different areas, the medium one (150 µm) provided an increase sensitivity of the sensors which was 125 cells per 150 µm number of cells observed (**Figure 2.8 (ii)** and **(iii)**) (Moscovici et al., 2013).

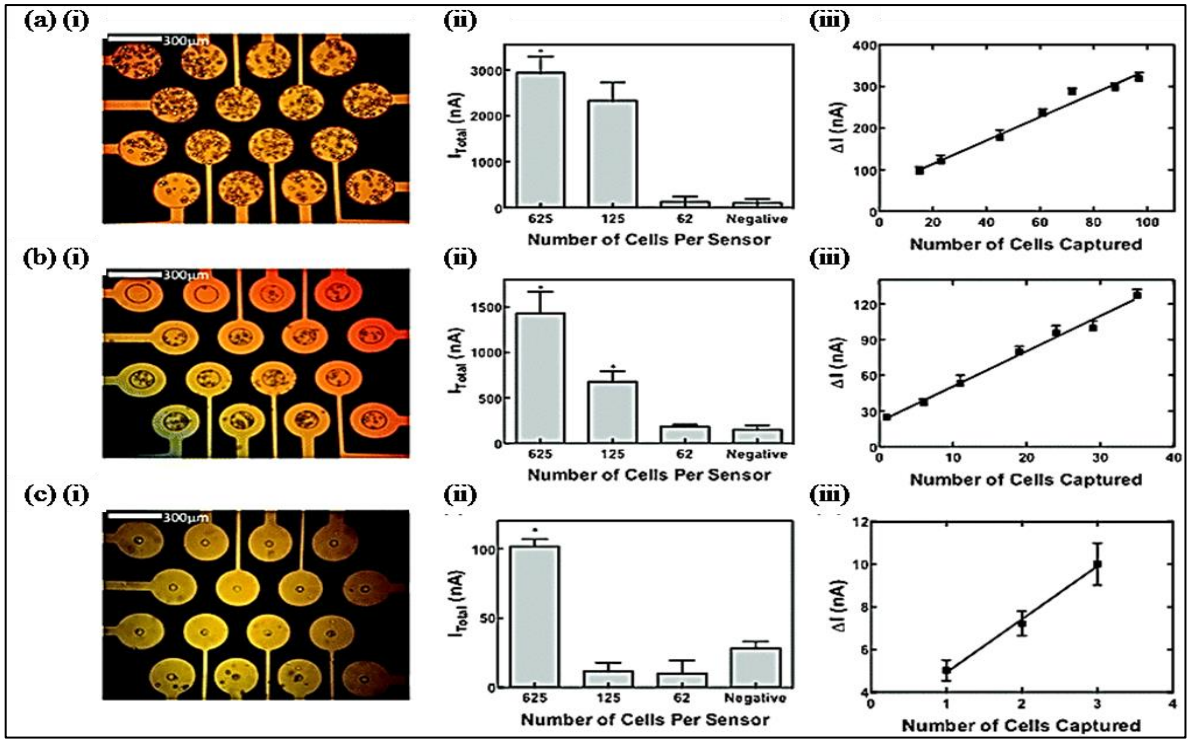

Figure 2.8 (i) Microscopic depictions of DU145 target cells bound to sensor arrays in three type of sizes: (a) 50 µm, (b) 150 µm, (c) 300 µm. (ii) The electrochemical signal with DU145 cells incubation, (iii) showed correlative signal change on sensor surface. Adapted from Moscovici et al. (2013).

In another study, Yang and co-workers reported a sandwich ECL biosensors using antibody as biorecognition for PCa cells detection (Yang et al., 2015). The ECL biosensor was constructed by covalently immobilizing anti-PSA antibody as biorecognition agent on glassy carbon electrode coated by graphene oxide (GO-coated GCE). As governed in sandwich architecture, PC3 cells were targeted on the surface of the system, allowing the bound ruthenium-labelled wheat germ agglutinin (WGA) lectin to yield signal corresponding to the captured cells (**Figure 2.9 (i)**). EIS was then employed to investigate interfacial profiles of the biosensor system. Approach to quantifying the cells was achieved by measuring the ECL intensities against the PC3 cells concentrations (**Figure 2.9 (ii)**). The detection limit was calculated of 2.6 x 10^2 cells/mL. Even though it shows quite good results for a fabricated

cancer cells biosensor, it is important to note that PSA was still used for antibodies recognition in this study, thus it might have suggested an ambiguous result if other factors causing PSA elevation could raise in the same time (Yang et al., 2015).

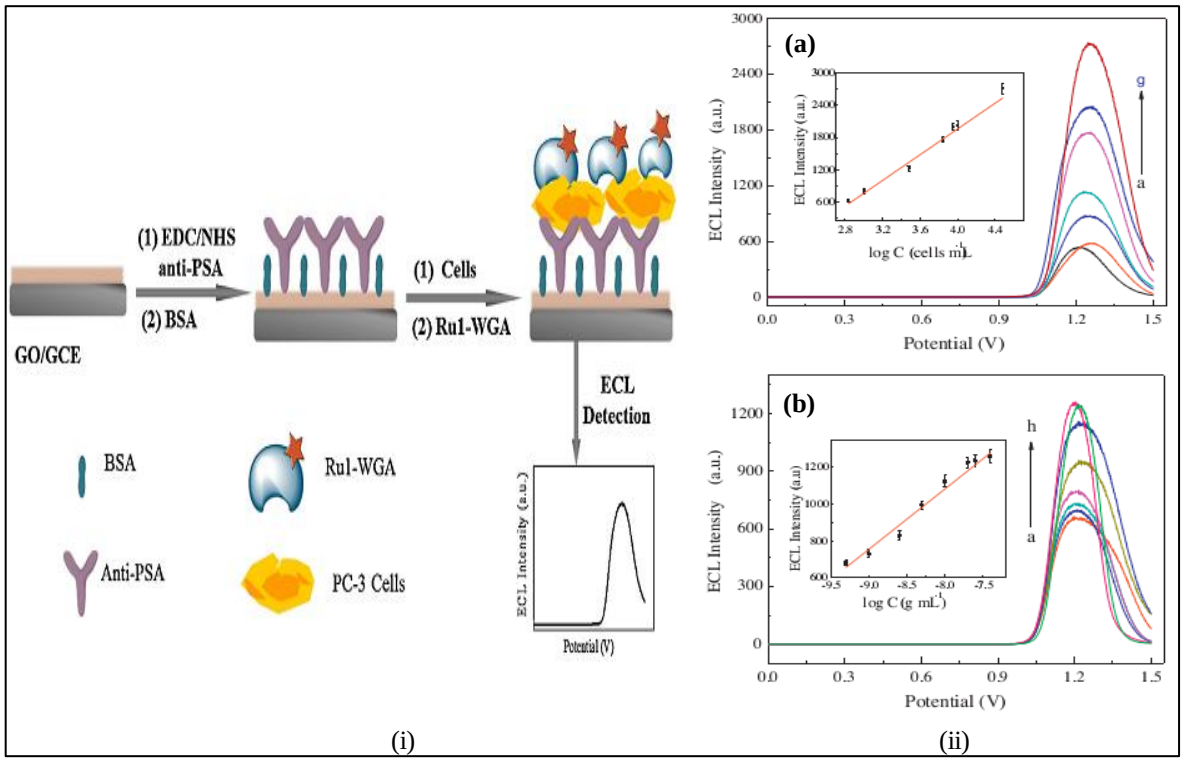

Figure 2.9 (i) Illustration of fabrication process of anti-PSA antibody/GO/GC biosensor; (ii) The ECL responses of biosensor after: (a) PC3 cells incubation at $7.0x10^2$ to $3.0x10^4$ cells/mL (a to g) concentrations; (b) PSA incubation at 0.5 to 40.0 ng/mL (a to h) concentrations. Adapted from Yang et al. (2015).

The electrochemical microfabricated chip with patterned microstructures has been developed by Safaei and co-workers to isolate and detect prostate cancer cells (VcaP cells) (Safaei et al., 2015). The VcaP cells initially were labelled with anti-EpCAM magnetic beads nanoparticles to distinguish among other cells in complex sample. The device employed gold electrodes chip as primary surface and entrapment patterns between two magnetic arrays which X-shaped design. The biosensing concept was based on electrochemical-ELISA (EC-ELISA), combining electrochemical and ELISA techniques which emerged different drag

force toward amplitude to obtain the labeled target cancer cells. At optimized potential, the target cells entrapped were recognized by biotin-anti-CK18 antibody and subsequently, alkaline phosphatase (ALP) catalyzed p-aminophenyl phosphate (p-APP) substrates into enzymatic products (p-aminophenol), which was sensitive to electrochemical changes. The oxidized p-aminophenol gave an amplified differential pulse voltammetry (DPV) signal which correlated with the total of VcaP cells captured on the chip surface. This study revealed detection limits down to 1 μM cells per chip in buffer medium. Yet, in the case of using more complex blood medium mixed with non-specific cells, the signals background was found to be increase as compared to the signals in the buffer medium. This indicated that there was still nonspecific binding coverage of the surface on the electrodes (Safaei et al., 2015).

2.2.4 Nanomaterials

Emerging nanomaterials in biosensor technology has been acknowledged as excellent strategy to enhance the biosensor performance (Cuenot et al., 2004, Chen et al., 2010, Jha and Ramaprabhu, 2010, Putzbach and Ronkainen, 2013). In particular, numerous nanomaterials such as quantum dots, metallic, magnetic, as well as carbon-based material e.g. graphene, graphene oxide, and carbon nanotubes (CNTs) have successfully shown a tremendous effectiveness in combination with various biorecognition, harvesting electrons on the transducer surface, and providing a virtuous electrocatalysis mechanism (Burda et al., 2005, Wang and Lu, 2009). A wide nanosurface feature (consisted of the less than equal to 100 nm particle) is very beneficial to build up sensitivity as well as to drop the limit of detection by means of immobilizing specific biomolecule for recognition (Holzinger et al., 2014). The example for this case, graphene and its derivatives have highly attracted the sensitivity in electrochemical biosensors due to its wide area surface and excellent

electrocatalysis and conductivity. Those benefits nowadays lead graphitic nanomaterials to be widely used in any biosensors development and drug delivery purposes (Li et al., 2009, Wu et al., 2013).

2.2.4.1 Graphene Oxide in Biosensors

The carbon-based structure seems to be an auspicious material employed in several fields over the latest decades due to its outstanding thermal, mechanical, and electrical properties. Its interactions with biomolecules benefit in numerous applications, particularly in biosensor medical diagnostic and drug delivery (Sun et al., 2008, Liu et al., 2008, Dong et al., 2010, Li et al., 2012, Xu et al., 2014). As one of the friendliest materials, graphite has been commonly used in our daily lives without any harmful effects. Its derivations into graphene and graphene oxide are expected to be less toxic in mild concentrations, hence readily applicable in biomedical functionalities. Graphene oxide (GO) is an exfoliated result of oxidized graphite consisting a single layer graphene sheet with oxygen functional moieties distributed along the surface. In its application, GO owns good aqueous dispersive process and provides major benefits in emerging by other materials, such as polymers in order to enhance the electrical and mechanical characteristics. These mesmerizing properties are drift by its unique compositions which consist of sp^2 carbon with sp^3 hybridized carbon and oxygen functional groups surrounding the surface. This particular presence of oxygen functional groups defines degree of GO solvation in organic solvent, which further is known as reduced-GO (rGO) (Chung et al., 2013).

The most commonly applied technique to synthesize GO is using Hummers method. The procedure is initiated by oxidizing graphite using $KMnO_4$ and H_2SO_4 to produce the graphite

salts, in which it will be governed as precursors of GO exfoliation during sonication process (Hummers Jr and Offeman, 1958). However, the real GO composition has not been defined yet since the different functional groups type would give different impact to GO properties. To date, several methods of GO synthesis have been anticipated. Most preliminary GO structures are proposed with a repeat-unit species on a lattice based model. The first model of GO had been deliberated by Hofmann and Holst, whether the GO has epoxy groups with formula C_2O playing a role on the surface plane (Hofmann and Holst, 1939). This model was further varied by Ruess with hydroxyl groups grafted on the surface plane, and sp^3 hybridized atoms were likely to be more considered than sp^2 (Ruess, 1947). Scholz and Boehm assumed a regular trend of quinoidal groups in crenellated backbone of GO surface and entirely detached the epoxy and ether species (Scholz and Boehm, 1969). Another work from Nakajima and Matsuo supposed that a GO lattice has similarity with $(C_2F)_n$ model suggesting a graphite intercalation compound where two layers of graphite substitute with an intercalated layer (Nakajima et al., 1988). The most recently model has been investigated by Lerf and Klinowski (He et al., 1996, Lerf et al., 1998). Different with the previous studies, the authors took into account an amorphous structure to describe the GO compositions based on the NMR and XRD studies, that GO contains epoxy and hydroxyl groups spread randomly along the surface plane. In further report, they updated that low numbers of carboxylic groups are also present on the edge of the GO surface (Lerf et al., 1998). Within this study, Lerf Klinowski model was considered for GO structure in MD studies.

Numerous biosensor platforms count on GO as a preferable material in biomedical application due to its good transfer process on substrate surface, low-cost synthesis, and its chemically modifiable surface. In addition, GO has been reported to have excellent

quenching performance for numerous fluorophores through non-radiative dipole coupling or fluorescence resonance energy transfer. GO has capability to drive the biomolecules from degradation impact of environment due to effect of steric-hindrance (Pu et al., 2011, Chung et al., 2013). In interaction with over all nucleotides, GO affords best exposure toward single-strand DNA (ssDNA). The adsorption pattern of ssDNA is more affordable than dsDNA since the helical structure of dsDNA avoids its nucleobases to interact directly with GO surface. This event benefits in detection of ssDNA with labelled-hybridization method encouraging a complex form of ssDNA (or aptamer) with its complement target thus, allowing a measurable signal change from a quenched to weakened signal. A fluorescence signal would be restored once the complex detached from GO surface (**Figure 2.10 (i)**) (Lu et al., 2009, He et al., 2010, Pu et al., 2011). GO and aptamer also give excellent response in live-cell biosensing. These platforms were also emerged in several studies subjected to discover the ability of GO in transporting the biomolecule to the molecular target. This provides *in situ* molecular detection, such as detection of adenosine triphosphate (ATP) concentration in cells using dye-labeled aptamer in **Figure 2.10 (ii)** and monitoring the alteration of Caspase-3 in live-cells through dye labeled substrate peptide which was conjugated with GO (Wang et al., 2010, Wang et al., 2011b).

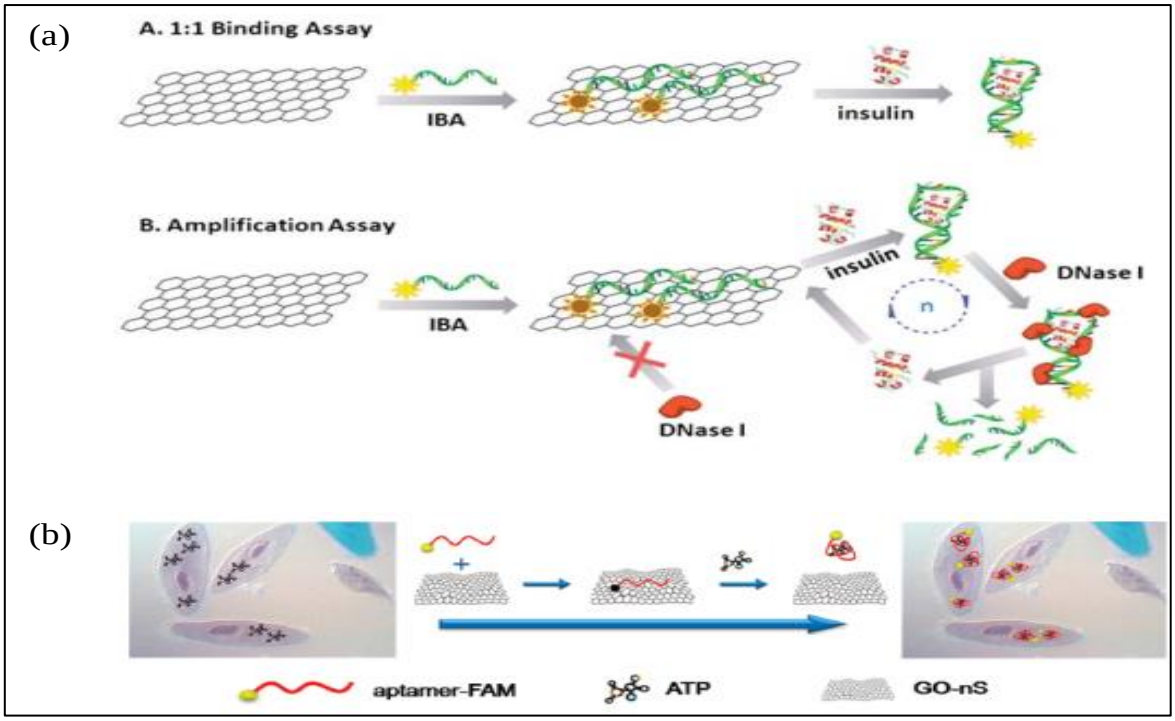

Figure 2.10 (a) Scheme of GO platform with hybridized labeled aptamer in insulin detection. Adapted from Pu et al. (2011); (b) Dye labeled aptamer functionalized GO in ATP cells detection. Adapted from Wang et al. (2010).

2.2.5 Thermal Responsive Polymers

Polymer is concretely a chain of repeated single molecules (or monomer) connected to one another through chemical or physical bonds. Through crosslinking or linear network, polymer enables to deliberate as a basic building block yielding a packed polymer with specific physical-chemistry properties. According to these properties, polymers can be defined into several applications of stimulus, including: pH, temperature, density, and concentration of analyte. Their varied features are also supported with their facts that they are easy to synthesize and modify, wide range chemical functionalities, and inexpensive. Most of biosensors are turning into the one having specific properties in order to gain the quicker and more accurate results as well as to provide specific capability of point-of-care (POC) for patient with resource-limited settings (Islam et al., 2014). Hydrogels are known as

one of the network polymers with highly hydrophilic-crosslinked chain which are able to shrink once placed in aqueous solution. They are clustered into different groups based on their material origin, physical structure, electronic charge, crosslink type, and ability to response toward external stimulus (Peppas et al., 2000, Alzari et al., 2011, Ahmed, 2015). One of the most extensively investigated is poly-(*N*-isopropylacrylamide) (PNIPAM) which attracts sensitively to environmental condition (Hoare and Pelton, 2004, Kim et al., 2004, Kim et al., 2005, Wong et al., 2008, Sivakumaran et al., 2011, Campbell et al., 2013).

PNIPAM allows a reversible transition from coil to collapse states at the lower critical solution temperature (LCST) of 32^{o}C. PNIPAM retains its solvated coil structure in water below LCST, while it undergoes a desolvated globule at above LCST. This potential feature emerges PNIPAM to be applicable in various fields, particularly in diagnostic, drug delivery, regenerative medicine, and tissue engineering (Holtz and Asher, 1997, Langer, 1998, Sharma et al., 2004, Anderson et al., 2004, Kim et al., 2005, Tauro and Gemeinhart, 2005, Plunkett et al., 2005, Kim et al., 2006, Islam et al., 2014). In biosensors, PNIPAM is commonly used to situate the interaction event between biorecognition and the target relied on different temperature or pH. A sensing technique was developed by Kim and colleagues emerging PNIPAM-co acrylic acid (PNIPAM-AAc) microgel in a microlens array for tunable protein detection (Kim et al., 2004, Serpe et al., 2004). The concept was based on reversible *antibody-antigen* binding strategies, which were a direct binding and displacement responses. The protein binding event to vitamin biotin located on the microlens would increase the surface crosslinking of the PNIPAMM-AAc microlens. Once the free-biotin was added, the crosslinking disrupts by replacement and make the microlens swollen up. As impact, the refractive index and microgel diameter of the microlens changed along with the tunable

effects. Further, these systems benefitted from the temperature and pH functions where the water content of microgel reflected the lensing ability due to the refractive index change. Recently, Jung and colleagues proposed PNIPAM-based microfluidics to detect the protein adsorption on the droplet surface (Jung et al., 2014). They emerged b-poly(4-cyanobiphenyl-4'-oxyundecylacrylate) with the PNIPAM ($5CB_{PNIPAM}$) associated with sodium dodecyl sulfate (SDS) in microfluidic components to display change of radial-to-bipolar (R-B) orientation profile after exposure of certain temperature and pH corresponding for protein adsorption. At above LCST and pH below isoelectric point of the protein, the R-B altered during the adsorption and was reversible at temperature below LCST, accordingly. Further, the system employing PNIPAM is expected to be applicable for aptamers, peptides, proteins, antibodies, and other selective units of biosensors method.

The outcomes obtained from the current study provide new insights into PCa research. These findings can be utilized in novel methods for the early diagnosis of prostate cancer.

CHAPTER 3

THEORETICAL PRINCIPLE

This chapter highlights the theoretical background and the functional techniques underpinning the density functional theory (DFT), molecular docking, and molecular mechanics (MM) methods. The first section of DFT methods is within the context of the Schrödinger and Hartree Fock theories including description of exchange correlation terms, basis sets, and self-consistent field theories. The molecular docking covers the ZDOCK and ZRANK conceptual backgrounds which are applied in the studies of aptamer and protein interactions. Further, the force fields and molecular dynamics simulations, including ensembles and thermostats, are explained under the molecular mechanic (MM) section.

3.1 Density Functional Theory

In computational chemistry, the energy (*E*), refers to the lowest energy reached by the most stable system. In addition, it is important to notice that the system of interest having zero energy as it defines the completion of all nuclei and electrons in the system. Quantum mechanics (QM) is used to describe the behavior of electrons or atoms or molecules and its properties, including the total energy. Density functional theory (DFT) is one of powerful techniques based on the QM, which characterizes the profile and coordinates of the atoms of a system by giving attention to the exchange correlation functions, algorithms-variables of convergence criteria, and integrated method (e.g. pseudopotentials) of calculating electron core. DFT defines many important profiles by calculating the total energy. The difference of the energy between the crystal and point defect could be revealed through using thermodynamics properties or calculating the energy of diffusion barrier. The phonon

properties can also be obtained by removing atoms as well as calculating the force from the remaining atoms, thus deriving the capacity of vibrational heat. On the other hand, DFT methods can also be used for the outputs, such as the electronic band structure, orbitals configuration, electrostatic potentials, magnetic configuration, and density of charges. Overall, it has been intensively employed in predicting and interpreting important properties of materials through simpler handling for user, quicker and more stable algorithms in solving the calculations (**Figure 3.1**) (Parr and Weitao, 1989, Cramer, 2013, Jain et al., 2016). In this thesis, DFT was employed to study the interaction between PNIPAM monomer-functionalized GO with DNA through describing the energetic structures and electronic properties of molecular systems, for a better understanding of the molecular species undergoing interaction within the system.

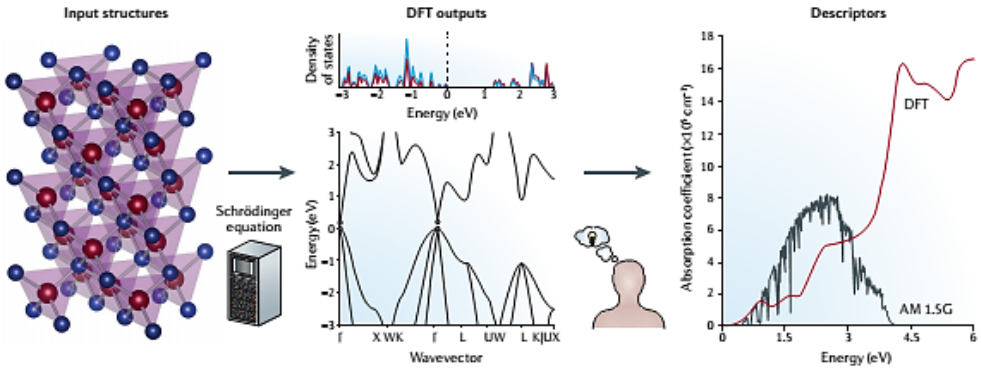

Figure 3.1 The DFT calculation scheme regarding processing and interpretation the data. Adapted from Jain et al. (2016).

3.1.1 Schrödinger Equation

Principally, QM is available for physical property prediction, such as transition phase of pressure and temperatures of the electrons, ions, and other complexes of periodic lattice and bulk compound, that could be attained by solving the Schrödinger equation (Payne et al.,

1992). In the beginning, the Schrödinger equations are introduced based on the time independent form in correlation with the wave function (Ψ) to describe the particles system besides their total energy (*E*), that could be stated as:

$$\hat{H}\Psi = E\Psi \tag{3.1}$$

$\hat{H}$ acts as the Hamiltonian operator which corresponds to the potential and kinetic energetics. However, there are several drawbacks when using QM. This method is computationally expensive to complete the Schrödinger calculation for many-body system. Therefore, several approximations are designed in order to accomplish a solution. Born-Oppenheimer is the assumption which allows the many-nuclei and their related electrons to be simplified by considering the mass of the electrons since the nuclei has several orders of size and more immense than the electron mass. It enables a prompt electronic relaxation compared to the nuclear motion, thus separates the motion of the electrons and nuclei. This approximation can overcome the Schrödinger equation for fixing the nuclei positions. As a result, the **Equation (3.1)** is divided into nuclei (*n*) and electronic (*e*) elements:

$$\hat{H}_e\Psi_e = \mathrm{E}_e\Psi_e \tag{3.2}$$

$$\hat{H}_n\Psi_n = \mathrm{E}_n\Psi_n \tag{3.3}$$

When *E* splits into kinetic ($\hat{T}$) and potential energy ($\hat{V}$):

$$\hat{H}_e = \hat{T}_e + \hat{V}_{en} + \hat{V}_{ee} \tag{3.4}$$

$$\hat{H}_n = \hat{V}_{nn} \tag{3.5}$$

the electronic Hamiltonian contains two terms of energies, which are kinetic energy of the electrons ($\hat{T}_e$) and potential energies of both electron-nuclei ($\hat{V}_{en}$) and electron-electron ($\hat{V}_{ee}$) interactions. Since it belongs to the nuclei position, the nuclear Hamiltonian only consists of electrostatic term of the nuclei-nuclei interactions within the system, no kinetic energy is

included. The electronic Hamiltonian of an isolated *N* electron can be expanded to summation of whole electrons in the system using $V(r_i)$ as potential energy of the i^{th} electron in nuclei field:

$$\widehat{H}_e = \sum_{i=1}^{N}\left(-\frac{1}{2}\nabla_i^2\right) + \sum_i^N V(r_i) + \sum_{i<j}^{N}\frac{1}{r_{ij}} \tag{3.6}$$

There are several valid equations for **Equation (3.1)**. Each wave function (Ψ_k) associates to an eigenvalue of energy (E_k), and there is Ψ_0 as a ground state with E_0. These terms are required in order to acquire the most stable condition of a system. The ideal values for observable system are described as:

$$< \hat{A} >= \frac{\int \Psi^* \hat{A} \Psi dx}{\int \Psi^* \Psi dx} = \frac{<\Psi|\hat{A}|\Psi>}{<\Psi|\Psi>} \tag{3.7}$$

Once Ψ is normalized, the $< \hat{A} >$ will be reduced to:

$$< \hat{A} >= \int \Psi^* \hat{A} \Psi dx \tag{3.8}$$

If the system is in Ψ state, which is unnecessarily an eigenfunction of the system, the estimated energy value will be given as:

$$E[\Psi] =< \widehat{H} > \int \Psi^* \widehat{H} \Psi dx \tag{3.9}$$

The above energy term (E) should have either equal or greater value than E_0 to reach the upper bound on the system energy or actual ground-state. Therefore, for further derivation the correlation can be expressed as (Parr and Weitao, 1989):

$$E[\Psi_{trial}] \geq E_0 \tag{3.10}$$

3.1.2 Hartree-Fock Approximation

The complexity of the Schrödinger could be reduced by the term of Born-Oppenheimer, however, there was no analytical solution to determine the system containing more than one electron with the correlated motions. Furthermore, the relativistic effect has not already been

combined, and the spin effect interaction is not included to the current approximation. The Hartree-Fock approaches try to simplify these issues by treating the electron motions independently and neglecting other interactions among them. This admits the wave function of all-electron for *N* electron system to be defined as a total of the one-electron wave function.

Further, the Hartree Fock method itself employs integration of Coulombic electron-electron repulsion as an approximate energy from real energy by calculating the QM. The energy is commonly equal or greater as compared to the exact energy since the use of primary approximation is the central field. This method harnesses in simplifying the complex Schrödinger electron-equations into single-electron equations (Young, 2001).

Therefore, an electron of a wave function will be a result of the spatial wave-form which represents the spin. There are two degenerate spin functions for an electron, α and β, as spin-up and spin-down, respectively. Both functions are orthogonal and normalized. The combination between the spin component and spatial wave function ($\psi(x)$) can generate a set of one-electron spin orbital (ϕ_i), where many-electron wave function may be created. The total wave functions of electrons are asymmetric products toward the exchange of electron position, which can be written on Slater determinant wave function:

$$\Phi_{SD} = \frac{1}{\sqrt{N!}} \begin{vmatrix} \phi_1(1) & \phi_2(1) & \cdots & \phi_N(1) \\ \phi_1(2) & \phi_2(2) & \cdots & \phi_N(2) \\ \vdots & \vdots & \ddots & \vdots \\ \phi_1(N) & \phi_2(N) & \cdots & \phi_N(N) \end{vmatrix} \tag{3.11}$$

The spin orbitals of whole one-electron are arranged within the matrix in which the rows represent the coordinates of the electrons and columns consist of the spin orbitals.

Literally, although the Slater determinants can be used as preliminary trial of electronic wave function, the single determinant of electronic wave function can be assumed through Hartree Fock. Therefore, the electronic energy can be written as (Parr and Weitao, 1989):

$$E_e = \langle \Phi_{SD} | \widehat{H}_e | \Phi_{SD} \rangle = \sum_{i=1}^{N} \mathrm{h}_i + \frac{1}{2} \sum_{i,j=1}^{N} (j_{ij} - k_{ij}) \quad (3.12)$$

The h_i stands for potential and kinetic energies of electron (i) around nuclei. The repulsion of classical electrostatic between electrons is defined by Coulomb integral (j_{ij}), whereas the exchange integral is called k_{ij}. In short terms, these functions can be described as operators same with the one used to determine new Fock operators $(\hat{f}_i)$ using whole expression of:

$$\hat{f}_i = \hat{h}_i + \sum_{j=1}^{N} (\hat{j}_{ij} - \hat{k}_{ij}) \quad (3.13)$$

With applying variation principle to minimize the **Equation (3.12)**, function can promote to the Hartree Fock equations, which create pseudo-eigenvalue issue:

$$\hat{f}_i \chi_i = \epsilon_i \chi_i \quad (3.14)$$

The χ_i is a molecular orbital in a system and ϵ_i is energy related to molecular orbital. To calculate the system energy, the total of wave function must be achieved first by means of solving the molecular orbital in Hartree Fock equations iteratively. The iterations process is acknowledged as self-consistent field (SCF), in which, a solution with self-consistent condition can be obtained if the energy difference calculated within successive iterations is lower than the convergence value. In other words, one can describe the total energy of a system with total electronic energy (as mentioned in **Equation (3.12)**) and nuclei energy when SCF orbitals have been determined:

$$E_{HF} = E_e + E_n \quad (3.15)$$

3.1.3 Linear Combination of Atomic Orbitals

Hartree Fock equation can be solved into methods by splitting the molecular orbital (χ_i) into a known function, termed basis set, which restricts every electron to be in a particular district of space or, combines atomic orbitals to expand to the molecular orbital (Roothaan, 1951, Hall, 1951).

$$\chi_i = \sum_{m=1}^{L} c_{mi} v_m \tag{3.16}$$

From the above equation, every χ_i is constructed from L basis functions (atomic orbitals), v_m. In order to solve the Hartree Fock equation, the 3.16 equation is substituted to Hartree Fock equation to get a set of Roothan-Hall matrix equations, as well as the basis function parameters, which can be changed to obtain a minimized energy of system. The solutions for the system which is well-described using this method is called by Hartree Fock solution.

Several types of basis functions can be employed to produce the system orbitals. It is importance to ensure that any computational issues are significantly considered, such as the atomic orbital should be positioned in center of the nuclei. Sometimes, it will be a computational cost for the system that cannot be well described by exponential functions. Therefore, some different types of basis sets have been developed, and will be briefly explained in subsequent section.

However, the non-interactive single wave function of Hartree Fock is not effective to describe the system containing the interactions of many electrons of heavy atoms since the techniques are likely to lead to inconsistency between the observed and predicted molecules. In another hand, since single Slater determinant can only be used to determine the exact wave

function of all electrons in a system as *N* non-interacting electrons, it can overestimate the repulsive coulomb interaction. Consequently, the extensions of quantum mechanical functions and some parameterizations are enhanced to be able to reproduce the experimental results. Therefore, the Coulomb repulsions need to be integrated on electron density principle in order to induce more accurate and faster calculations as compared to that of Hartree Fock (Young, 2001).

The correlation energy (E_{corr}^{HF}) describes the difference between the Hartree Fock energy and exact ground state energy of the system that can be expressed as:

$$E_{corr}^{HF} = E - E_{HF} \tag{3.17}$$

DFT based on the rewriting Hamiltonian of *N* electrons system in an external field, offers an alternative way to solve the Schrödinger equation. Principally, this theory explains how to determine molecular energy from electron density in a linear combination of basis functions that is close to Hartree Fock method by using Kohn-Sham approach. It allows to replace a complex of *N* electrons wave function with electron density ($\rho(\mathbf{r})$). The $\rho(\mathbf{r})$ defines the distribution model of the charge within the molecular system:

$$\int \rho(\mathbf{r})\, d\mathbf{r} = N \tag{3.18}$$

Basically, the DFT was initiated by Thomas and Fermi in which the electrons were described as gas and their correlation in terms of total kinetic energy and density. This work performed as a fundamental principle, which further would be used to attain information about electronic properties within a system. Currently, the DFT form is relied on the Hohenberg and Kohn theory that correlates the exact energy function ($E[\rho]$) with its variation principle to describe the electron density ($\rho(\mathbf{r})$) (Hohenberg and Kohn, 1964). The ($\rho(\mathbf{r})$) may explain

the electronic properties that allows to calculate the ground-state of a system resulting a greater or equivalent energy to the ground-state:

$$E_0 \leq E[\rho(\mathbf{r})] \tag{3.19}$$

By using the Hamiltonian equation to correspond the electronic energy of a system, the DFT energy function can be described in:

$$E[\rho] = T[\rho] + V_{ee}[\rho] + V_{ne}[\rho] \tag{3.20}$$

$T[\rho]$, $V_{ee}[\rho]$, and $V_{ne}[\rho]$ stand for kinetic energy, potential energy of electrons interaction, and potential energy of the nuclear field effect of electron, respectively. Regarding the terms of $T[\rho]$ and $V_{ee}[\rho]$, the equation forms are unidentified yet. Previous methods had been attempted to solve these equations by using coulomb interaction to explain electron-electron potential and kinetic terms of similar non-interacting electron gas. However, the methods could not successfully predict the bonds among the atoms.

The Kohn and Sham later separated the kinetic energy into two sections (Kohn and Sham, 1965):

$$T[\rho] = T_{ks}[\rho] + (T[p] - T_{ks}[\rho]) \tag{3.21}$$

The kinetic energy of the non-interacting *N* particles $T_{ks}[\rho]$ defines the present fault caused by the electrons interaction in a real system, in which it is similar to those described in Hartree Fock approach, with single Slater determinant explaining the wave function of ground state for this system. Despite employing the spin-orbitals to solve Slater determinant, Kohn-Sham (KS) orbitals are used to describe this matter. Unlike the spin-orbitals, KS orbitals do not associate with atomic orbitals. The exact electron density formed by emerging the KS orbitals can be stated as:

$$\rho(\mathbf{r}) = \sum_i^N |\phi_i|^2 \tag{3.22}$$

Furthermore, KS operator can be obtained by using similar procedure for Fock operator, while the kinetic energy of this system can be solved using Schrödinger equation:

$$T_{ks} = -\frac{1}{2}\sum_i^N \int \phi_i^*(r)\nabla^2\phi_i(r)dr \tag{3.23}$$

The similar principle can be applied to determine the electron-electron interactions $V_{ee}[\rho]$:

$$V_{ee}[\rho] = V_{ks}[\rho] + (V_{ee}[\rho] - V_{ks}[\rho] \tag{3.24}$$

The $V_{ks}[\rho]$ is equivalent to the Coulomb-Coulomb interactions of the Hartree Fock technique, in which it undertakes error present due to the classical Coulomb interaction. Overall, the errors obtained from non-interacting electron gas presumption as well as Coulomb interactions to display the electrostatic potential between electrons leads to a new term called exchange correlation function (XC). Therefore, the density functions for the system energy can be expressed in:

$$E[\rho] = T_{ks}[\rho] + V_{ne}[\rho] + V_{ks}[\rho] + E_{xc}[\rho] \tag{3.25}$$

In general, XC term defines the connection of electron energies and its exchange with the correction of kinetic energy. The above equation does not explain the XC form explicitly, yet for other terms have been described explicitly for use in Hartree Fock method. By expanding the correlation with XC, total energy of the system now becomes (Jensen, 2016):

$$E[\rho] = -\frac{1}{2}\sum_i \int \phi_i^*(r)\nabla^2\phi_i(r)dr - \sum_a \int \frac{Z_a\rho(r)}{|R_a - r|}dr + \frac{1}{2}\iint \frac{\rho(r)\rho(r')}{|r - r'|}drdr'$$

$$+E_{xc}[\rho] \tag{3.26}$$

Similar to the Hartree Fock, those equations can be expressed as Hamiltonian operator for KS orbitals (ϕ_i), that further can be expanded into basis set terms by following the SCF approach.

3.1.4 Approximation of The Exchange Correlation Term

The main problem of Kohn-Sham application is whether XC function is only for free-electron gas, while for others are still unknown. If the electron density is deliberately varying, the XC energy at any point (*r*) will be equal to the one in homogenous electron gas which has the same density at *r* (Kohn and Sham, 1965). Therefore, in simple form the unknown XC can be formulated as (Parr and Weitao, 1989):

$$E_{xc} = \int \rho(r)\epsilon_{xc}[\rho, r]dr \tag{3.27}$$

The ϵ_{xc} corresponds to XC energy for each electron of homogenous electron gas along with $\rho(r)$. However, since ϵ_{xc} approximation is unknown, the exact form need to be predicted. The most used form of XC is recognized as local density approximation (LDA) which relies on the electron density score in every point (*r*) of the system (Paul, 1931). This function works good for a system containing slowly varying function of electron density.

$$E_{xc(LDA)} = \int \rho(r)\epsilon_{xc}(\rho(r))dr \tag{3.28}$$

Even though LDA produces satisfied geometry results, phonon frequencies, and bulk system, it is still not accurate enough to describe system with molecular species, or ionization energy and cohesive energies thus, likely to fail in highly complex system involving electron interactions (Kohn, 1999). In generalized gradient approximation (GGA), one is able to give

a semi local equation of E_{xc} to solve the insignificancy in electron density by assembling the gradient correction in (Becke, 1988):

$$E_{xc,GGA} = \int \rho(r)\epsilon_{xc}(\rho(r), \nabla\rho(r), \dots)dr \quad (3.29)$$

The $(\rho(r), \nabla\rho(r), \dots)$ terms associate to the advancement factor which depends on the local density and density gradient.

Several works have successfully completed the above GGA form of **Equation (3.29)** derived from the first principle calculations or by reproducing experimental data for parameterizations. The common employed functions of GGA are PBE proposed by Perdew, Burke, and Ernzerhof (Perdew et al., 1996) as well as PW91 by Perdew and Wang (Perdew and Wang, 1992). In terms of atomic energy, binding energy, and the hydrogen bond, GGA demonstrates an enhancement over the LDA, which is an inexpensive method. Thereby, it is expected to perform better than LDA for the exchange and correlation energies in large computational system. This study employed the PBE functional in the form of E_{xc} since it has shown an accurate result in defining the interactions involving hydrogen bond (Benedek et al., 2005).

DFT calculations performed within DMol3 package (Frisch et al., 2009) is derivative form of LDA as a previous method of atomic spin calculation. DMOl3 will be applied for the assessment of the electronic properties, such as conductivity and electronic transfers. It will be useful in the modelling and prediction of the process of adsorption.

3.1.5 Basis Set

Both Hartree-Fock and Kohn-Sham solutions can be broken down into a functional set defining the density of the system and the wave function, wherein molecular orbital of a system representing the atomic orbitals is described by these sets of functions. Two main basis functions that involved in electronic properties calculations are Gaussian type orbitals (GTO) and Slater type orbitals (STO), where STO function is given as (Slater, 1930):

$$\chi_{\zeta,n,l,m}(\mathbf{r},\theta,\phi) = NY_{l,m}(\theta,\phi)\mathbf{r}^{n-1}e^{-\zeta\mathbf{r}} \tag{3.30}$$

ζ is constant associated with effective charge of the nucleus; N defines the normal constant; $Y_{l,m}(\theta,\phi)$ is spherical harmonic terms; r is the electron-nucleus distance, and n stands for number of principal quantum. STO provides a good approximation for considering a small set of functions in an atom. However, when the number of atoms or functions increases, the exponential term is difficult to evaluate the molecular integrals. Therefore, the calculations involving huge number of atoms are preferable to conduct the GTO function rather than STO, which is expressed in polar or Cartesian coordinates solution (Boys, 1950).

The dependence of r^2 in the exponential of GTO would gain a lesser approximation results in evaluating the integrals as compared to STO. Nevertheless, a reasonable accuracy within the time can still be obtained by increasing the number of Gaussian basis functions (Raffenetti, 1973, Davidson and Feller, 1986, Foresman and Frisch, 1996). Therefore, in order to obtain a reliability in accuracy and calculation speed, it is preferable to apply the smallest possible number of functions within the studied system.

Minimal (MIN) basis set is the smallest number of basis functions to possibly describe whole electrons in a system. This basis set uses the proper functions which are essential to define each filled orbital, for example, single s-orbital (1_s) would be sufficient for H and He atoms; three s-orbitals and two p-orbitals functions are required for the second row of elements of periodic table. MIN basis set is usually used to obtain quicker and coarse approximation at the early stage of calculation. The STO-nG is the most frequently used type of minimal basis set, which emerges a linear combination of n-Gaussian functions to represent the orbitals (Hehre et al., 1969, Hehre et al., 1970, Pietro and Hehre, 1983). For example, STO-3G needs about three GTO functions consisting three Gaussian peaks (3G) to fit one STO function to provide a realistic orbital model built from simple functions.

The accuracy of the MIN basis set is able to be enhanced by doubling all the basis functions resulting in Double-Zeta (DZ) basis set. It is known to provide better calculation of the anisotropy of electron distribution (Dunning Jr, 1970, Dunning, 1970, Schäfer et al., 1992). DZ calculates the pi bonds, but sometimes may over-specify orbitals number in describing a system (Jensen, 2016). Thus, the split valence basis sets (valence double zeta (VDZ)) are commonly used in the case of the doubled valence orbitals (Binkley et al., 1980, Gordon et al., 1982, Dobbs and Hehre, 1986, Dobbs and Hehre, 1987a, Dobbs and Hehre, 1987b).

In this thesis, DFT employs numerical orbitals basis sets where each function corresponds to one atomic orbital (AO) beside Gaussian orbitals. The angular element of the function is spherical harmonic ($Y_{l,m}(\theta, \varphi)$) and the radial element is achieved by solving the DFT equation numerically. The accuracy is usually obtained by employing 300 radial points from the nucleus to the ~5.3 Å outer distance. These functions are commonly used in DFT method

to offer good transparency in interpreting the results since all integrals are calculated efficiently.

Under DMol3, the basis functions are provided on an atomic centered spherical-polar mesh numerically. Within a confined cutoff value (r_c), atomic basis sets are suitable to describe particular level of DMol3 quality. Further, DMol3 uses the soft confinement potentials for basis set in terms of strict localization within range of r_c value, thus leads to faster calculation. Particularly, these basis sets provide better functions and one of the advantages is that the molecule is possible to be separated to its constituent atoms. Due to the quality of these orbitals, it is able to describe the weak bonds excellently and the basis set superposition effects are minimized. DMol3 covers a range of basis sets from MIN to doubly polarized numerical (DNP) basis sets. The DNP is used within this work. It includes all non-hydrogen atoms with their valence orbitals and additional polarized d-functions, and all hydrogen atoms with the polarized p-functions. This polarization corresponds to the important modelling in hydrogen bonding interactions. The DNP itself is similar to the 6-31G** basis set, yet due to the fact that AO is physically realistic, it is expected that more accurate results are possible to be achieved than that of Gaussian basis sets (Delley, 1990).

3.1.6 Self-Consistent Field (SCF)

Since several integrals of DFT parts could not be done analytically, as consequence, there is a step to evaluate the integrals over atomic orbitals, by using interpolation of the numerical atomic basis set of grid points. DMol3 has three options of qualities to define the accuracy of integral calculations, which are Coarse, Medium, and Fine. The combination between the spin and charge densities from the previous iteration is taken into account in order to increase

the speed of SCF convergence. Further, a direct inversion of the iterative subspace (DIIS) sub-technique implemented under DMol3 is also applied to enhance the SCF speed performance (Cremer and He, 1996). This method enables to minimize the error by approximating a significant error for the density function. As result, it reduces the iteration numbers with efficient compelling the convergence and allows the next estimated density functional to be closer with the actual ground state density without exploring full SCF iterations for each estimation at the density (Jensen, 2016).

3.2 Molecular Docking

Understanding the interaction of the protein and DNA can address the fundamental processes of cellular information since it undergoes the conformational changes in binding, such as DNA conformation, gene regulation, predictive bonding, as well as constructing the complex for functional magnitudes (Smith and Sternberg, 2002, Mukherjee and Zhang, 2011). Experimental research consists of the compiled methods in the form of variable designs to discover those mechanism functions (Roberts et al., 2013). In aptamer biosensor, it is known that only the best aptamer selected from the SELEX process can interact selectively toward the protein/cell of interest. The performance of binding is further investigated using NMR to define the corresponding biomolecules which are responsible in the interaction (Roberts et al., 2013). However, in some conditions, discovering the aptamer sequences with excellent binding performance needs long time process and instrumental laborious. One of the computational advantages is to discover the untouchable part of a conductive research to be accessible since experimental determination will not be conceivable for intruding such a complex system. Therefore, a comprehensive study of the aptamer interaction through computational prediction is intensively considered since it enables a preliminary

investigation to perform binding selection using three-dimensional models of protein-aptamer effectively and efficiently (Vakser I 2014).

Molecular docking is one of the computational approaches based on the three-dimensional structural design to simulate the interaction behind biomolecule toward drug or other substantial compounds in protein-ligand interface system (Lengauer and Rarey, 1996a). The "best" binding approximation between the protein and ligand will lead to comprehensive binding interaction studies of two entities, such as DNA-ligand (Morris and Lim-Wilby, 2008, Kumar et al., 2012). Initially, the term of *dock* was introduced by Kuntz and co-workers to describe an appropriate conjunction of small molecule aligned into its receptor (Kuntz et al., 1982). In docking interaction, the information about molecular conformation is needed to determine a good bonding within two molecular structures through scoring function (Gaba et al., 2010).

Molecular docking can be linked to "lock and key" analogy. The "lock" roles as the protein receptor which supposed to be docked, while the "key" corresponds to the ligand. The key will open the lock when they bind each other with proper direction and conformation. Molecular docking describes "the best-fit" orientation of ligand binding to its receptor through optimization process (**Figure 3.2**) (Jorgensen, 1991).

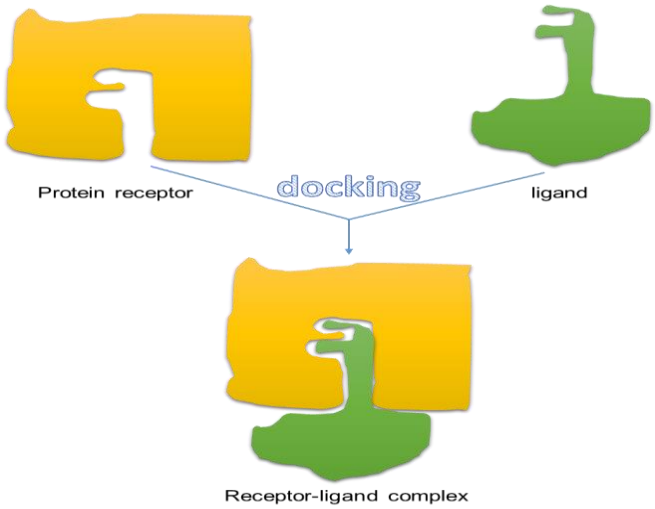

Figure 3.2 Docking schematic model between ligand and receptor.

There are three main parts of the docking, (1) displaying the molecular system, (2) searching the direction and conformational space, and (3) ranking the final docked model. Since the docking associated with the protein surface, the first prerequisite is to determine the surface protein before beginning the simulation by means of the grids, descriptors of geometrical shape, or conducting the protein treatment in its rigid or flexible condition (Halperin et al., 2002). The binding interaction site is commonly obtained using conformational sampling which is subsequently followed by scoring stage which allows to recreate the experimental binding manner along with the sort of the rankings corresponding to the favorable docking (Meng et al., 2011). Those general ways underline the steps to perform molecular docking within protein and ligand.

3.2.1 Rigid Body Model Construction

DNA-protein docking remained some challenges as well as constraint in any parts. It is well-known that relative analysis of complexes between DNA-protein and protein-protein presented an analogue profile in terms of interaction specificity, as well as induced fit due to

binding (Harrison, 1991, Larson and Verdine, 1996, Jones et al., 1999). Therefore, modelling the DNA-protein can be possible as defined in protein-protein docking by substituting the determined structure of DNA with populating the conformation principle. In comparison, the DNA and protein binding interface provides more polarity due to the hydrogen bonding intermolecular interaction as compared to the protein and protein interaction (Halperin et al., 2002). The screening performance of docking is based on the accuracy and speed (Taylor et al., 2002). The pictorial workflow for running docking as virtual screening tools is described by **Figure 3.3**. The workflow resumes how the docking of biomolecular proceeded from obtaining the database information of two simulated molecules, choosing the parameters involved during the docking stage to interpretation of the scoring results as well as the final model selection. The molecular docking portion of the screening is usually categorized according to the approach employed (Lyne, 2002).

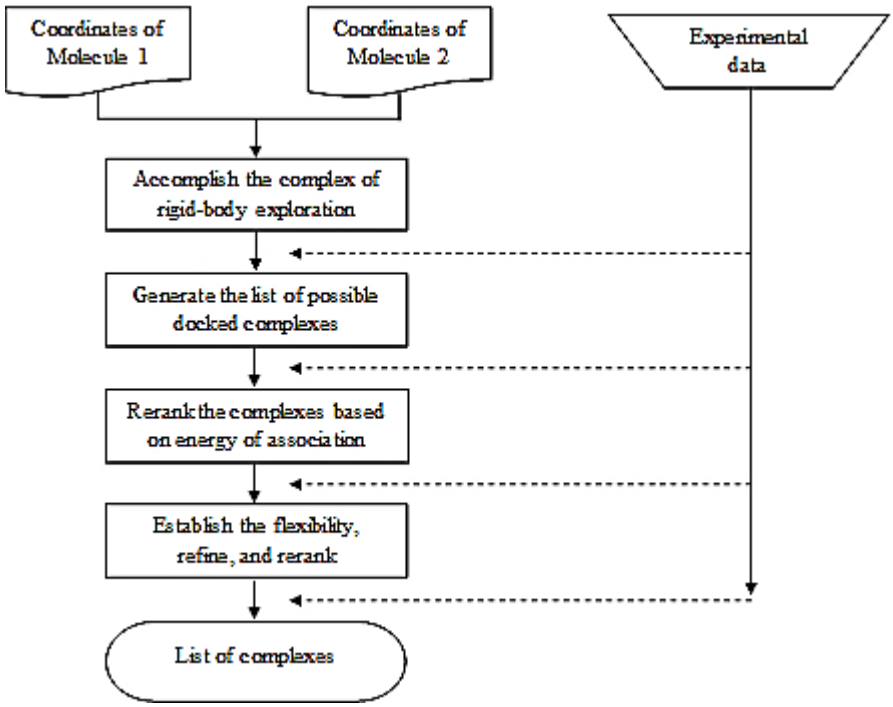

Figure 3.3 The flowchart of protein docking. Adapted from Smith and Sternberg (2002).

Protein-protein/DNA-protein docking studies are necessary to deal with these issues, such as figuring the separated proteins to be assembled into a complex using computational approach. Protein docking is clustered into bound and unbound docking which is reunited or pulled apart. The common two-stage approach known as: (1) preliminary stage, where the receptor with ligand is preserved as rigid bodies, while conformational changes of rotational and translation 6^0 are performed under scoring functions; (2) refinement stage, where the scored docking models are refined using more comprehensive energy function as well as reranking taking into account the conformational changes (Chen et al., 2003).

Fast fourier transform (FFT) method is able to compensate a huge molecular size of protein calculation and also reduce the searching space of docking prediction. To avoid impact of the surface side-chains changes, many particular docking methods have been developed (Vakser, 1997, Gabb et al., 1997, Ritchie and Kemp, 2000, Sternberg et al., 2000, Mandell et al., 2001, Smith and Sternberg, 2002). One of the methods that uses initial stage algorithm is ZDOCK that employs desolvation, grid-based shape complementary, and electrostatic computations. It is an initial-stage rigid body docking based on Fast Fourier Transform (FFT) which achieved high accuracy in protein-protein docking with more than 70% success in the first 1000 predictions as compared to the most recent benchmarks (Pierce et al., 2011). The FFT platform also simplified the searching and scoring functions. The calculation is then ensued by conducting the pairwise shape complementary (PSC) function to determine number of protein-ligand atom pairs using distance cut-off detriment clash penalty (Chen et al., 2003). In addition, the bound conformational finding depends on the predictive sampling chosen, 15^0 or 6^0 sampling, which produces output predictions of 3,600 or 54,000, respectively.

3.2.2 Structure Refinement and Reranking

The refinement stage of ZDOCK is commonly done by performing RDOCK which uses CHARMm basis to compute the minimization of energy of the top 2,000 of ZDOCK predictions and re-rank them based on electrostatic and desolvation (Brooks et al., 1983, Li et al., 2003). However, the RDOCK-refined results only assume small number in partial subset of ZDOCK predictions and roughly yield one minute step for energy minimization in each case. Meanwhile, ZRANK is presented with its capability to re-rank the rigid body of ZDOCK results to be more accurate and quicker, particularly in biomolecule with huge atoms number. This method combines the repulsive and attractive van der Waals energies, short-long repulsive and attractive energies, as well as desolvation platforms.

Principally, the PSC function in ZDOCK can distinguish the huge pocket of binding sites of protein-protein complexes effectively, yet sometimes it meets challenges in scoring the interfaces. ZRANK has a basic energy function which enables the differentiation of hits from non-hits in a sort of rigid-body approximations based on the weights. Its repulsive function of van der Waals provides the essential smoothness in the prediction of rigid body. The terms of van der Waals and short range electrostatic energies are resolved by CHARMm 19 parameters using polar hydrogen potential (Neria et al., 1996). The charged side-chain atoms are applied to calculate long range interaction, while regarding desolvation, it is relied on the pairwise atomic contact energy (ACE). Due to these features, ZRANK is more specific and gives faster performance of ZDOCK full predictions.

In the application, RDOCK can only be applied for ligand with maximum atom numbers of 999 atoms, while ZRANK can afford more than 1,000 atoms which is appropriate to calculate

huge number of aptamer atoms. Therefore, involving ZRANK in the typical case of DNA-protein interaction is essential for improving the initial ZDOCK scores since it also allows to process successively all 54,000 predicted conformations in more details without acquiring the high computational time (Pierce and Weng, 2007).

3.3 Molecular Mechanics

3.3.1 Force field Energy

As mentioned above, the QM methods are computationally accurate for atomic and molecular system in general. However, it sometimes requires a comparatively long period of time since most of them are only applicable for small molecule or system which contains 10 to 100 atoms. Therefore, it is quite not practically appropriate to calculate a large system, for example, a condensed polymer or biomolecules containing thousands of atoms. Extracting abundant statistical properties by considering the location of atom nuclei or its configuration is a purpose to do molecular mechanics (MM) simulation for a large system using parameters attained empirically or from the DFT approach (BIOVIA, 2016).

Basically, MM method defines different molecules having the chemical group of the structure same to each other since the constants of the bond forces are alike, regardless of the molecule with the functional group is involved. For these terms, the atoms within the functional groups will be defined particularly as the joining group or neighboring atom. This rule allows each different atom to be provided on its own parameter settings, stating its interaction with the other atoms. Therefore, in the case of sp^2, it has different typical atom as compared to sp^3 hybridized carbon. Since the forces are referred by the typical atoms, the sort of typical atoms with their parameters are acknowledged as force field (Jensen, 2016).

Classical simulations are based on the configuration of earliest method which integrates the Newtonian (classical) equation of motion. The total of potential terms constitutes a molecular force field that is beneficial for MM, molecular dynamics, and Monte Carlo simulations. Several techniques have been established to generate distributions and functions and mostly are mentioned for a classical simulation. **Equation (3.5)** associates to the model with system energy properties plotted perpendicularly toward time evolution. Due to the relatively heavy nuclei, solving the QM could be difficult and impact the solvation insignificantly. Thus, an empirical function of force field is performed here to approximate the data to fit toward the potential energy surface in simulation approach. The main purpose of force field is to define the surface potential energy of any molecule type accurately. Moreover, it seems to generalize the information of semi-empirical model set to be parameterized as a larger set of the related models. Regarding to work with larger size of computational model, there are three advantages of the force field, *viz.*:

a. It can handle large system faster and computationally cheap than quantum based calculation. It can be applied for a single type of organic macromolecules, condensed-phase molecules, and inorganic-organic interphases,
b. It benefits in analysis of the contribution of energy, such as bond, angle, and non-bond energies, at the level of individual or interaction,
c. One can impose an absolute condition (constraints) to modify energy expression in order to bias the calculation. This can be done by fixing some atoms in its certain geometry.

The components of force field comprise the important parts of the calculation of energy and force, including the type of the force field, partial charges, input rules of force field, parameters for the function terms, and method to assign a functional form and parameters (BIOVIA, 2016).

A combination between structure coordinate and a force field produces an energy expression which labels the potential energy surface for typical molecule as its atomic coordinates function. This can be determined as total of energy (E_{total}):

$$E_{total} = E_{valence} + E_{cross\ term} + E_{non-bond} \tag{3.31}$$

Firstly, the $E_{valence}$ interaction is calculated from diagonal terms as a sum of bond stretch, valence angle bending, dihedral torsion, out-of-plane interaction (inversion) of covalent model force field, and Urey-Bradley (UB) term of atom pairs interaction of certain configuration of *1-3*:

$$E_{valence} = E_{bond} + E_{angle} + E_{torsion} + E_{OOP} + E_{UB} \tag{3.32}$$

The valence cross term is generally applied in second-generation of force field to calculate some factors caused by nearby atoms such as bond or angle distortions. Cross term is required to regenerate the experimental vibrational frequencies as well as the dynamic properties of molecules. The calculation of cross term comprises the properties of: stretch-stretch, stretch-bend-stretch, bend-bend, torsion-stretch, torsion-bend-bend, bend-torsion-bend, stretch-torsion-stretch. Meanwhile, the interaction energy of non-bonded atoms, is calculated as the sum of:

$$E_{non-bond} = E_{vdW} + E_{Coulomb} + E_{H-bond} \tag{3.33}$$

Most force fields will include a non-bonded contribution in the valence bond and angle terms. These force fields will exclude van der Waals and electrostatic interactions between *1-2* and *1-3* atoms. Here, *1* and *2* refer to the end atoms. Some simulation engines may have exceptions to this. Forcite module provides several choices to perform an extensive range of MM calculations for periodic and non-periodic systems by means of the force field methods.

Basically, Forcite will include *1-2* and *1-3* interactions if the bond and angle functional forms are set to ignore or the interaction is missing. The way that *1-4* pairs are treated differs between force fields. Many force fields comprise the van der Waals and electrostatic interactions for these pairs in full, while others scale the interaction by a fixed numerical factor (BIOVIA, 2016).

A force field type reflects a microchemical circumstance for particular atom. Choosing a matched force field can lead to an optimal potential energy surface that can be applied to calculate the forces between the atoms. Under Forcite module, there are types of force field that allow any analytic expression during the simulation representing the potential energy surface. The expression of energy within large system consists of several terms and Forcite accommodate an automated performance to undertake the energy expression (BIOVIA, 2016).

3.3.1.1 COMPASS Force Field

COMPASS (Condensed-phase Optimized Molecular Potentials for Atomistic Simulation Studies) corresponds to the first *ab initio*-based force fields enabling simultaneous and accurate calculation of the properties of vacuum as well as condensed phase system. It has been parameterized for general organic molecules, inorganic materials (i.e. metals, metal oxides, metal halides), as well as the force field for polymers using *ab initio* and empirical parameterization. By generating *ab initio* data, the atomic partial charges and valence parameters are calculated, as well as van der Waals energy which is derived from conducting the MD simulation of liquids and measuring cohesive energy model as well as densities of equilibrium to experimental data, several valences and van der Waals parameters are derived

accordingly representing a significantly improved quality of force field (Sun, 1998, Sun et al., 1998).

The first parameterization is in atomic partial charges generated through *ab initio* electrostatic potentials and valence parameters from consistent force field (CFF) *ab initio* parameterization (a consistent force field, adapted to a wide-variety of organic compounds as well as metals, etc.). From the *ab initio* information, one can establish the valence parameters including total energies and the two first derivatives of the total energies respecting to the atomic Cartesian coordinates. The Lennard Jones 6-9 and other van der Waals parameters are arranged as initial values derived from CFF. The second parameterization emphasizes on force field optimization to compromise the experimental data. Several critical valence parameters are fitted relied on the experimental data in gas phase condition. Whereas, van der Waals are minimized to adjust the condensed-phase one. In covalent molecular system, these refinements are attained from MD simulation of liquids. The Lennard Jones 6-9 parameters are determined relied on the liquid MD simulations and comparison of the predictive results with the experiments (Sun, 1998, Sun et al., 1998).

3.3.1.2 Universal Force Field

Universal force field (UFF) is produced from set of rules relied on the hybridization, element, and connectivity. Its parameters contain a full implementation of bond order assignments which are physically realistic. The angle bending is described by the expansion rule of three-term Fourier cosine, while bond-stretch is characterized through harmonic term. The torsions as well as inversion are based on the cosine Fourier expansions. The electrostatic interactions

follow the atomic monopoles and distance-dependent of Coulombic terms whereby, the van der Waals is described relied on the Lennard Jones potential (Rappe et al., 1992).

The unique of UFF is that it can fit to all generated atoms types since the parameter was set for the full periodic table. It is moderately accurate in prediction of conformational energy differences and structural geometries of the atoms. It also has been validated for the organic molecules, main-group of compounds, as well as metal system, therefore, excellent to designate the general-purpose force field. Further, UFF contains parameter generators which allows to calculate parameter for any combination of force field types. By combining the set of atomic parameters equations, the parameters for bonds, torsions, angles, and out-of-plane inversion, van der Waals, and Coulombic energies can be generated. The application of UFF enables to calculate many combinations of atoms, including protein, organics, or nucleic acids (Rappe et al., 1992). Therefore, in this work, UFF was applied for the calculation of the system with complex structures.

3.3.1.3 Dreiding Force Field

Dreiding force field is built based on simple hybridization, element, and connectivity rules for general force constant and geometry parameters rather than on particular combination of atoms. It is a decently diagonal force field along with a cosine Fourier expansion torsion as well as the harmonic valence terms. Herein, Lennard Jones potential is employed to define van der Waals interaction. For inversion, the umbrella functional is performed based on Wilson out-of-plane fundamental. The interaction of electrostatic is determined by a distance-dependent Coulombic and atomic monopoles terms. Whereas, hydrogen bonding is resolved using Lennard Jones 12-10 potential (Mayo et al., 1990). This force field has

moderately accurate in regards of geometry, intermolecular binding energy, conformational energy, and crystal packing. However, Dreiding defines a good robust in prediction of structure and MD simulations on biological, organics, and foremost group of inorganic molecules for all-purpose calculation.

3.3.2 Molecular Dynamics Simulations

Molecular dynamics (MD) is a time dependent simulation of a molecular system giving routes to dynamical properties of system, such as transport coefficient calculation, rheological properties, and spectra. Different with DFT, MD corresponds to the relationship of system evolution based on MM with infinitesimal length and timescales frame to yield a global energy minimum. It may reveal the hidden information behind the bulk measurement, where MD performs as bridge between theory and experiment providing the inter-connection each other. It may check the principal background by undertaking an MD simulation using the same model and compared with experimental results. In other words, MD allows to access information or data that is difficult or impossible to be conducted in experimental works (for instance, working at very high temperature or pressure) (**Figure 3.4**).

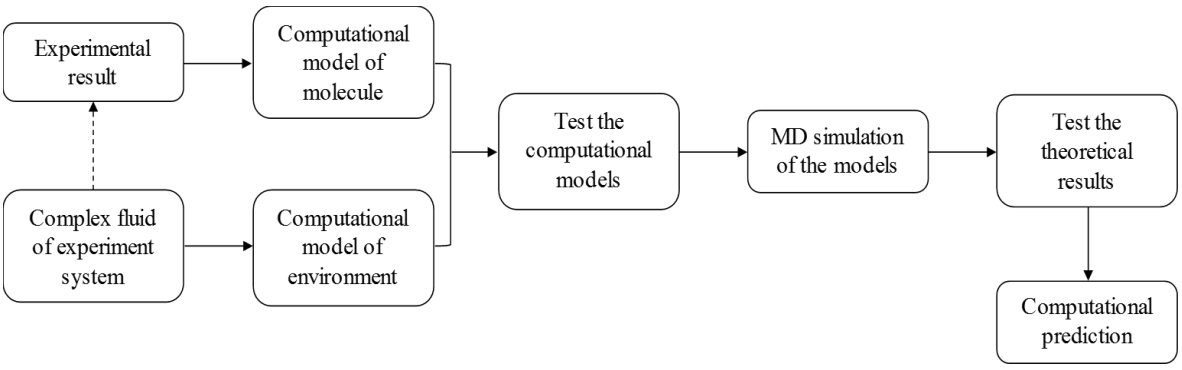

Figure 3.4 MD simulation as a bridge to complement and verify experimental data.

MD becomes a standard tool to investigate the biomolecules. There are three concepts of it in order to simulate the molecules in a system. First of all, MD brings the molecule into a system to have natural dynamics on different timescales in certain environment which gives new insight about its physical and chemical behaviors in given conditions. The second concept is that it provides the thermal average properties of the molecule in a system. Based on ergodic hypothesis, a molecule is able to be simulated in its environment for a period of time to approach the experimentally measurable collective averages, such as molecule in the fluids and the free energy difference in order to understand the ligand binding.

MD can also be employed to discover the molecules conformation or their complex in space, as long as it is thermally accessible, which benefits in understanding the ligand-protein or protein-protein docking. In the correlation with the experimental data, as long as the data is available as restraining potentials that guides the dynamics calculation, MD is flexible to associate the knowledge of the general features of the molecule of interest which is assembled in the parameters of a molecular mechanic force field (Hansson et al., 2002, Allen, 2004). MD consists of gradual scale to solve the classical equation of Newton's motion to describe the system progression by determining the forces involving in the atoms of molecules. From their coordinates definition, the potential energy can be calculated directly.

By defining the positions and momentum, a system containing huge number of particles can be defined using classical system (Cramer, 2013). In this regards, a system with *N* number of atoms in three-dimensional space can be determined as *6N* coordinates:

$$\mathbf{X} = (x_1, y_1, z_1, p_{x1}, p_{y1}, p_{z1}, x_2, y_2, z_2, p_{x2}, p_{y2}, p_{z2}, \dots) \tag{3.34}$$

Within phase space point (**X**), those coordinates are possibly separated to two vectors, describing momentum (**p**) and position (**q**).

$$\mathbf{p} = (p_{x1}, p_{y1}, p_{z1}, p_{x2}, p_{y2}, p_{z2}, \ldots.) \tag{3.35}$$

$$\mathbf{q} = (x_1, y_1, z_1, x_2, y_2, z_2, \ldots.) \tag{3.36}$$

$$\mathbf{X} = (\mathbf{p}, \mathbf{q}) \tag{3.37}$$

Based on the equation above, a distinct trajectory will be defined out by **X** term depending on every change of the system within the time frame. Every new phase point will be calculated following the previous phase point using Newtonian motion rules. Entire phase points will be produced within the trajectory as long as the system is physically realistic thus respond to the real approximation of geometric structure of the system.

The **q** position of atom in t_2 with atom velocity of $\frac{\mathbf{p}(t)}{m}$ is stated as:

$$\mathbf{q}(t_2) = \mathbf{q}(t_1) + \int_{t_1}^{t_2} \frac{\mathbf{p}(t)}{m} dt \tag{3.38}$$

The **p** in given times t_1 and t_2 is written as:

$$\mathbf{p}(t_2) = \mathbf{p}(t_1) + m \int_{t_1}^{t_2} \mathbf{a}(t) dt \tag{3.39}$$

$$\mathbf{a} = \frac{\mathbf{F}}{m} \tag{3.40}$$

The acceleration of **a** is performed from the second law of Newton's. Whereas, the atom force can be achieved from the derived potential energy in correlation with atomic coordinates:

$$-\frac{\delta V}{\delta \mathbf{q}} = m\mathbf{a} \tag{3.41}$$

Further, the potential energy can be solved through MM simulation and the approximation is mostly acquired to calculate the system. In the condition of $\Delta t \rightarrow 0$, the **Equations (3.38)** and **(3.39)** can be approximated by Euler's model:

$$\mathbf{q}(t + \Delta t) = \mathbf{q}(t) + \frac{\mathbf{p}(t)}{m}\Delta t \tag{3.42}$$

$$\mathbf{p}(t + \Delta t) = \mathbf{p}(t) + m\mathbf{a}(t)\Delta t \tag{3.43}$$

Therefore, it is preferable to simulate the trajectory of the system in space of phase to obtain the system potential while evaluating reliability of the initial system within small Δt. The initial coordinates may be attained by performing optimization of system geometry using MM. In order to get the initial momentum of atoms, a randomly assignation can be achieved by incorporating temperature with momentum (Cramer, 2013):

$$T(t) = \frac{1}{(3N-n)k_B} + \sum_{i=1}^{N} \frac{|\mathrm{p}_i(t)|^2}{m_i} \tag{3.44}$$

N represents the total of atoms within the system, while *n* belongs to the constrained number of the degree of freedom with the momentum comparatively defined toward the center of mass motion. Euler's estimation is quite unstable for calculating the approximation of the system motion and may not accurately reproduce the system trajectory within rational values of Δt. Therefore, in several simulations Verl*et al*gorithm is employed to integrate the motion equations (Verlet, 1967).

3.3.2.1 Ensembles

In general, Newton's law of motion provides stability to a system by exploring the surface energy. However, majority of natural coincidence arises under external environments in which the total energy could not reach convergence. Therefore, the prolonged systems simulations are desired. Several techniques with principles have been developed to control

the pressure as well as temperature by allowing selected variables to be fixed therefore, enabling the diverse statistical ensembles to be produced. Some variables including the particles numbers, pressure, volume, temperature, or stress can affect the dynamic and structural energetic based on the changes of system sizes toward the ensemble employed. The ensembles that have been identified so far include isothermal and adiabatic which correspond to the option of the use of temperature exchange during the constant thermodynamic. Under Forcite module, some ensembles are provided with respect to the different type of constant simulation, such as NVT, NVE, NPH, and NPT (N: number of atoms, V: system volume, T: temperature, E: energy, P: pressure, and H:enthalpy (BIOVIA, 2016).

Within this study, the MD simulation was performed under NVT ensemble since the system is preferable to permit the particles, volume, and temperature to be fixed. The particular control of temperature depends on the use of M chain of Nosé-Hoover thermostat that can be written in correlation with the Q_i and ξ_1 as the thermostat of manipulated masses and degree of freedom, respectively:

$$H = \langle \Psi | \widehat{H_e} | \Psi \rangle + \frac{1}{2}\sum_{i=1}^{N}\sum_{j=1}^{N}\frac{Z_i Z_j}{|\mathbf{R}_i - \mathbf{R}_j|} + \sum_{i=1}^{N}\frac{P_i^2}{2M_i} + \sum_{i=1}^{M}\frac{P_{\xi i}^2}{2Q_i} + N_f k_B T \xi_1 + k_B T \sum_{i=2}^{M} \xi_i \quad (3.45)$$

This typical ensemble is commonly applied for the molecules in vacuum without periodic boundary condition. In this study, since the pressure is not a significant variable throughout the works, the NVT would be an appropriate choice that allows to lower the effect of system perturbation caused by the absence of pairing to a pressure bath (BIOVIA, 2016).

3.3.2.2 Thermostat

Temperature, as a variable status is one of the important properties in MD studies which involves the thermodynamic into a system. It associates with the kinetic energy distribution through atomic velocities which is described under Maxwell-Boltzmann equation. This method rules out how a mass molecule with the velocities behaves under various temperatures by relating the temperature averages with the kinetic energy. In some conditions, the system could not configure a minimum energy due to the incomplete structure minimization which is only to eliminate the system hot spots. During the MD, the temperature changes as a consequence of the potential and kinetic energy fluctuations. To control and keep the temperature in the right values, the calculated velocities must be adjusted and the correct ensemble is created accordingly based on the statistical mechanic principles. The techniques of temperature control have been established which are Berendsen, Nosé, NHL, direct velocity, and Andersen.

Herein, NHL (Nosé-Hoover-Langevin) method is employed throughout the MD in order to give a reliable thermostat for the system by resolving the equilibrium issue that may arise during the simulation. Fundamentally, the NHL is written from Nosé-Hoover algorithm which is adjusted to deal with a typical condition where the simulated system may not reach the equilibrium state within the run time (Nosé, 1984b, Nosé, 1984a, Shuichi, 1991). To induce the system into equilibrium stage, one could integrate the rapid change of the thermostat variable by altering the time-step, yet it may require multiple stages and more times to accomplish the simulation. A modification is made at Nosé thermostat equation by adding Langevin and noise terms to become (Samoletov et al., 2007):

$$\frac{\mathrm{d}\zeta}{\mathrm{d}t} = \frac{\sum_{i=1}^{N} \frac{\mathbf{p}_i^2}{2m_i} - N_f k_B T_0}{Q} - \gamma\zeta + \sqrt{\frac{2\gamma k_B T_0}{Q}}\dot{W} \tag{3.46}$$

The d*t* discretizes the Wiener process ($\dot{W}$) and γ represents the strength of arbitrary process. The role of γ as decay constant ($^1/_\gamma$) may induce shifting in thermostat variables to recuperate the Nosé-Hoover thermostat. Further, the combination of these fractions to regulating the scaling of ζ reflects to the improvement of thermodynamic equilibrium as well as production of a system without executing multiple stages simulation (Leimkuhler et al., 2011).

3.3.3 Periodic Boundary Condition (PBC)

During the simulation, the system volume increases along with the surface in square radius, where sometimes creating an unwanted artificial outcome for the particles which are not closer by neighboring atoms at all positions. Thereby, most of the simulations involving lattices of periodic boundary apply periodic boundary condition (PBC) around the simulated structures. PBC also allows some influences to take into account the interaction during simulation, such as solvent or crystalline circumstances. Correspondingly, in order to assess the non-bond interactions, cut-off distances are included thus, the simulation system requires one nearest simulation trajectory where the particles placed. When the trajectory of particle leaves during simulation, another one of its images concurrently enters the cell from the position nearby or opposite direction (**Figure 3.5**). This rule is applied for other image particles subsequently (Steinhauser and Hiermaier, 2009, Cramer, 2013).

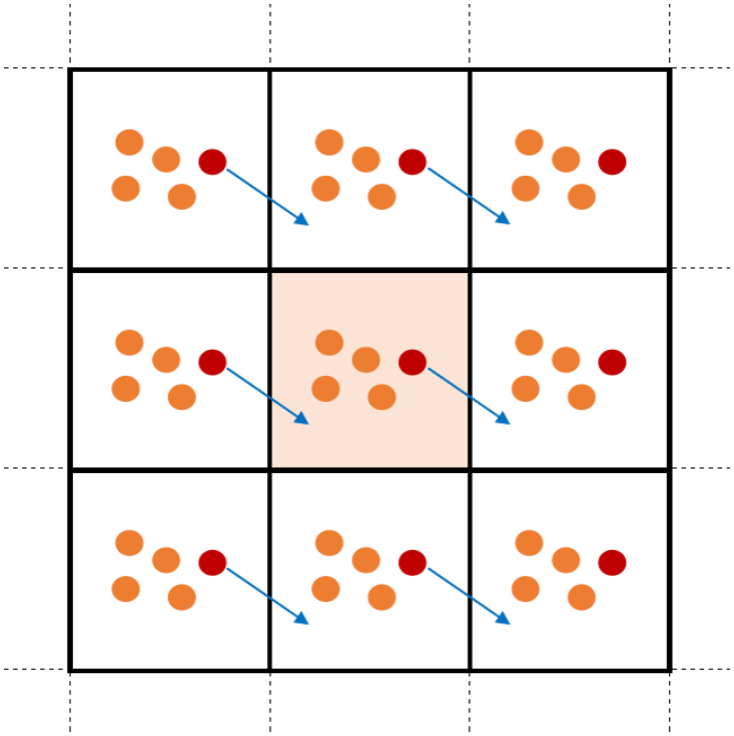

Figure 3.5 The schematic model of PBC in two-dimensional trajectories. The particles in the central trajectory are multiplied in all directions. Adapted from Steinhauser and Hiermaier (2009).

CHAPTER 4

MATERIALS AND METHODS

This chapter focuses on the methodologies of computational as well as experimental studies. The computational methods applied during the calculations are explained, including the functional and basis sets used for density functional theory (DFT). Additionally, the ZDOCK and ZRANK employed in the molecular docking, and the simulation stages along with their preferences in molecular dynamics (MD) simulations are described here. The initial methodologies performed for the construction of the structures/materials within the computational calculations are also defined. The materials and apparatus such as graphene oxide (GO), poly-(*N*-isopropylacrylamide) (PNIPAM), type of the electrodes, and other supporting chemicals used for the experimental sections are mentioned. The methods used in maintaining the aptamer and whole-cancer cell preparation are described here. Further, stepwise procedures as well as the construction of the "sandwich-format" aptamer biosensor are presented here.

4.1 Computational Studies

The application of DNA along with carbon based-structures in biosensors as a nanorecognizer plays a crucial role in self-assembling on the electrode surface (Che et al., 2007, Sessler et al., 2007, Cho et al., 2013). Graphene oxide (GO) is one of the mostly used material which has attracted a vast attention owing to its physical, optical, and electrochemical properties in biomedical applications, particularly in the biosensor research (Ding et al., 2013, Vovusha and Sanyal, 2015, Mudedla et al., 2016). Derived from graphene, GO consists of graphene plane with hydroxyl and epoxide grafted on it along with minor

carboxyl groups on its boundaries thus, benefits in molecular functionalization (Dreyer et al., 2010). In biosensors field, GO has mesmerized a significant interest due to their free π electrons and immensely high surface area which permits stronger interactions with various biomolecules, gaining them to be utilized in molecular imaging, drug/gene delivery system, or tissue engineering (Sun et al., 2008, Yang et al., 2011, Goenka et al., 2014). Particularly, it has been recognized whether GO associates to DNA through non-covalent interactions which allows to generate a complex intercalated structure (Min et al., 2011, Vovusha et al., 2013).

Poly-(*N*-isopropylacrylamide) (PNIPAM) is recognized as a smart-polymer in biosensor area. It owns tremendous interests due to its nature of lower critical solution temperature (LCST), which is around human body temperature at 32^{o}C. PNIPAM is completely water-soluble in coil state below LCST, and more hydrophobic in globular form above LCST. Several studies of PNIPAM-grafted GO have been reported in many biosensors applications. In the previous studies, the thermal-responsive characteristic of PNIPAM has been benefitted in triggering the biorecognition interaction with its target (Wong et al., 2008, Zhou et al., 2016). However, the principal properties behind the nature of interaction has not been explicated yet.

In this thesis, three different steps of computational studies have been done. First, the DFT calculation was employed to investigate the details of the interaction on the sensing surface, which was PNIPAM-grafted GO surface complexed with the immobilized aptamer. In DFT calculation, those elements were simplified into the essential basic elements. The PNIPAM molecule was represented by its single monomer (NIPAM) which was functionalized on the

GO flake (GO/NIPAM). Whereas, the aptamer was depicted by the single nucleobase adsorbed on the surface of GO/NIPAM. Nucleobases are the elementary building blocks of nucleic acids that enable to reflect the general chemical properties of intricate biomolecules (Larijani et al., 2015). Generally, the computational data obtained would comprehend the biomolecular interactions with organic molecules on the nanomaterial surface, which is important for constructing a better sensor with the high specificity (Gowtham et al., 2007, Wu et al., 2011). Similarly, recent reports have established that nanomaterials interacted with the biomolecules such as nucleic acid, protein, DNA-RNA bases have gained intensive interest by determining the binding strength of different nucleobases or their pairs on the nanosurfaces. This study enables to take the biosensor research to further levels in the field of biomedical applications (Ortmann et al., 2005, Gowtham et al., 2007, Antony and Grimme, 2008, Wu et al., 2011, Vovusha et al., 2013). Therefore, the theoretical sections are aimed to explicate the interaction behavior of nucleobases on the surface of GO in terms of binding strength and electroconductivity in the presence of insulator monomer (NIPAM).

Secondly, in order to select and to evaluate the specific aptamer to interact with the target cells (PC3 cells) in experimental, docking studies were performed toward the aptamers candidates which are previously well-understood as the corresponding aptamers to PC3 cells. The simulations of the protein binding with the aptamer were carried out together with the PNIPAM and GO molecules presented in MD simulation, as the final part of the computational works. Known as thermal-responsive polymer, PNIPAM can induce a switchable interface of interaction or electronic properties with GO organized by external signals, such as temperatures (Zhou et al., 2016). Finally, the MD simulations would combine the external environments used in wet experiment (i.e. solvent and temperature) as selected

variables to simulate the real behavior or binding event occurred during the experimental evaluation.

4.1.1 Density Functional Theory

4.1.1.1 Structure Construction

Each of graphene oxide (GO), PNIPAM monomer, and nucleobase were sketched using the molecule constructor in Materials Studio version 2016. The structure of GO employed in DFT was based on the literatures (Rosas et al., 2011, Vovusha et al., 2013). It contained one epoxide and three hydroxyl groups on the basal plane and a carboxyl group at the border. The structure of PNIPAM monomer capped with hydrogen atom and methyl group was constructed as single molecule, as well as grafted as a functionalized molecule on the GO surface through the carboxyl conjunction. The depictions of basal surfaces are presented in **Figure 4.1**. The nucleobases were built based on each original structure and in the system, they were placed parallel above the functional groups ring of the GO or GO/NIPAM surfaces systems **(Figure 4.2)**. It has been studied in other previous reports that the adsorption of aromatic ring is more favorable in parallel configuration toward the graphene structure (Rajesh et al., 2009, Ding et al., 2014). The initial distance between nucleobase molecule and the functional groups was about 2.5 Å prior to weak bonding interaction.

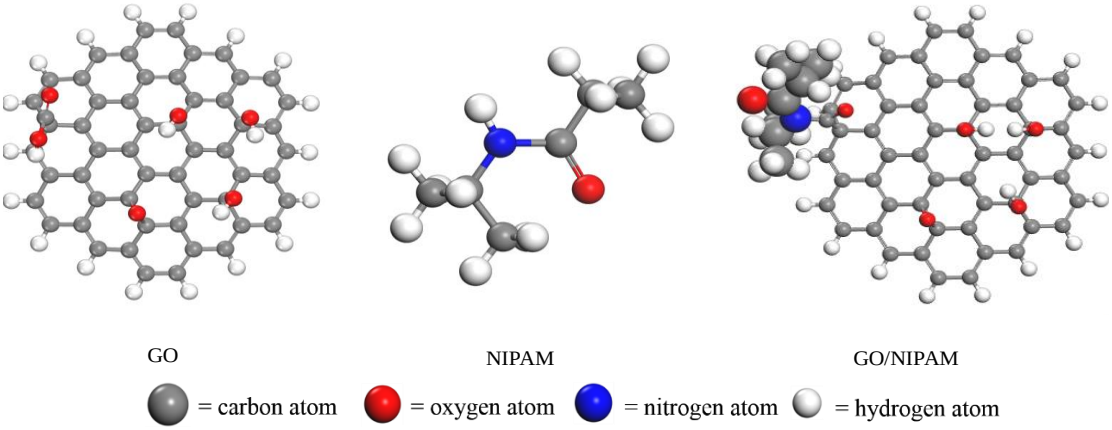

Figure 4.1 Initial structures of GO, PNIPAM monomer, and GO/NIPAM for DFT calculations.

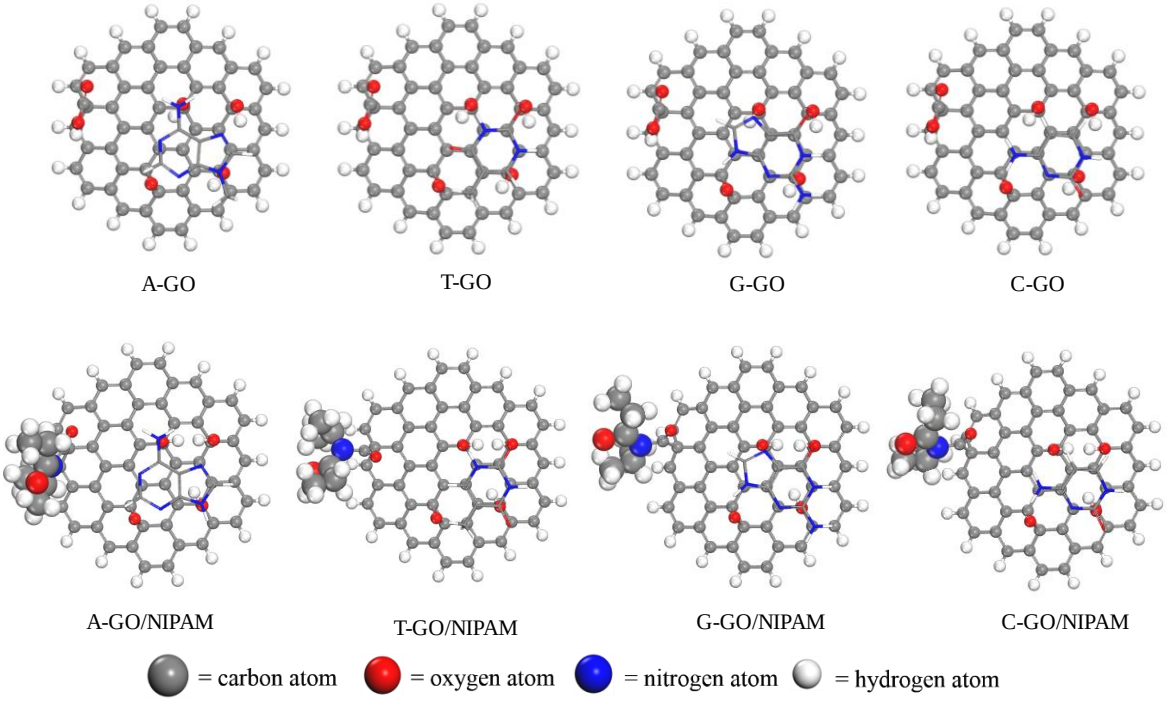

Figure 4.2 Initial structures of nucleobases in complexes with GO and GO/NIPAM for DFT calculations.

4.1.1.2 Calculation Using DMol3

The initial geometries of each structure and their complex systems were calculated using DMol3 package along with the electronic properties calculation employing generalized gradient approximation (GGA) with Perdew-Burke-Ernzerhof (PBE) functional (Perdew et al., 1996). Local density approximation (LDA) is known not to able to explicate the dispersion force among molecules properly thus, may lead to severely act in the limit of negligible overlap between electron densities and overvalue the interaction energy. The GGA overcomes these obstacles since it describes better electronic interactions between two subsystems and corrects the overestimated interaction energy produced by LDA (Srepusharawoot et al., 2009, Liang et al., 2009, Sun et al., 2010). Meanwhile, the PBE functional was employed in order to explain a weak interaction ruled by hydrogen bonding and van der Waals (Wang and Lin, 2003, Benedek et al., 2005, Li et al., 2006). The double numerical quality basis set with polarized orbital (DNP) was applied to describe all electron Kohn-Sham functions, where the 2s and 2p orbitals are employed for the carbons. Further, the DNP function set is analogous with the 6-31G** basis set and since it is based on the atomic orbitals, the results are expected better than using Gaussian basis. SCF tolerance was customized to be 10^{-6} eV/atom with 1,000 iterations. The energy tolerance, force, as well as maximum displacement of energy were determined to be 10^{-5} Ha, 2.0 x 10^{-3} Ha/Å, and 5.0 x 10^{-3} Å, respectively. In order to accurately define the van der Waals and hydrogen bonding correlations, DFT-dispersion (DFT-D) option was employed by using Tkatchenko and Scheffler (TS) functional which is applied to extended system where nucleobase is adhered on the GO surface (Tkatchenko and Scheffler, 2009). In this particular calculation, the hybrid functional was excluded since it was not computational efficient for single system calculation. The adsorption energy (E_{ads}) was calculated using this relation of:

$$E_{ads} = E_{GO(/GO\text{-}NP)} + E_{nucleobase} - E_{complex}$$

where the $E_{GO(/GO\text{-}NP)}$, $E_{nucleobase}$, $E_{complex}$ belong to the total energies of either GO or GO/NIPAM surface; single molecule of nucleobase (adenine (A), guanine (G), thymine (T), or cytosine (C)); as well as complex formation between the nucleobase and surface, respectively. Herein, the counterpoise correction was not involved during the calculation of adsorption energy under DMol3 since DNP numerical basis set was employed to minimize the basis set superposition error (Saikia and Deka, 2013a). All calculations were treated with all-electron core employing self-consistent field (SCF) with the convergence criteria of 10^{-6} a.u. In this correlation, chemical structure of the *N*-electron system is able to influence reactivity profile of the molecule, which further explains that its electronegativity is directly proportional to its ability in accepting the electrons. The correlation of electronegativity (χ) with the total energy (E) and external potential $v(\vec{r})$ is equal to minus of electronegativity $(-\mu)$. Therefore, the quantum descriptors for the systems calculations were defined as follows (Saikia and Deka, 2013a):

$$\chi = -\left(\frac{\delta E}{\delta N}\right)_{v(\vec{r})} = -\mu \tag{4.1}$$

While, the second derived energy toward the external potential $v(\vec{r})$ is expressed as hardness (η) in:

$$\eta = \frac{1}{2}\left(\frac{\delta^2 E}{\delta N^2}\right)_{v(\vec{r})} \tag{4.2}$$

The equations of each μ and η are described using the Mulliken principle (Mulliken, 1935) in restricted method, in which, they are correlated with the potential of ionization *(I)* as well as the electron affinity *(A)*:

$$\mu = -\chi = \frac{1}{2}(I + A) \tag{4.3}$$

and

$$\eta = \frac{1}{2}(I - A) \tag{4.4}$$

I and *A* is equivalent to the $-\mathrm{E}_{\mathrm{HOMO}}$ and $-\mathrm{E}_{\mathrm{LUMO}}$, respectively (Chermahini et al., 2015).

The geometry optimization of a single molecule and each complex system was configured to attain the lowest energy state of the structure. During the optimization, position of the atoms was allowed to relax to decrease the total energy within the system. The iteration cycle occupied during the process determines the potentials gradient at each atomic position to be minimized. The convergence tolerance employed will be fit with each iteration, thus yielding the minimum energy between two successive iterations which is less than the convergence tolerance. The electronic properties derived from this calculation are density of states, highest-occupied molecular orbital (HOMO), lowest-unoccupied molecular orbital (LUMO), electrostatic potential, total energy, and vibrational spectra.

4.1.2 Molecular Docking

4.1.2.1 Molecular Construction of Aptamers

There were ten aptamers with different types investigated individually toward α6β4 protein under docking simulations (**Table 4.1**). According to the literatures, these aptamers were used to recognize biological part of PC3 cells, such as protein or cells. Since each aptamer has different unique three-dimensional structure of conformations to recognize each target, in this computational method each secondary structure of the aptamer was predicted to obtain the conserved region of *motifs* within their sequences. To obtain prediction of the secondary structure (2D) with more information details, Mathews Lab RNA Structure software was

used (available online at http://rna.urmc.rochester.edu/RNAstructure.html). This software allows to predict either ssDNA or RNA structures into any possible folding**.** Firstly, in order to predict a three-dimensional aptamer structure, MFold software was utilized (Zuker and Jacobson, 1998, Lee et al., 2015) to fold the initial sequence of each aptamer into its secondary structure. The folding temperature was set to 25^0C with solvent condition in default setting. The model which had the lowest Gibbs energy (*G*) was picked and its output, the dot-bracket (Vienna) format, was fetched for tertiary (3D) prediction. For this purpose, RNA Composer software was applied to generate the 3D structure automatically.

The 3D construction concept is a kind of search-engine based on the translation of RNA Fragment Base Search Engine (RNA FRABASE) database which associates with RNA 3D structure database. The Vienna format imported to the RNA Composer was generated into PDB (protein data base) format of 3D structure as outcome. Notably, the RNA Composer only generates the Vienna format input into the PDB file of RNA. If compared to ssDNA aptamer structure, hydroxyl group appeared at 2'-carbon atom of ribose, while uracil was at the thymine position. The Discovery Studio Visualizer (or ver.2016) was employed to adjust this condition into ssDNA format (Heiat et al., 2016). For doing this, PDB file of each aptamer was activated individually and "Macromolecule" command was allowed to modify the ribose backbone into deoxyribose (all oxygen in 2'-carbon ribose atoms were changed into hydrogen atoms) and convert all the uracil bases into thymine (hydrogen assembled to the 5-carbon pyrimidine uracil atom was replaced by carbon atoms forming methyl group) (Hu et al., 2015, Heiat et al., 2016, Ahirwar et al., 2016).

Table 4.1 The aptamers sequences applied in docking studies.

No.	Name	Type	Sequences	Sequences length	Reference
1	Wy5a	ssDNA	TGCCACTACAGCTGGTTCGG TTTGGTGACTTCGTTCTTCGT TGTGGTGCTTAGTGGC	57	Wang et al. (2014)
2	Wy5b	ssDNA	TGCCACTAAGCTGGTTCGGT TTGGTGACTTCGTTCTTCGTT GTGGTGCTTAGTGGC	56	
3	PSap4#5	ssDNA	AATTAAAGCTCGCCATCAAA TAGC	24	Jolly et al. (2016)
4	IDA	ssDNA	GCCTGTTGTGAGCCTCCTAA CCGTGCGTATTCGTACTGGA ACTGATATCGATGT	54	Berg et al. (2016)
5	ApS6	dsDNA	GGCGGCTTGTGCGGCCTTTTT TGGTGGTGGTGGTTGTGGTG GTGGTGG	96 (double helix)	Liu et al. (2016)
6	A9g	RNA	GGGACCGAAAAAGACCUGA CUUCUAUACUAAGUCUACG UUCCC	43	Dassie et al. (2014)
7	A10	RNA	GGGAGGACGAUGCGGAUCA GCCAUGUUUACGUCACUCCU UGUCAAUCCUCAUCGGC	56	Lupold et al. (2002), Dhar et al. (2008), Bagalkot et al. (2007)
8	A10-3-J1	RNA	GGGAGGAAUAGCUGACGGG AGGACGAUGCGGAUCAGCC AUGUUUACGUCACUCCUUG UCAAUAAUAAGGGGC	72	Leach et al. (2016)
9	CSC1	ssDNA	ACCTTGGCTGTCGTGTTGTAG GTGGTTTGCTGCGGTGGGCT CAAGAAGAAAGCGCAAAGT CAGTGGTCAGAGCGT	75	Sefah et al. (2013), Wang et al. (2013)
10	CSC13	ssDNA	ACCTTGGCTGTCGTGTTGTGG GGTGTCGTATCTTTCGTGTCT TATTATTTTCTAGGTGGAGGT CAGTGGTCAGAGCGT	78	

4.1.2.2 Preparation of Input Structures and Optimization

The α6β4 protein structure was extracted into PDB file from RSCB biomolecular bank. Before protein-protein docking, the water and ligand molecules were removed and hydrogen atoms were added in the protein structure. Each structure of aptamer and protein were

adjusted first using Dreiding-like force field tool to pre-optimize the structural geometry. The minimization processes were done by using steepest descent minimization of 32,000 steps using CHARMm force field under Discovery Studio Ver. 2016.

4.1.2.3 Aptamer - Protein Docking with ZDOCK-ZRANK

ZDOCK molecular docking and ZRANK refinement module as part of Discovery Studio ver.2016 were utilized to provide docking prediction and reranking refinement, respectively. ZDOCK was used to perform coarse-grained search of binding characteristics between the aptamers and α6β4 protein. According to this, ZDOCK-ZRANK has been widely employed for complex systems prediction between protein-protein and peptide-nucleic acid (Chen et al., 2003, Huang et al., 2015, Hu et al., 2015, Xia et al., 2016). The 6^{o} sampling was employed in ZDOCK to attain more accurate movement of 54,000 of the predictive complexes. The first top 2,000 ranks were subsequently carried out for the interaction analysis with ZRANK to achieve more accurately reranking the docked complexes.

4.1.3 Molecular Dynamics Simulations

4.1.3.1 Structure Construction

As an initial step of MD, each element of the system was constructed individually, including GO, PNIPAM, and aptamer molecules. The basis structure of GO surface was first constructed from the graphite three-dimensional periodic structure which is available at Structure Library in Materials Studio software, into pristine graphene periodic layer. The periodic graphene was subsequently changed into a non-periodic structure by keeping one layer and eliminating the unused layers. The final two-dimensional structure of graphene was obtained in a size of 8.5 x 4.0 nm^2 (1,271 carbon atoms, **Figure 4.3**), providing an appropriate

size for the aptamer to be placed onto it. The epoxy and hydroxyl groups then were grafted randomly on both basal graphene surface. Whereas, the carboxyl groups were randomly assembled on the edge of the structure. The oxygen functional groups considered for the GO model was a typical outcome from a standard oxidation process (Argyris et al., 2008, Patra et al., 2009, Medhekar et al., 2010). In this structure, for every 20 carbon atoms, there are two epoxy, two hydroxy, and one carboxyl groups (i.e. $C_{10}O_1(OH)_1(COOH)_{0.5}$), where the carboxyl groups are deprotonated to mimic the behavior of GO at pH 7.4 (Sun et al., 2014, Baweja et al., 2015, Zeng et al., 2016). Carbon to oxygen (C:O) has ratio of about 4:1 (Dreyer et al., 2010, Baweja et al., 2015). Two PNIPAM chains with a repeat unit of 50 monomers per chain (MW: 5660) were constructed using the optimized monomer structure prepared under DMol3 employing polymer builder. The PNIPAMs were assembled to the GO surface *via* carboxylic conjunctions on the middle of both wider edges of GO, oppositely.

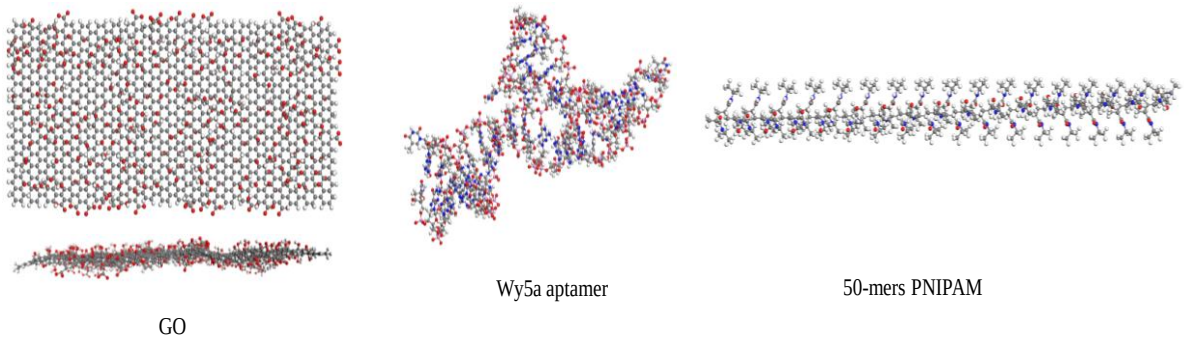

Figure 4.3 Initial structures of GO surface (in top and side views), Wy5a aptamer, and PNIPAM chain for MD simulations.

The optimized Wy5a aptamer from Discovery Studio optimization was placed approximately 5 Å from the GO surface vertically by considering that the active binding sites were placed away from the GO according the docking orientation with the α6β4 protein. The construction of the whole system was initiated from GO as the basal surface, followed by the PNIPAM

chains on the sides, aptamer, and protein. Before situated at the periodic boundary condition (PBC), each molecule was optimized separately and, subsequently, built as layers in PBC system. The periodic lattice was created with parameters of *a*= 15.0 nm, *b*= 12.0 nm, and *c*= 12.0 nm and the system was positioned in the center, accordingly. A vacuum space of around 15 Å was applied in order to avoid the artifact effects of non-periodic directions within the PBC box. Using Amorphous Cell module, the solvent was packed into the system to describe the water characteristics (employing 11,399 water molecules). The 122 of sodium and 92 of chloride atoms were added to neutralize the charges within the system.

4.1.3.2 Calculation Using Forcite

(i) Geometry Optimization

Before incorporated into the PBC box, each molecular structure of MD components was previously optimized by using Forcite module under Materials Studio. Forcite is a collection of programs and settings of MM calculations, including: single point energy, geometry optimization, and dynamics calculations. The GO surface, PNIPAM chains, Wy5a aptamer, α6β4 protein were individually optimized using the Universal force field (UFF). Several evaluations previously have been made using different force fields, and UFF seemed to give a fairly good result among other forcefields according to the various materials employed. It enables to calculate many combinations of atoms, including protein, organics, or nucleic acids (Rappe et al., 1992). Around 50,000 steps of Smart minimization were applied to converge the system to a value of 0.001 kcal/mol with force of 0.5 kcal/mol/Å. Smart algorithm implements a combination of the others algorithms of steepest descent, adjusted basis set Newton-Raphson (ABNR), and Quasi-Newton. Once all components were

optimized, they were united in the same PBC and optimized subsequently by UFF. For big system compiling different atom types, UFF is a choice which can deal with general rules of many types of atoms parameters. Instead, considering the empirical force field for huge biomolecules calculation is important to calculate the hydrogen bonding that may be intricated within the biomolecules, such as aptamer (DNA). The UFF roles the simulation of the electrostatic contributions by estimating the atomic partial charges of the optimized geometry (Ogawa et al., 2003). The optimization process allows to define the structural conformation, involving the atoms angle, bonds length, minimum total energy, and other essential properties with a defined force field. The results of optimized structures (either periodic or non-periodic) were involved in MD simulations.

(ii) Simulation Procedure

The MD simulation processes were divided into two types of subsequent simulations, which were: *System I*, without α6β4 protein and *System II*, with α6β4 protein (**Figure 4.4**). In general, all the MD simulations had been done in the size of simulation box of 15.0 nm × 12.0 nm × 12.0 nm. In the System I, the protein molecule was not introduced in PNIPAM-GO-aptamer system yet. After the molecules were assembled as a System I, the system was subsequently optimized with UFF. The equilibrium of the System I was performed for 200 ps by keeping the main system fixed and allowing the PNIPAMs and water molecules to equilibrate. Afterwards, the thermal responsive behaviors of PNIPAM-grafted GO were further investigated by performing MD for 4,800 ps at temperatures of 298 K and 310.7 K, which correspond to the temperatures below and above the LCST, respectively. The temperature of 310.7 K was selected in order to mimic the condition of human body

temperature which has biological activity around 37ºC (~310 K). To verify the thermal-responsive characteristic of the constructed PNIPAM, the initial simulation of single PNIPAM chain was firstly carried out. The simulation employed the optimized single PNIPAM chain dissolved in water within PBC system. The MD was done under NVT ensemble for 10 ns at 298 K and 15 ns at 310.7 K.

For the interaction of α6β4 protein with Wy5a aptamer on the PNIPAM functionalized-GO surface, the α6β4 protein was placed hovering over the system surface with distance of 0.5 nm from the aptamer, which was so-called the System II. The orientation of the protein was set using the similar orientation as in docking result with the Wy5a aptamer. Upon protein introduction, the system was kept fixed and subsequently optimization was performed using the same optimization parameters. Afterward, the simulation of System II was performed for 500 ps with 1.0 fs of time steps by allowing the protein moving freely, while the elements of GO surface, PNIPAM chains, and Wy5a aptamer were kept constraint. The final results would be appearing as trajectories which contain the energetics datasheet and piece of simulated system during the simulation time in every 100 fs. The interaction energies were obtained by the single points energies calculations conducted using COMPASS force field (Sun, 1998). The use of COMPASS was applied since it is one of the efficient force fields which is closer to the experimental result (Kunzel and Gross, 2013, Martinho et al., 2014).

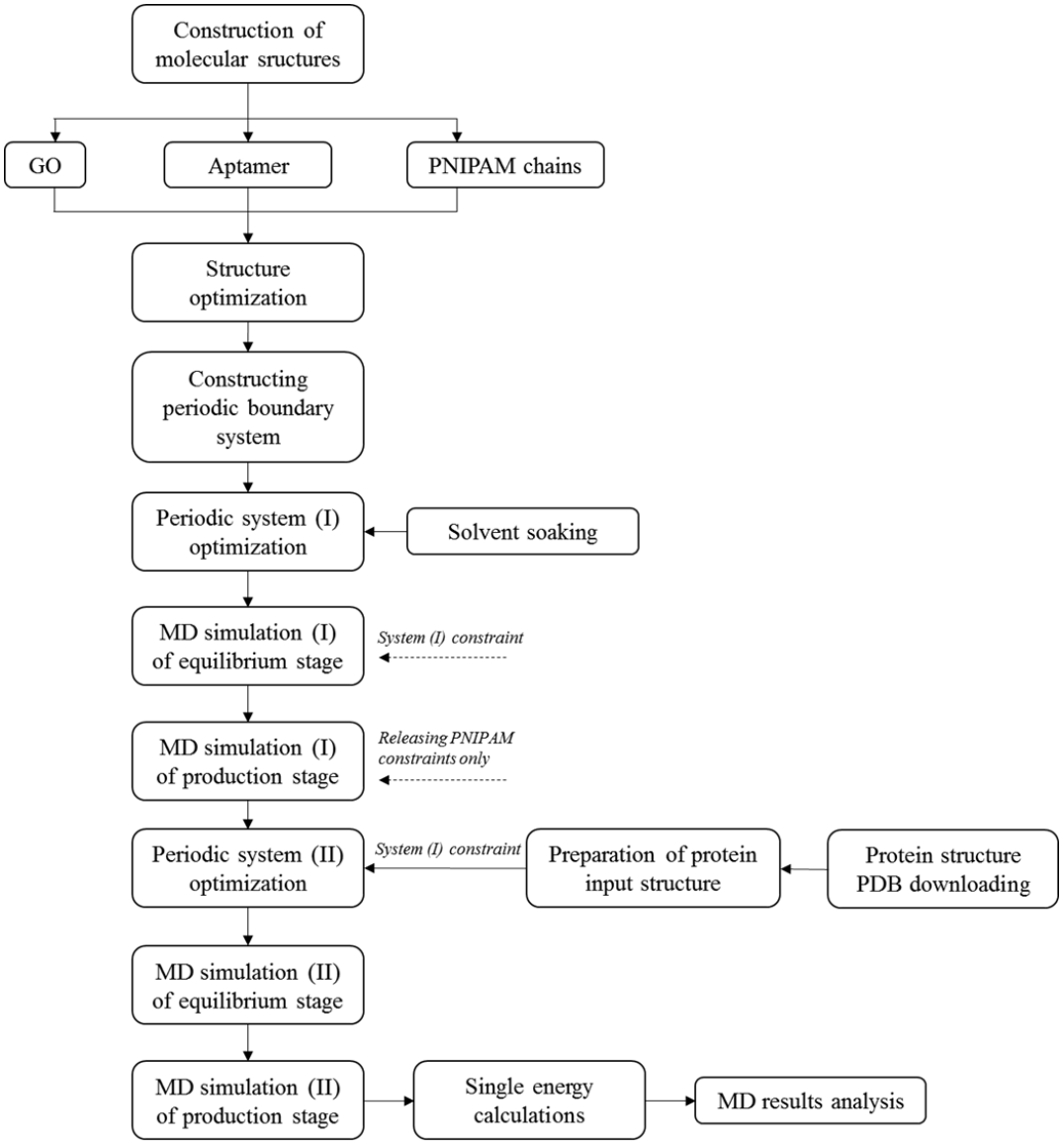

Figure 4.4 Flow chart of MD simulation of aptamer-protein interaction mediated by PNIPAM functionalized GO at temperatures of 298 K and 310.7 K.

All the simulations were performed at constant temperature and volume (NVT). The Nosé-Hoover-Langevin (NHL) thermostat was employed using coupling time of 1 ps. In this study, two summation methods, are adopted: Particle-Particle Particle-Mesh Ewald (PPPM) to evaluate the electrostatic interactions and atom based cut-off to evaluate the van der Waals interaction. The PPPM uses a Discrete Fourier Transform to evaluate the reciprocal space portion of the Ewald summation method (Hockney and Eastwood, 1988). The performance

can be significantly improved (rather faster) than the ordinary Ewald method primarily for large systems. In practice, the PPPM was verified to be faster in calculation of larger systems due to the reducing time on less cores numbers (Gargallo et al., 2003, BIOVIA, 2016). The atom-based cut-offs, a direct summation method, has been widely used to compute the long-range non-bond interactions in which the non-bond parameters are calculated based on a selected cut-off value and any interactions beyond the cut-off are not considered. Nevertheless, this method enables to cause the disruptions of energy and its derivatives. Since the distance of atom pair move in and out based on the cut-off value, the energy will jump and the non-bond energy is involved in one step and lost from subsequent step (BIOVIA, 2016).

4.2 Experimental Studies

4.2.1 Materials and Instruments

Potassium chloride, magnesium chloride, sodium chloride, sodium dihydrogen phosphate, disodium hydrogen phosphate, potassium ferricyanide, potassium ferrocyanide, ruthenium hexamine (RuHex), 1-ethyl-3-(3-dimethylaminopropyl) carbodiimidehydrochloride (EDC), N-hydroxysuccinimide (NHS), potassium persulfate, N, N, N, N-tetramethylethylenediamine (TEMED), and poly-(*N*-isopropylacrylamide) were purchased from Sigma-Aldrich (Sweden) as analytical grade.

The Wy5a aptamer was synthesized and purified by integrated DNA technologies (Coralville, IA). The lyophilized powder of aptamer was next diluted into the phosphate buffer saline (PBS 1x) with Milli-Q water and kept at -20^{o}C. The voltammetric measurements were done using Ivium Stat.XR (Eindhoven, Netherlands) electrochemical analyzer.

Whereas, the impedance measurements were established with Autolab potentiostat-galvanostat. Glassy carbon with three-electrode cells (GCE) (0.07 cm^2 surface area), Ag/AgCl (3 M KCl), and platinum wire were employed as working, reference, and auxiliary electrodes, respectively, in the voltammetric measurements (Parlak et al., 2014).

4.2.2 Cell Culture and Immobilization

PC3 (human prostate cancer cells) was cultured using Roswell Park Memorial Institute (RPMI 1640) medium. At the first step, the vial containing cells was taken in frozen medium from nitrogen tank. Then vial was immediately placed in a 37ºC water bath to quickly thaw cells. Before the opening the vial, it was wiped with 70% ethanol. At the second step, vial contents were transferred to 15.0 mL tube with culture medium. Afterwards, centrifugation was done at 1,200 rpm for 3 minutes. The supernatant was discarded and new flask with fresh culture medium was prepared. In this step, cell culture medium was added and the cells were mixed well by pipetting. The cell mixture was transferred to a flask and mixed well. The prepared flask was then examined under microscope. Subsequently, cells were incubated at 37ºC under a 5% CO_2-humidified chamber. Cells were passaged when cell confluence reaches to 80% ~ after 72 h. In this step, medium was removed and cells were washed with Dulbecco's phosphate buffered saline (DPBS) to remove the residual medium.

After washing step, Trypsin-EDTA was added to the flask. The flask containing cells and Trypsin-EDTA was then incubated at 37ºC for a couple of minutes. Next, cells were observed under the microscope to see the cells detachment. About 2.0 mL medium was added to stop trypsinization followed by pipet to detach all cells. Afterwards, the cell suspension was

transferred to 15.0 mL tube. Subsequently, cell culture medium was added to a new flask. The cells were then diluted as appropriate into a flask and mixed well and incubated at 37^{o}C. After 72 h, the culture was centrifuged for 3 minutes at 1,200 ppm to separate the cells from the medium. The cells were then rinsed using DPBS (pH 7.4) containing 10 mM of $CaCl_2$ and 5 mM of $MgCl_2$. Next, the cell sediment was subsequently re-suspended in DPBS (pH 7.4) to obtain a homogenized cell suspension and counted using Beckman cell counter.

4.2.3 GO and PNIPAM Composite Preparation

GO was prepared from graphite with the Hummers method (Lerf et al., 1998) and exfoliated to GO by sonication (Park and Ruoff, 2009). PNIPAM and GO composite was prepared through free-radical polymerization. Further, 100 mg of PNIPAM was dissolved into 20.0 mL water and subsequently, dispersed to the GO suspension by stirring under nitrogen atmosphere. The solution of KPS 10 mg and TEMED 10 µL in 1.0 mL of water was added into the mixture at ~ 0^{o}C during stirring. Next, the free-radical polymerization was started to proceed at 30^{o}C for 24 h. The GO-PNIPAM composite was then purified by washing repetitively and dialysis. In the last step, the obtained composite solution was centrifuged to remove the excess PNIPAM (Qi et al., 2012).

4.2.4 Aptamer and Cell Applications on The Electrode Surface

In order to optimize the aptamer immobilization, the Wy5a aptamer was diluted into several concentrations 2.0, 4.0, 6.0, 10.0 µM and applied on to the electrode surface upon activation of carboxylic groups by GO. Furthermore, the cell immobilization was done by incubating the various amounts of PC3 cells suspension on to Wy5a aptamer (APT)-immobilized electrode for 2 h (GCE/GO-PNIPAM/APT/Cell). To remove the non-specific cell biding on

the APT-immobilized electrode, the electrode was rinsed using PBS 1X buffer. In the last step, additional 10 µL aliquot of 4.0 µM of the Wy5a aptamer solution was applied on the electrode surface to obtain the sandwich architecture (GCE/GO-PNIPAM/APT/Cell/APT). All electrochemical measurements were carried out in 0.1 M KCl solution and 5×10^{-4} $[Fe(CN)_6]^{3-}$ redox solution using cyclic voltammetry at room temperature and scan rate of 100 mV/s.

4.2.5 MTT Assay

Methylthiazoletetrazolium (MTT) assay was performed in order to determine the growth inhibition or cell proliferation of cells quantitively using colorimeter. The protocol was performed upon aptamer treatment following the MTT protocol. The PC3 cells (1×10^4 in 100 µL) were plated in 96-well tissue-culture cluster and grown at 37°C overnight. The cells were treated with some aptamers concentrations for 24 h or left untreated for the control experiments. After post-treatment of 24 h, 10 µL of MTT 5mg/mL was applied to each well and incubated for 5 h at 37°C. The cultured medium containing MTT was then removed and 150 µL of ethanol/DMSO (1:1) was added into each well and incubated for 30 minutes with gentle shaking. Absorption at 570 nm was measured using Bio-Rad ELISA Microplate Reader (US) with 630 nm as the reference wavelength. The measurements were done in three-replications and the results were presented as a mean of ±SD.

CHAPTER 5

RESULTS AND DISCUSSION

In this chapter, the results obtained from the computational as well as experimental studies presented. The computational part comprises three sections, *viz.*, (1) density functional theory (DFT), (2) molecular docking, and (3) molecular dynamics (MD) simulations. The DFT method presented here describes the theoretical background of the nucleobases adsorption on the GO flake in the presence of the thermal responsive polymer (poly-(*N*-isopropylacrylamide; PNIPAM monomer), in correlation with the tunable surface in biosensor experiment. Within this section, the structural energetics, electronic properties, and binding characteristic of the adsorption complexes are elucidated. The molecular docking section confirms the most favorable binding interaction among the aptamers Wy5a, Wy5b, and also other aptamers with the target protein (representing PCa whole-cell). The best pose containing the active residue of the protein is introduced as the interactive biorecognition-target for the MD studies. Accordingly, the wide surface of GO, Wy5a aptamer, PNIPAM and proteins are employed under MD simulations using selected environments. The first MD study is on the investigation of stimulated-temperatures of PNIPAM (298 K and 310.7 K) and the second MD study accommodates the interaction of Wy5a aptamer with the protein under temperatures of 298 K and 310.7 K, distinctively. Next, the experimental studies are subsequently discussed concerning the threshold value of the PC3 aptasensor at 298 K and 310.7 K, characterization profile of PC3 aptasensor surface, EIS spectra measurements of the concentrations range, and sensitivity of the PC3 aptasensor among other cells. Conclusively, both parts are interrelated with each other based on the results obtained.

5.1 Computational Studies

5.1.1 Density Functional Theory

The DFT calculations were performed in order to establish the role of PNIPAM monomer in affecting the electronic properties and structural energetics of the nucleobases adsorption on to the graphene oxide (GO) surface. This is an important preliminary study carried out to understand the fundamental interaction of the molecular interface in aptasensor. First of all, each structure was constructed and optimized using DMol3 package until it reached the minimum eigenvalue score of energy in which it was appropriate with the potential gradient of position of each atom. The initial configuration of each element was relaxed and the minimum energy orientation obtained was selected for the further calculations.

The optical characterizations (Raman and FT-IR spectra) of GO and NIPAM molecules are firstly discussed here in order to verify the existence of their structural units compared to the experimental results of the previous published works. Following these parts, the discussions of structure and energetics of the isolated element/complexes of nucleobases with GO and GO/NIPAM as well as their electronic properties are subsequently elucidated.

5.1.1.1 Optical Raman Spectra of NIPAM and GO Molecules

Raman spectroscopy is commonly used technique to characterize the crystal structure of materials including its defects and disorders, based on the emission or absorption of phonons (Saito et al., 2011). The calculated spectra of PNIPAM monomer is compared to the experiment in **Figure 5.1**. The peaks identified below 1,000 cm^{-1} indicate the presence of C-C skeletal stretching mode. Further, the peaks within the region of 1,400 cm^{-1} to 1,500 cm^{-1} are recognized as bending vibrations of aliphatic CH_2 and correlated to the N-H vibrations.

A weak peak is also seen around 1,650 cm^{-1}, which is presumably related to the C=O vibration. In higher wavenumber of > 2,800 cm^{-1}, the distinct peaks are noticed as C-H symmetric or antisymmetric stretching modes (Tsuboi et al., 2008, Nur et al., 2009). In general, these results are found comparable with those in the previous experimental study (Nur et al., 2009) (**Figure 5.1 (b)**).

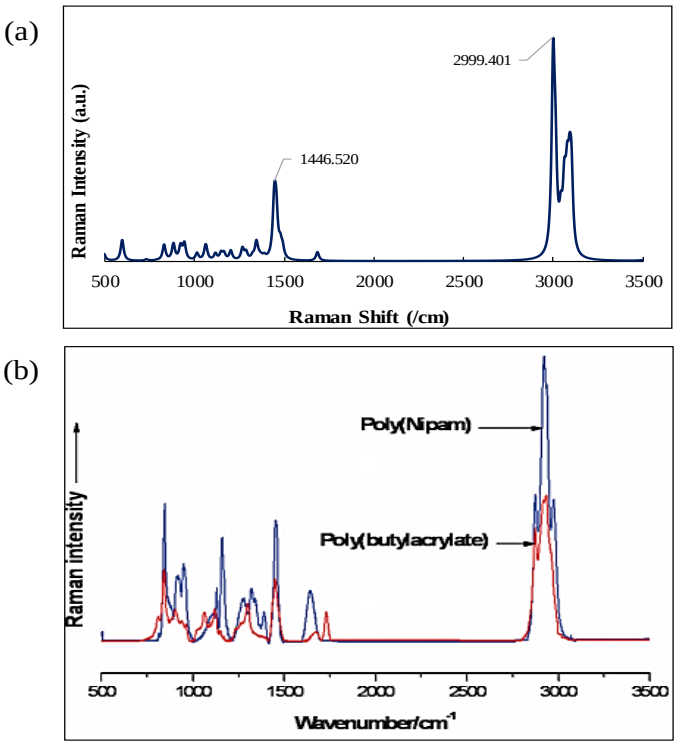

Figure 5.1 Raman spectra of NIPAM molecule obtained from theoretical calculations (a) and experimental (adapted from Nur et al. (2009))(b).

In GO case, there exist D and G bands which commonly reflect the main intensities over the spectra. Generally, the D band represents the defects occurred in sp^2 domains and usually arises around 1,355 cm^{-1}, while G band frequently lies in the range of 1,500 cm^{-1} to 1,630 cm^{-1} and corresponds to the first order of E_{2g} scattering mode describing the size of sp^2 clusters. As seen in **Figure 5.2 (a)**, both D and G-bands are distinctively recognized within the wavelength range from 500 cm^{-1} to 2,000 cm^{-1} which are similar with that of experimental

results (**Figure 5.2 (b)**) (Faucett and Mativetsky, 2015). Whilst, the other peaks appeared within the wavelength may be due to the effects of GGA/PBE functional in which some conditional systems overestimate the optical calculations. However, this method is reliable enough to provide the complex vibrational calculation employing the non-covalent properties without interfering the main spectra profiles.

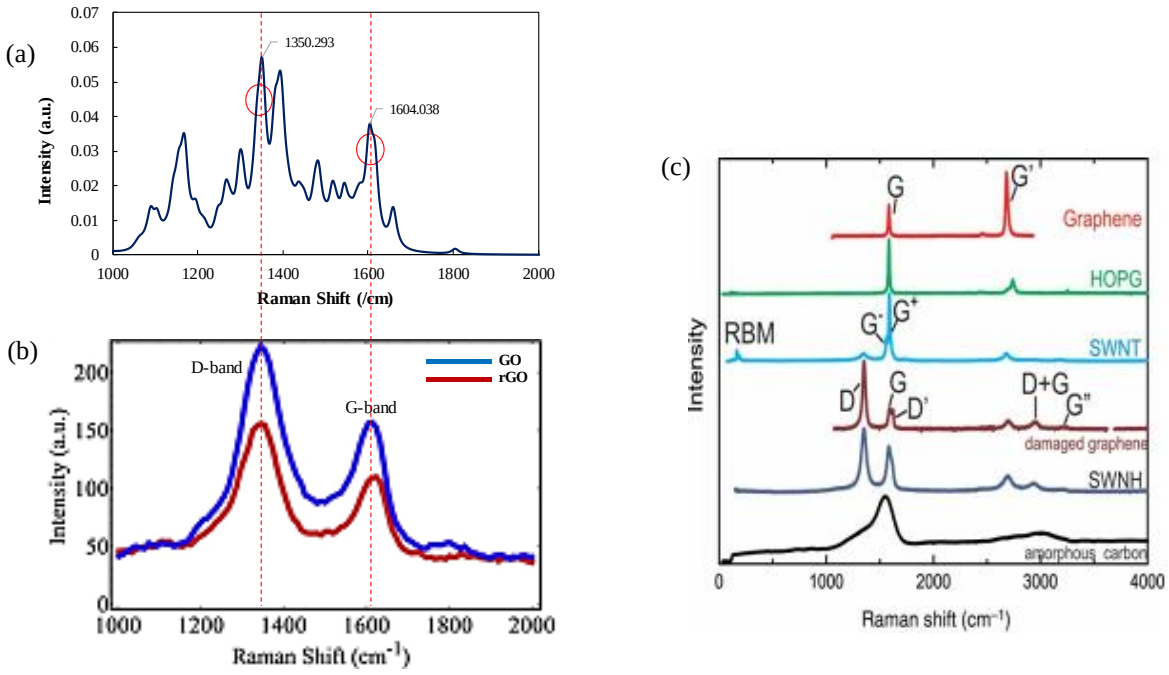

Figure 5.2 Raman spectra of GO obtained from (a) theoretical calculations and (b) experiment (adapted from Faucett and Mativetsky (2015)), with (c) additional spectra data of graphitic materials (adapted from Saito et al. (2011)).

It is also worth to note that the obtained spectral profile of GO can be distinguished from those with the graphene or graphite spectra, where the D band is absent or may be found in very low intensity (**Figure 5.2 (c)**). The reason is due to the original feature of the molecular structure of graphite or graphene that do not characterize significant oxidative defects (Saito et al., 2011, Hafiz et al., 2014). Therefore, the presence of D band in GO indicates the reduction in sp^2 C-C domains which correlates with the defects of oxygen group

functionalization. Accordingly, the correlation between D and G bands are further expressed in relative intensity ratio (I_D/I_G) defining a degree of disorder that inversely associated with the size of sp^2 clusters. The I_D/I_G intensity ratio for the constructed GO is 1.5, where D band is observed higher than G band (Mattevi et al., 2009, Mativetsky et al., 2010, Ambrosi et al., 2011, Faucett and Mativetsky, 2015). Higher number of the observed ratio indicates that the constructed GO plane contains more C-C bonds rather than the functionalization of oxygen groups on the surface.

5.1.1.2 Optical IR Spectra of NIPAM and GO Molecules

The calculated IR spectrum of PNIPAM monomer shown in **Figure 5.3 (a)** is compared with the experimental IR spectra obtained from the works done by Lin and co-workers (**Figure 5.3 (b)**) (Lin et al., 2014). The peaks observed at 1,511 cm^{-1} and 1,652 cm^{-1} are close with those observed at 1,550 cm^{-1} and 1,650 cm^{-1} of the experimental results, which are attributed to the absorptions of the -N-H and -C=O groups of the PNIPAM, respectively. The peak at 3,369 cm^{-1} recognized within region of 3,000 cm^{-1} - 4,000 cm^{-1} refers to the stretching vibration of the -O-H group which is detected as broader peak in experiment (3,424 cm^{-1}). The broader peak and low resolution of the spectra observed in experimental spectra is due to the residual water moisturizing the PNIPAM molecules (Dybal et al., 2009, Guiney et al., 2009, Hu et al., 2014). Whereas, the peaks corresponding to the stretching vibrations of the CH_2 and CH_3 groups are found around 3,075 cm^{-1} and 2,995 cm^{-1} while in experimental results, they appear at around 2,973 cm^{-1}; 2,935 cm^{-1}; and 2,876 cm^{-1} (Lin et al., 2014).

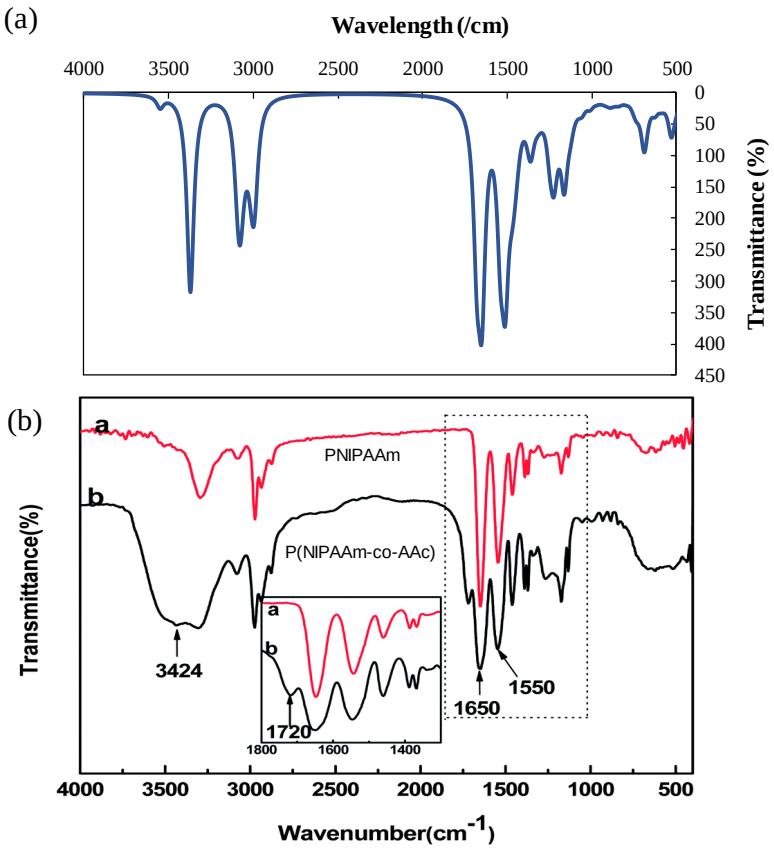

Figure 5.3 FT-IR spectra of NIPAM molecules obtained from (a) theoretical calculations and (b) experimental result (adapted from Lin et al. (2014)).

Figures 5.4 (a) and **(b)** compare the IR spectra of the GO molecule obtained from the present theoretical calculations with the previous experimental studies performed by Oh and co-workers (Oh et al., 2010). The absorption spectra due to stretching vibrations of -C-O- and –C=O appears at 1,093 cm^{-1} and 1,880 cm^{-1}, respectively, which are comparable with the vibrations occurred around 1,000 cm^{-1} and 1,740 cm^{-1} in the experiment. For the epoxy group, it is apparently observed at two points, around 868 cm^{-1} and 1,293 cm^{-1}, in which these results are near to the experimental spectra found at 850 cm^{-1} and 1,220 cm^{-1}. Further, the absorption of -O-H is detected around 3,450 cm^{-1} in theoretical and 3,390 cm^{-1} in experimental works. Similar with NIPAM spectra, it is recognized that the -O-H group in theoretical spectra does not appear as broad as in the experimental spectra, which is caused by the absence of water

disturbance that was not included in the spectra calculation. Whilst, in the fact that the broad absorption band is affected not only by the presence of -O-H group but also the absorbed water molecules (Oh et al., 2010).

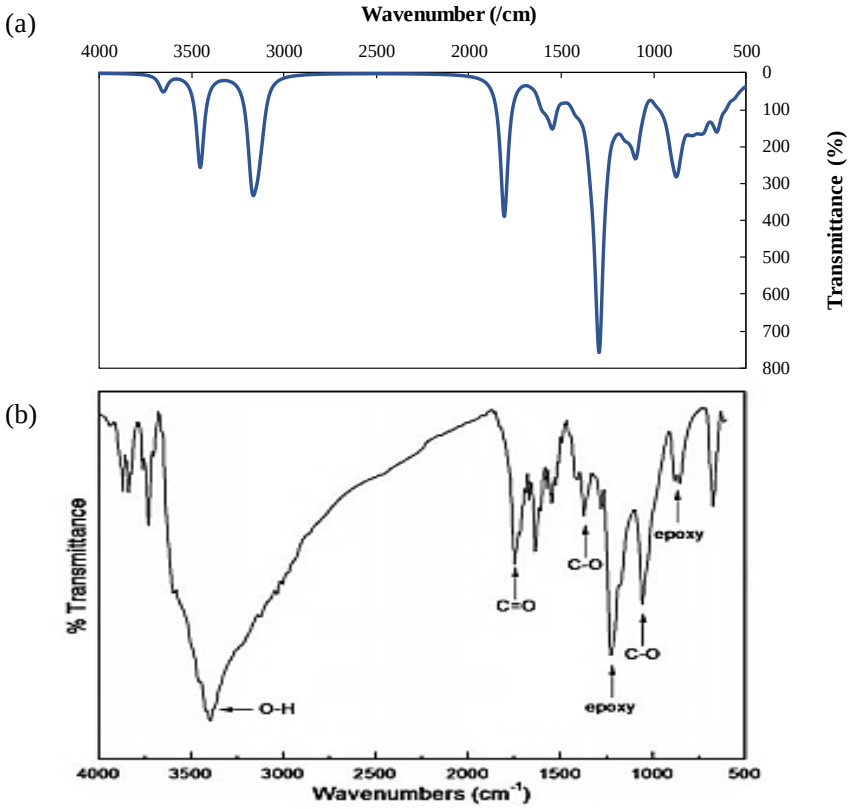

Figure 5.4 FT-IR spectra of GO obtained from (a) theoretical calculation and (b) experimental result from Oh et al. (2010)).

In accordance with the above results, the comparisons made toward the experimental range of each molecule reveal that the constructed GO and NIPAM molecules applied within these computational studies accomplished their real compositions in nature.

5.1.1.3 Structure and Energetics

In structural geometry studies, the nucleobase complex either with GO or GO/NIPAM surfaces including the geometrical changes, atomic hydrogen bonding of nucleobase toward

the surfaces and its effect to the adsorption energy are compared. The optimized structures of each nucleobase along with the labeled atoms are presented in **Figure 5.5**. Whereas, the optimized GO, PNIPAM monomer, and GO/NIPAM structures are depicted in **Figure 5.6**. Since there is no specific model assuming GO, the basic structure of GO was shaped in circular geometry. This kind of structure was selected in order to hinder the anisotropic effects induced by the size differences of GO in designing a specific direction. The optimized geometry of GO shows a bended structure as a result of the oxygen functional group assemblies (Rosas et al., 2011). The bond length observed in functionalized C-C bonds of GO and GO/NIPAM upon optimization is found to be 1.44 Å for each contiguous carbon atom, in which this is similar with the previous results (Wallace, 1947, Eduardo et al., 2010, Gao and Liu, 2017). On the other hand, the conjunction bonds connecting NIPAM to GO, C12-C58 and C58-N, change from 1.548 Å to 1.635 Å and 1.521 Å to 1.427 Å, respectively (**Appendix I**). The changes of bond lengths upon optimization are subjected to achieve better conformational force in the atom bonded at space, thus affecting bond length alteration and displacement and minor perturbation of the NIPAM in GO system. The stretched bond length indicates that there is charge transfer from carbon atoms of GO around the NIPAM molecule to the nitrogen atom of the NIPAM molecule, affecting the weakened C12-C58 after adsorption. The shorter bond length noticed within the C58-N atoms suggests stronger binding and stable functionalization formed with the GO surface (Abbasi and Jahanbin Sardroodi, 2016). This also confirms an sp^3 hybridization of C-N bond (Solomons et al., 2014).

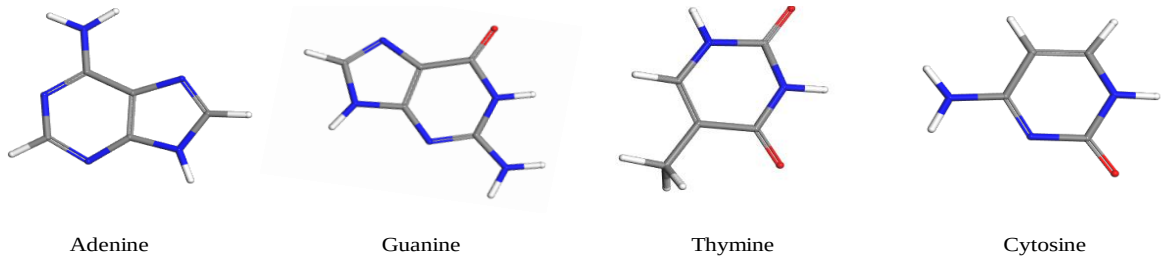

Figure 5.5 The optimized structure of nucleobase molecules.

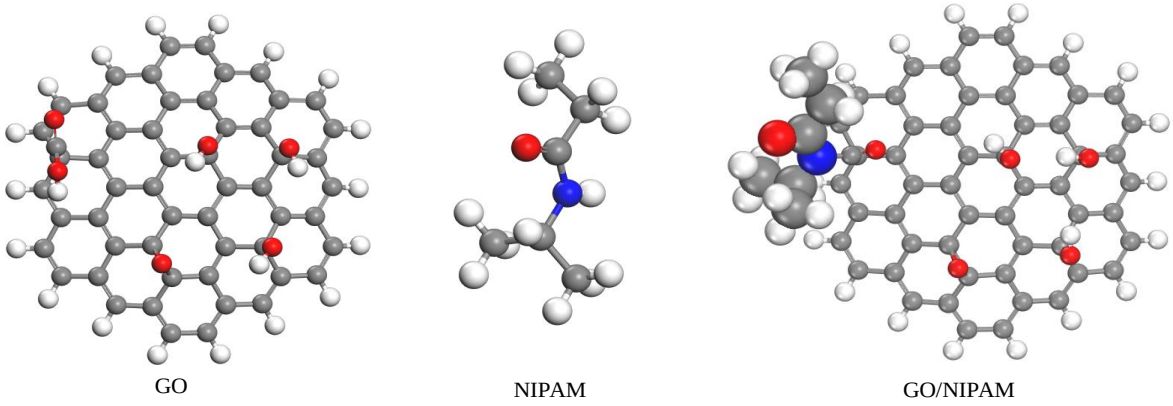

Figure 5.6 The optimized structures of GO, NIPAM, and GO/NIPAM.

Similar confirmation was also investigated for nucleobases adsorption in GO and GO/NIPAM systems, particularly in the site of carboxylic group conjunction which connects the NIPAM molecule with the GO surface. Attention is given to this in order to discover the influence of the NIPAM molecule present on the geometrical configuration of nucleobases in adsorption evidence on the GO surface. The atoms involved in carboxylic conjunction were labeled as C12, C13, C28, and C58 as depicted in **Appendix I**. The comparisons were tabulated defining the changes observed prior to and upon NIPAM molecule assembly toward the corresponding atoms in each nucleobase complex (**Tables 5.1-5.4**). The presence of NIPAM exhibit the alterations in term of bond length and bond angle in every interactive system of nucleobase with GO surface (**Tables 5.1-5.4**). Most of the bond lengths within the corresponding atoms are shortened slightly around 0.002-0.007 Å as opposed to those

systems without NIPAM. The shortened bond length indicates the stronger pull of interaction and higher bond-order of the total of bonded electrons between two atoms.

Obvious differences are found in bridging angles, especially at C11-C12-C58 and C58-C12-C28. The changes observed in C11-C12-C58 are 3.771^{o}, 1.283^{o}, 8.891^{o}, and 2.899^{o} for A, C, T and G, respectively (**Tables 5.1-5.4**). The interesting part belongs to the T system, in which there is a noticeable alteration among other nucleobases systems in regards to the attractiveness occurred in the corresponding angle. While three of the nucleobases have the bond angles increased, the T system experienced the lowest decrease from 109.573^{o} to 100.862^{o} upon emerging the NIPAM molecule. Similarly, a distinct change is indicated at C58-C12-C28 angle of the T system. The changes of this corresponding angle observed in A, C, T, G systems are in the order of 5.258^{o}, 3.970^{o}, 6.555^{o}, and 5.607^{o} difference toward the geometries without NIPAM. Among the nucleobase systems, the alteration in T system is the highest increase. A strong repulsion of the nitrogen and oxygen of the anion atoms toward the carbon atoms gives impact to the increase of the C58-C12-C28 and decrease of the C11-C12-C58 angles (Gomes and Gomes, 1999). These significant changes reflect the strongest interaction exposed in the presence of the T molecule in the GO/NIPAM system.

Table 5.1 The optimized configuration of PNIPAM monomer on the A-GO and A-GO/NIPAM systems before and after nucleobases adsorption calculated by GGA/DNP.

	Geometry Structures	Optimized Structures	
		A-GO	**A-GO-NIPAM**
Bond length (Å)	C11-C12	1.494	1.491
	C12-C13	1.516	1.511
	C12-C58	1.630	1.636
	C12-C28	1.504	1.508
Bridging angles (^{0})	C11-C12-C13	111.894	111.352
	C13-C12-C28	112.650	112.924
	C13-C12-C58	103.157	104.732
	C28-C12-C11	112.680	112.825
	C11-C12-C58	109.853	113.624
	C58-C12-C28	105.969	100.711

Table 5.2 The optimized configuration of PNIPAM monomer on the C-GO and C-GO/NIPAM systems before and after nucleobases adsorption calculated by GGA/DNP.

	Geometry Structures	Optimized Structures	
		C-GO	**C-GO-NIPAM**
Bond length (Å)	C11-C12	1.495	1.492
	C12-C13	1.516	1.509
	C12-C58	1.634	1.630
	C12-C28	1.503	1.508
Bridging angles (^{0})	C11-C12-C13	111.978	111.900
	C13-C12-C28	112.619	112.702
	C13-C12-C58	103.124	105.382
	C28-C12-C11	112.939	113.304
	C11-C12-C58	109.608	110.891
	C58-C12-C28	105.881	101.911

Table 5.3 The optimized configuration of PNIPAM monomer on the T-GO and T-GO/NIPAM systems before and after nucleobases adsorption calculated by GGA/DNP.

	Geometry Structures	Optimized Structures	
		T-GO	**T-GO-NIPAM**
Bond length (Å)	C11-C12	1.493	1.495
	C12-C13	1.516	1.512
	C12-C58	1.631	1.631
	C12-C28	1.503	1.505
Bridging angles (^{0})	C11-C12-C13	111.884	112.193
	C13-C12-C28	112.722	111.915
	C13-C12-C58	103.403	105.385
	C28-C12-C11	112.541	113.235
	C11-C12-C58	109.573	100.682
	C58-C12-C28	106.106	112.661

Table 5.4 The optimized configuration of PNIPAM monomer on the G-GO and G-GO/NIPAM systems before and after nucleobases adsorption calculated by GGA/DNP.

	Geometry Structures	Optimized Structures	
		G-GO	**G-GO-NIPAM**
Bond length (Å)	C11-C12	1.496	1.492
	C12-C13	1.516	1.510
	C12-C58	1.625	1.634
	C12-C28	1.503	1.509
Bridging angles (^{0})	C11-C12-C13	111.466	111.805
	C13-C12-C28	112.866	112.651
	C13-C12-C58	102.700	104.745
	C28-C12-C11	112.598	113.001
	C11-C12-C58	109.890	112.789
	C58-C12-C28	106.715	101.108

Regarding the non-covalent interaction of the complexes, each nucleobase molecule was firstly positioned on the top of either GO or GO/NIPAM surface as the prior configuration. The distance was arranged about 2.5 Å from the oxygen-containing group's area of the surface with π-π parallel stacking direction toward the GO. The initial configuration of each

system was relaxed using the same preferences and the minimum energies obtained were selected for the next calculations. The minimum force of the nucleobase-GO/NIPAM and nucleobase-GO structures along with the hydrogen bonds are presented in **Figures 5.7** and **5.8**, respectively. The distance within the nucleobase and both surfaces are compared before and after nucleobase adsorption. It is perceptible that there are changes observed in every nucleobase complex distance along with their orientations upon the adsorption (**Table 5.5**). In this regards, PBE function within GGA was employed since it is adequate to describe the weak interactions of van der Waals and hydrogen bond (Wang and Lin, 2003), particularly in nucleobase system toward GO molecule (Vovusha et al., 2013).

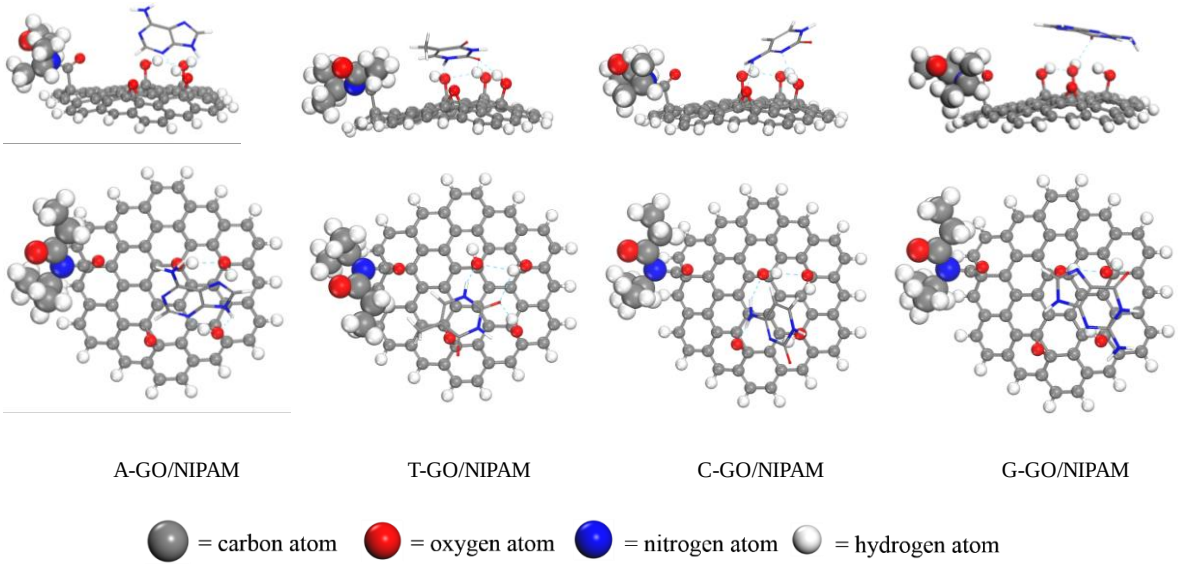

Figure 5.7 The optimized structures of nucleobases on GO/NIPAM complexes along with atomic hydrogen bonding orientation calculated by GGA/DNP.

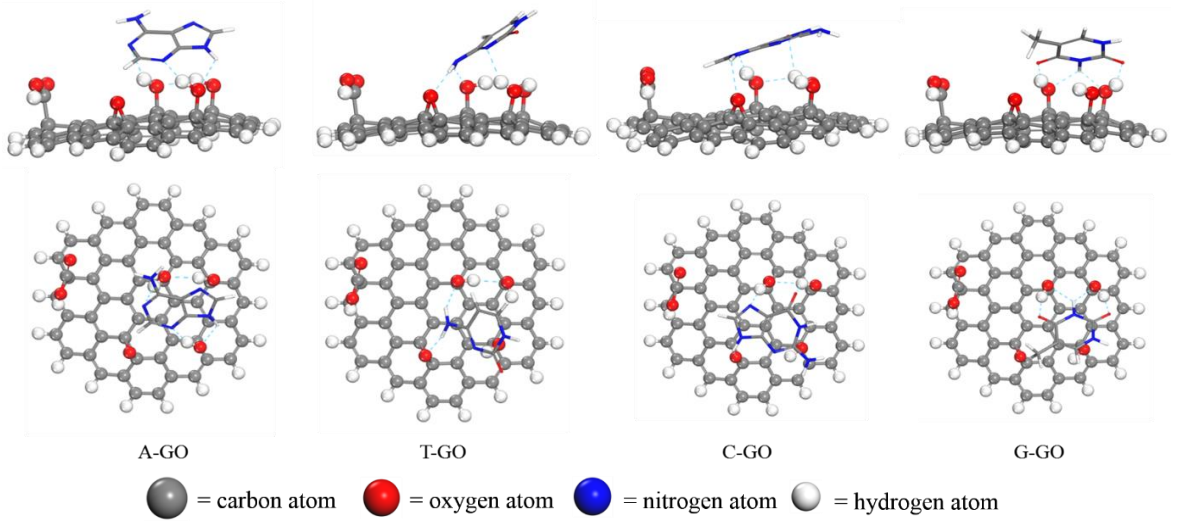

Figure 5.8 The optimized structures of nucleobases on GO complexes along with atomic hydrogen bonding orientation calculated by GGA/DNP.

As presented in **Figures 5.7** and **5.8**, the nucleobase molecules are susceptible not to be in parallel direction toward the surfaces. It is shown in the optimized complex system that the nitrogen, oxygen, or hydrogen atoms of nucleobase tend to tilt or heading toward the hydroxyl or epoxy functional groups of the surface forming hydrogen bonding, thus attracting the nucleobase to be closer with the molecular surfaces. This suggests that those atoms interact most with the dangling oxygen groups of the surface during the adsorption. For A molecule in complex with the GO/NIPAM (**Figure 5.7**), two hydrogen bonds are indicated within N···H1 at 1.775 A and H2···O1 at 2.115 Å with 1 intramolecular between hydroxyl groups (H3···O2 at 2.032 Å). As compared to other nucleobases systems, the intermolecular bonds are mostly found in C and T. In the C system, the intermolecular bonds are indicated within N···H1, H4···O4, H3···O3 at 2.072, 2.093, and 2.133 Å, respectively, along with intramolecular bond at 2.070 Å (H2···O2). In the T system, the bonds observed are within O1···H1, O1···H2, and H3···O2 at 1.755, 2.494, and 1.785 Å, respectively, as well as intramolecular within O2···H2 at 2.408 Å. Whereas in the G system, only one

intramolecular and intermolecular bonds are observed within O1···H2 at 2.029 Å and O2···H1 at 2.180 Å, respectively. The similar calculations have been applied for nucleobases in the GO surface complex. The **Figure 5.8** shows the optimized geometries of the nucleobases-GO complexes along with the hydrogen bonding (dashed blue color). It is observed that almost all the nucleobase structures have four hydrogen bonds intricate in GO complex which may suggest more physical interactions occurred within GO complex rather than within GO/NIPAM. Based on these results, the complex between nucleobase and GO or GO/NIPAM is mostly stabilized by hydrogen bonding interactions.

It is noteworthy that all adsorption energies observed in GO as well as GO/NIPAM complexes are in negative signs implicating that the adsorption of nucleobases on the both surfaces are in stable configuration and exothermic (**Table 5.6**), in turn, more negative adsorption energy respects to the more energetically preferable states (Kitchin et al., 2008). Herein, to straightforwardly describe the aspect of functional energetics among the systems, the term of adsorption energy sign is deliberated as positively value. The trend shown in nucleobase-GO/NIPAM complexes is in the order of T>G>C>A. The diverse adsorption energy is due to the variety of electrostatic interaction among the nucleobase systems. Higher adsorption energy corresponds to stronger electrostatic attraction between positively and negatively charges of nucleobase and oxygen groups of GO, respectively. Whereas, the decrease of it attributes to the repulsion force of electrostatic interaction between delocalized π electrons and oxygen lone pair electrons (Farimani et al., 2014, Larijani et al., 2015). The varied adsorption energies are also persuaded by the number and strength of hydrogen bonding. Among the nucleobase-GO/NIPAM complexes, T system has the highest adsorption energy as it favors high number of hydrogen bonds with shorter distances among

other nucleobase-GO/NIPAM systems. Analogues with this trend, the T system has the most attractive configuration toward GO/NIPAM surface due to the noticeable changes indicated in bond angle of the surface geometry.

Similar calculations were performed for GO complex as well. The adsorption energies trend found is in the order G>A>T>C, which is in accordance with the experimental report (Varghese et al., 2009, Liu et al., 2014) and previous DFT studies employing graphitic surfaces (Gowtham et al., 2007, Farimani et al., 2014, Vovusha and Sanyal, 2015, Sun et al., 2017). The adsorption energy of each nucleobase complex seems quite close each other (around ~ 100 kJ/mol) with G as the highest binding. The trend of adsorption energy in the nucleobases-GO systems is influenced by the presence of the hydrogen bonds observed within their complexes corresponding to the similar high numbers of bonding (four hydrogen bonds). Furthermore, the adsorption energies found are relatively higher than those in nucleobases-GO/NIPAM complexes (**Figure 5.9**). This evidence may be suggested by absence of NIPAM molecule thus, the evidences of electrostatic forces are more polarized within the nucleobase and oxygen functional groups of GO complex. However, the adsorption energies found in GO/NIPAM complexes are within the range of negative eigenvalues, suggesting that the adsorption is energetically favorable in all cases of nucleobases. In the end, from the adsorption energies range as well as equilibrium distances indicated within those results suggest the existence of a moderately strong interaction between nucleobase and the surfaces, which is typically physisorption.

Table 5.5 The comparison of atomic hydrogen bonding distance (in (Å)) between the optimized (O) and initial (I) nucleobase and GO/NIPAM complexes calculated by GGA/DNP.

System	Intramolecular bonding			Intermolecular bonding		
	Atom	Distance (O)	Distance (I)	Atom	Distance (O)	Distance (I)
A-GO/NIPAM	H3-O2	2.032	2.393	N-H1	1.775	3.226
				H2-O1	2.115	2.999
C-GO/NIPAM	H2-O2	2.070	2.501	N-H1	2.072	2.373
				H4-O4	2.093	3.008
				H3-O3	2.133	2.509
T-GO/NIPAM	O2-H2	2.389	2.408	O1-H1	1.755	4.021
				O1-H2	2.494	2.129
				H3-O2	1.785	2.337
G-GO/NIPAM	O1-H2	2.029	2.545	O2-H1	2.180	2.212

Table 5.6 The adsorption energies (in kJ/mol) distribution of GO and GO/NIPAM complexes with nucleobases calculated by GGA/DNP.

System	Adsorption Energies (kJ/mol)	
	GO/NIPAM	GO
A	-41.940	-120.786
T	-82.752	-114.043
G	-66.368	-121.654
C	-51.956	-104.326

According to the previous study, it is known that the adsorption energies derived from different functional group of GO complex (hydroxyl, epoxy, and carboxyl) showed slight variations or similar each other (Vovusha et al., 2013). Different physiochemical properties of the GO surface will vary the configuration and energetic behavior of the nucleobase adsorption. Since the calculation involving whole-functional groups is more preferable to signify the GO molecule, the calculation of different functional group is not established within these studies, but rather to present the capabilities of all functional groups in a

compartment of GO to accomplish a reliable model for complex interaction (Vovusha et al., 2013).

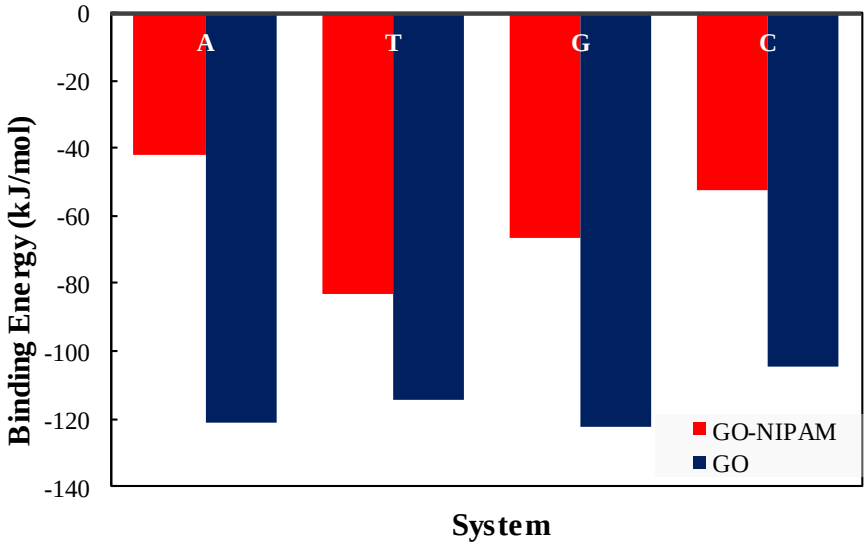

Figure 5.9 Comparison of adsorption energies (in kJ/mol) of GO and GO/NIPAM complexes with nucleobases calculated by GGA/DNP.

5.1.1.4 Electronic Properties

The calculated values of the frontier orbitals for individual element as well as the complex of GO/NIPAM, nucleobases-GO, and nucleobases-GO/NIPAM are figured in **Table 5.7**. The frontier orbitals or electronic gap energy refers to the finite difference expression of the hardness in the solid-state chemistry and solid-state physics, expressed by frontier orbital energies of highest occupied molecular orbital (HOMO) and lowest unoccupied molecular orbital (LUMO). In such a way, the wide gap represents high stability and low reactivity. Whereas, one expects low stability and high reactivity when the gap is narrow (Kohn et al., 1996). The calculated gap energies of the GO, NIPAM, GO/NIPAM are 0.631, 0.656, and 5.124 eV, respectively. Meanwhile, the nucleobase of A, T, G, and C have the energy gap in the order of 3.886, 3.820, 3.951, and 3.690 eV.

It is well-known, that GGA underestimates the energy gap calculation, whereby the real energy gaps are expected to be higher (Xiao et al., 2011). From the results, it indicates that single GO surface owns a semiconductor behavior (Lahaye et al., 2009, Yan et al., 2009, Tang and Cao, 2011). This result is close to the previous study employing the similar structure (Rosas et al., 2011). Higher energy gap is found in other literatures which employed GO structure with high states of oxidation (Lahaye et al., 2009). The C:O ratio mostly certain the electronic behavior of the designed GO, in which the higher ratio is the shorter energy gap (Ito et al., 2008). Practically, a fully oxidized GO characterizes an insulating property when the ratio of C:O is not more than the 2 or approximately contains 50% oxidized carbons (Buchsteiner et al., 2006, Szabó et al., 2006, Lahaye et al., 2009). A high conductivity achieved in GO will be more affected by the presence of carbon sp^2 in huge number thus taking part in affecting the conductivity of the structure. Herein, the GO employed 9:1 of C:O, attributed to six oxygens from the functional groups with 56 carbons as majority decorated on the surface. As consequence, the structure attains small gap energy which closes to the semiconductor character due to low oxidation (Lahaye et al., 2009).

Table 5.7 The calculated energy gaps (eV) for pure nucleobases, GO, GO/NIPAM, and their complexes with nucleobases.

System	Pure Molecule			+ GO			+ GO/NIPAM		
	HOMO	**LUMO**	**Energy Gap**	**HOMO**	**LUMO**	**Energy Gap**	**HOMO**	**LUMO**	**Energy Gap**
GO	-4.697	-4.065	0.631	-	-	-	-	-	-
NIPAM	-5.393	-0.269	5.124	-	-	-	-	-	-
GO/NIPAM	-4.444	-3.788	0.656	-	-	-	-	-	-
A	-5.391	-1.505	3.886	-4.452	-3.842	0.610	-4.357	-3.739	0.618
T	-5.957	-2.136	3.820	-4.408	-3.793	0.615	-4.503	-3.859	0.645
G	-5.059	-1.108	3.951	-4.452	-3.875	0.577	-4.408	-3.780	0.629
C	-5.548	-1.859	3.690	-4.585	-3.957	0.629	-4.498	-3.861	0.637

The high-energy gaps found in isolated NIPAM and nucleobases indicate that the molecules own stability rather than being reactive. The observed energy gaps also represent an insulating character. Meanwhile, the presence of NIPAM molecule tends to induce more stability into the GO structure shown by slightly increase of energy gap once the NIPAM was assembled.

Regarding nucleobase in GO complex, the energy gap decreases upon adsorption of four nucleobases. For instance, after adsorption of A and G on the GO surface, the energy gap altered from 0.631 eV of GO to 0.610 eV and 0.577 eV, respectively. The energy gaps also vary due to the different element of nucleobases structure which reveal a trend increasing from G, A, T, to C. The presence of nitrogen and additional five-membered ring of A and G nucleobases increase the probability of sharing higher level of electronic interaction toward the GO (Farimani et al., 2014). Interestingly, this trend is analogous with the adsorption energy trend of nucleobases in GO complex. Similar approach has been described in the previous study employing graphitic surface (Lee et al., 2013, Farimani et al., 2014). The conductivity properties correlate exponentially toward the negative value of the energy gap, therefore the adsorption of nucleobases on GO surface enhances a significant change for the electronic conductivity in this case.

It is recognized in the nucleobases on the GO/NIPAM complex with the trend of A<G<C<T, in which the energy gap is contradictory with its adsorption energies. The presence of NIPAM molecule may explain the unconscious energy gaps in this regards which is due to its insulating properties that relatively stabilizes the GO molecule, thus affecting conductivity in adsorbed nucleobases. As consequence, the profile of nucleobase molecule on GO/NIPAM

complex tends to be inconsistent toward the adsorption energy. The phenomenon may be also strengthened due to the impact of imperfect quantitatively description of the GGA employed, that immediately underestimates the energy in the complex structure (Girifalco and Hodak, 2002, Saikia and Deka, 2013b).

The global reactivity of isolated molecule as well as adsorbed nucleobases in the GO and GO/NIPAM complexes are presented in **Table 5.8**. The results showed the global hardness (η) and chemical potential (μ) of each molecule prior to and upon adsorption with nucleobases. Approaching the NIPAM molecule on the GO surface increases the η value of GO from 0.316 eV to 0.328 eV, which is coincidence with its trend of energy gap. Whereas, the μ value shows decrease from -4.229 eV to -4.116 eV. The greater η value reflects to the more stability or lower reactivity owned in a system. However, the variation of μ does not follow any regular trend since it is liable to describe the escaping potency of electrons from the molecular system in an equilibrium state, in turn, higher the μ value indicates more reactive and less stable of the species (Saikia and Deka, 2014, Chermahini et al., 2015). Therefore, in correlation with the insulator properties NIPAM, this result confirms that the functionalization of NIPAM tends to render stability to GO rather than to exhibit the reactivity.

Meanwhile, the adsorption of nucleobases either in GO or GO/NIPAM surface decrease the η at four studied nucleobases complexes (**Table 5.8**). For instance, with approaching G molecule to the GO and GO/NIPAM surfaces, the η values turn from 0.316 eV into 0.288 eV and from 0.328 eV into 0.314 eV, respectively. This suggests that adsorption of nucleobase molecule in GO or GO/NIPAM surface enables to enhance the reactivity of the complex. The

η values vary due to the different HOMO and LUMO characterized by each nucleobase structure toward each surface, therefore, their values absolutely gain a similar trend with the electronic energy gap. Further, the overall η values of nucleobases in GO/NIPAM are found higher than those in GO. This is in accordance with the energy gaps observed in every adsorption evidence. Due to the presence of NIPAM in GO, the GO/NIPAM complex generates quite lower reactivity as compared to the nucleobases in GO surface, which is also suggested by higher energy gap. However, the μ values of nucleobases complexes in GO and GO/NIPAM show decrease relatively upon adsorption revealing the rise in stability of the system. Therefore, even though the reactivity of adsorbed nucleobases increases toward GO and GO/NIPAM, the entire systems at both surfaces are thermodynamically stable (Saikia and Deka, 2014).

Table 5.8 Calculated global reactivity (eV) for pure nucleobases, pristine GO, GO/NIPAM, and their complexes with nucleobases.

System	Pure Molecule		+ GO		+GO/NIPAM	
	η (eV)	**μ (eV)**	**η (eV)**	**μ (eV)**	**η (eV)**	**μ (eV)**
GO	0.316	-4.229	-	-	-	-
NIPAM	2.559	-2.796	-	-	-	-
GO/NIPAM	0.328	-4.116	-	-	-	-
A	1.943	-3.448	0.305	-4.147	0.309	-4.048
T	1.910	-4.046	0.307	-4.101	0.322	-4.181
G	1.976	-3.083	0.288	-4.163	0.314	-4.094
C	1.845	-3.703	0.314	-4.271	0.318	-4.180

The frontier orbitals behavior of the individual molecule and the complexes can be defined qualitatively through the electron distribution models. The HOMO and LUMO orbitals of the GO, NIPAM, and GO/NIPAM are described in **Figure 5.10**. For GO surface, the electron moiety of HOMO is found spreading evenly, typically on carbon sp^2 and sp^3 conjunctions, while LUMO isosurface is mostly delocalized at around oxygen functional groups (**Figure**

5.10 (a)). In the case of single NIPAM molecule, the HOMO and LUMO isosurfaces are uniformly present along its backbone, particularly in oxygen and nitrogen atoms (**Figure 5.10 (b)**). Meanwhile, the modification of GO with NIPAM molecule shows no significant changes on the locations of GO orbitals isosurfaces (**Figure 5.10 (c)**). This result suggests that entire surface of GO generates a polarized electronic transfer. Interestingly, both HOMO and LUMO moieties are identified and lied on the atoms of the carboxylic groups, where the NIPAM is attached. This confirms that there is possibly electronic transfer occurred from the GO surface through the carboxylic group to the NIPAM.

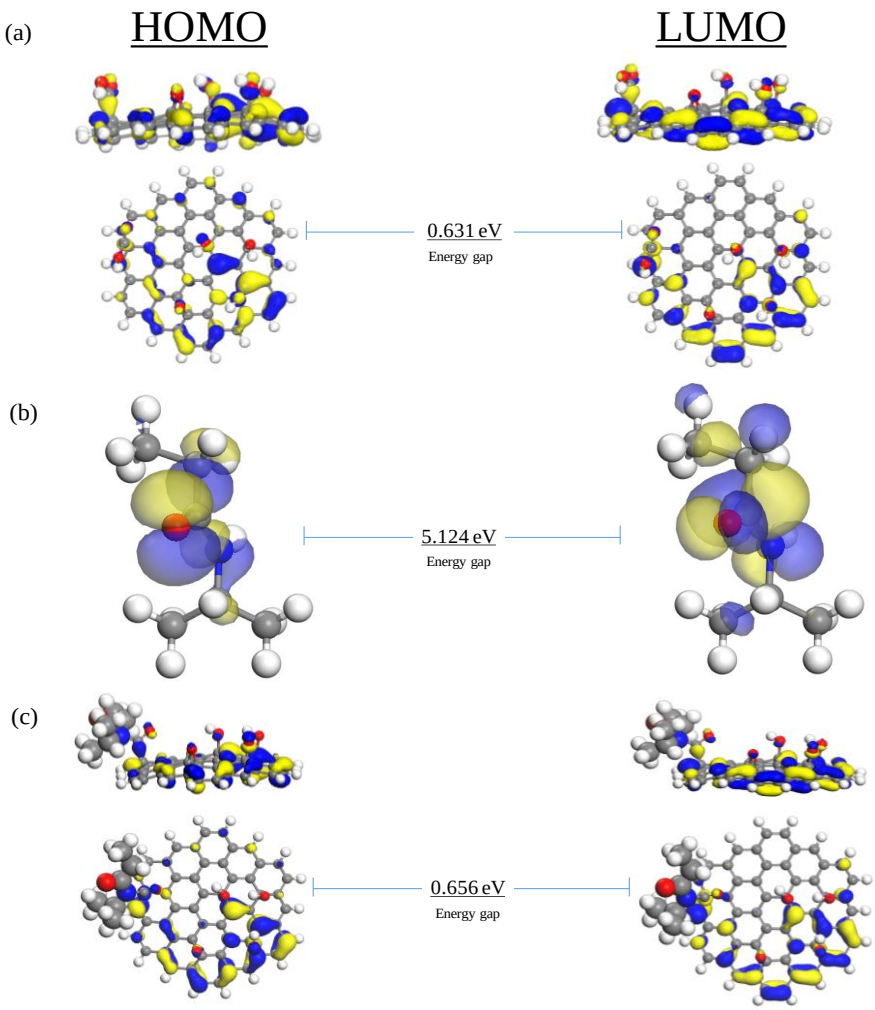

Figure 5.10 The isosurfaces of HOMO and LUMO of (a) GO, (b) PNIPAM monomer, and (c) GO/NIPAM calculated by GGA/DNP.

Further, the electronic distributions of the nucleobases adsorption in GO and GO/NIPAM complexes are investigated as follows. The HOMO (**Figure 5.11**) and LUMO (**Figure 5.12**) isosurfaces in each complex of nucleobase and GO are totally distributed on the GO surface in which, they remain the same with the isolated GO surface. There is no significant hybridization evidence between nucleobase and the surface. In closer look, most nucleobases do not involve significantly in the electronic contribution of both orbitals. A slightly variation is recognized on GO surface of G system that fewer HOMO contours are delocalized as compared to other nucleobases, and another minor isosurface of HOMO is also noticed close to nitrogen of C molecule in its complex (**Figure 5.11**). The fewer HOMO regions may indicate that lesser electrons are amounted in the G complex at HOMO level than in other nucleobases. Whereas, HOMO isosurface present near to the C molecule probably indicates more electrons condensed within the C and GO complex as compared to its LUMO level. Lesser isosurfaces in HOMO may suggest that the particular complex gains fewer electrons in its HOMO, in turn, the complex is less stable but more reactive to transfer the electrons to the next level of orbitals (LUMO). Conversely, higher HOMO isosurfaces may associate to the more stable complex and less reactive for transferring the electrons. These coincidences correlate with the gap energies trend of GO complex with respect to the G complex as the lowest and C complex as the widest gap energies.

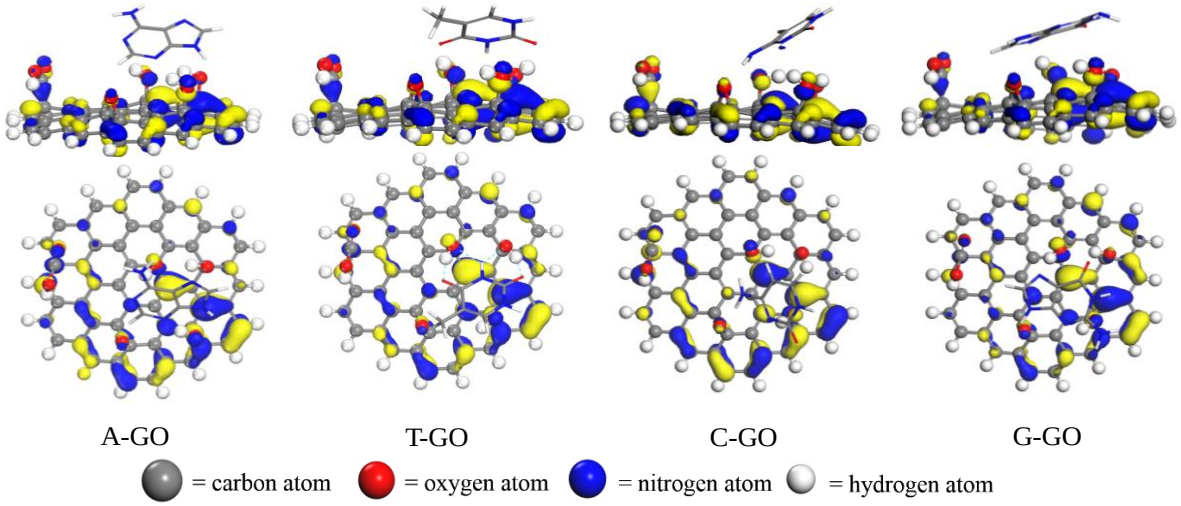

Figure 5.11 The HOMO isosurfaces of nucleobases and GO complex calculated by GGA/DNP.

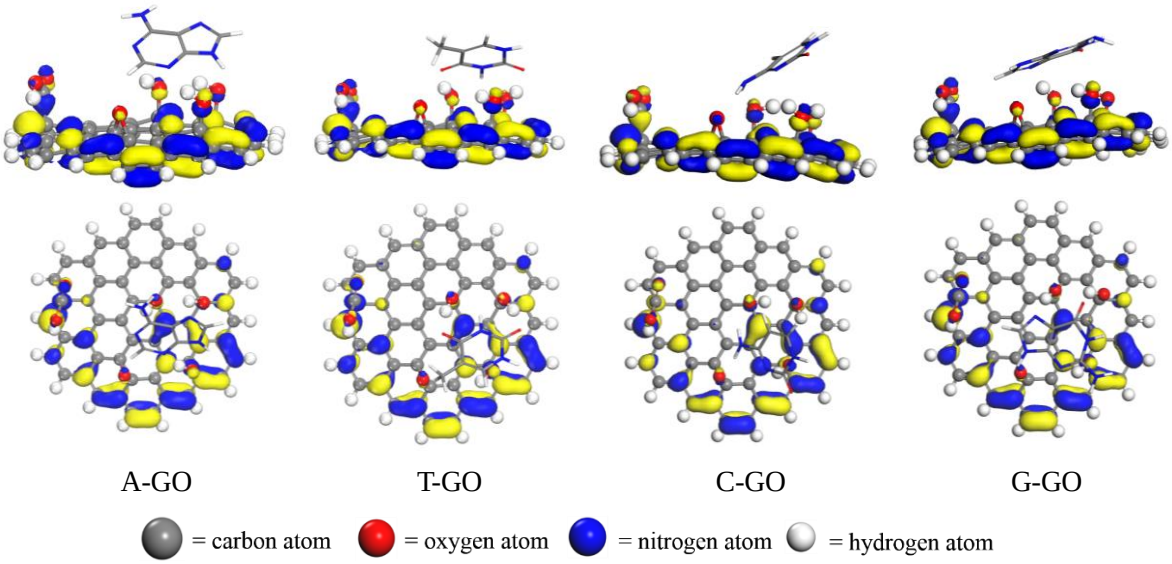

Figure 5.12 The LUMO isosurfaces of nucleobases and GO complex calculated by GGA/DNP.

A similar pattern is obtained in every nucleobase at GO/NIPAM complex, where most orbitals are lied down on the surface area (**Figures 5.13** and **5.14**). The HOMO isosurface is localized evenly along the edge of GO and mostly delocalized on oxygen functional groups area of GO surface (**Figure 5.13)**. Meanwhile, the LUMO region is found delocalized on the similar area near to HOMO isosurface (**Figure 5.14)**. As compared to the GO/NIPAM

surface only, no perceptible alterations are further indicated in the carboxylic atom group after nucleobase adsorption, especially at the C12, C58, and oxygen atoms. Combining those above results, it is important to point that the nucleobases adsorption either on GO or GO/NIPAM complex characterizes a typical physical adsorption verified by the absence of electronic level perturbation upon the adsorption, and the contribution of electronic conductivity is triggered by GO surface (Saikia and Deka, 2013a).

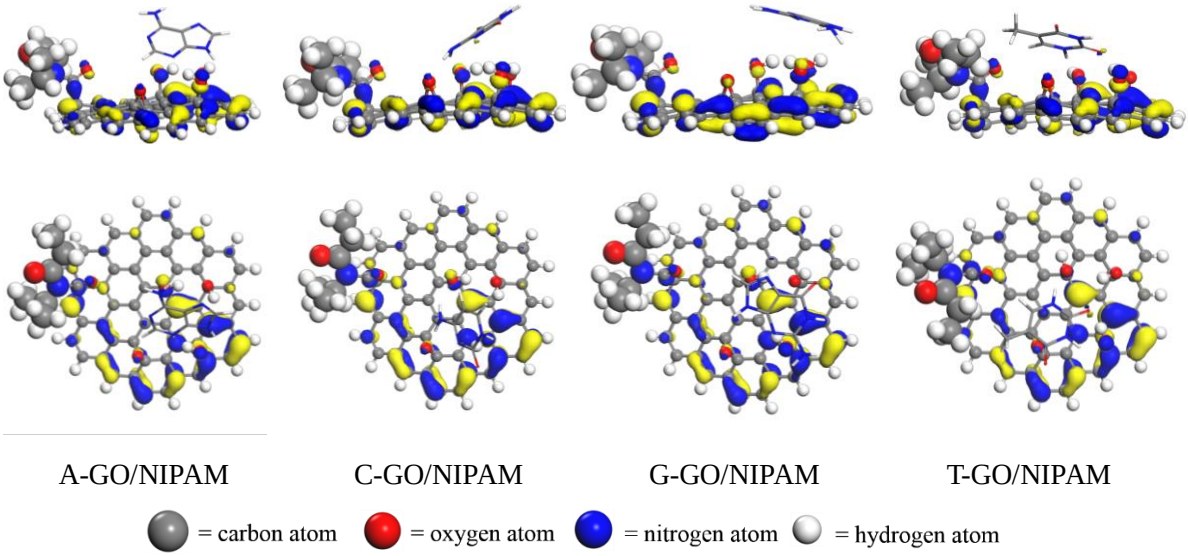

Figure 5.13 The HOMO isosurfaces of nucleobases and GO/NIPAM complex calculated by GGA/DNP.

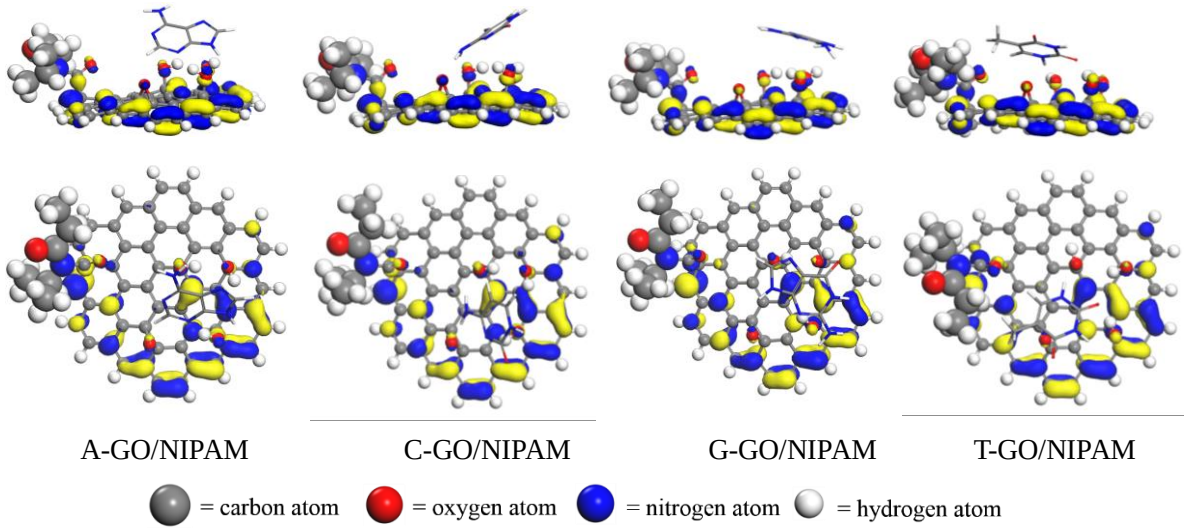

Figure 5.14 The LUMO isosurfaces of nucleobases and GO/NIPAM complex calculated by GGA/DNP.

The electrostatic potentials (ESP) of complexes are illustrated in **Figures 5.15** and **5.16**. In general, ESP is useful to determine the properties of intermolecular system, for example difference of charge density, which represents the cumulative reactivity within the molecules. The calculated ESP strongly relies on the models considered (Basiuk et al., 2014). **Figure 5.15** shows the ESP isosurfaces plotted on the nucleobase and GO complex. The yellow and blue colored-areas refer to the negative electrophilic and positive nucleophilic charges, respectively.

As seen in **Figures 5.15** and **5.16**, each complex of nucleobase either in GO or GO/NIPAM harvests more electrons originated mostly from the oxygen functional groups of GO due to higher electronegativity compared to the carbon atom in isovalue of 0.016. In some cases of nucleobases with nitrogen atom at the corner angle, i.e. A, G, and C nucleobases, there exist negative charges accumulated resulting electronic transfer. Particularly, the complexation between both molecules with the GO surface expands the negative lobes to the side of GO

opposite to the adsorbed nucleobase (Basiuk et al., 2014), where it is similarly found in GO/NIPAM complex. It is also seen in the **Figure 5.16** that the NIPAM functionalization on the GO surface brings the negative charges instigated from its oxygen atom. Due to its ratio of oxygen and carbon groups, the distribution of electrophilic region are highly centered in its surface functional groups of surface (Ulianas et al., 2014, Saha et al., 2016). The resulting isosurface recognized between two molecules indicates the charge transfer occurred from the GO surface to the nucleobase.

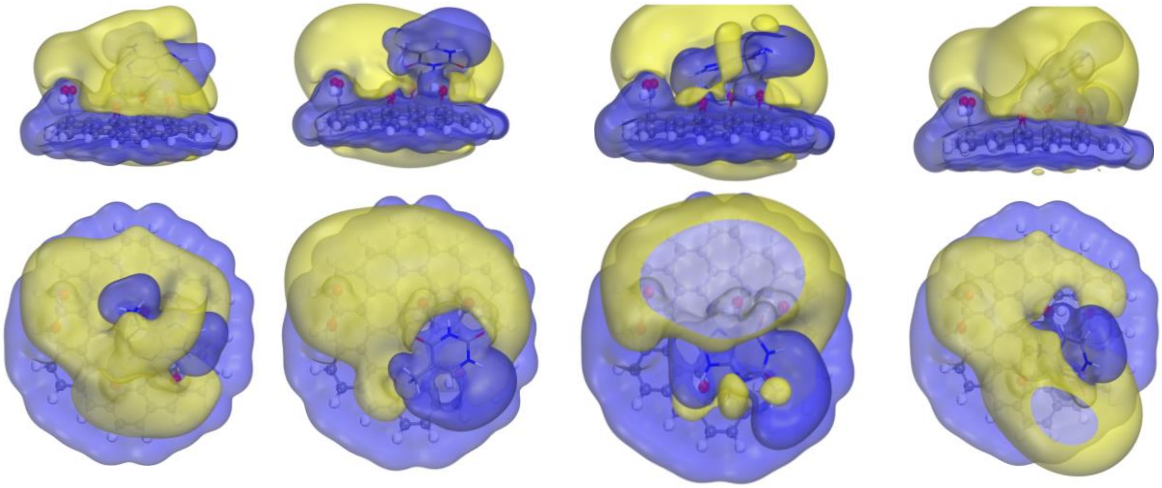

Figure 5.15 The isosurfaces of electrostatic potential of nucleobases and GO complexes calculated by GGA/DNP.

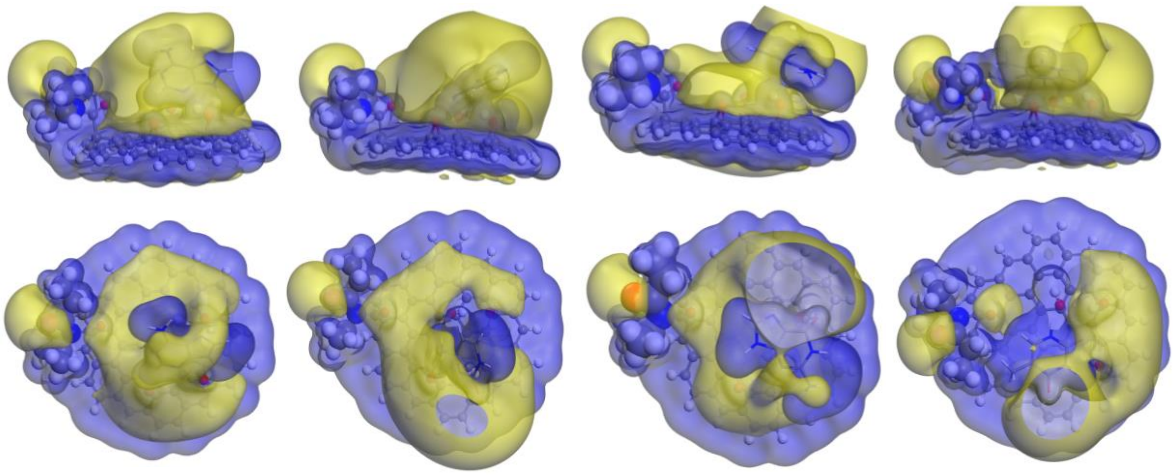

Figure 5.16 The isosurfaces of electrostatic potential of GO-NIPAM and nucleobases-GO/NIPAM complexes calculated by GGA/DNP.

The total density of states (TDOS) of isolated molecule of nucleobase, GO, NIPAM, GO/NIPAM, and nucleobases complex with GO and GO/NIPAM were determined in order to obtain better understanding the interaction of nucleobase and both surfaces. As presented in **Figure 5.17**, the TDOS of each nucleobase shows different peaks profile due to difference of the structural composition. However, each profile suggests a similar trend of electronic behavior as non-conductive molecule due to the appearance of extensive gap and several distinct peaks near the Fermi level. The depiction of each nucleobase shows a discrete peak which obeys the different energy of electronic energy level. Likewise, the NIPAM peaks are observed to be overlap toward the Fermi energy, suggesting a wide-space electron transferred from the highest occupied to the lowest unoccupied states of corresponding molecule (**Figure 5.18 (a)**). Interrelated with the above-mentioned results of gap energies that these characterizations results confirm the insulating properties of nucleobases and NIPAM molecules.

Meanwhile, the TDOS of GO molecule shows many peak-states continuously and scattered along the energy axis (**Figure 5.18 (b)**). Small gap below 1.0 eV present between the valence and conduction peaks around the Fermi level indicates a conductive pattern preserved by the molecule. In correlation with the gap energy obtained, the constructed GO owns the semiconductor properties. Further, this structure was employed since it had shown successful results in the previous DFT studies (Rosas et al., 2011, Vovusha et al., 2013). The TDOS of modified GO with NIPAM has also been calculated based on the optimized molecule to explore the possible hybridization as depicted in **Figure 5.18 (c)**. As results, the calculated TDOS exhibits new peaks, especially around -22 eV, in response to NIPAM molecule. The peaks around Fermi level also remain the same, indicating that the attachment of NIPAM molecule does not give significant impact in GO conductivity. This is in accordance with the surface characteristics results approached by the previous experimental report using cyclic voltammetry (CV) (Kumar et al., 2014). As seen in **Figure 5.19**, it is recognizable that PNIPAM has poor electroconductivity. Under the redox environment, the PNIPAM does not induce any significant redox peak, which further suggests the absence of electrocatalytic characteristic in PNIPAM. Furthermore, the incorporation of nanoparticles, such as GO to the PNIPAM, plays an important role in exhibiting the electro-active surface properties.

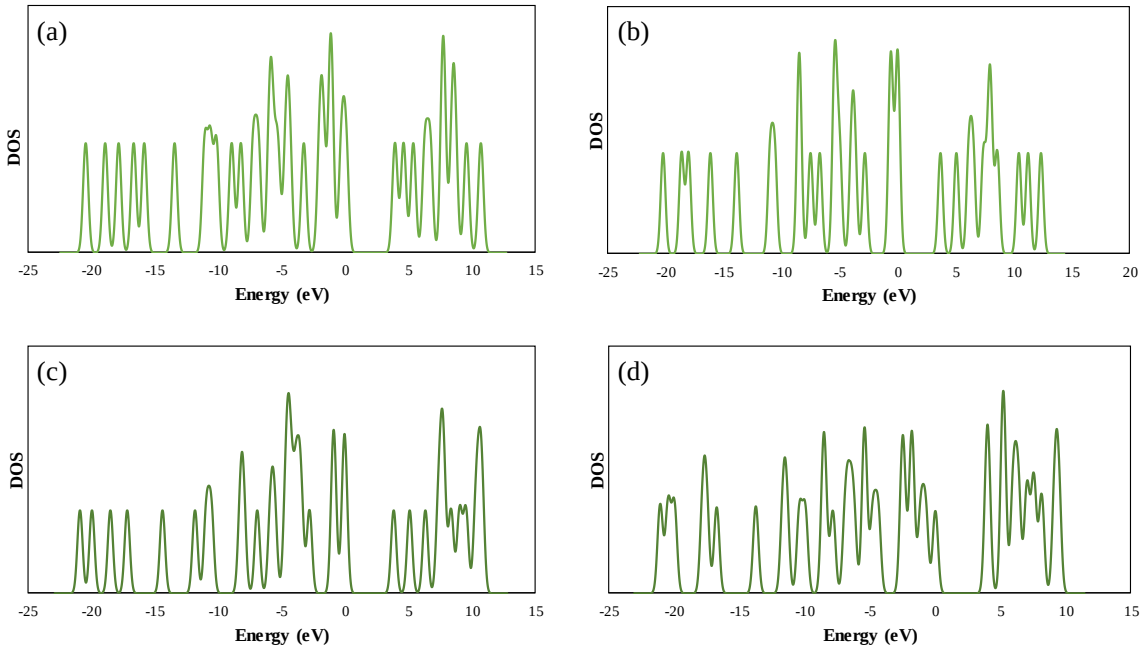

Figure 5.17 The calculated total density of states of: (a) adenine, (b) cytosine, (c) thymine, and (d) guanine molecules in the scheme of DFT-D of GGA function.

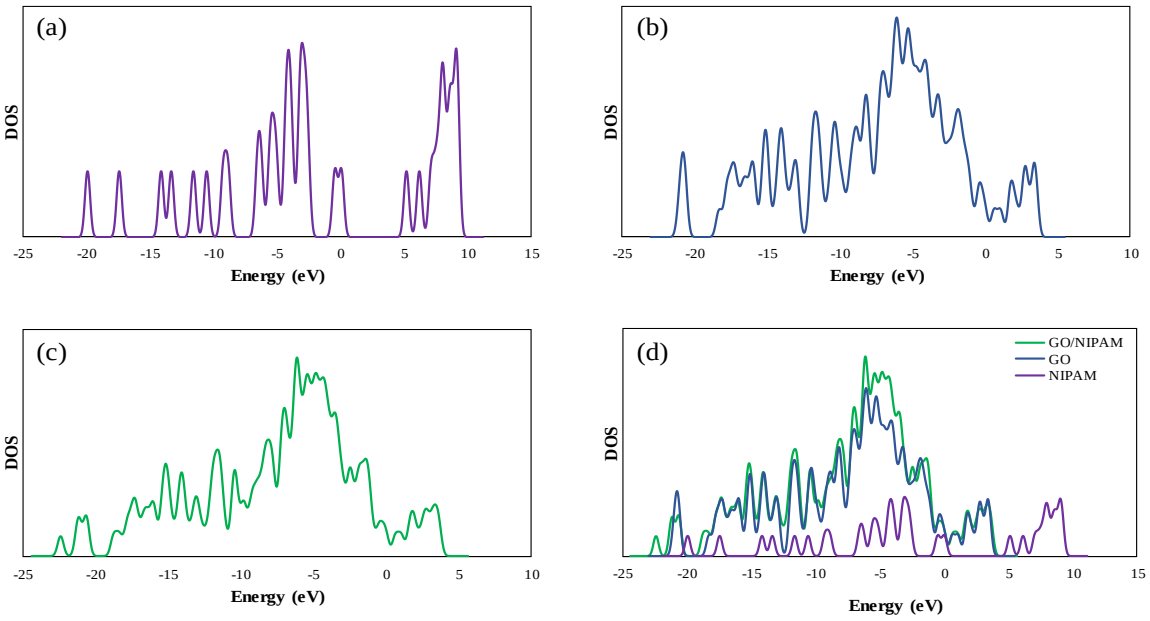

Figure 5.18 The calculated total density of states of: (a) NIPAM, (b) GO, (c) GO/NIPAM molecules, and (d) the comparison among those in the scheme of DFT-D of GGA function.

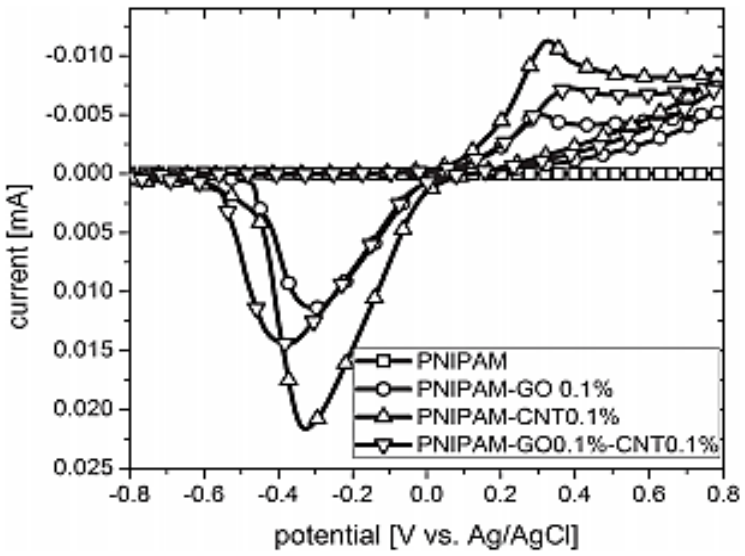

Figure 5.19 The electrocatalytic behavior of the PNIPAM and PNIPAM grafted GO surface showing that the addition of nanoparticles GO can induce the electronic activity of PNIPAM. Adapted from Kumar et al. (2014).

The TDOS of adsorbed nucleobase in GO and GO/NIPAM complexes are calculated in order to elucidate the electronic properties upon adsorption event. In comparison with the isolated nucleobase before adsorption, the peaks around the Fermi level in GO and GO/NIPAM relatively moved to the negative energy, giving impact to the gap energy becoming narrower (**Figure 5.20**). On the other hand, the behavior of the negative peaks in GO and GO/NIPAM complexes seem to shift toward more negative value suggesting that the adsorptions on both surfaces change nucleobase to be more conductive than its isolated phase. In addition, the presence of NIPAM in GO surface influences the electronic states of nucleobase to be less conductive as opposed to those in GO complex, shown by less shifting peaks toward the negative axis. For instance, the last peak of G in GO system (**Figure 5.20**) present at more negative axis compared to G at GO/NIPAM system and G as the isolated molecule. Similar patterns are also revealed in the other three adsorbed nucleobases. These phenomena have been confirmed by the energy gaps results, that due to its poor conductivity characteristic,

NIPAM molecule tends to increase the gap energies of the GO and complex surfaces of nucleobase adsorptions, suggesting lower electronic transition as compared to the unfunctionalized GO system.

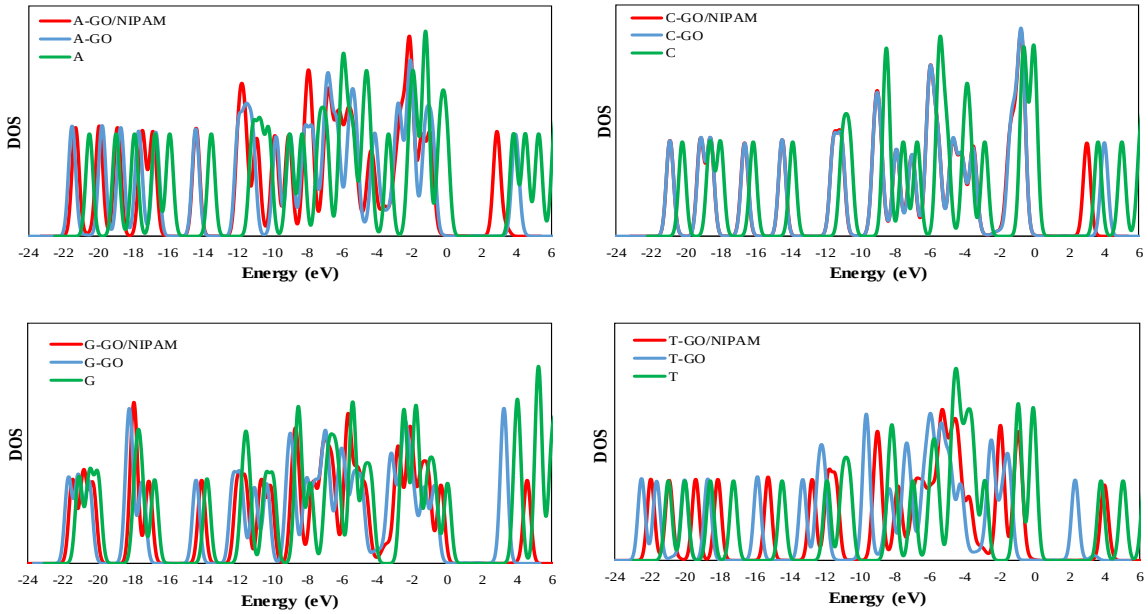

Figure 5.20 Total of density of states of adsorbed nucleobase on GO and GO/NIPAM systems at DFT-D/GGA scheme.

In order to further explicate the electronic function of the surface, the partial density of states (PDOS) of the GO and GO/NIPAM complexes after nucleobases adsorption are calculated. The PDOS of nucleobase and GO complex shows origin peaks of nucleobase and new impurity rising (**Figure 5.21**). The origin peaks of G, A, T, and C complex appear near to the Fermi level in the order of -2.28, -2.04, -2.25, and -1.58 eV. Whilst the impurity exhibits peaks at the end of the negative peak around -21 eV. In contrast, the GO/NIPAM complex did not induce any impurity upon the adsorption and original peaks of nucleobases are very weakly noticed at around Fermi level. This confirms the electronic behavior of NIPAM in GO surface which does not contribute electrical conductivity in adsorption process (**Figure 5.22**).

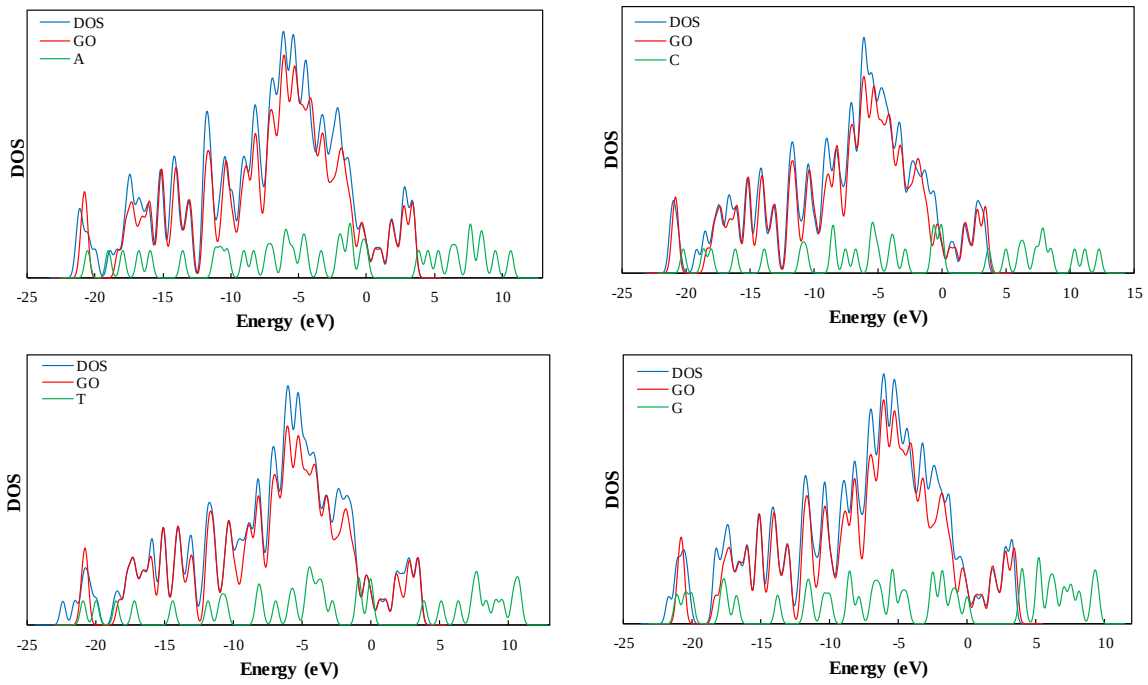

Figure 5.21 Total and local density of states of nucleobases-GO complex system.

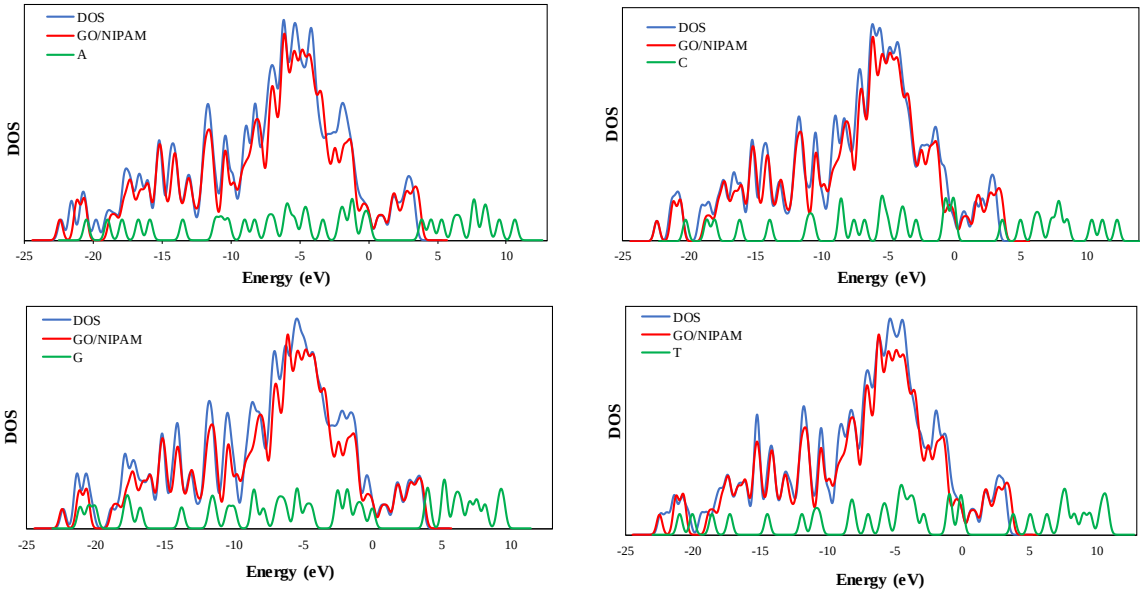

Figure 5.22 Total and local density of states of nucleobases-GO/NIPAM complex system.

5.1.2 Molecular Docking Studies

5.1.2.1 Structural Optimization

In this study, molecular docking was designed in order to choose the best aptamer through interaction studies with target protein of PC3 cells. The selected aptamer was used in the interaction with the whole-cell PCa (PC3 type) in experimental studies. Since the computational techniques employed have limitations in the case of construction the whole-cell structure, we therefore modeled the protein of PC3 cells as the cell-representative molecule for further simulation studies. Additionally, this was done to mimic the main purpose of the experimental work.

Ten aptamers candidates were employed and validated using the interaction methodology with the corresponding protein to find the potential biorecognition for PCa. Since the initial aptamers structures have lacked a three-dimensional simulated model, they were firstly converted into three-dimensional structures using the technique aforementioned in the Materials and Methods (**Chapter 4**). These structures were then continued to the folded-structures processing which was done to accomplish their nature of conceivable conformation. Moreover, determining the folded-structure of nucleotide composing of hairpin/stem-loop structures is essential since it associates directly to the important role as transcription regulation, translation, as well as recognition regions in conjugative elements (Bikard et al., 2010, Jeddi and Saiz, 2017). The proteins considered within this study were selected based on the previous experimental works (Sefah et al., 2013, Berg et al., 2016), so called eCadherin and α6β4 proteins, which are well-known as over-expressed proteins on the surface of metastatic PC3 cells. Instead, those proteins were opted since their protein

sequences are available in protein database (.pdb) format (Gabb et al., 1997, Smith and Sternberg, 2002, Chen et al., 2003, Mukherjee and Zhang, 2011, Roberts et al., 2013).

Subsequently, the proteins were correlated with the ten aptamers candidates through docking simulations employing ZDOCK-ZRANK methods in Discovery Studio ver. 2016. To obtain comprehensive and effective docking studies, this thesis only restrained and discussed the interaction results of α6β4 protein which has smaller number of atoms. This was also to avoid high computational demand that might occur during the simulations. Depicted in **Figure 5.23**, the optimized structures of Wy5a aptamer and α6β4 protein are displayed in two types of molecular figures, which are solid ribbon as a common display in Discovery Studio and ball-stick style of Materials Studio. For figure depiction under this section, the solid ribbon was used as the main preference style in Discovery Studio thus, enabling to distinguish the two docked molecules separately.

Solid Ribbon style[a]	Ball and Stick style[b]
Wy5a aptamer	
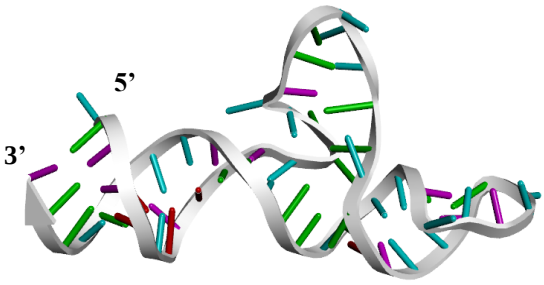	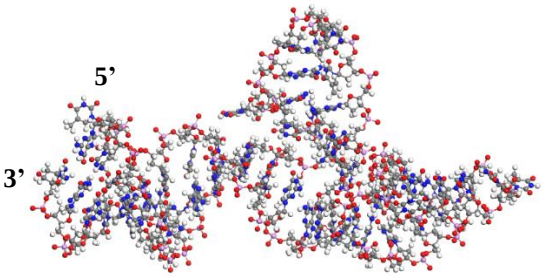
α6β4 protein	
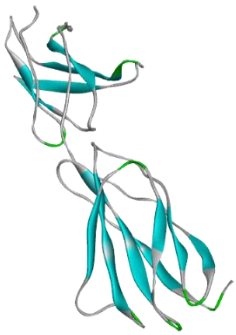	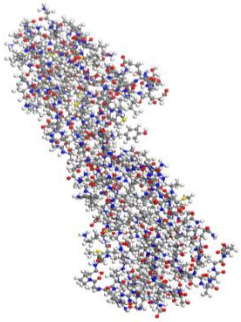

[a]Discovery Studio ver.2016 Interface; [b]Materials Studio ver.2016 Interface

Figure 5.23 The optimized three-dimensional structures of Wy5a aptamer and α6β4 protein in two different displays of solid ribbon (Discovery Studio ver. 2016) and ball and stick (Materials Studio ver. 2016).

5.1.2.2 Comparison of Docking Results

An extensive docking of ten aptamers toward α6β4 protein has been investigated applying six degree (6^{o}) of sampling freedom of the FFT methods. About 2,000 predicted models were obtained from every aptamer docked with α6β4 protein. Herein, the protein as *receptor* and aptamer as *ligand* were set into rigid bodies with respect to the conformational changes due to the translational and rotational of 6^{o} scoring function. The assessments including the docking scores (ZDOCK-ZRANK), intermolecular H-bonds, and interactive residues were taken into account to define the best-docked model representing a virtuous correlation between the aptamer and α6β4 protein complex. The best-docked model was derived from the top poses of the largest cluster for each docking simulation which was determined by the

PSC function. As seen in the **Figure 5.24** and **Table 5.9**, the ZDOCK of CSC1 aptamer has the highest score (23.72) amongst single strand-DNA (ssDNA), RNA, and DNA aptamers types, followed by the Wy5a aptamer (22.92). However, the ZDOCK will be representing better result if the docked proteins complex could be improved into more detail sampling along with the successive rate of interaction using ZRANK reranking method. ZRANK score has been considered here to give more trustworthy results as compared to the ZDOCK. Therefore, the Wy5a aptamer is found higher than CSC1 (-93.399) and suggested as the best-binding aptamer for the α6β4 protein according to the lowest score of -95.745; lower ZRANK corresponds to a better docking prediction (**Figure 5.24** and **Table 5.9**). Other high binding aptamers following these scores are in the order of Wy5b, IDA, CSC13, and A10-J (RNA) (**Table 5.9**).

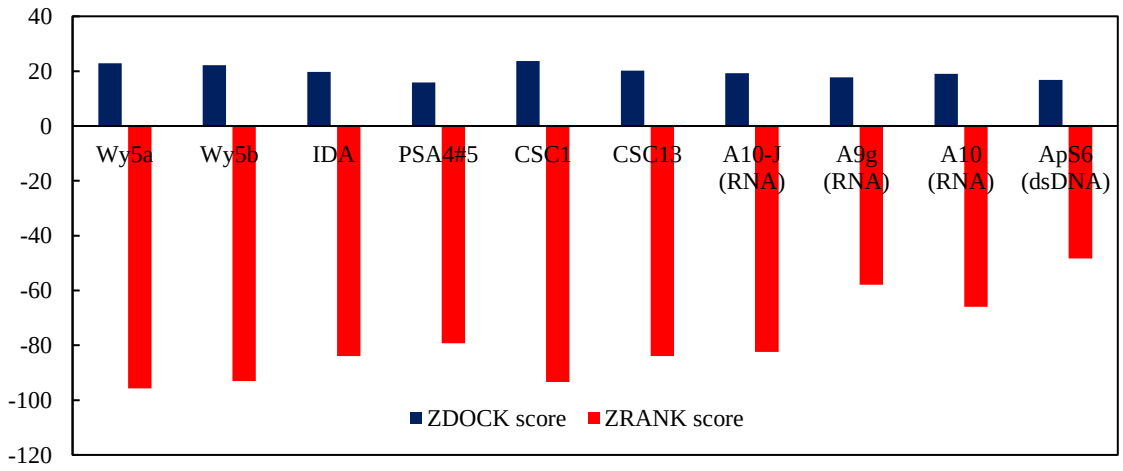

Figure 5.24 Chart profile of docking scoring difference between ZDOCK and ZRANK of aptamers and α6β4 protein.

Table 5.9 ZDOCK and ZRANK scoring results of docking between aptamers and α6β4 protein.

Aptamers	Protein	Interface Area	Interface Residues		H-Bonds	Hydrophobic Contacts	ZDOCK score	ZRANK score
			∑ amino acids	∑ nucleotides				
Wy5a	α6β4	1201.335	23	24	13	6	22.92	-95.745
Wy5b	α6β4	944.824	17	15	6	3	22.16	-93.013
IDA	α6β4	1053.938	14	19	8	4	19.76	-83.942
PSA4#5	α6β4	904.571	12	17	3	2	15.82	-79.300
CSC1	α6β4	1331.034	27	19	15	13	23.72	-93.399
CSC13	α6β4	1083.395	18	24	8	5	20.18	-83.893
A10-3J1 (RNA)	α6β4	1160.703	24	24	12	6	19.26	-82.471
A9g (RNA)	α6β4	1006.494	19	19	5	5	17.78	-57.907
A10 (RNA)	α6β4	1136.118	18	20	10	2	19.06	-65.910
ApS6 (chain-A; dsDNA)	α6β4	347.593	5	22	1	0	16.76	-48.305
ApS6 (chain-B; dsDNA)	α6β4	674.097	13	22	6	0		

Due to the closest similarity in docking scoring, the CSC1 and Wy5a systems were further compared. The CSC1 obtained more extensive intact area compared to the Wy5a aptamer as indicated in **Table 5.9**. It is shown by the wider interaction region of CSC1 system (1331.034 $Å^2$) than that of Wy5a (1201.335 $Å^2$). The different number of nucleobases length composed within each aptamer, however, may give different possibilities to provoke an interaction with the molecular target. Herein, CSC1 aptamer consisted of 75 nucleobases with around 19 nucleobases residues involved in interaction with 27 amino acids of the protein. Whereas, around 24 of 57 Wy5a nucleobases interacted with 23 amino acids of the protein. The residues attained are those which are responsible in non-bond interaction within the α6β4 protein region including hydrogen bond, hydrophobic, electrostatic, or unfavorable bond, such as bumps interaction. Further, this study will strictly attach to hydrogen bond and

hydrophobic contacts since both interactions have highest number of binding evidence in any cases of docking. Higher number of amino acid residues somehow reflect more active regions of the aptamer to take part in the interaction with the target molecule. As consequence, more hydrogen bonds and hydrophobic contacts are indicated in interaction between CSC1 and α6β4 protein employing 15 bonds and 13 contacts, respectively (**Table 5.9**). On the other hand, Wy5a aptamer obtains lesser number of interactions with the 13 hydrogen bonds and 6 hydrophobic contacts. These coincidences correlate with the length of nucleobases as well as the total of active residues involved during the docking (Wang et al., 2015, Ahirwar et al., 2016), in which, shorter nucleobases length may contribute to limited probabilities to exhibit more non-bond interactions with the target molecule.

Interestingly, almost all the aptamers donated more hydrogen bonds rather than hydrophobic contact in interaction with the protein. This phenomenon is relevant with the trend of their ZRANK scores (**Figure 5.25**), which indicates that the reranking method of ZRANK is appropriate in describing the non-bond interactions occupied by the majority of aptamers in complex with the α6β4 protein. In addition, according to Rohs and co-workers, the hydrogen bond interaction and hydrophobic contact play a key role in binding specificity between ssDNA and protein (Rohs et al., 2010). The presence of hydrophobic contact is likely to support and to stabilize the aptamer and protein binding (Pace et al., 2011). All hydrophobic contacts found here are conducted from the π-orbitals of the nucleotides to the alkyl atom of the amino acids. The role of hydrophobic contact exhibit the stability of the ligand in binding interface with the protein, in turn, higher number of hydrophobic will increase the active region where the ligand and protein bound (Patil et al., 2010).

The long sequences of the CSC1 tends to lead to more complex structure for further computational modelling (Hu et al., 2015). Therefore, to achieve the feasibility and rationality of the docking result, Wy5a has been considered as aptamer with high binding to the α6β4 protein here since it is able to afford better refinement scoring and plausible binding confirmed by high residues and non-bond interactions with only relied on shorter length of sequences (Pierce and Weng, 2007).

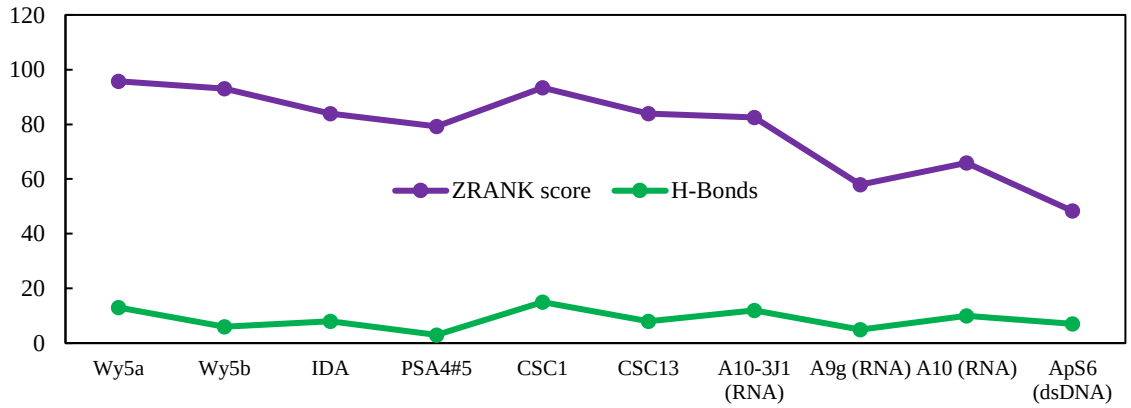

Figure 5.25 Correlation profile between the obtained ZRANK scores and number of H-bonds in aptamers- α6β4 protein interaction.

5.1.2.3 Comparison of Wy5a Docking Results with Wy5b Aptamer

Further, to confirm the preeminent binding of α6β4 protein to the Wy5a and Wy5b aptamers designed in experimental studies, the docking interaction between Wy5b and the α6β4 protein has also been investigated (Wang et al., 2014). As presented in **Table 5.9**, the ZDOCK score of Wy5b interaction is relatively closer to either Wy5a or CSC1 aptamer (22.16). Even after the docking was refined with ZRANK, the score is quite high (-93.013) as compared to other aptamers, particularly with A10 RNA (-82.471), which has the same length of 56 nucleobases. This may indicate that Wy5b is one of the substantial aptamers in recognizing the α6β4 protein in nature.

Table 5.10 Nucleotide residues observed in Wy5a aptamers and α6β4 interaction.

No.	Name	ID	Name Code
1	DA5	5	A:Ade5
2	DC6	6	A:Cyt6
3	DT7	7	A:Thy7
4	DA8	8	A:Ade8
5	DT13	13	A:Thy13
6	DT16	16	A:Thy16
7	DC18	18	A:Cyt18
8	DG19	19	A:Gua19
9	DG20	20	A:Gua20
10	DT21	21	A:Thy21
11	DT23	23	A:Thy23
12	DG24	24	A:Gua24
13	DG25	25	A:Gua25
14	DT26	26	A:Thy26
15	DG27	27	A:Gua27
16	DA28	28	A:Ade28
17	DT38	38	A:Thy38
18	DC39	39	A:Cyt39
19	DG40	40	A:Gua40
20	DG45	45	A:Gua45
21	DG46	46	A:Gua46
22	DT47	47	A:Thy47
23	DG48	48	A:Gua48
24	DC49	49	A:Cyt49

Abbreviations: D = Deoxyribose chain, A: = Source of complex (chain-A)

Table 5.11 Amino acid residues observed in Wy5a aptamers and α6β4 interaction.

No.	Name	ID	Name Code	Hydrophobicity
1	ASN1134	1,134	A:Asn1134	-3.5
2	LYS1136	1,136	A:Lys1136	-3.9
3	LYS1160	1,160	A:Lys1160	-3.9
4	ILE1163	1,163	A:Ile1163	4.5
5	GLN1164	1,164	A:Gln1164	-3.5
6	GLY1165	1,165	A:Gly1165	-0.4
7	ASP1166	1,166	A:Asp1166	-3.5
8	GLU1168	1,168	A:Glu1168	-3.5
9	TYR1189	1,189	A:Tyr1189	-1.3
10	CYS1190	1,190	A:Cys1190	2.5

11	ASP1191	1,191	A:Asp1191	-3.5
12	GLU1193	1,193	A:Glu1193	-3.5
13	LYS1195	1,195	A:Lys1195	-3.9
14	PRO1206	1,206	A:Pro1206	-1.6
15	TYR1207	1,207	A:Tyr1207	-1.3
16	SER1208	1,208	A:Ser1208	-0.8
17	LEU1210	1,210	A:Leu1210	3.8
18	VAL1211	1,211	A:Val1211	4.2
19	CYS1213	1,213	A:Cys1213	2.5
20	ARG1214	1,214	A:Arg1214	-4.5
21	GLU1242	1,242	A:Glu1242	-3.5
22	ALA1244	1,244	A:Ala1244	1.8
23	ARG1281	1,281	A:Arg1281	-4.5

The non-bond interactions of Wy5a are also compared with the Wy5b to explicate the binding potential toward the α6β4 protein. The Wy5a system contributes 24 nucleobases residues involved in the interaction of 23 amino acids residues with the α6β4 protein (**Tables 5.10** and **5.11**). These total residues are higher than Wy5b aptamer complex, which employed 15 and 17 residues of nucleotides and amino acids, respectively (**Tables 5.12** and **5.13**). In correlation with the binding interface, the Wy5a-α6β4 bonding also has greater intact area ($Å^2$) as opposed to the Wy5b and α6β4. This wider interface may contribute to the more accessible interaction of the ssDNA on the protein site (**Table 5.9**).

Further, the hydrogen bonds formed between the protein and Wy5b interactions are 19 bonds, comprising of 8 donor bonds and 7 acceptor bonds of amino acid where some of them connected to more than one nucleobase (**Table 5.14**). For instance, HIS1172 is an electron donor for C31 and T30 in Wy5b aptamer. As compared to the Wy5a interaction, there are 26 hydrogen bonds in 10 amino acids standing as donor bonds and 7 as acceptor bonds (**Table 5.15**). Similarly, some amino acids are governed as donor and acceptor all at once toward the

different nucleotides, such as GLN1164 amino acid as donor bond to T16 and as acceptor bond from G48 in Wy5a complex. The same behavior is also seen in GLU1170 of Wy5b complex.

Table 5.12 Nucleotide residues observed in Wy5b aptamers and α6β4 interaction.

No.	Name	ID	Name Code
1	DG26	26	A:Gua26
2	DA27	27	A:Ade27
3	DC28	28	A:Cyt28
4	DT29	29	A:Thy29
5	DT30	30	A:Thy30
6	DC31	31	A:Cyt31
7	DG32	32	A:Gua32
8	DG39	39	A:Gua39
9	DT40	40	A:Thy40
10	DT41	41	A:Thy41
11	DG42	42	A:Gua42
12	DT43	43	A:Thy43
13	DG44	44	A:Gua44
14	DG45	45	A:Gua45
15	DT46	46	A:Thy46

Abbreviations: D = Deoxyribose chain, A: = Source of complex (chain-A)

Table 5.13 Amino acid residues observed in Wy5b aptamers and α6β4 interaction.

No.	Name	ID	Name Code	Hydrophobicity
1	ILE1163	1,163	A:Ile1163	4.5
2	ASP1166	1,166	A:Asp1166	-3.5
3	SER1169	1,169	A:Ser1169	-0.8
4	GLU1170	1,170	A:Glu1170	-3.5
5	ALA1171	1,171	A:Ala1171	1.8
6	HIS1172	1,172	A:His1172	-3.2
7	TYR1187	1,187	A:Tyr1187	-1.3
8	TYR1189	1,189	A:Tyr1189	-1.3
9	CYS1190	1,190	A:Cys1190	2.5
10	ARG1214	1,214	A:Arg1214	-4.5
11	GLU1242	1,242	A:Glu1242	-3.5
12	PRO1243	1,243	A:Pro1243	-1.6
13	ALA1244	1,244	A:Ala1244	1.8

14	GLU1245	1,245	A:Glu1245	-3.5
15	THR1246	1,246	A:Thr1246	-0.7
16	GLU1249	1,249	A:Glu1249	-3.5
17	LYS1279	1,279	A:Lys1279	-3.9

Table 5.14 Hydrogen bonds analysis of Wy5b aptamers and α6β4 protein interaction.

No.	Name	From[1]	To[2]	Distance
1	A:ALA1171:HN - A:DG32:OP2	A:ALA1171:HN	A:DG32:OP2	2.934
2	A:HIS1172:HD1 - A:DC31:OP1	A:HIS1172:HD1	A:DC31:OP1	1.571
3	A:ARG1214:HH22 - A:DT43:OP1	A:ARG1214:HH22	A:DT43:OP1	2.487
4	A:THR1246:HN - A:DT43:O2	A:THR1246:HN	A:DT43:O2	2.811
5	A:DG26:H22 - A:GLU1242:O	A:DG26:H22	A:GLU1242:O	2.318
6	A:DG26:H1 - A:PRO1243:O	A:DG26:H1	A:PRO1243:O	1.767
7	A:GLU1170:HA - A:DG32:OP1	A:GLU1170:HA	A:DG32:OP1	1.569
8	A:HIS1172:HE1 - A:DT30:O3'	A:HIS1172:HE1	A:DT30:O3'	1.736
9	A:ALA1244:HA - A:DA27:N3	A:ALA1244:HA	A:DA27:N3	1.866
10	A:GLU1245:HA - A:DC28:O2	A:GLU1245:HA	A:DC28:O2	2.711
11	A:GLU1249:HA - A:DG44:OP1	A:GLU1249:HA	A:DG44:OP1	1.561
12	A:DA27:H2 - A:ALA1244:O	A:DA27:H2	A:ALA1244:O	1.517
13	A:DC31:H4' - A:GLU1170:O	A:DC31:H4'	A:GLU1170:O	2.019
14	A:DG32:H4' - A:GLU1170:OE1	A:DG32:H4'	A:GLU1170:OE1	2.439
15	A:DT41:H4' - A:ASP1166:OD1	A:DT41:H4'	A:ASP1166:OD1	2.275
16	A:DT41:H1' - A:ASP1166:OD1	A:DT41:H1'	A:ASP1166:OD1	2.526
17	A:DT43:H5'1 - A:TYR1189:O	A:DT43:H5'1	A:TYR1189:O	2.175
18	A:DT43:H1' - A:THR1246:OG1	A:DT43:H1'	A:THR1246:OG1	2.799
19	A:DG45:H4' - A:GLU1242:OE1	A:DG45:H4'	A:GLU1242:OE1	2.614

Annotation[1] ("Source of complex: donor molecule: donor atom number"); Annotation[2] ("Source of complex: acceptor molecule: acceptor atom number").

Table 5.15 Hydrogen bonds analysis of Wy5a aptamers and α6β4 protein interaction.

No.	Name	From[1]	To[2]	Distance
1	A:ASN1134:HD22 - A:DC39:OP1	A:ASN1134:HD22	A:DC39:OP1	2.797
2	A:LYS1136:HZ1 - A:DC39:OP1	A:LYS1136:HZ1	A:DC39:OP1	2.159
3	A:LYS1160:HZ3 - A:DG20:OP1	A:LYS1160:HZ3	A:DG20:OP1	2.997
4	A:GLN1164:HE21 - A:DT16:O4	A:GLN1164:HE21	A:DT16:O4	2.255
5	A:LYS1195:HZ3 - A:DG19:N3	A:LYS1195:HZ3	A:DG19:N3	3.002
6	A:ARG1214:HH12 - A:DG46:O3'	A:ARG1214:HH12	A:DG46:O3'	2.107
7	A:ARG1214:HH21 - A:DG46:N3	A:ARG1214:HH21	A:DG46:N3	2.543
8	A:ARG1214:HH21 - A:DT47:O4'	A:ARG1214:HH21	A:DT47:O4'	2.201

9	A:GLU1242:HN - A:DT7:OP1	A:GLU1242:HN	A:DT7:OP1	2.279
10	A:ARG1281:HH21 - A:DA8:OP1	A:ARG1281:HH21	A:DA8:OP1	2.172
11	A:DG24:H21 - A:GLU1193:OE1	A:DG24:H21	A:GLU1193:OE1	2.512
12	A:DG46:H22 - A:CYS1213:O	A:DG46:H22	A:CYS1213:O	2.186
13	A:DG48:H21 - A:GLN1164:O	A:DG48:H21	A:GLN1164:O	2.905
14	A:ASN1134:HA - A:DG40:OP1	A:ASN1134:HA	A:DG40:OP1	2.402
15	A:LYS1136:HA - A:DG27:O3'	A:LYS1136:HA	A:DG27:O3'	2.452
16	A:LYS1136:HA - A:DA28:OP1	A:LYS1136:HA	A:DA28:OP1	2.763
17	A:GLY1165:HA1 - A:DC18:OP1	A:GLY1165:HA1	A:DC18:OP1	3.008
18	A:GLY1165:HA2 - A:DC18:OP1	A:GLY1165:HA2	A:DC18:OP1	3.000
19	A:PRO1206:HA - A:DT21:O4	A:PRO1206:HA	A:DT21:O4	1.875
20	A:DC18:H1' - A:GLU1193:OE1	A:DC18:H1'	A:GLU1193:OE1	2.657
21	A:DG19:H1' - A:GLU1168:OE2	A:DG19:H1'	A:GLU1168:OE2	1.670
22	A:DG24:H5'1 - A:SER1208:O	A:DG24:H5'1	A:SER1208:O	2.474
23	A:DC39:H4' - A:ASN1134:OD1	A:DC39:H4'	A:ASN1134:OD1	2.585
24	A:DG48:H1' - A:GLN1164:O	A:DG48:H1'	A:GLN1164:O	2.625
25	A:DC49:H5'1 - A:ASP1166:OD1	A:DC49:H5'1	A:ASP1166:OD1	2.166
26	A:DC49:H5'2 - A:ASP1166:OD1	A:DC49:H5'2	A:ASP1166:OD1	2.617

Annotation[1] ("Source of complex: donor molecule: donor atom number"); Annotation[2] ("Source of complex: acceptor molecule: acceptor atom number").

Analogue responses are also indicated in the nucleotides toward the protein (**Table 5.14** and **Table 5.15**). The evidence of these hydrogen bonds is typically due to the existence of carboxylic and nitrogen groups which abundantly present surrounding the side or main chains of the aptamer and protein structures, and abridged interactively maintaining the dominant role among the protein and nucleic acids interaction. According to the previous studies, some hydrogen bond donors are mostly recognized in amino groups of protein in conventional planar configuration of protein-DNA complex. This is in-line with the results obtained from both Wy5a and Wy5b docking studies. The most electrons are donated by the amino acid residues of the protein (McDonald and Thornton, 1994, Hooft et al., 1996, Mukherjee et al., 2005). Hydrophobic contact is also indicated here to define the importance of hydrophobicity in binding interaction. There are 6 and 3 hydrophobic interactions indicated in Wy5a and Wy5b complexes with the protein, accordingly (**Tables 5.16** and **5.17**).

Table 5.16 Hydrophobic analysis of Wy5a aptamers and α6β4 protein interaction.

No.	Name	From[3]	To[4]	Distance
1	A:DT21 - A:PRO1206	A:DT21	A:PRO1206	5.136
2	A:DG24 - A:LEU1210	A:DG24	A:LEU1210	5.240
3	A:DT26 - A:LEU1210	A:DT26	A:LEU1210	4.318
4	A:DT26 - A:VAL1211	A:DT26	A:VAL1211	5.436
5	A:DG27 - A:ARG1214	A:DG27	A:ARG1214	4.067
6	A:DG27 - A:ARG1214	A:DG27	A:ARG1214	4.498

Annotation[3] (Source of complex : π-orbitals molecule)
Annotation[4] (Source of complex : alkyl molecule)

Table 5.17 Hydrophobic analysis of Wy5b aptamers and α6β4 protein interaction.

No.	Name	From[3]	To[4]	Distance
1	A:DG26 - A:ALA1244	A:DG26	A:ALA1244	5.008
2	A:DA27 - A:ALA1244	A:DA27	A:ALA1244	4.568
3	A:DA27 - A:ALA1244	A:DA27	A:ALA1244	4.176

Annotation[3] (Source of complex : π-orbitals molecule)
Annotation[4] (Source of complex : alkyl molecule)

Based on the non-bond interaction environment, the hydrophobic contact is also enhanced around the outlay of the hydrogen bonds where the hydrophobic interaction also favored to take place within the region of hydrogen bonds (Qian et al., 2009). The Wy5a, since it obtains more hydrophobic contacts with the α6β4 protein, then more stable binding affinity is more accomplished in this regard as opposed to the Wy5b aptamer. In summary, those results explicate higher number of hydrogen bond interactions and hydrophobic contact obtained by Wy5a aptamer, therefore executes Wy5a as the top interaction aptamer of the α6β4 protein. Based on the consideration of the ZRANK scores, interaction surface region, total residues, as well as number of non-bond interactions, the Wy5a aptamer has been selected as the best aptamer to interact with the α6β4 protein that would be further used within the study.

5.1.2.4 Analysis of Docking Interaction between Wy5a Aptamer and α6β4 Integrin

Principally, the α6β4 integrin is transmembrane receptors which support a strong junction between the intermediate filament complex and the extracellular matrix through laminin binding (Lee et al., 1992, Niessen et al., 1994, de Pereda et al., 1999). The β4 integrin, is a dominant subunit for α6 rather than β1 in its nature. It is kind of a huge cytoplasmic tail consisting of cytoskeleton and signaling system assembled through the extensive region of amino acid domain (Cress et al., 1995). In general, this domain defines the entire functions of α6β4 integrin in phosphorylation and inducing the release of α6β4 body as well as signaling pathways. The α6β4 integrin itself was found in PC3 cells as a promotor for invasive signaling tumor cell growth, aggressiveness, and metastasis (Cress et al., 1995, Shaw et al., 1997, Mariotti et al., 2001, Stewart and O'connor, 2015, Berg et al., 2016). The previous experimental study accomplished by Berg and co-workers employed this corresponding integrin as a target biomolecule representing the PC3 metastatic cells for determining the selectivity of their candidate aptamer (Bonaccorsi et al., 2000, Bonaccorsi et al., 2004, Berg et al., 2016). This thesis indicates an interaction that might be performed by the candidate aptamers toward the α6β4 integrin.

The docked model of Wy5a toward the α6β4 protein is depicted in **Figure 5.26** in yellow highlighted area interpreting the binding region of aptamer with protein. This region involves active residues from nucleotide of the Wy5a and amino acid residues of the α6β4 protein (**Tables 5.10** and **5.11**).

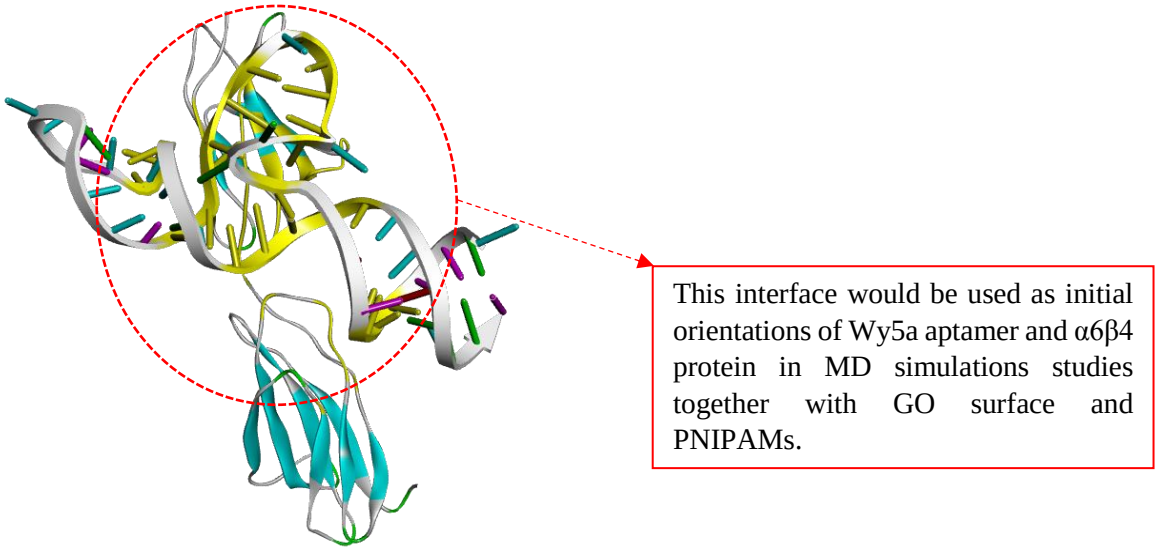

Figure 5.26 The binding region (yellow -highlighted) of Wy5a aptamer and α6β4 protein investigated by ZDOCK-ZRANK rerank score.

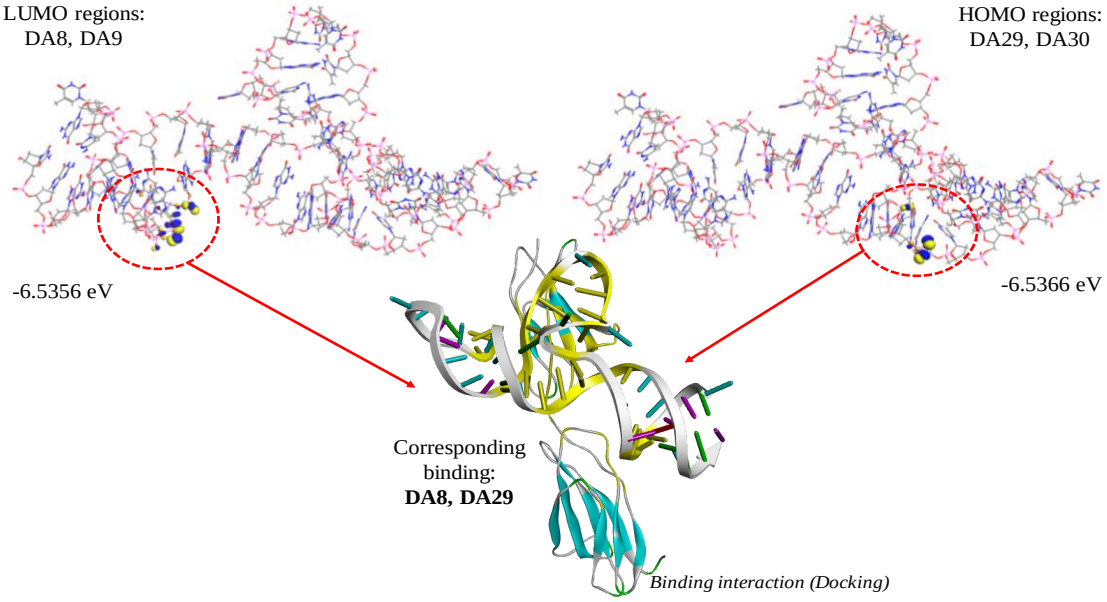

Figure 5.27 The HOMO and LUMO regions of Wy5a aptamer calculated by density functional tight binding (DFTB). The regions of HOMO and LUMO isosurfaces associate to the nucleotide residues involved in binding interaction with α6β4 integrin.

The nucleotides residues have been confirmed by the calculation of orbital isosurfaces showing that the active residues also consist of HOMO and LUMO isosurfaces (**Figure 5.27**),

which indicate that there is electronic transfer occurred around the docked area. In addition, considering the importance of folded structure of single stranded nucleotide, the investigation of the secondary structure of Wy5a aptamer has also been done.

As presented in **Figure 5.28**, the Wy5a aptamer showed a unique denoting of stem-loop conjunction. The stem-loop regions are acknowledged as the responsible site of single-stranded nucleotides structure for recognizing the target molecule, especially in bulge-hairpin motif (recurring pattern of DNA which has biological function (D'Haeseleer, 2006)). Reported by Bing et al. (2010), that streptavidin specific DNA aptamer could remain to have similar sequences of stem-loop motifs even though it was reproduced using different templates and at different laboratories. This unchanged properties suggested that nucleotides present in the loop and bulge sites have long-life characteristics subjected to define high affinity binding toward the molecule target (Hasegawa et al., 2016). As denoted in the blue-highlighted sequences in **Figure 5.28**, the observed annotated nucleotides of Wy5a aptamer in α6β4 protein interaction occurred specifically in bulge-stem regions.

Further, to specify and validate the docking results, the residues of the protein present in the interaction were examined. Based on the previous crystallography study from de Pereda and team, the α6β4 protein contains some active amino acids residues controlling the ability of the protein to interact with another ligand or molecule or with the aptamer (de Pereda et al., 1999). These amino acid residues mostly regulate the potential binding ability toward biomolecule according to the connected segment and variety of binding modes, including the loops/proteins. There are two important domains of α6β4 protein responsible for a successful binding which contain six important residues at C-C' (ASP1166, GLU1170), E-F

(ASP1191), and B-C (GLU1242, GLU1245, GLU1249) loops in each domain (de Pereda et al., 1999). These loops correspond to protein-binding motifs, which contribute directly or indirectly in molecular interaction. On the other hand, additional residues present in the larger domain (domain 2) at the C-C' loop comprising ASP1262 and ASP1263. Therefore, within this study, the larger domain was employed as the target protein since it covers wider area of important residues to exhibit the interactions with the target biomolecule. The critical amino acid residues of the α6β4 protein involved during docking calculation was also taken into account. Five amino acids residues such as ASP1191, GLU1242, GLU1245, GLU1249 of the α6β4 protein are indicated in the interaction with Wy5a aptamer. Further, three of the amino acid residues including ASP1166 to C49, ASP1191 to G46, and GLU1242 to T7 are involved in hydrogen bonding with the Wy5a (**Figure 5.29**). These results demonstrated that the selected docked model of is quite reliable to represent the real behavior of Wy5a with α6β4 protein interaction and five amino acids residues of α6β4 protein are entirely or partially responsible in binding domain with the Wy5a aptamer.

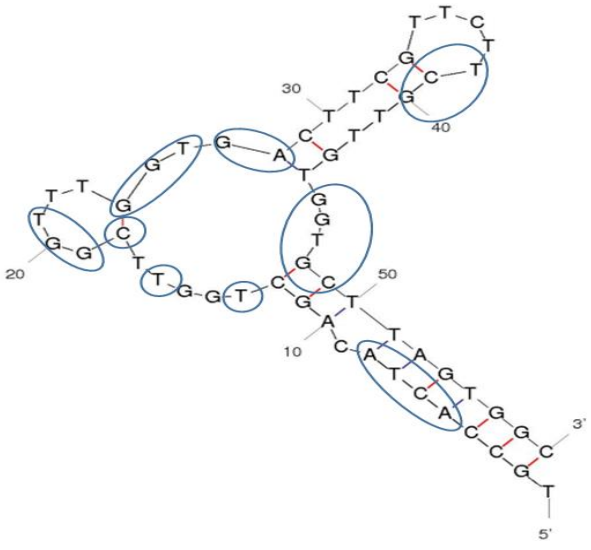

Sequence:
TGCC**ACTA**CAGC**T**GG**T**T**CGGT**TT**GGTGA**CT
TCGTTCT**TCG**TTGT**GGTGC**TTAGTGGC

Figure 5.28 The nucleotides region of Wy5a aptamer which is responsible in interaction with the α6β4 protein.

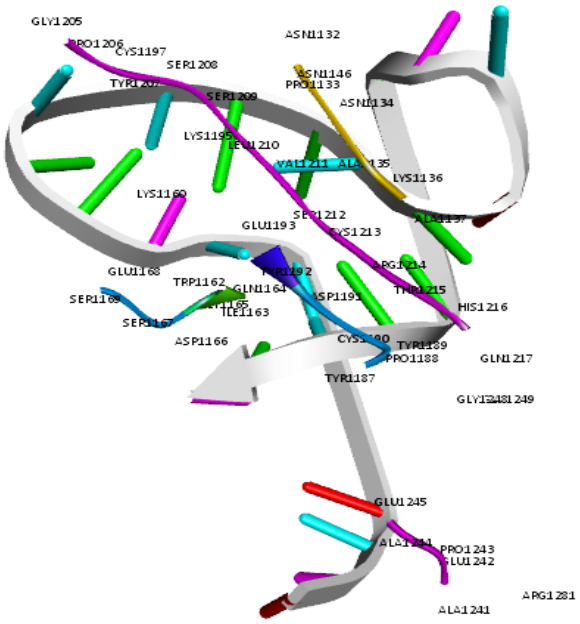

Figure 5.29 The corresponding residues derived from Wy5a-α6β4 binding interaction showing responsible nucleotides and amino acids of the complex.

5.1.3 Molecular Dynamics Simulations

Within this study, MD simulations were employed to investigate and to validate the experimental data regarding two important behaviors: (1) conformation changes of coil and globular states of PNIPAM and (2) biomolecule interaction between aptamer and protein modulated by PNIPAM as tunable-GO surface. Categorized as thermal responsive polymer, PNIPAM has characteristic to transform its configurational status into coil or globular condition depending on the temperature around its lower critical solution temperature (LCST) of 32^{o}C (~305 K). Therefore, in order to check the reliability of the constructed PNIPAM in response to stimuli, the single chain of PNIPAM has been simulated under two different temperatures, 298 K and 310.7 K.

Figure 5.30 shows the radius of gyration, R_g, over the production simulation time of 10 ns and 15 ns for 298 K and 310.7 K, respectively. The R_g defines the compactness of the specific conformation size of the polymer, that can be calculated by correlating the mass (m_i) of the atom (i) within polymer with internal coordinate (r_i) of the atom (i) of conformation:

$$R_g = \left(\frac{\sum_j \|r_i\|^2 m_i}{\sum_i m_i}\right)^{\frac{1}{2}} \quad (5.1)$$

The molecular interactions between PNIPAM and the GO surface is determined as a function of temperature. As shown in **Figure 5.30**, the R_g in 298 K is higher compared to 310.7 K at the end of simulation time of 10 ns indicating that the formation of polymer is more compact at above LCST (red line) rather than at 298 K. The R_g at both temperatures showed similar length in initial time. But after 1.5 ns, the R_g at 310.7 K started to decrease the linearity to about 9 Å, while it showed flexible and more extended at 298 K (~23 Å). Indeed, the PNIPAM molecule consists of repeating unit of hydrophobic and hydrophilic groups which allows it to undergo transition into water-soluble or insoluble order depending on the temperature thus, resulting the conformational change. It exists in water solution as coil form due to the domination of enthalpic contribution from hydrogen bonding between water and amide groups below LCST. When temperature reaches higher than LCST, its hydrogen bonds are weakened since the kinetic energies turn to be greater than the energy of hydrogen bonding. As consequence, the solvation entropy of hydrophobic interaction between isopropyl group and its backbone is dominant and induces more intra/intermolecular aggregation of hydrophobic groups altering the polymer conformation from flexible coil to be globular state (Meersman et al., 2005, Esteve et al., 2007, Du et al., 2010, Jain et al., 2015). This behavior can be distinguished in **Figure 5.31** as a result of different temperature applications. At initial step, the PNIPAM chain looks linear and keep positioned at the middle

(**Figure 5.31 (a)**). After 10 ns, the chain is still quite linear and moved to the edge of PBC box in 298 K due to the dynamics effect (**Figure 5.31 (b)**), while it is found in globular state at the end of simulation in 310.7 K (**Figure 5.31 (c)**).

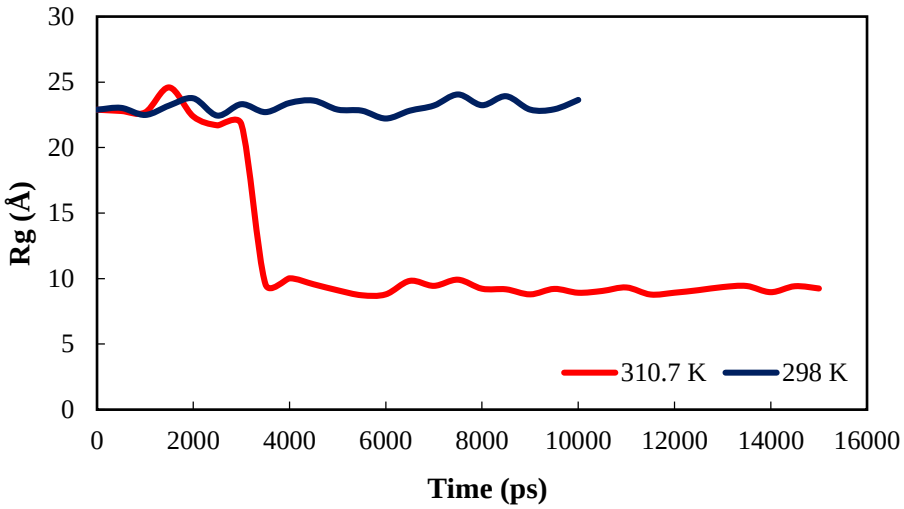

Figure 5.30 Radius of gyration of single PNIPAM at temperatures of 298 K (blue line) and 310.7 K (red line).

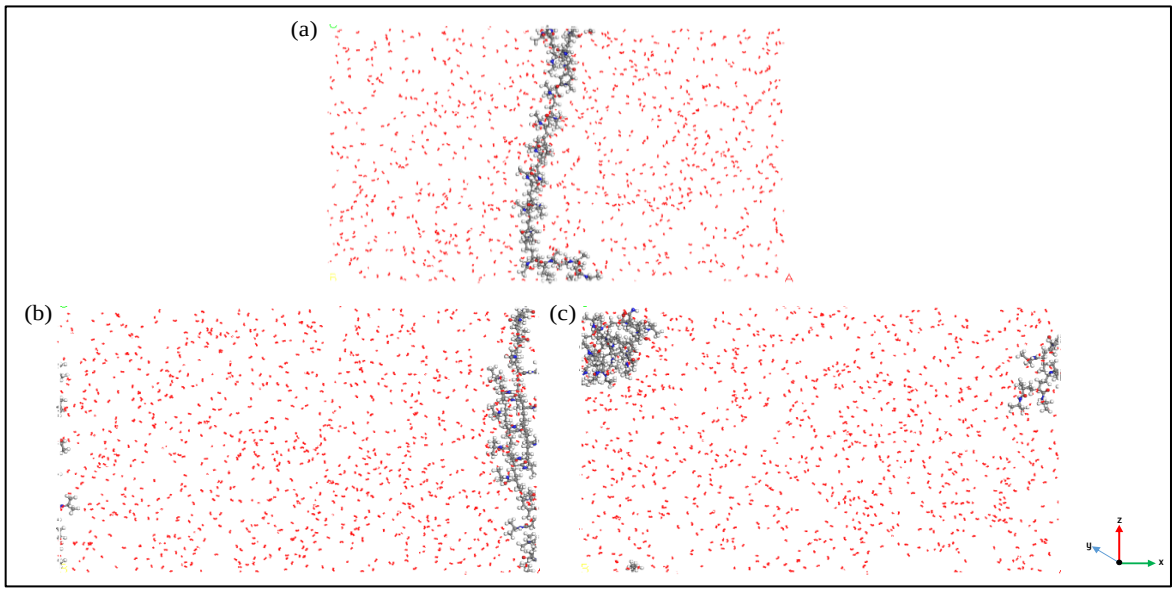

Figure 5.31 The MD snapshots of the single PNIPAM at the (a) starting simulation, and its behavior after MD simulations under (b) 298 K as well as (c) 310.7 K. These explain the natural properties of PNIPAM which is swollen above LCST and coiled under LCST temperatures.

For the next step, we applied the similar structure of the PNIPAM in complete construction of system involving GO, aptamer, and protein molecules. Herein, we separated the simulations into two different systems. The first system (System I (GO/PNs/Apt)) was built to attain the conformational change of PNIPAM-grafted GO at different temperatures below and above LCST first, which are 298 K and 310.7 K. Once the conformational transition obtained, the protein molecule was introduced into the system as the second stage (System II (GO/PNs/Apt/pro)), for interaction with the aptamer under the same temperatures applied in the first stage. Due to the constraints of huge numbers of atoms and computationally expensive, the time duration of the System I was set to 5,000 ps and was considered not to be longer. However, the simulated systems should have met our needs for simulations within the duration of time since as presented in **Figure 5.32,** that the kinetic energy of the system is quite stable and less fluctuations during the given time and under the different temperatures. The increasing temperature breaks the hydrogen bonds and increases the kinetic motions of the molecules in the system therefore, the kinetic energy of the system at 310.7 K is found higher than that of 298 K.

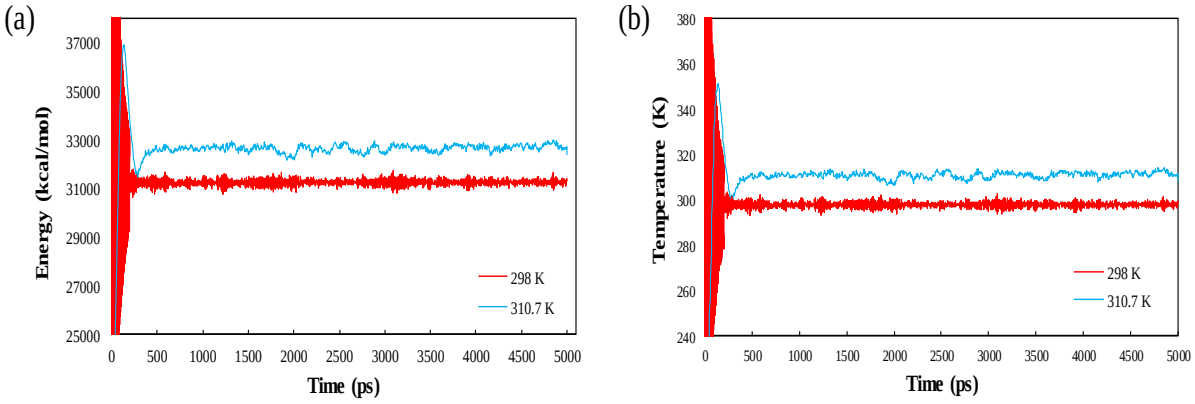

Figure 5.32 (a) The kinetic energy and (b) temperature profiles of the System I at below (298 K) and above (310.7 K) LCST of molecular dynamics simulations.

Figure 5.33 (a) shows the R_g of the grafted PNIPAM chains after 5 ns of simulation at 298 and 310.7 K. The R_g indicates the alteration of chains distance in average, over 5 ns intervals taken from 298 and 310.7 K dynamics simulations. In general, the values of the R_g at 310.7 K is smaller than the corresponding value at 298 K. The R_g values of 310.7 K (red) are around 11 Å which are smaller than that in 298 K (blue) at 19 Å. As shown in depiction, the grafted chains (green molecule) are more extended at 298 K (**Figure 5.33 (b)**) and looks collapsed in globular form at 310.7 K (**Figure 5.33 (c)**). These findings are consistent with the previous experimental studies of PNIPAM functionalized-GO surface (Wang et al., 2011a, Gong et al., 2016). The assembly of PNIPAM on the GO substrate enabled to induce a coil-state under LCST (298 K) as well as globular-state at above LCST (310.7 K). It is clearly seen in **Figure 5.34 (i)**, that the composite of GO/PNIPAM consequently tend to appear as precipitated-aggregate and more dispersive in water solution at above LCST rather than to be dissolved as at below LCST. The increase of temperature over the LCST allowed the hydrophobic features of PNIPAM to be interacting each other thus, causing the chains to be explicitly collapsed and water-insoluble (**Figure 5.34 (ii))** (Wang et al., 2011a).

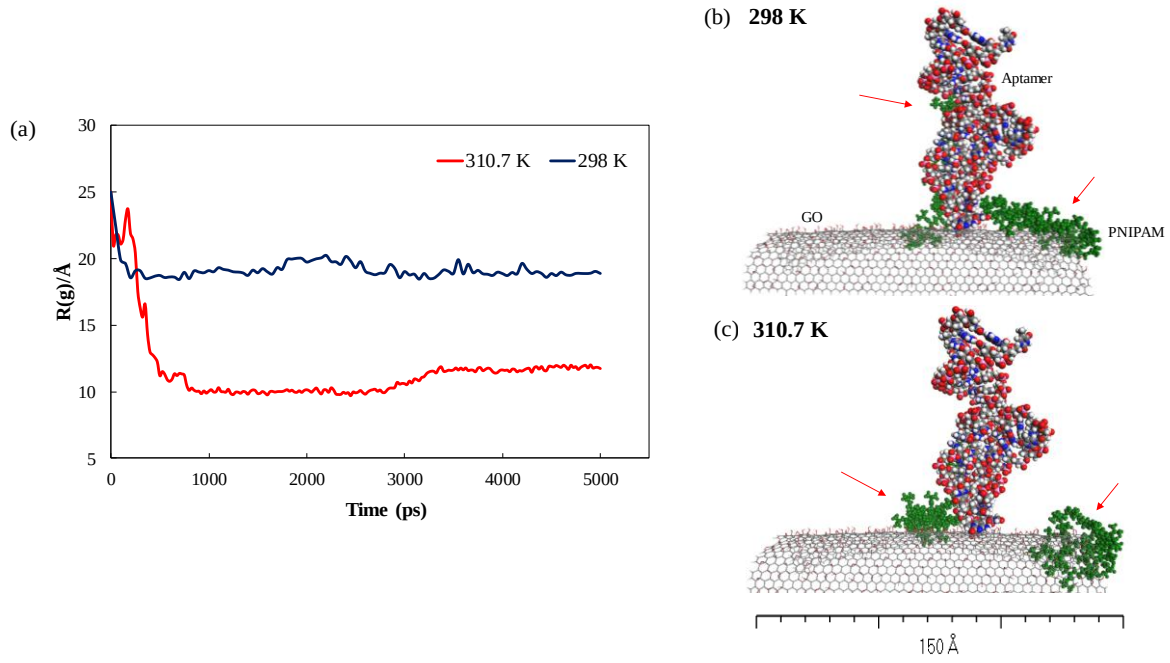

Figure 5.33 (a) Radius of gyration of the grafted PNIPAM on the System I at temperatures of 298 K (blue line) and 310.7 K (red line). The MD snapshots of the grafted PNIPAM in System I (green molecules) with behavior checked after MD simulations at (b) 298 K and (c) 310.7 K. These explain the natural properties of PNIPAM which are coiled under LCST and collapsed above LCST.

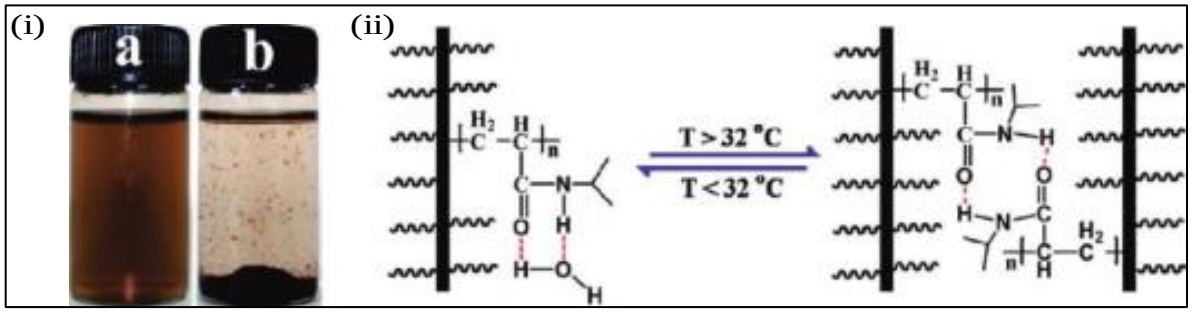

Figure 5.34 (i) Snapshots of GO/PNIPAM in aqueous solution at (a) below and (b) above LCST. (ii) The illustration of thermal responsive of the polymer chain within GO/PNIPAM. Adapted from Wang et al. (2011a).

In System II, the protein is involved in simulation with the Wy5a aptamer. The protein was placed hovering the grafted surface nearby the binding region of aptamer in about 5 Å. The initial orientation was approximated using the best-pose predicted in the docking study since according to the computational trial that its adequate parallel sampling allowed to determine

a molecular insight into adsorption. Within these simulations, the GO, PNIPAMs, and aptamer atoms were constrained while other elements including solvent were freely to move. Similarly, the MD simulations were only performed in 500 ps due to the computationally cost under the clusters progress.

As result, the protein contact to the Wy5a aptamer is found more intensive to bind in 310.7 K than 298 K as presented in **Figures 5.35** and **5.36**. The extended chains of PNIPAM in 298 K seems to "turn-off" the protein interaction access to the aptamer, thus both molecules are not capable to be fully participating (**Figure 5.36**). This explain that the protein is hindered by the PNIPAM chain to reach the aptamer when the system was at 298 K and due to the hydrophilic disturbance of PNIPAM, it seems to be shifted from its initial orientation. In contrast, when the temperature increases to above LCST, the protein is exposed ("turn-on" mode) and subsequently able to bind to the aptamer (**Figure 5.35**). The access to the interaction region at 310.7 K is opened thus allowing the protein to interact with the aptamer site. These are further confirmed by the distance calculations within the protein and the aptamer, in which lower distance indicates closer distance at temperature of 310.7 K than 298 K (**Figure 5.37**).

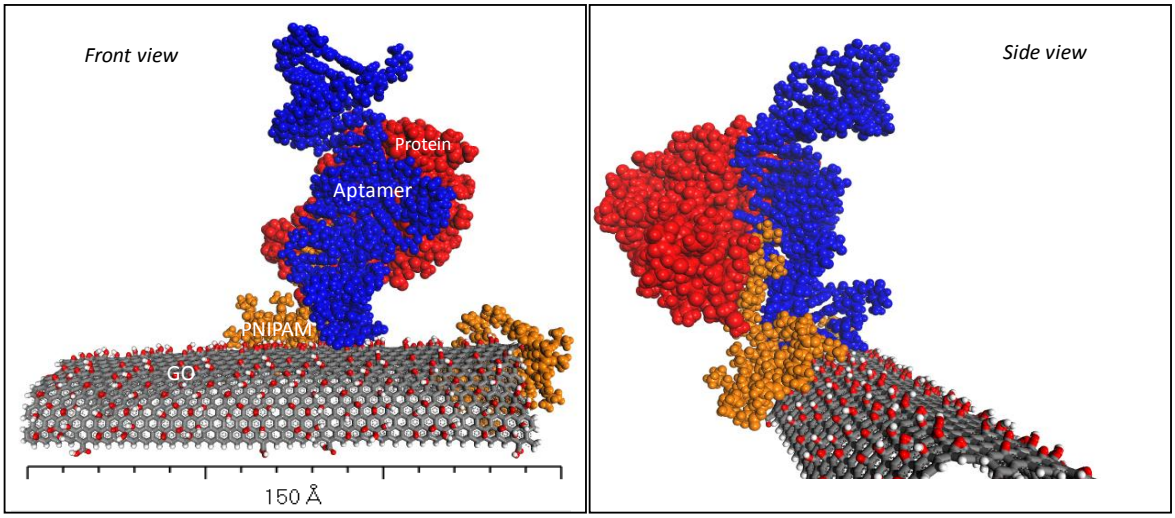

Figure 5.35 The depiction of the end-simulation of interaction studies between Wy5a aptamer and α6β4 protein at 310.7 K.

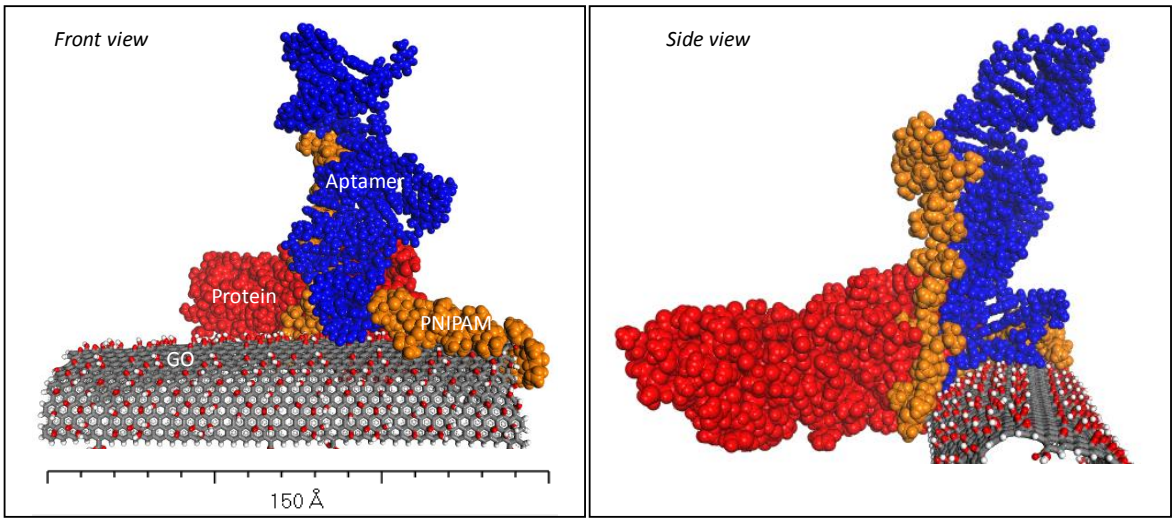

Figure 5.36 The depiction of the end-simulation of interaction studies between Wy5a aptamer and α6β4 protein at 298 K.

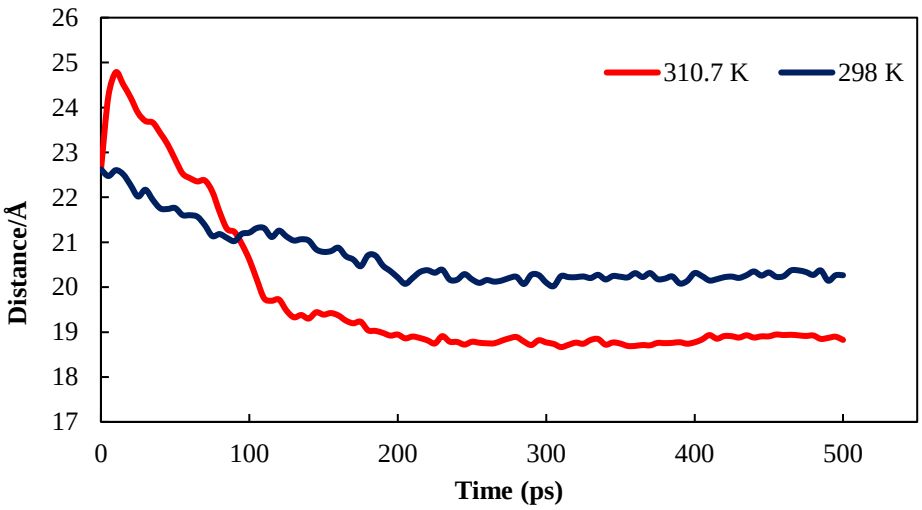

Figure 5.37 Distance between the protein and aptamer in the System II (GO/PNs/Apt/pro).

For the system in each temperature, the interaction energy between the surface complex and the protein was calculated after single point energy simulation in order to yield the sufficient binding energy of protein on the interactive surface. The interaction energies found within the system at 310.7 K shows lower than at 298 K suggesting stronger interaction performed at 310.7 K and more efficient the energy required to approach the interaction between the protein and aptamer (**Table 5.18**).

Table 5.18 Interaction energy of the protein with aptamer under two different temperatures of 298 K (below LCST) and 310.7 K (above LCST).

System	Total Energy (kcal/mol)	
	298 K	**310.7 K**
E_{system}	162,142.17	161,213.84
$E_{solvent}$	39,788.83	40,230.59
$E_{surface}$	44,572.92	44,587.80
$E_{protein}$	2,491.59	2,226.53
$E_{aptamer}$	76,085.72	76,085.72
$\mathbf{E_{interaction}}$	-796.88	-1,916.79

$$\mathbf{E_{interaction} = E_{system} - (E_{solvent} + E_{surface} + E_{aptamer} + E_{protein})}$$

Since the non-covalent interaction usually takes part in affecting the binding affinity, the number of binding interactions as well as the most binding types involved within the molecules were thereby investigated. The different molecular interactions are shown in **Figures 5.38** and **5.39**, where higher number of bond interactions has evidence at 310.7 K than at 298 K, which attributes to the non-covalent interactions, such as electrostatic, van der Waals, and hydrophobic between the aptamer and protein. Therefore, the contribution of the binding is analyzed to be electrostatic and hydrophobic in nature. There exist about 15 hydrogen bonds and six hydrophobic contacts which may exhibit stronger interaction at 310.7 K as compared to the system at 298 K with only six hydrogen bonds and four hydrophobic contacts. However, it can be understood literally due to more accessible binding region between the protein and aptamer stimulated by the tunable surface of PNIPAM when it is on globular state.

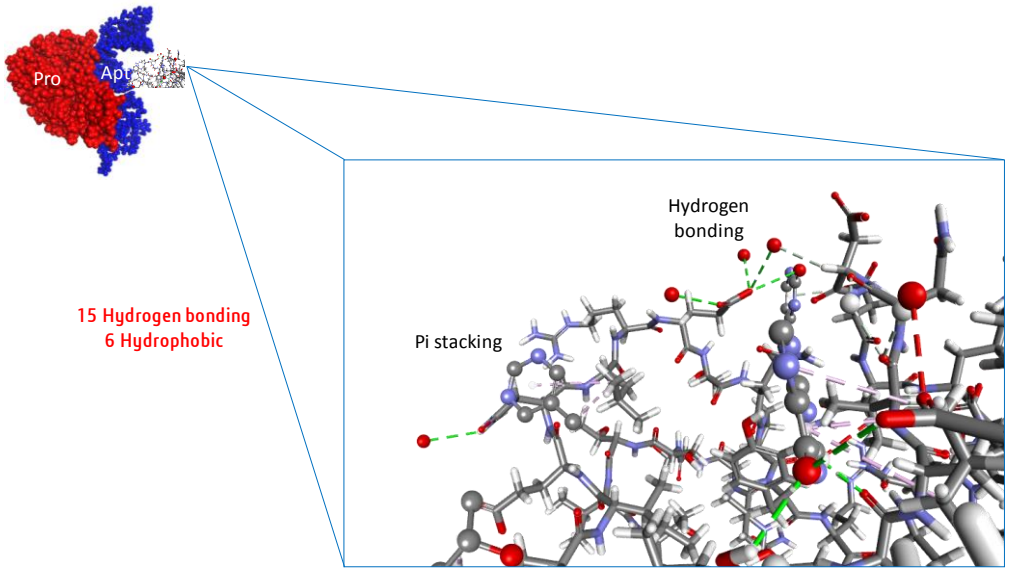

Figure 5.38 The interaction of the protein-aptamer in 310.7 K involving 15 hydrogen bonds and 6 hydrophobic interaction.

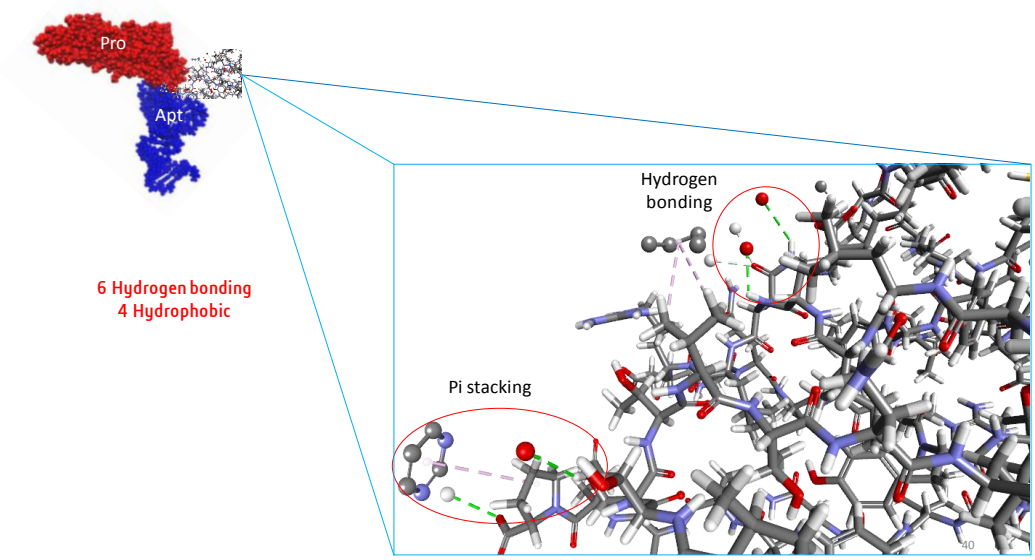

Figure 5.39 The interaction of the protein-aptamer in 298 K involving 6 hydrogen bonds and 4 hydrophobic interaction.

5.2 Experimental Studies

In this study, the experimental works have been done to further establish the PC3 whole-cell aptasensor based on the tunable surface properties. Electrochemical impedance spectroscopy (EIS) is one of the effective methods in monitoring the feature alteration taking place on the surface, particularly on the interface between solution and electrode surface. EIS allows to investigate the changes in capacitance or the properties of the solids resistance in electrolyte interface without giving destructive impact due to narrow range of potential application (Bayoudh et al., 2008). The Nyquist plot in higher frequencies is observed as semicircle portion corresponding to the limit process of electron transfer as well as linear portion representing the diffusion activity. This method has previously shown its excellence due to capabilities in quantifying the insulator characteristic of the living cells at low frequencies and their dielectrics at high frequencies (Katz and Willner, 2003). The active redox solution of $[Fe(CN)_6]^{3-/4-}$ was employed here as an electrochemical agent for the detection of the whole-cancer cells of PC3 target. The immobilized PNIPAM and other biomaterials present

on the electrode surface of EIS system hindered or potentially reduced the double layer capacitance and limited the kinetic transfer of electrons. The sensing performance was measured at ~37^{o}C relied on the construction of hierarchal-sandwich models which from bottom to top are glassy carbon electrode (GCE), GO/PNIPAM, Wy5a aptamer, PC3 cell, and Wy5a aptamer (GCE/GO-PNIPAM/APT/cell/APT).

The optimum aptamer concentration in this study was established and used for further experiments. When the aptamer was electrodeposited, the EIS exhibits a markedly increase in the charge transfer resistance higher than the GCE/GO-PNIPAM surface. This reflects the fact that original nature of negatively charged compositions of nucleobases and phosphate backbones of the Wy5a aptamer enables to induce the electronic repulsion toward the anionic probe thus, hindering the direct access on to the electrode surface. During the measurements, EIS exhibits the charge transfer resistance along with the concentration increase of the aptamers up to 4.0 μM (**Figure 5.40 (a)**). This optimum concentration was then employed in further experiments. The increase charge transfer phenomenon is due to the accumulation of negative charges of higher aptamer concentrations thus, increasing the electronic blockage of $[Fe(CN)_6]^{3-/4-}$ toward the electrode surface. Meanwhile, the intermolecular hybridization would be possibly amplified toward the complementary sections of aptamer when the concentrations were continued to increase more than 4.0 μM, thus resulted in decreasing the aptamer immobilization on the electrode surface. These results are confirmed by the error bars associated to the standard deviations from three independent biosensors (**Figure 5.40 (b)**).

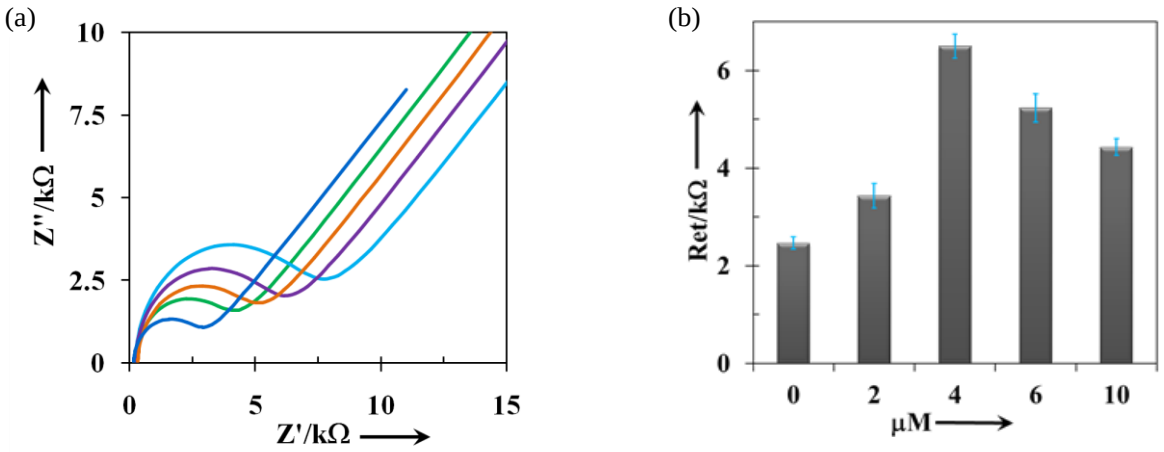

Figure 5.40 (a) Signal increases obtained with different concentration of Wy5a aptamer. EIS spectra for 0 µM (Blue), 2.0 µM (green), 4.0 µM (light blue), 6.0 µM (violet), and 10.0 µM (orange) aptamer. (b) The bar graph for different concentrations of Wy5a aptamer.

The incubation time of the PC3 cancer cells on the electrode surface were further optimized since it contributed great effect to the analytical performance. When the incubation time increased, more cells were adsorbed, therefore exhibiting the quenching efficiency. The EIS peaks result a profile of the optimum incubation time, showing more cells captured onto electrode surface along with the maximum resistance of electronic transfer during 2 h. Within this time, the maximum cells loading occurred and lengthier incubation times (~ 3 h) do not further impact the cell capture. Therefore, the incubation time of 2 h was chosen as the best time for the detection of PC3 cells (**Figure 5.41)**.

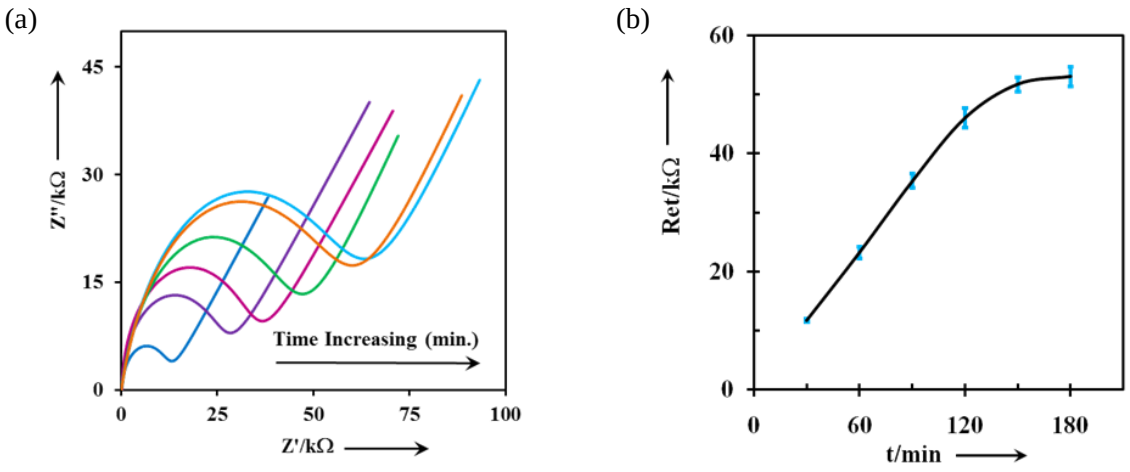

Figure 5.41 (a) Impedance spectra and (b) optimization graph for various incubation time of PC3 cell on the aptasensor surface; 30 (Blue), 60 (Violet), 90 (Purple), 120 (Green), 150 (Orange) and 180 min (Light blue).

Further, we conducted the Wy5a aptamer modified-tunable surface with the various concentrations of cells in order to signify the label-free performance of aptasensor using CV in 5×10^{-4} M $[Fe(CN)_6]^{3-}$ containing 0.1 M KCl solution. As shown in **Figure 5.42**, the spectra peaks of CV at scan rate 100 mV/s starts to decrease at the time the cell concentration introduced, up to concentration of $1.5x10^6$ cells/mL. This evidence is in accordance with the significantly decreases of the currents resulting higher separations of peak-to-peak potential (ΔE_p). The increase of the concentration of the PC3 cell decreases the peak of CV due to the kinetic barrier created between the redox probe and the cell which further correlates to higher content of PC3 cells deposited on the aptasensor. Since this is whole-cell model detection where electrode materials were hierarchal-assembled on the electrode surface and the application of aptamers as well as whole-cancer cells can influence the resistance of electronic transfer, therefore the most interactions are driven by electrostatic interactions.

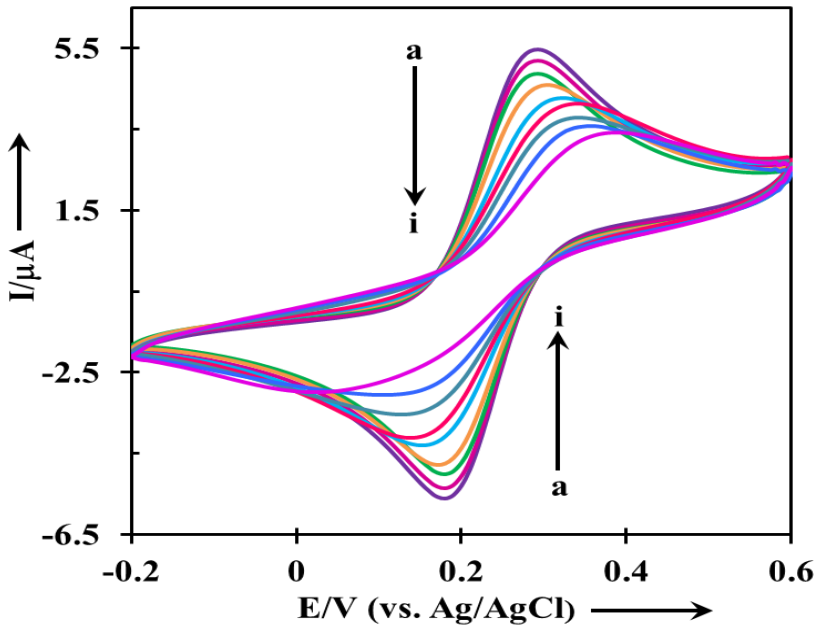

Figure 5.42 Cyclic voltammograms at 100 mV/s scan rate, (a-i) GCE/GO-PNIPAM/APT/cell/APT (0, 10, 0.5×10^2, 1×10^3, 1×10^4, 1×10^5, 5×10^5, 1×10^6 and 1.5×10^6 PC3 cells/mL).

The performance of the aptasensor is compared to the recent label-free biosensor reports using different transduction method. The limit detection obtained in this particular study is recognized lower than those previously reported (**Table 5.19**), showing that overall construction of biosensor is well-established for detection of PC3 cells.

Table 5.19 Comparison between the proposed aptasensor and other reported sensors for cancer cell detection.

Type of Cell	Technique	LOD (cells/mL)	Linearity Range	Ref.
MCF-7	Stripping voltammetry	26	-	(Zhu et al., 2012)
MCF-7	Voltammetry	100	1×10^2-1×10^7	(Zhu et al., 2013)
MCF-7	Fluorescence	500	5×10^2-5×10^6	(Zhao et al., 2012)
CCRF-CEM	Fluorescence	-	-	(Herr et al., 2006)
CCRF-CEM	QCM	800	1×10^4-1.5×10^5	(Pan et al., 2010)
CCRF-CEM	EIS	6,000	1×10^4-1×10^7	(Pan et al., 2009)
Ramos	ECL	50	-	(Ding et al., 2012)
Ramos	Stripping voltammetry	67	1×10^2-1×10^5	(Ding et al., 2010a)
Ramos	Microfluidic	800	4×10^3-2×10^5	(Liu et al., 2009)
LnCap	Microchip	1,000	-	(Kim et al., 2013)
PC3	**EIS**	**14**	**$0.5 \times 10^2 – 1.5 \times 10^6$**	**Present work**

5.2.1 Synergies between The Computational and Experimental Studies

The synergies found between the computational and experimental works are as follows: First, the computational models of PNIPAM monomer and GO molecules used within these studies are observed close to their real structural compositions confirmed by the similarity between theoretical characteristics of calculated Raman and IR and their results in the previous experimental works. These results showed that the constructed molecules of PNIPAM monomer and GO molecules could be employed as reliable models for the computational studies. In the experimental approach, functionalization of GO surface with the polymer was acquired to obtain a stable dispersity of GO (Liu et al., 2008, Bak et al., 2012, Gong et al., 2016). It is well known that grafting the polymer chains onto the GO surface can be afforded

by covalently linking through amide or esterification reactions (Dreyer et al., 2010, Lin et al., 2011, Deng et al., 2011). In this regard, the PNIPAM has been successfully conjugated with the carboxylic group of GO surface (Fang et al., 2009, Qi et al., 2012). The application of nucleobase on the GO/NIPAM surface decreased the energy gap of the initial GO/NIPAM surface, implying that the nucleobases donate the electronegativity reflected by more reactive interaction complex. This result is validated by the experiment where the EIS peaks increased the resistance upon the introduction of aptamer molecule onto the electrode. This is due to the electrostatic repulsion from the negatively charged aptamer toward the anionic redox probe.

The docking results clearly suggests that the best binding aptamer toward the α6β4 protein is Wy5a, in which this aptamer would further be applied as the biorecognition toward the PC3 whole-cancer cells in experimental works. In the experimental studies, this aptamer enabled the biosensor to detect the PCa cell down to 14 cells/mL, indicating a high-performance sensor system has been successfully fabricated. Further, the interaction between the aptamer and protein in the simulation also has been confirmed at above LCST, indicated by a lower energy interaction at 310.7 K (-1,916.79 kcal/mol) than that at 298 K (-796.88 kcal/mol). The results obtained are in accordance with the CV profile which explicates the decrease peak of the applied cells concentration measured at 310.7 K.

5.2.2 Conclusions

Herein, the first theoretical principle studies were employed to establish the electrical nature of PNIPAM along with other surface components using PNIPAM functionalization-enhanced properties. The presence of PNIPAM monomer tends to stabilize the system

interaction, which is confirmed by higher energy gap observed in nucleobase and GO/NIPAM complex than nucleobase and GO complex. Few alterations are also noticed in the bond length and angles of the carboxylic conjunction implicating the small perturbation occurred in its functionalization. These results further correlate to the fact that PNIPAM presence may possibly provide a tunable surface between the aptamer and protein without influencing the electroconductivity of the whole system. Whilst, the conductivity role is generally influenced by the approached-structural surface, such as GO in this case.

Most of the nucleobases do not interact with the GO and GO/NIPAM in parallel orientation. Conversely, their interaction complexes are mostly stabilized by hydrogen bonding between the nucleobase atoms and the oxygen functional groups of GO. The trend of binding strengths of nucleobases-GO complexes is G>A>T>C, which is in a good agreement with the previous studies. On the other hand, the order of binding strengths of the nucleobases and GO/NIPAM complexes is T>G>C>A. Further, the presence of PNIPAM monomer reduces the adsorption energy of the nucleobases on the GO surface within the range of negative eigenvalue, suggesting that the original properties of PNIPAM is favorable to be used in a biosensor application, since its presence may possibly stabilize and support the entire elements of the biosensor. Most of their interaction cases do not alter the geometrical structures of the surface entities, in which contemplates the physisorption characteristic behind the interaction nature between nucleobase and GO/NIPAM surface.

The results of the docking studies suggest that the best binding aptamer toward the α6β4 protein belongs to the Wy5a aptamer, in which case aptamer would further be applied as the biorecognition toward the PC3 whole-cancer cells in experimental works. This is due to the

lowest ZRANK score, higher number of H-bonds and contact area, and the presence of hydrophobic contacts involved in the interaction with the protein. Further, the results reveal that Wy5a contains the active binding sites incorporating the protein represented by the active residues involved in the interaction. This confirms that the selectivity of the aptamer binding to the α6β4. The thermal-responsive of PNIPAM-grafted GO surface has successfully been simulated using MD simulations and the PNIPAM can induce an "on" or "off" surface-states in response to the temperature changes around its LCST. This behavior has been benefitted for further investigation of the aptamer and protein interaction, which ensues stronger interaction observed at 310.7 K rather than 298 K.

In the experimental section, it is worth to mentioning that the presence of the PNIPAM molecule in GO based aptasensor do not conduct significant electronic properties which is shown by the absence of electroactive peaks on the cyclic voltammogram. The application of aptamer concentration increases the repulsion activities toward the redox probes on the electrode surface, due to the accumulation of negative charges of the aptamer and the phosphate backbone contents, thus exhibiting a charge transfer in EIS evaluation. The limit of detection shown by CV measurements showed that this whole-cell aptasensor enables the recognition of the PC3 cells as low as 14 cells/mL.

CHAPTER 6

CONCLUDING REMARKS AND FUTURE PERSPECTIVES

6.1 Concluding Remarks

In summary, the electrochemical aptamer-based biosensor for the detection of PCa cells have been characterized through computational studies i.e. density functional theory (DFT), molecular docking, and molecular dynamics (MD) simulations, in agreement with biosensor works using electrochemical impedance spectroscopy (EIS) and cyclic voltammetry (CV). Herein, the concept is that the presence of poly-(*N*-isopropylacrylamide) (PNIPAM) is substantial for exhibiting a tunable surface during the sensing mechanism, thus undergoes an interaction between the aptamer and the whole-cancer cell. The DFT calculations exhibit an understanding of the energetics and electronic behavior at the molecular level of the simplest constructions of PNIPAM-associated biosensing surface.

The optical calculations showed that the constructed structures of GO and PNIPAM monomer have similar profiles with the previous optical experimental studies, suggesting that the structures are fairly reliable for further theoretical calculations. In general, the presence of PNIPAM monomer has a role in stabilizing the surface interaction complex between the GO and the nucleobases molecules, confirmed by negative eigenvalue of adsorption energies and higher energy gaps as compared to the complex of unfunctionalized-GO and nucleobases molecules. Further, the Wy5a aptamer has been selected as the best binding aptamer based on docking-scores and bond-parameters among other aptamer candidates toward the α6β4 protein. Accordingly, the Wy5a aptamer used for further MD simulations along with the target proteins have successfully been accomplished in describing

the thermal-responsive PNIPAM-grafted GO in a solvent system at below and above LCST. This promising property benefits to undergo the tunable function in further MD simulations of aptamer-protein interactions in complete molecular system comprising of GO surface, PNIPAMs, Wy5a aptamer, and α6β4 protein.

Further, biosensor applications have been investigated using EIS techniques. EIS employs a narrow small range of potential current therefore, it is suitable in designing a non-destructive electrochemical method. In this study, the detection using aptamer-based tunable biosensor has been carried out in whole-cancer cells of PC3. The sensing construction of the surface electrode has the similar components with those in MD and further confirm the similar characteristics of surface conductivity with those established in the DFT studies. The optimum aptamer concentration for effective binding at 310.7 K is found to be 4.0 μM while the finest incubation time for cell application time is 2 h. The specific and high-affinity interaction between the whole-cancer cell of PCa with the Wy5a aptamer is as low as 14 cells/mL, showing high performance results of PCa whole-cells detection among the previous reported methods. By integrating the computational and experimental works in designing biosensor system, the structural energetics as well as the electronic properties have been well-described and high performance of tunable biosensing have been successfully fabricated.

6.2 Future Perspectives

The future works could be directed toward experimental characterization of tunable surface in different temperatures as well as conducting the interference study using real biological sample. The use of biodegradable and biocompatible nanopolymer i.e. chitosan (Putri et al.,

2017) may be beneficial to increase the immunosensor performance toward complying point-of-care diagnosis of prostate cancer.

REFERENCES

ABBASI, A. & JAHANBIN SARDROODI, J. 2016. N-doped TiO2 anatase nanoparticles as a highly sensitive gas sensor for NO2 detection: insights from DFT computations. *Environmental Science: Nano,* 3**,** 1153-1164.

AHIRWAR, R., NAHAR, S., AGGARWAL, S., RAMACHANDRAN, S., MAITI, S. & NAHAR, P. 2016. In silico selection of an aptamer to estrogen receptor alpha using computational docking employing estrogen response elements as aptamer-alike molecules. *Scientific Reports,* 6.

AHMED, E. M. 2015. Hydrogel: Preparation, characterization, and applications: A review. *Journal of Advanced Research,* 6**,** 105-121.

ALLEN, M. P. 2004. Introduction to molecular dynamics simulation. *Computational soft matter: from synthetic polymers to proteins,* 23**,** 1-28.

ALMEIDA, M. O., MALTAROLLO, V. G., DE TOLEDO, R. A., SHIM, H., SANTOS, M. C. & HONORIO, K. M. 2014. Medicinal electrochemistry: integration of electrochemistry, medicinal chemistry and computational chemistry. *Current Medicinal Chemistry,* 21**,** 2266-75.

ALVAREZ, M. & LECHUGA, L. M. 2010. Microcantilever-based platforms as biosensing tools. *Analyst,* 135**,** 827-36.

ALZARI, V., NUVOLI, D., SCOGNAMILLO, S., PICCININI, M., GIOFFREDI, E., MALUCELLI, G., MARCEDDU, S., SECHI, M., SANNA, V. & MARIANI, A. 2011. Graphene-containing thermoresponsive nanocomposite hydrogels of poly (N-isopropylacrylamide) prepared by frontal polymerization. *Journal of Materials Chemistry,* 21**,** 8727-8733.

AMBROSI, A., BONANNI, A., SOFER, Z., CROSS, J. S. & PUMERA, M. 2011. Electrochemistry at Chemically Modified Graphenes. *Chemistry – A European Journal,* 17**,** 10763-10770.

AMERICAN CANCER SOCIETY 2011. Cancer Facts & Figures. *American Cancer Society*.

AMERICAN CANCER SOCIETY 2016. Cancer Facts & Figures 2016. *American Cancer Society*.

ANDERSON, D. G., BURDICK, J. A. & LANGER, R. 2004. Smart biomaterials. *Science,* 305**,** 1923-1924.

ANISIMOV, V. N. 2007. Biology of aging and cancer. *Cancer Control,* 14**,** 23-31.

ANONYM 1996. Clinical practice guidelines for the use of tumor markers in breast and colorectal cancer. Adopted on May 17, 1996 by the American Society of Clinical Oncology. *Journal of Clinical Oncology,* 14**,** 2843-77.

ANTONY, J. & GRIMME, S. 2008. Structures and interaction energies of stacked graphene–nucleobase complexes. *Physical Chemistry Chemical Physics,* 10**,** 2722-2729.

ARGYRIS, D., TUMMALA, N. R., STRIOLO, A. & COLE, D. R. 2008. Molecular structure and dynamics in thin water films at the silica and graphite surfaces. *The Journal of Physical Chemistry C,* 112**,** 13587-13599.

ARYA, S. K. & BHANSALI, S. 2011. Lung Cancer and Its Early Detection Using Biomarker-Based Biosensors. *Chemical Reviews,* 111**,** 6783-6809.

BAADE, P. D., YOULDEN, D. R. & KRNJACKI, L. J. 2009. International epidemiology of prostate cancer: geographical distribution and secular trends. *Molecular Nutrition & Food Research,* 53**,** 171-84.

BAGALKOT, V., ZHANG, L., LEVY-NISSENBAUM, E., JON, S., KANTOFF, P. W., LANGER, R. & FAROKHZAD, O. C. 2007. Quantum Dot−Aptamer Conjugates for Synchronous Cancer Imaging, Therapy, and Sensing of Drug Delivery Based on Bi-Fluorescence Resonance Energy Transfer. *Nano Letters,* 7**,** 3065-3070.

BAI, Z., LI, G., LIANG, J., SU, J., ZHANG, Y., CHEN, H., HUANG, Y., SUI, W. & ZHAO, Y. 2016. Non-enzymatic electrochemical biosensor based on Pt NPs/RGO-CS-Fc nano-hybrids for the detection of hydrogen peroxide in living cells. *Biosensors and Bioelectronics,* 82**,** 185-194.

BAK, J. M., LEE, T., SEO, E., LEE, Y., JEONG, H. M., KIM, B.-S. & LEE, H.-I. 2012. Thermoresponsive graphene nanosheets by functionalization with polymer brushes. *Polymer,* 53**,** 316-323.

BASIL, C. F., ZHAO, Y., ZAVAGLIA, K., JIN, P., PANELLI, M. C., VOICULESCU, S., MANDRUZZATO, S., LEE, H. M., SELIGER, B., FREEDMAN, R. S., TAYLOR, P. R., HU, N., ZANOVELLO, P., MARINCOLA, F. M. & WANG, E. 2006. Common cancer biomarkers. *Cancer Research,* 66**,** 2953-61.

BASIUK, E. V., MARTÍNEZ-HERRERA, M., ÁLVAREZ-ZAUCO, E., HENAO-HOLGUÍN, L. V., PUENTE-LEE, I. & BASIUK, V. A. 2014. Noncovalent functionalization of graphene with a Ni (II) tetraaza [14] annulene complex. *Dalton Transactions,* 43**,** 7413-7428.

BAWEJA, L., BALAMURUGAN, K., SUBRAMANIAN, V. & DHAWAN, A. 2015. Effect of graphene oxide on the conformational transitions of amyloid beta peptide: A molecular dynamics simulation study. *Journal of Molecular Graphics & Modelling,* 61**,** 175-185.

BAYOUDH, S., OTHMANE, A., PONSONNET, L. & OUADA, H. B. 2008. Electrical detection and characterization of bacterial adhesion using electrochemical impedance spectroscopy-based flow chamber. *Colloids and Surfaces A: physicochemical and engineering aspects,* 318**,** 291-300.

BECKE, A. D. 1988. Density-functional exchange-energy approximation with correct asymptotic behavior. *Physical review A,* 38**,** 3098.

BECKER, C., PIIRONEN, T., PETTERSSON, K., HUGOSSON, J. & LILJA, H. 2000. Clinical value of human glandular kallikrein 2 and free and total prostate-specific antigen in serum from a population of men with prostate-specific antigen levels 3.0 ng/mL or greater. *Urology,* 55**,** 694-9.

BENEDEK, N., SNOOK, I., LATHAM, K. & YAROVSKY, I. 2005. Application of numerical basis sets to hydrogen bonded systems: a density functional theory study. *The Journal of chemical physics,* 122**,** 144102.

BERG, K., LANGE, T., MITTELBERGER, F., SCHUMACHER, U. & HAHN, U. 2016. Selection and Characterization of an alpha6beta4 Integrin blocking DNA Aptamer. *Molecular Therapy. Nucleic Acids,* 5**,** e294.

BHATIA, P. & GUPTA, B. D. 2011. Surface-plasmon-resonance-based fiber-optic refractive index sensor: sensitivity enhancement. *Appl Opt,* 50**,** 2032-6.

BIKARD, D., LOOT, C., BAHAROGLU, Z. & MAZEL, D. 2010. Folded DNA in action: hairpin formation and biological functions in prokaryotes. *Microbiology and Molecular Biology Reviews,* 74**,** 570-588.

BING, T., YANG, X. J., MEI, H. C., CAO, Z. H. & SHANGGUAN, D. H. 2010. Conservative secondary structure motif of streptavidin-binding aptamers generated by different laboratories. *Bioorganic & Medicinal Chemistry,* 18**,** 1798-1805.

BINKLEY, J. S., POPLE, J. A. & HEHRE, W. J. 1980. Self-consistent molecular orbital methods. 21. Small split-valence basis sets for first-row elements. *Journal of the American Chemical Society,* 102**,** 939-947.

BIOVIA, D. S. 2016. Material Studio Modelling. 8.0 ed. San Diego : Dassault Systemes.

BLOBEL, C. P. 2005. ADAMs: key components in EGFR signalling and development. *Nat Rev Mol Cell Biol,* 6**,** 32-43.

BOHUNICKY, B. & MOUSA, S. A. 2010. Biosensors: the new wave in cancer diagnosis. *Nanotechnology, Science and Applications,* 4**,** 1-10.

BONACCORSI, L., CARLONI, V., MURATORI, M., FORMIGLI, L., ZECCHI, S., FORTI, G. & BALDI, E. 2004. EGF receptor (EGFR) signaling promoting invasion is disrupted in

androgen-sensitive prostate cancer cells by an interaction between EGFR and androgen receptor (AR). *Int J Cancer,* 112**,** 78-86.
BONACCORSI, L., CARLONI, V., MURATORI, M., SALVADORI, A., GIANNINI, A., CARINI, M., SERIO, M., FORTI, G. & BALDI, E. 2000. Androgen Receptor Expression in Prostate Carcinoma Cells Suppresses α6β4 Integrin-Mediated Invasive Phenotype*. *Endocrinology,* 141**,** 3172-3182.
BOYS, S. F. Electronic wave functions. I. A general method of calculation for the stationary states of any molecular system. Proceedings of the Royal Society of London A: Mathematical, Physical and Engineering Sciences, 1950. The Royal Society, 542-554.
BRADFORD, T. J., TOMLINS, S. A., WANG, X. & CHINNAIYAN, A. M. 2006. Molecular markers of prostate cancer. *Urologic Oncology,* 24**,** 538-51.
BRAWER, M. K., CHETNER, M. P., BEATIE, J., BUCHNER, D. M., VESSELLA, R. L. & LANGE, P. H. 1992. Screening for prostatic carcinoma with prostate specific antigen. *Journal of Urology,* 147**,** 841-5.
BROOKS, B. R., BRUCCOLERI, R. E., OLAFSON, B. D., STATES, D. J., SWAMINATHAN, S. & KARPLUS, M. 1983. CHARMM: A program for macromolecular energy, minimization, and dynamics calculations. *Journal of Computational Chemistry,* 4**,** 187-217.
BUCHSTEINER, A., LERF, A. & PIEPER, J. 2006. Water dynamics in graphite oxide investigated with neutron scattering. *The Journal of Physical Chemistry B,* 110**,** 22328-22338.
BURDA, C., CHEN, X., NARAYANAN, R. & EL-SAYED, M. A. 2005. Chemistry and properties of nanocrystals of different shapes. *Chem Rev,* 105**,** 1025-102.
CALIENDO, A. M., GILBERT, D. N., GINOCCHIO, C. C., HANSON, K. E., MAY, L., QUINN, T. C., TENOVER, F. C., ALLAND, D., BLASCHKE, A. J., BONOMO, R. A., CARROLL, K. C., FERRARO, M. J., HIRSCHHORN, L. R., JOSEPH, W. P., KARCHMER, T., MACINTYRE, A. T., RELLER, L. B., JACKSON, A. F. & AMERICA, F. T. I. D. S. O. 2013. Better Tests, Better Care: Improved Diagnostics for Infectious Diseases. *Clinical Infectious Diseases,* 57**,** S139-S170.
CAMPBELL, S. B., PATENAUDE, M. & HOARE, T. 2013. Injectable superparamagnets: highly elastic and degradable poly (N-isopropylacrylamide)–superparamagnetic iron oxide nanoparticle (SPION) composite hydrogels. *Biomacromolecules,* 14**,** 644-653.
CATALONA, W. J., SMITH, D. S. & ORNSTEIN, D. K. 1997. Prostate cancer detection in men with serum PSA concentrations of 2.6 to 4.0 ng/mL and benign prostate examination. Enhancement of specificity with free PSA measurements. *Journal of the American Medical Association,* 277**,** 1452-5.
CENTER, M. M., JEMAL, A., LORTET-TIEULENT, J., WARD, E., FERLAY, J., BRAWLEY, O. & BRAY, F. 2012. International Variation in Prostate Cancer Incidence and Mortality Rates. *European Urology,* 61**,** 1079-1092.
CERCHIA, L. & DE FRANCISCIS, V. 2010. Targeting cancer cells with nucleic acid aptamers. *Trends Biotechnol,* 28**,** 517-25.
CHANG, S. S. 2004. Overview of Prostate-Specific Membrane Antigen. *Rev Urol,* 6**,** S13-8.
CHE, Y., DATAR, A., BALAKRISHNAN, K. & ZANG, L. 2007. Ultralong nanobelts self-assembled from an asymmetric perylene tetracarboxylic diimide. *Journal of the American Chemical Society,* 129**,** 7234-7235.
CHEN, R., LI, L. & WENG, Z. P. 2003. ZDOCK: An initial-stage protein-docking algorithm. *Proteins-Structure Function and Genetics,* 52**,** 80-87.
CHEN, R., PAN, S., YI, E. C., DONOHOE, S., BRONNER, M. P., POTTER, J. D., GOODLETT, D. R., AEBERSOLD, R. & BRENTNALL, T. A. 2006. Quantitative proteomic profiling of pancreatic cancer juice. *PROTEOMICS,* 6**,** 3871-3879.
CHEN, X., XU, S., YAO, N. & SHI, Y. 2010. 1.6 V nanogenerator for mechanical energy harvesting using PZT nanofibers. *Nano Lett,* 10**,** 2133-7.

CHERMAHINI, A. N., TEIMOURI, A. & FARROKHPOUR, H. 2015. A DFT-D study on the interaction between lactic acid and single-wall carbon nanotubes. *RSC Advances,* 5**,** 97724-97733.

CHIEN, F. C. & CHEN, S. J. 2004. A sensitivity comparison of optical biosensors based on four different surface plasmon resonance modes. *Biosens Bioelectron,* 20**,** 633-42.

CHO, Y., MIN, S. K., YUN, J., KIM, W. Y., TKATCHENKO, A. & KIM, K. S. 2013. Noncovalent interactions of DNA bases with naphthalene and graphene. *Journal of Chemical Theory and Computation,* 9**,** 2090-2096.

CHOVIN, A., GARRIGUE, P. & SOJIC, N. 2004. Electrochemiluminescent detection of hydrogen peroxide with an imaging sensor array. *Electrochimica Acta,* 49**,** 3751-3757.

CHTITA, S., LARIF, M., GHAMALI, M., ADAD, A., RACHID, S., BOUACHRINE, M. & LAKHLIFI, T. 2013. Studies of two different cancer cell lines activities (MDAMB-231 and SK-N-SH) of imidazo[1,2-a]pyrazine derivatives by combining DFT and QSAR results. *International Journal of Innovative Research in Science, Engineering and Technology,* 2**,** 16.

CHUNG, C., KIM, Y.-K., SHIN, D., RYOO, S.-R., HONG, B. H. & MIN, D.-H. 2013. Biomedical applications of graphene and graphene oxide. *Accounts of chemical research,* 46**,** 2211-2224.

COOPERBERG, M. R., LUBECK, D. P., MEHTA, S. S., CARROLL, P. R. & CAPSURE 2003. Time trends in clinical risk stratification for prostate cancer: implications for outcomes (data from CaPSURE). *Journal of Urology,* 170**,** S21-5; discussion S26-7.

CRAMER, C. J. 2013. *Essentials of computational chemistry: theories and models,* John Wiley & Sons.

CREMER, D. & HE, Z. 1996. Sixth-Order Møller− Plesset Perturbation Theory On the Convergence of the MP n Series. *The Journal of Physical Chemistry,* 100**,** 6173-6188.

CRESS, A. E., RABINOVITZ, I., ZHU, W. & NAGLE, R. B. 1995. The α6β1 and α6β4 integrins in human prostate cancer progression. *Cancer and Metastasis Reviews,* 14**,** 219-228.

CUENOT, S., FRÉTIGNY, C., DEMOUSTIER-CHAMPAGNE, S. & NYSTEN, B. 2004. Surface tension effect on the mechanical properties of nanomaterials measured by atomic force microscopy. *Physical Review B,* 69**,** 165410.

CUNHA, A. C., WEIGLE, B., KIESSLING, A., BACHMANN, M. & RIEBER, E. P. 2006. Tissue-specificity of prostate specific antigens: comparative analysis of transcript levels in prostate and non-prostatic tissues. *Cancer Letters,* 236**,** 229-38.

D'HAESELEER, P. 2006. What are DNA sequence motifs? *Nat Biotechnol,* 24**,** 423-5.

DAS, J., CEDERQUIST, K. B., ZARAGOZA, A. A., LEE, P. E., SARGENT, E. H. & KELLEY, S. O. 2012. An ultrasensitive universal detector based on neutralizer displacement. *Nature Chemistry,* 4**,** 642-648.

DASSIE, J. P., HERNANDEZ, L. I., THOMAS, G. S., LONG, M. E., ROCKEY, W. M., HOWELL, C. A., CHEN, Y., HERNANDEZ, F. J., LIU, X. Y., WILSON, M. E., ALLEN, L. A., VAENA, D. A., MEYERHOLZ, D. K. & GIANGRANDE, P. H. 2014. Targeted inhibition of prostate cancer metastases with an RNA aptamer to prostate-specific membrane antigen. *Mol Ther,* 22**,** 1910-22.

DAVIDSON, E. R. & FELLER, D. 1986. Basis set selection for molecular calculations. *Chemical Reviews,* 86**,** 681-696.

DE MARZO, A. M., PLATZ, E. A., SUTCLIFFE, S., XU, J., GRONBERG, H., DRAKE, C. G., NAKAI, Y., ISAACS, W. B. & NELSON, W. G. 2007. Inflammation in prostate carcinogenesis. *Nature Reviews Cancer,* 7**,** 256-69.

DE PEREDA, J. M., WICHE, G. & LIDDINGTON, R. C. 1999. Crystal structure of a tandem pair of fibronectin type III domains from the cytoplasmic tail of integrin alpha 6 beta 4. *Embo Journal,* 18**,** 4087-4095.

DELLEY, B. 1990. An all-electron numerical method for solving the local density functional for polyatomic molecules. *The Journal of chemical physics,* 92**,** 508-517.
DELONGCHAMPS, N. B., SINGH, A. & HAAS, G. P. 2007. Epidemiology of prostate cancer in Africa: another step in the understanding of the disease? *Curr Probl Cancer,* 31**,** 226-36.
DENG, Y., LI, Y., DAI, J., LANG, M. & HUANG, X. 2011. An efficient way to functionalize graphene sheets with presynthesized polymer via ATNRC chemistry. *Journal of Polymer Science Part A: Polymer Chemistry,* 49**,** 1582-1590.
DEY, D. & GOSWAMI, T. 2011. Optical Biosensors: A Revolution Towards Quantum Nanoscale Electronics Device Fabrication. *Journal of Biomedicine and Biotechnology,* 2011**,** 7.
DHAR, S., LIU, Z., THOMALE, J., DAI, H. & LIPPARD, S. J. 2008. Targeted single-wall carbon nanotube-mediated Pt(IV) prodrug delivery using folate as a homing device. *J Am Chem Soc,* 130**,** 11467-76.
DHARMASIRI, U., BALAMURUGAN, S., ADAMS, A. A., OKAGBARE, P. I., OBUBUAFO, A. & SOPER, S. A. 2009. Highly efficient capture and enumeration of low abundance prostate cancer cells using prostate-specific membrane antigen aptamers immobilized to a polymeric microfluidic device. *Electrophoresis,* 30**,** 3289-300.
DHIR, R., VIETMEIER, B., ARLOTTI, J., ACQUAFONDATA, M., LANDSITTEL, D., MASTERSON, R. & GETZENBERG, R. H. 2004. Early identification of individuals with prostate cancer in negative biopsies. *Journal of Urology,* 171**,** 1419-23.
DI VENTURA, B., LEMERLE, C., MICHALODIMITRAKIS, K. & SERRANO, L. 2006. From in vivo to in silico biology and back. *Nature,* 443**,** 527-33.
DIGIUSEPPE, J. A., SAUVAGEOT, J. & EPSTEIN, J. I. 1997. Increasing incidence of minimal residual cancer in radical prostatectomy specimens. *The American Journal of Surgical Pathology,* 21**,** 174-8.
DIMAKAKOS, A., ARMAKOLAS, A. & KOUTSILIERIS, M. 2014. Novel tools for prostate cancer prognosis, diagnosis, and follow-up. *BioMed Research International,* 2014**,** 890697.
DING, C., GE, Y. & ZHANG, S. 2010a. Electrochemical and Electrochemiluminescence Determination of Cancer Cells Based on Aptamers and Magnetic Beads. *Chemistry – A European Journal,* 16**,** 10707-10714.
DING, C., GE, Y. & ZHANG, S. 2010b. Electrochemical and electrochemiluminescence determination of cancer cells based on aptamers and magnetic beads. *Chemistry,* 16**,** 10707-14.
DING, C., ZHENG, Q., WANG, N. & YUE, Q. 2012. An electrochemiluminescence strategy based on aptamers and nanoparticles for the detection of cancer cells. *Analytica Chimica Acta,* 756**,** 73-78.
DING, N., CHEN, X. & WU, C.-M. L. 2014. Interactions between polybrominated diphenyl ethers and graphene surface: a DFT and MD investigation. *Environmental Science: Nano,* 1**,** 55-63.
DING, N., CHEN, X. F., WU, C. M. L. & LI, H. 2013. Adsorption of nucleobase pairs on hexagonal boron nitride sheet: hydrogen bonding versus stacking. *Physical Chemistry Chemical Physics,* 15**,** 10767-10776.
DJORDJEVIC, M. 2007. SELEX experiments: new prospects, applications and data analysis in inferring regulatory pathways. *Biomol Eng,* 24**,** 179-89.
DOBBS, K. & HEHRE, W. 1986. Molecular orbital theory of the properties of inorganic and organometallic compounds 4. Extended basis sets for third-and fourth-row, main-group elements. *Journal of computational chemistry,* 7**,** 359-378.
DOBBS, K. & HEHRE, W. 1987a. Molecular orbital theory of the properties of inorganic and organometallic compounds 5. Extended basis sets for first-row transition metals. *Journal of Computational Chemistry,* 8**,** 861-879.

DOBBS, K. D. & HEHRE, W. 1987b. Molecular orbital theory of the properties of inorganic and organometallic compounds. 6. Extended basis sets for second-row transition metals. *Journal of computational chemistry,* 8**,** 880-893.
DOERR, A. 2011. Imaging impedance. *Nature Methods,* 8**,** 202-202.
DONG, H., GAO, W., YAN, F., JI, H. & JU, H. 2010. Fluorescence resonance energy transfer between quantum dots and graphene oxide for sensing biomolecules. *Analytical chemistry,* 82**,** 5511-5517.
DOUGLAS, T. H., MORGAN, T. O., MCLEOD, D. G., MOUL, J. W., MURPHY, G. P., BARREN, R., 3RD, SESTERHENN, I. A. & MOSTOFI, F. K. 1997. Comparison of serum prostate specific membrane antigen, prostate specific antigen, and free prostate specific antigen levels in radical prostatectomy patients. *Cancer,* 80**,** 107-14.
DOWNWARD, J. 2003. Targeting RAS signalling pathways in cancer therapy. *Nat Rev Cancer,* 3**,** 11-22.
DREYER, D. R., PARK, S., BIELAWSKI, C. W. & RUOFF, R. S. 2010. The chemistry of graphene oxide. *Chemical Society Reviews,* 39**,** 228-240.
DRUMMOND, T. G., HILL, M. G. & BARTON, J. K. 2003. Electrochemical DNA sensors. *Nature Biotechnology,* 21**,** 1192-1199.
DU, H. B., WICKRAMASINGHE, R. & QIAN, X. H. 2010. Effects of Salt on the Lower Critical Solution Temperature of Poly (N-Isopropylacrylamide). *Journal of Physical Chemistry B,* 114**,** 16594-16604.
DUFFY, M. J. 2002. Urokinase-type plasminogen activator: a potent marker of metastatic potential in human cancers. *Biochemical Society Transactions,* 30**,** 207-10.
DUNNING JR, T. H. 1970. Gaussian basis functions for use in molecular calculations. I. Contraction of (9s5p) atomic basis sets for the first-row atoms. *The Journal of Chemical Physics,* 53**,** 2823-2833.
DUNNING, T. 1970. Gaussian basis functions for use in molecular calculations. Contraction of (12s9p) atomic basis sets for the second row atoms. *Chemical Physics Letters,* 7**,** 423-427.
DYBAL, J., TRCHOVÁ, M. & SCHMIDT, P. 2009. The role of water in structural changes of poly(N-isopropylacrylamide) and poly(N-isopropylmethacrylamide) studied by FTIR, Raman spectroscopy and quantum chemical calculations. *Vibrational Spectroscopy,* 51**,** 44-51.
EDUARDO, V. C., NOVOSELOV, K. S., MOROZOV, S. V., PERES, N. M. R., SANTOS, J. M. B. L. D., JOHAN, N., GUINEA, F., GEIM, A. K. & NETO, A. H. C. 2010. Electronic properties of a biased graphene bilayer. *Journal of Physics: Condensed Matter,* 22**,** 175503.
ERDILE, L. F., SMITH, D. & BERD, D. 2001. Whole cell ELISA for detection of tumor antigen expression in tumor samples. *Journal of Immunological Methods,* 258**,** 47-53.
ESTEVE, A., BAIL, A., LANDA, G., DKHISSI, A., BRUT, M., ROUHANI, M. D., SUDOR, J. & GUE, A. M. 2007. A new insight into the understanding of poly(N-isopropylacrylamide) the collapsed form of molecules. *Chemical Physics,* 340**,** 12-16.
ETAYASH, H., JIANG, K., AZMI, S., THUNDAT, T. & KAUR, K. 2015. Real-time Detection of Breast Cancer Cells Using Peptide-functionalized Microcantilever Arrays. *Sci Rep,* 5**,** 13967.
FAN, X., WHITE, I. M., SHOPOVA, S. I., ZHU, H., SUTER, J. D. & SUN, Y. 2008. Sensitive optical biosensors for unlabeled targets: A review. *Analytica Chimica Acta,* 620**,** 8-26.
FANG, M., WANG, K., LU, H., YANG, Y. & NUTT, S. 2009. Covalent polymer functionalization of graphene nanosheets and mechanical properties of composites. *Journal of Materials Chemistry,* 19**,** 7098-7105.
FANG, X. & TAN, W. 2010. Aptamers generated from cell-SELEX for molecular medicine: a chemical biology approach. *Acc Chem Res,* 43**,** 48-57.
FARIMANI, A. B., MIN, K. & ALURU, N. R. 2014. DNA Base Detection Using a Single-Layer MoS2. *ACS Nano,* 8**,** 7914-7922.

FAUCETT, A. C. & MATIVETSKY, J. M. 2015. Nanoscale reduction of graphene oxide under ambient conditions. *Carbon,* 95**,** 1069-1075.
FERLAY, J., SOERJOMATARAM, I., DIKSHIT, R., ESER, S., MATHERS, C., REBELO, M., PARKIN, D. M., FORMAN, D. & BRAY, F. 2015. Cancer incidence and mortality worldwide: Sources, methods and major patterns in GLOBOCAN 2012. *International Journal of Cancer,* 136**,** E359-E386.
FORESMAN, J. B. & FRISCH, Æ. 1996. Exploring chemistry with electronic structure methods: a guide to using Gaussian.
FRISCH, M. J., TRUCKS, G. W., SCHLEGEL, H. B., SCUSERIA, G. E., ROBB, M. A., CHEESEMAN, J. R., SCALMANI, G., BARONE, V., MENNUCCI, B., PETERSSON, G. A., NAKATSUJI, H., CARICATO, M., LI, X., HRATCHIAN, H. P., IZMAYLOV, A. F., BLOINO, J., ZHENG, G., SONNENBERG, J. L., HADA, M., EHARA, M., TOYOTA, K., FUKUDA, R., HASEGAWA, J., ISHIDA, M., NAKAJIMA, T., HONDA, Y., KITAO, O., NAKAI, H., VREVEN, T., MONTGOMERY JR., J. A., PERALTA, J. E., OGLIARO, F., BEARPARK, M. J., HEYD, J., BROTHERS, E. N., KUDIN, K. N., STAROVEROV, V. N., KOBAYASHI, R., NORMAND, J., RAGHAVACHARI, K., RENDELL, A. P., BURANT, J. C., IYENGAR, S. S., TOMASI, J., COSSI, M., REGA, N., MILLAM, N. J., KLENE, M., KNOX, J. E., CROSS, J. B., BAKKEN, V., ADAMO, C., JARAMILLO, J., GOMPERTS, R., STRATMANN, R. E., YAZYEV, O., AUSTIN, A. J., CAMMI, R., POMELLI, C., OCHTERSKI, J. W., MARTIN, R. L., MOROKUMA, K., ZAKRZEWSKI, V. G., VOTH, G. A., SALVADOR, P., DANNENBERG, J. J., DAPPRICH, S., DANIELS, A. D., FARKAS, Ö., FORESMAN, J. B., ORTIZ, J. V., CIOSLOWSKI, J. & FOX, D. J. 2009. Gaussian 09. Wallingford, CT, USA: Gaussian, Inc.
FRITZ, J. 2008. Cantilever biosensors. *Analyst,* 133**,** 855-63.
GABA, M., GABA, P., SINGH, S. & GUPTA, G. 2010. An overview on molecular docking. *Int J Drug Dev Res,* 2**,** 219-31.
GABB, H. A., JACKSON, R. M. & STERNBERG, M. J. E. 1997. Modelling protein docking using shape complementarity, electrostatics and biochemical information. *Journal of Molecular Biology,* 272**,** 106-120.
GAO, H. & LIU, Z. 2017. DFT study of NO adsorption on pristine graphene. *RSC Advances,* 7**,** 13082-13091.
GARGALLO, R., HÜNENBERGER, P. H., AVILÉS, F. X. & OLIVA, B. 2003. Molecular dynamics simulation of highly charged proteins: Comparison of the particle-particle particle-mesh and reaction field methods for the calculation of electrostatic interactions. *Protein Sci,* 12**,** 2161-72.
GHOSSEIN, R. A. & BHATTACHARYA, S. 2000. Molecular detection and characterisation of circulating tumour cells and micrometastases in solid tumours. *Eur J Cancer,* 36**,** 1681-94.
GIRIFALCO, L. A. & HODAK, M. 2002. Van der Waals binding energies in graphitic structures. *Physical Review B,* 65**,** 125404.
GLEASON, D. F. 1966. Classification of prostatic carcinomas. *Cancer Chemotherapy Reports,* 50**,** 125-8.
GOENKA, S., SANT, V. & SANT, S. 2014. Graphene-based nanomaterials for drug delivery and tissue engineering. *Journal of Controlled Release,* 173**,** 75-88.
GOMES, J. R. B. & GOMES, J. A. N. F. 1999. A DFT study of dioxymethylene adsorption on the copper (111) surface. *Electrochimica Acta,* 45**,** 653-658.
GONG, Z., LI, S., HAN, W., WANG, J., MA, J. & ZHANG, X. 2016. Recyclable graphene oxide grafted with poly(N-isopropylacrylamide) and its enhanced selective adsorption for phenols. *Applied Surface Science,* 362**,** 459-468.
GORDON, M. S., BINKLEY, J. S., POPLE, J. A., PIETRO, W. J. & HEHRE, W. J. 1982. Self-consistent molecular-orbital methods. 22. Small split-valence basis sets for second-row elements. *Journal of the American Chemical Society,* 104**,** 2797-2803.

GOWTHAM, S., SCHEICHER, R. H., AHUJA, R., PANDEY, R. & KARNA, S. P. 2007. Physisorption of nucleobases on graphene: density-functional calculations. *Physical Review B,* 76**,** 033401.

GRIESHABER, D., MACKENZIE, R., VOROS, J. & REIMHULT, E. 2008. Electrochemical biosensors - Sensor principles and architectures. *Sensors,* 8**,** 1400-1458.

GU, Z., THOMAS, G., YAMASHIRO, J., SHINTAKU, I. P., DOREY, F., RAITANO, A., WITTE, O. N., SAID, J. W., LODA, M. & REITER, R. E. 2000. Prostate stem cell antigen (PSCA) expression increases with high gleason score, advanced stage and bone metastasis in prostate cancer. *Oncogene,* 19**,** 1288-96.

GUINEY, L. M., AGNELLO, A. D., THOMAS, J. C., TAKATORI, K. & FLYNN, N. T. 2009. Thermoresponsive behavior of charged N-isopropylacrylamide-based hydrogels containing gold nanostructures. *Colloid and Polymer Science,* 287**,** 601-608.

GUPTA, A., LOTAN, Y., ASHFAQ, R., ROEHRBORN, C. G., RAJ, G. V., ARAGAKI, C. C., MONTORSI, F. & SHARIAT, S. F. 2009. Predictive value of the differential expression of the urokinase plasminogen activation axis in radical prostatectomy patients. *European Urology,* 55**,** 1124-33.

GUPTA, B. D. & VERMA, R. K. 2009. Surface Plasmon Resonance-Based Fiber Optic Sensors: Principle, Probe Designs, and Some Applications. *Journal of Sensors,* 2009**,** 12.

GUPTA, V. K., YOLA, M. L., QURESHI, M. S., SOLAK, A. O., ATAR, N. & ÜSTÜNDAĞ, Z. 2013. A novel impedimetric biosensor based on graphene oxide/gold nanoplatform for detection of DNA arrays. *Sensors and Actuators B: Chemical,* 188**,** 1201-1211.

HAAS, G. P., DELONGCHAMPS, N., BRAWLEY, O. W., WANG, C. Y. & DE LA ROZA, G. 2008. The worldwide epidemiology of prostate cancer: perspectives from autopsy studies. *The Canadian Journal of Urology,* 15**,** 3866-71.

HAFIZ, S. M., RITIKOS, R., WHITCHER, T. J., RAZIB, N. M., BIEN, D. C. S., CHANLEK, N., NAKAJIMA, H., SAISOPA, T., SONGSIRIRITTHIGUL, P., HUANG, N. M. & RAHMAN, S. A. 2014. A practical carbon dioxide gas sensor using room-temperature hydrogen plasma reduced graphene oxide. *Sensors and Actuators B-Chemical,* 193**,** 692-700.

HALL, G. G. The molecular orbital theory of chemical valency. VIII. A method of calculating ionization potentials. Proceedings of the Royal Society of London A: Mathematical, Physical and Engineering Sciences, 1951. The Royal Society, 541-552.

HALPERIN, I., MA, B., WOLFSON, H. & NUSSINOV, R. 2002. Principles of docking: An overview of search algorithms and a guide to scoring functions. *Proteins: Structure, Function, and Bioinformatics,* 47**,** 409-443.

HANAHAN, D. & WEINBERG, ROBERT A. 2011. Hallmarks of Cancer: The Next Generation. *Cell,* 144**,** 646-674.

HANSSON, T., OOSTENBRINK, C. & VAN GUNSTEREN, W. 2002. Molecular dynamics simulations. *Current opinion in structural biology,* 12**,** 190-196.

HARA, N., KASAHARA, T., KAWASAKI, T., BILIM, V., OBARA, K., TAKAHASHI, K. & TOMITA, Y. 2002. Reverse transcription-polymerase chain reaction detection of prostate-specific antigen, prostate-specific membrane antigen, and prostate stem cell antigen in one milliliter of peripheral blood: value for the staging of prostate cancer. *Clinical Cancer Research,* 8**,** 1794-9.

HARRISON, S. C. 1991. A structural taxonomy of DNA-binding domains. *Nature,* 353**,** 715-9.

HASEGAWA, H., SAVORY, N., ABE, K. & IKEBUKURO, K. 2016. Methods for Improving Aptamer Binding Affinity. *Molecules,* 21.

HE, H., RIEDL, T., LERF, A. & KLINOWSKI, J. 1996. Solid-state NMR studies of the structure of graphite oxide. *The Journal of physical chemistry,* 100**,** 19954-19958.

HE, S., SONG, B., LI, D., ZHU, C., QI, W., WEN, Y., WANG, L., SONG, S., FANG, H. & FAN, C. 2010. A graphene nanoprobe for rapid, sensitive, and multicolor fluorescent DNA analysis. *Advanced Functional Materials,* 20**,** 453-459.

HEHRE, W., DITCHFIELD, R., STEWART, R. & POPLE, J. 1970. self-consistent molecular orbital methods. iv. use of Gaussian expansions of Slater-type orbitals. Extension to second-row molecules. *The Journal of Chemical Physics,* 52**,** 2769-2773.

HEHRE, W. J., STEWART, R. F. & POPLE, J. A. 1969. self-consistent molecular-orbital methods. i. use of gaussian expansions of Slater-type atomic orbitals. *The Journal of Chemical Physics,* 51**,** 2657-2664.

HEIAT, M., NAJAFI, A., RANJBAR, R., LATIFI, A. M. & RASAEE, M. J. 2016. Computational approach to analyze isolated ssDNA aptamers against angiotensin II. *Journal of Biotechnology,* 230**,** 34-39.

HERR, J. K., SMITH, J. E., MEDLEY, C. D., SHANGGUAN, D. & TAN, W. 2006. Aptamer-Conjugated Nanoparticles for Selective Collection and Detection of Cancer Cells. *Analytical Chemistry,* 78**,** 2918-2924.

HESSELS, D. & SCHALKEN, J. A. 2013. Urinary biomarkers for prostate cancer: a review. *Asian J Androl,* 15**,** 333-9.

HOARE, T. & PELTON, R. 2004. Functional group distributions in carboxylic acid containing poly (N-isopropylacrylamide) microgels. *Langmuir,* 20**,** 2123-2133.

HOCKNEY, R. W. & EASTWOOD, J. W. 1988. *Computer simulation using particles*, CRC Press.

HOFMANN, U. & HOLST, R. 1939. The acidic nature and the methylation of graphitoxide. *Berichte der deutschen chemischen Gesellschaft,* 72**,** 754-771.

HOHENBERG, P. & KOHN, W. 1964. Inhomogeneous electron gas. *Physical review,* 136**,** B864.

HOLLINGSWORTH, M. A. & SWANSON, B. J. 2004. Mucins in cancer: protection and control of the cell surface. *Nat Rev Cancer,* 4**,** 45-60.

HOLTZ, J. H. & ASHER, S. A. 1997. Polymerized colloidal crystal hydrogel films as intelligent chemical sensing materials. *Nature,* 389**,** 829-832.

HOLZINGER, M., LE GOFF, A. & COSNIER, S. 2014. Nanomaterials for biosensing applications: a review. *Frontiers in Chemistry,* 2**,** 63.

HOOFT, R. W., SANDER, C. & VRIEND, G. 1996. Positioning hydrogen atoms by optimizing hydrogen-bond networks in protein structures. *Proteins: Structure, Function, and Bioinformatics,* 26**,** 363-376.

HOROSZEWICZ, J. S., KAWINSKI, E. & MURPHY, G. P. 1987. Monoclonal antibodies to a new antigenic marker in epithelial prostatic cells and serum of prostatic cancer patients. *Anticancer Res,* 7**,** 927-35.

HU, J. Y., BRACKEMYER, C. A., BYUN, H. & KIM, J. H. 2014. Enhanced Stability of Anisotropic Gold Nanoparticles by Poly(N-isopropylacrylamide). *Journal of Materials Science & Technology,* 30**,** 441-448.

HU, W. P., KUMAR, J. V., HUANG, C. J. & CHEN, W. Y. 2015. Computational selection of RNA aptamer against angiopoietin-2 and experimental evaluation. *Biomed Res Int,* 2015**,** 658712.

HUANG, O., WU, D. D., XIE, F. Y., LIN, L. L., WANG, X. B., JIANG, M., LI, Y. F., CHEN, W. G., SHEN, K. W. & HU, X. Q. 2015. Targeting rho guanine nucleotide exchange factor ARHGEF5/TIM with auto-inhibitory peptides in human breast cancer. *Amino Acids,* 47**,** 1239-1246.

HUMMERS JR, W. S. & OFFEMAN, R. E. 1958. Preparation of graphitic oxide. *Journal of the American Chemical Society,* 80**,** 1339-1339.

IINUMA, H., OKINAGA, K., ADACHI, M., SUDA, K., SEKINE, T., SAKAGAWA, K., BABA, Y., TAMURA, J., KUMAGAI, H. & IDA, A. 2000. Detection of tumor cells in blood using CD45 magnetic cell separation followed by nested mutant allele-specific amplification of p53 and K-ras genes in patients with colorectal cancer. *International Journal of Cancer,* 89**,** 337-344.

ISLAM, M. R., GAO, Y. F., LI, X. & SERPE, M. J. 2014. Responsive polymers for biosensing and protein delivery. *Journal of Materials Chemistry B,* 2**,** 2444-2451.
ITO, J., NAKAMURA, J. & NATORI, A. 2008. Semiconducting nature of the oxygen-adsorbed graphene sheet. *Journal of applied physics,* 103**,** 113712.
JAIN, A., SHIN, Y. & PERSSON, K. A. 2016. Computational predictions of energy materials using density functional theory. *Nature Reviews Materials,* 1**,** 15004.
JAIN, K., VEDARAJAN, R., WATANABE, M., ISHIKIRIYAMA, M. & MATSUMI, N. 2015. Tunable LCST behavior of poly (N-isopropylacrylamide/ionic liquid) copolymers. *Polymer Chemistry,* 6**,** 6819-6825.
JEDDI, I. & SAIZ, L. 2017. Three-dimensional modeling of single stranded DNA hairpins for aptamer-based biosensors. *Scientific Reports,* 7**,** 1178.
JEMAL, A., SIEGEL, R., WARD, E., MURRAY, T., XU, J., SMIGAL, C. & THUN, M. J. 2006. Cancer statistics, 2006. *CA: A Cancer Journal for Clinicians* 56**,** 106-30.
JEMAL, A., WARD, E., WU, X., MARTIN, H. J., MCLAUGHLIN, C. C. & THUN, M. J. 2005. Geographic patterns of prostate cancer mortality and variations in access to medical care in the United States. *Cancer Epidemiology, Biomarkers, & Prevention,* 14**,** 590-5.
JENSEN, F. 2016. *Introduction to computational chemistry,* John wiley & sons.
JHA, N. & RAMAPRABHU, S. 2010. Development of Au nanoparticles dispersed carbon nanotube-based biosensor for the detection of paraoxon. *Nanoscale,* 2**,** 806-10.
JOHNSON, R. R., JOHNSON, A. C. & KLEIN, M. L. 2008. Probing the structure of DNA-carbon nanotube hybrids with molecular dynamics. *Nano Letters,* 8**,** 69-75.
JOLLY, P., TAMBOLI, V., HARNIMAN, R. L., ESTRELA, P., ALLENDER, C. J. & BOWEN, J. L. 2016. Aptamer–MIP hybrid receptor for highly sensitive electrochemical detection of prostate specific antigen. *Biosensors and Bioelectronics,* 75**,** 188-195.
JONES, P. A. & BAYLIN, S. B. 2002. The fundamental role of epigenetic events in cancer. *Nature Reviews Genetics,* 3**,** 415-428.
JONES, S., VAN HEYNINGEN, P., BERMAN, H. M. & THORNTON, J. M. 1999. Protein-DNA interactions: A structural analysis. *Journal of Molecular Biology,* 287**,** 877-96.
JOON-YONG, C., NARI, K., HYUN, J., JAE BOUM, Y., WON SUN, P., SANG-KYOUNG, L., MOHAMAD, W. & JIN, H. 2006. Tissue Microarrays in Biomedical Research.
JORGENSEN, W. L. 1991. Rusting of the lock and key model for protein-ligand binding. *Science,* 254**,** 954-5.
JUNG, Y.-D., KHAN, M. & PARK, S.-Y. 2014. Fabrication of temperature-and pH-sensitive liquid-crystal droplets with PNIPAM-b-LCP and SDS coatings by microfluidics. *Journal of Materials Chemistry B,* 2**,** 4922-4928.
KALÉ, L., SKEEL, R., BHANDARKAR, M., BRUNNER, R., GURSOY, A., KRAWETZ, N., PHILLIPS, J., SHINOZAKI, A., VARADARAJAN, K. & SCHULTEN, K. 1999. NAMD2: greater scalability for parallel molecular dynamics. *Journal of Computational Physics,* 151**,** 283-312.
KARAZANASHVILI, G. & ABRAHAMSSON, P.-A. 2003. Prostate Specific Antigen and Human Glandular Kallikrein 2 in Early Detection of Prostate Cancer. *The Journal of Urology,* 169**,** 445-457.
KATZ, E. & WILLNER, I. 2003. Probing biomolecular interactions at conductive and semiconductive surfaces by impedance spectroscopy: routes to impedimetric immunosensors, DNA-sensors, and enzyme biosensors. *Electroanalysis,* 15**,** 913-947.
KAUR, G., ADHIKARI, R., CASS, P., BOWN, M. & GUNATILLAKE, P. 2015. Electrically conductive polymers and composites for biomedical applications. *RSC Advances,* 5**,** 37553-37567.
KAUR, S., SINGH, G. & KAUR, K. 2014. Cancer stem cells: an insight and future perspective. *Journal of Cancer Research and Therapeutics,* 10**,** 846-52.

KIM, J., LEE, G.-H., JUNG, W. & HAH, S. S. 2013. Selective and quantitative cell detection based both on aptamers and the conventional cell-staining methods. *Biosensors and Bioelectronics,* 43**,** 362-365.
KIM, J., NAYAK, S. & LYON, L. A. 2005. Bioresponsive hydrogel microlenses. *Journal of the American Chemical Society,* 127**,** 9588-9592.
KIM, J., SERPE, M. J. & LYON, L. A. 2004. Hydrogel microparticles as dynamically tunable microlenses. *Journal of the American Chemical Society,* 126**,** 9512-9513.
KIM, J., SINGH, N. & LYON, L. A. 2006. Label-Free Biosensing with Hydrogel Microlenses. *Angewandte Chemie International Edition,* 45**,** 1446-1449.
KITCHIN, J. R., MILLER, S. D. & SHOLL, D. S. 2008. Density functional theory studies of alloys in heterogeneous catalysis. *Chemical Modelling: Applications and Theory Volume 5*. The Royal Society of Chemistry.
KOHN, W. 1999. Nobel Lecture: Electronic structure of matter—wave functions and density functionals. *Reviews of Modern Physics,* 71**,** 1253.
KOHN, W., BECKE, A. D. & PARR, R. G. 1996. Density functional theory of electronic structure. *The Journal of Physical Chemistry,* 100**,** 12974-12980.
KOHN, W. & SHAM, L. J. 1965. Self-Consistent Equations Including Exchange and Correlation Effects. *Physical Review,* 140**,** A1133-A1138.
KUKOWSKA-LATALLO, J. F., CANDIDO, K. A., CAO, Z., NIGAVEKAR, S. S., MAJOROS, I. J., THOMAS, T. P., BALOGH, L. P., KHAN, M. K. & BAKER, J. R., JR. 2005. Nanoparticle targeting of anticancer drug improves therapeutic response in animal model of human epithelial cancer. *Cancer Research,* 65**,** 5317-24.
KUMAR, G. G., HASHMI, S., KARTHIKEYAN, C., GHAVAMINEJAD, A., VATANKHAH-VARNOOSFADERANI, M. & STADLER, F. J. 2014. Graphene Oxide/Carbon Nanotube Composite Hydrogels-Versatile Materials for Microbial Fuel Cell Applications. *Macromolecular Rapid Communications,* 35**,** 1861-1865.
KUMAR, S., PANDYA, P., PANDAV, K., GUPTA, S. P. & CHOPRA, A. 2012. Structural studies on ligand-DNA systems: A robust approach in drug design. *Journal of Biosciences,* 37**,** 553-61.
KUNII, T., OGURA, S.-I., MIE, M. & KOBATAKE, E. 2011. Selection of DNA aptamers recognizing small cell lung cancer using living cell-SELEX. *Analyst,* 136**,** 1310-1312.
KUNTZ, I. D., BLANEY, J. M., OATLEY, S. J., LANGRIDGE, R. & FERRIN, T. E. 1982. A geometric approach to macromolecule-ligand interactions. *Journal of Molecular Biology,* 161**,** 269-88.
KUNZEL, D. & GROSS, A. 2013. Influence of the solvent on the stability of bis(terpyridine) structures on graphite. *Beilstein Journal of Nanotechnology,* 4**,** 269-277.
LAHAYE, R., JEONG, H., PARK, C. & LEE, Y. 2009. Density functional theory study of graphite oxide for different oxidation levels. *Physical Review B,* 79**,** 125435.
LANGER, R. 1998. Drug deliveryand targeting. *Nature,* 392**,** 5-10.
LARIJANI, H. T., GANJI, M. D. & JAHANSHAHI, M. 2015. Trends of amino acid adsorption onto graphene and graphene oxide surfaces: a dispersion corrected DFT study. *RSC Advances,* 5**,** 92843-92857.
LARSON, C. L. & VERDINE, G. L. 1996. *The chemistry of protein-DNA interactions bioorganic chemistry: nucleic acids (Hecht SM ed.),* New York, Oxford University Press.
LAUBENBACHER, R., HOWER, V., JARRAH, A., TORTI, S. V., SHULAEV, V., MENDES, P., TORTI, F. M. & AKMAN, S. 2009. A systems biology view of cancer. *Biochim Biophys Acta,* 1796**,** 129-39.
LEACH, J. C., WANG, A., YE, K. & JIN, S. 2016. A RNA-DNA Hybrid Aptamer for Nanoparticle-Based Prostate Tumor Targeted Drug Delivery. *International Journal of Molecular Sciences,* 17.

LEE, E. C., LOTZ, M. M., STEELE, G. D. & MERCURIO, A. M. 1992. The integrin alpha 6 beta 4 is a laminin receptor. *The Journal of cell biology,* 117**,** 671-678.
LEE, J., YANG, H., PARK, C. H., CHO, H. H., YUN, H. & KIM, B. J. 2016. Colorimetric Thermometer from Graphene Oxide Platform Integrated with Red, Green, and Blue Emitting, Responsive Block Copolymers. *Chemistry of Materials,* 28**,** 3446-3453.
LEE, J. H., CHOI, Y. K., KIM, H. J., SCHEICHER, R. H. & CHO, J. H. 2013. Physisorption of DNA Nucleobases on h-BN and Graphene: vdW-Corrected DFT Calculations. *Journal of Physical Chemistry C,* 117**,** 13435-13441.
LEE, J. H., SHIN, S. K., JIANG, Y., CHOI, W. H., HONG, C., KIM, D. E. & LEE, M. J. 2015. Facilitated Tau Degradation by USP14 Aptamers via Enhanced Proteasome Activity. *Scientific Reports,* 5.
LEIMKUHLER, B., NOORIZADEH, E. & PENROSE, O. 2011. Comparing the efficiencies of stochastic isothermal molecular dynamics methods. *Journal of Statistical Physics,* 143**,** 921-942.
LENGAUER, T. & RAREY, M. 1996a. Computational methods for biomolecular docking. *Curr Opin Struct Biol,* 6**,** 402-6.
LENGAUER, T. & RAREY, M. 1996b. Computational methods for biomolecular docking. *Current Opinion in Structural Biology,* 6**,** 402-406.
LERF, A., HE, H., FORSTER, M. & KLINOWSKI, J. 1998. Structure of graphite oxide revisited‖. *The Journal of Physical Chemistry B,* 102**,** 4477-4482.
LI, J., GUO, S., ZHAI, Y. & WANG, E. 2009. High-sensitivity determination of lead and cadmium based on the Nafion-graphene composite film. *Analytica Chimica Acta,* 649**,** 196-201.
LI, L., CHEN, R. & WENG, Z. P. 2003. RDOCK: Refinement of rigid-body protein docking predictions. *Proteins-Structure Function and Genetics,* 53**,** 693-707.
LI, S., APHALE, A. N., MACWAN, I. G., PATRA, P. K., GONZALEZ, W. G., MIKSOVSKA, J. & LEBLANC, R. M. 2012. Graphene oxide as a quencher for fluorescent assay of amino acids, peptides, and proteins. *ACS applied materials & interfaces,* 4**,** 7069-7075.
LI, X., CHEN, W., ZHAN, Q., DAI, L., SOWARDS, L., PENDER, M. & NAIK, R. R. 2006. Direct Measurements of Interactions between Polypeptides and Carbon Nanotubes. *The Journal of Physical Chemistry B,* 110**,** 12621-12625.
LIANG, T., LI, W.-X. & ZHANG, H. 2009. A first-principles study on the behavior of HCl inside SWCNT. *Journal of Molecular Structure: THEOCHEM,* 905**,** 44-47.
LIGHTCAP, I. V. & KAMAT, P. V. 2013. Graphitic Design: Prospects of Graphene-Based Nanocomposites for Solar Energy Conversion, Storage, and Sensing. *Accounts of Chemical Research,* 46**,** 2235-2243.
LIN, P. Y., CHENG, K. L., MCGUFFIN-CAWLEY, J. D., SHIEU, F. S., SAMIA, A. C., GUPTA, S., COONEY, M., THOMPSON, C. L. & LIU, C. C. 2012. Detection of Alpha-Methylacyl-CoA Racemase (AMACR), a Biomarker of Prostate Cancer, in Patient Blood Samples Using a Nanoparticle Electrochemical Biosensor. *Biosensors (Basel),* 2**,** 377-87.
LIN, X., TANG, D., YU, Z. & FENG, Q. 2014. Stimuli-responsive electrospun nanofibers from poly(N-isopropylacrylamide)-co-poly(acrylic acid) copolymer and polyurethane. *Journal of Materials Chemistry B,* 2**,** 651-658.
LIN, Y., JIN, J. & SONG, M. 2011. Preparation and characterisation of covalent polymer functionalized graphene oxide. *Journal of Materials Chemistry,* 21**,** 3455-3461.
LISDAT, F. & SCHÄFER, D. 2008. The use of electrochemical impedance spectroscopy for biosensing. *Analytical and bioanalytical chemistry,* 391**,** 1555.
LIU, A., WANG, K., WENG, S., LEI, Y., LIN, L., CHEN, W., LIN, X. & CHEN, Y. 2012. Development of electrochemical DNA biosensors. *TrAC Trends in Analytical Chemistry,* 37**,** 101-111.

LIU, G., MAO, X., PHILLIPS, J. A., XU, H., TAN, W. & ZENG, L. 2009. Aptamer−Nanoparticle Strip Biosensor for Sensitive Detection of Cancer Cells. *Analytical Chemistry,* 81**,** 10013-10018.

LIU, J., WEI, T., ZHAO, J., HUANG, Y., DENG, H., KUMAR, A., WANG, C., LIANG, Z., MA, X. & LIANG, X.-J. 2016. Multifunctional aptamer-based nanoparticles for targeted drug delivery to circumvent cancer resistance. *Biomaterials,* 91**,** 44-56.

LIU, Z., LIU, B., DING, J. & LIU, J. 2014. Fluorescent sensors using DNA-functionalized graphene oxide. *Analytical and Bioanalytical Chemistry,* 406**,** 6885-6902.

LIU, Z., ROBINSON, J. T., SUN, X. & DAI, H. 2008. PEGylated Nanographene Oxide for Delivery of Water-Insoluble Cancer Drugs. *Journal of the American Chemical Society,* 130**,** 10876-10877.

LOWE, F. C. & TRAUZZI, S. J. 1993. Prostatic acid phosphatase in 1993. Its limited clinical utility. *The Urologic Clinics of North America,* 20**,** 589-95.

LU, C. H., YANG, H. H., ZHU, C. L., CHEN, X. & CHEN, G. N. 2009. A graphene platform for sensing biomolecules. *Angewandte Chemie,* 121**,** 4879-4881.

LUCARELLI, F., MARRAZZA, G., TURNER, A. P. & MASCINI, M. 2004. Carbon and gold electrodes as electrochemical transducers for DNA hybridisation sensors. *Biosensors and Bioelectronics,* 19**,** 515-530.

LUCARELLI, F., TOMBELLI, S., MINUNNI, M., MARRAZZA, G. & MASCINI, M. 2008. Electrochemical and piezoelectric DNA biosensors for hybridisation detection. *analytica chimica acta,* 609**,** 139-159.

LUO, J., ISAACS, W. B., TRENT, J. M. & DUGGAN, D. J. 2003. Looking beyond morphology: cancer gene expression profiling using DNA microarrays. *Cancer Investigation,* 21**,** 937-49.

LUPOLD, S. E., HICKE, B. J., LIN, Y. & COFFEY, D. S. 2002. Identification and Characterization of Nuclease-stabilized RNA Molecules That Bind Human Prostate Cancer Cells via the Prostate-specific Membrane Antigen. *Cancer Research,* 62**,** 4029-4033.

LUZI, E., MINUNNI, M., TOMBELLI, S. & MASCINI, M. 2003. New trends in affinity sensing: aptamers for ligand binding. *Trends in Analytical Chemistry,* 22**,** 9.

LYNE, P. D. 2002. Structure-based virtual screening: an overview. *Drug Discovery Today,* 7**,** 1047-1055.

MADU, C. O. & LU, Y. 2010. Novel diagnostic biomarkers for prostate cancer. *Journal of Cancer,* 1**,** 150-77.

MANDELL, J. G., ROBERTS, V. A., PIQUE, M. E., KOTLOVYI, V., MITCHELL, J. C., NELSON, E., TSIGELNY, I. & TEN EYCK, L. F. 2001. Protein docking using continuum electrostatics and geometric fit. *Protein Engineering,* 14**,** 105-113.

MARIOTTI, A., KEDESHIAN, P. A., DANS, M., CURATOLA, A. M., GAGNOUX-PALACIOS, L. & GIANCOTTI, F. G. 2001. EGF-R signaling through Fyn kinase disrupts the function of integrin α6β4 at hemidesmosomes. *The International Journal of Biochemistry & Cell Biology,* 155**,** 447-458.

MARSHALL, K. A. & ELLINGTON, A. D. 2000. In vitro selection of RNA aptamers. *Methods in Enzymology,* 318**,** 193-214.

MARTIN, B. J., FINLAY, J. A., STERLING, K., WARD, M., LIFSEY, D., MERCANTE, D., JAINTO, J. M., MARTIN, L. & RAYFORD, W. 2004. Early detection of prostate cancer in African-American men through use of multiple biomarkers: human kallikrein 2 (hK2), prostate-specific antigen (PSA), and free PSA (fPSA). *Prostate Cancer and Prostatic Diseases,* 7**,** 132-137.

MARTINHO, N., FLORINDO, H., SILVA, L., BROCCHINI, S., ZLOH, M. & BARATA, T. 2014. Molecular Modeling to Study Dendrimers for Biomedical Applications. *Molecules,* 19**,** 20424-20467.

MASCINI, M., TOMBELLI, S. & PALCHETTI, I. 2005. New trends in nucleic acid based biosensors: University of Florence (Italy), 25–28 October 2003. *Bioelectrochemistry,* 67**,** 131-133.

MATIVETSKY, J. M., TREOSSI, E., ORGIU, E., MELUCCI, M., VERONESE, G. P., SAMORÌ, P. & PALERMO, V. 2010. Local Current Mapping and Patterning of Reduced Graphene Oxide. *Journal of the American Chemical Society,* 132**,** 14130-14136.

MATTEVI, C., EDA, G., AGNOLI, S., MILLER, S., MKHOYAN, K. A., CELIK, O., MASTROGIOVANNI, D., GRANOZZI, G., GARFUNKEL, E. & CHHOWALLA, M. 2009. Evolution of electrical, chemical, and structural properties of transparent and conducting chemically derived graphene thin films. *Advanced Functional Materials,* 19**,** 2577-2583.

MAYO, S. L., OLAFSON, B. D. & GODDARD, W. A. 1990. DREIDING: a generic force field for molecular simulations. *Journal of Physical chemistry,* 94**,** 8897-8909.

MCDONALD, I. K. & THORNTON, J. M. 1994. Satisfying Hydrogen Bonding Potential in Proteins. *Journal of Molecular Biology,* 238**,** 777-793.

MEDHEKAR, N. V., RAMASUBRAMANIAM, A., RUOFF, R. S. & SHENOY, V. B. 2010. Hydrogen bond networks in graphene oxide composite paper: structure and mechanical properties. *Acs Nano,* 4**,** 2300-2306.

MEERSMAN, F., WANG, J., WU, Y. & HEREMANS, K. 2005. Pressure effect on the hydration properties of poly (N-isopropylacrylamide) in aqueous solution studied by FTIR spectroscopy. *Macromolecules,* 38**,** 8923-8928.

MENG, X. Y., ZHANG, H. X., MEZEI, M. & CUI, M. 2011. Molecular docking: a powerful approach for structure-based drug discovery. *Current Computer-Aided Drug Design,* 7**,** 146-57.

MIN, K., SONG, K. M., CHO, M., CHUN, Y. S., SHIM, Y. B., KU, J. K. & BAN, C. 2010. Simultaneous electrochemical detection of both PSMA (+) and PSMA (-) prostate cancer cells using an RNA/peptide dual-aptamer probe. *Chemical Communications (Cambridge, England),* 46**,** 5566-8.

MIN, S. K., KIM, W. Y., CHO, Y. & KIM, K. S. 2011. Fast DNA sequencing with a graphene-based nanochannel device. *Nature nanotechnology,* 6**,** 162-165.

MORRIS, G. M. & LIM-WILBY, M. 2008. Molecular docking. *Methods in Molecular Biology,* 443**,** 365-82.

MOSCOVICI, M., BHIMJI, A. & KELLEY, S. O. 2013. Rapid and specific electrochemical detection of prostate cancer cells using an aperture sensor array. *Lab Chip,* 13**,** 940-6.

MUDEDLA, S. K., BALAMURUGAN, K., KAMARAJ, M. & SUBRAMANIAN, V. 2016. Interaction of nucleobases with silicon doped and defective silicon doped graphene and optical properties. *Physical Chemistry Chemical Physics,* 18**,** 295-309.

MUKHERJEE, S., MAJUMDAR, S. & BHATTACHARYYA, D. 2005. Role of Hydrogen Bonds in Protein−DNA Recognition: Effect of Nonplanar Amino Groups. *The Journal of Physical Chemistry B,* 109**,** 10484-10492.

MUKHERJEE, S. & ZHANG, Y. 2011. Protein-Protein Complex Structure Predictions by Multimeric Threading and Template Recombination. *Structure,* 19**,** 955-966.

MULLIKEN, R. S. 1935. Electronic structures of molecules. XI. Electroaffinity, molecular orbitals and dipole moments. *Journal of Chemical Physics,* 3**,** 573-585.

MURPHY, G. P., KENNY, G. M., RAGDE, H., WOLFERT, R. L., BOYNTON, A. L., HOLMES, E. H., MISROCK, S. L., BARTSCH, G., KLOCKER, H., POINTNER, J., REISSIGL, A., MCLEOD, D. G., DOUGLAS, T., MORGAN, T. & GILBAUGH, J., JR. 1998. Measurement of serum prostate-specific membrane antigen, a new prognostic marker for prostate cancer. *Urology,* 51**,** 89-97.

NAKAJIMA, T., MABUCHI, A. & HAGIWARA, R. 1988. A new structure model of graphite oxide. *Carbon,* 26**,** 357-361.

NEGM, R. S., VERMA, M. & SRIVASTAVA, S. 2002. The promise of biomarkers in cancer screening and detection. *Trends in Molecular Medicine,* 8**,** 288-293.
NERIA, E., FISCHER, S. & KARPLUS, M. 1996. Simulation of activation free energies in molecular systems. *The Journal of chemical physics,* 105**,** 1902-1921.
NIESSEN, C. M., HOGERVORST, F., JASPARS, L. H., DEMELKER, A. A., DELWEL, G. O., HULSMAN, E. H. M., KUIKMAN, I. & SONNENBERG, A. 1994. The Alpha-6-Beta-4 Integrin Is a Receptor for Both Laminin and Kalinin. *Experimental Cell Research,* 211**,** 360-367.
NISHIZUKA, S. 2006. Profiling cancer stem cells using protein array technology. *European Journal of Cancer,* 42**,** 1273-1282.
NOSÉ, S. 1984a. A molecular dynamics method for simulations in the canonical ensemble. *Molecular physics,* 52**,** 255-268.
NOSÉ, S. 1984b. A unified formulation of the constant temperature molecular dynamics methods. *The Journal of chemical physics,* 81**,** 511-519.
NUR, H., CORNELIUS, V. J., BENEE, L. S., MITCHELL, J. C., DAY, I. J. & SNOWDEN, M. J. 2009. Semi-quantitative analysis of the monomer composition in co-polymer microgels using solid state Raman and NMR spectroscopy. *Analyst,* 134**,** 1366-1372.
OGAWA, T., KURITA, N., SEKINO, H., KITAO, O. & TANAKA, S. 2003. Hydrogen bonding of DNA base pairs by consistent charge equilibration method combined with universal force field. *Chemical Physics Letters,* 374**,** 271-278.
OH, J., LEE, J. H., KOO, J. C., CHOI, H. R., LEE, Y., KIM, T., LUONG, N. D. & NAM, J. D. 2010. Graphene oxide porous paper from amine-functionalized poly(glycidyl methacrylate)/graphene oxide core-shell microspheres. *Journal of Materials Chemistry,* 20**,** 9200-9204.
OMENN, G. S. 2006. Plasma proteome profiles associated with cancers. *Faseb Journal,* 20**,** A422-A422.
ORTMANN, F., SCHMIDT, W. & BECHSTEDT, F. 2005. Attracted by long-range electron correlation: adenine on graphite. *Physical review letters,* 95**,** 186101.
PACE, C. N., FU, H., FRYAR, K. L., LANDUA, J., TREVINO, S. R., SHIRLEY, B. A., HENDRICKS, M. M. N., IIMURA, S., GAJIWALA, K., SCHOLTZ, J. M. & GRIMSLEY, G. R. 2011. Contribution of Hydrophobic Interactions to Protein Stability. *Journal of Molecular Biology,* 408**,** 514-28.
PAN, C., GUO, M., NIE, Z., XIAO, X. & YAO, S. 2009. Aptamer-Based Electrochemical Sensor for Label-Free Recognition and Detection of Cancer Cells. *Electroanalysis,* 21**,** 1321-1326.
PAN, Y., GUO, M., NIE, Z., HUANG, Y., PAN, C., ZENG, K., ZHANG, Y. & YAO, S. 2010. Selective collection and detection of leukemia cells on a magnet-quartz crystal microbalance system using aptamer-conjugated magnetic beads. *Biosensors and Bioelectronics,* 25**,** 1609-1614.
PAPSIDERO, L. D., WANG, M. C., VALENZUELA, L. A., MURPHY, G. P. & CHU, T. M. 1980. A prostate antigen in sera of prostatic cancer patients. *Cancer Research,* 40**,** 2428-32.
PARK, S. & RUOFF, R. S. 2009. Chemical methods for the production of graphenes. *Nature Nanotechnology,* 4**,** 217-224.
PARLAK, O., TURNER, A. P. F. & TIWARI, A. 2014. On/Off-Switchable Zipper-Like Bioelectronics on a Graphene Interface. *Advanced Materials,* 26**,** 482-486.
PARR, R. G. & WEITAO, Y. 1989. *Density-Functional Theory of Atoms and Molecules,* Oxford University Press.
PATIL, R., DAS, S., STANLEY, A., YADAV, L., SUDHAKAR, A. & VARMA, A. K. 2010. Optimized Hydrophobic Interactions and Hydrogen Bonding at the Target-Ligand Interface Leads the Pathways of Drug-Designing. *PLoS One,* 5.
PATRA, N., WANG, B. & KRAL, P. 2009. Nanodroplet activated and guided folding of graphene nanostructures. *Nano Letters,* 9**,** 3766-71.

PAUL, A. Dirac. Note on exchange phenomena in the Thomas-Fermi atom. Proc. Cambridge Philos. Soc, 1931. 376-385.
PAYNE, M. C., TETER, M. P., ALLAN, D. C., ARIAS, T. A. & JOANNOPOULOS, J. D. 1992. Iterative minimization techniques for \textit{ab initio} total-energy calculations: molecular dynamics and conjugate gradients. *Reviews of Modern Physics,* 64**,** 1045-1097.
PEPPAS, N. A., BURES, P., LEOBANDUNG, W. & ICHIKAWA, H. 2000. Hydrogels in pharmaceutical formulations. *European Journal of Pharmaceutics and Biopharmaceutics,* 50**,** 27-46.
PERDEW, J. P., BURKE, K. & ERNZERHOF, M. 1996. Generalized gradient approximation made simple. *Physical Review Letters,* 77**,** 3865.
PERDEW, J. P. & WANG, Y. 1992. Accurate and simple analytic representation of the electron-gas correlation energy. *Physical Review B,* 45**,** 13244.
PHEENEY, C. G., GUERRA, L. F. & BARTON, J. K. 2012. DNA sensing by electrocatalysis with hemoglobin. *Proceedings of the National Academy of Sciences of the United States of America,* 109**,** 11528-11533.
PIERCE, B. & WENG, Z. P. 2007. ZRANK: Reranking protein docking predictions with an optimized energy function. *Proteins-Structure Function and Bioinformatics,* 67**,** 1078-1086.
PIERCE, B. G., HOURAI, Y. & WENG, Z. 2011. Accelerating Protein Docking in ZDOCK Using an Advanced 3D Convolution Library. *PLoS ONE,* 6**,** e24657.
PIERCE, B. G., WIEHE, K., HWANG, H., KIM, B. H., VREVEN, T. & WENG, Z. 2014. ZDOCK server: interactive docking prediction of protein-protein complexes and symmetric multimers. *Bioinformatics,* 30**,** 1771-3.
PIETRO, W. J. & HEHRE, W. J. 1983. Molecular orbital theory of the properties of inorganic and organometallic compounds. 3. STO-3G basis sets for first-and second-row transition metals. *Journal of computational chemistry,* 4**,** 241-251.
PLUNKETT, K. N., BERKOWSKI, K. L. & MOORE, J. S. 2005. Chymotrypsin responsive hydrogel: application of a disulfide exchange protocol for the preparation of methacrylamide containing peptides. *Biomacromolecules,* 6**,** 632-637.
POHANKA, M. & SKLADAI, P. 2008. Electrochemical biosensors - principles and applications. *Journal of Applied Biomedicine,* 6**,** 57-64.
PU, Y., ZHU, Z., HAN, D., LIU, H., LIU, J., LIAO, J., ZHANG, K. & TAN, W. 2011. Insulin-binding aptamer-conjugated graphene oxide for insulin detection. *Analyst,* 136**,** 4138-4140.
PUTRI, A. D., TRI MURTI, B., SABELA, M., KANCHI, S. & BISETTY, K. 2017. Nanopolymer Chitosan in Cancer and Alzheimer Biomedical Application. *In:* AHMED, S. & IKRAM, S. (eds.) *Chitosan: Derivatives, Composites and Applications.* USA: Wiley-Scrivener.
PUTZBACH, W. & RONKAINEN, N. 2013. Immobilization Techniques in the Fabrication of Nanomaterial-Based Electrochemical Biosensors: A Review. *Sensors,* 13**,** 4811.
QI, J. J., LV, W. P., ZHANG, G. L., ZHANG, F. B. & FAN, X. B. 2012. Poly(N-isopropylacrylamide) on two-dimensional graphene oxide surfaces. *Polymer Chemistry,* 3**,** 621-624.
QIAN, S. B., WALDRON, L., CHOUDHARY, N., KLEVIT, R. E., CHAZIN, W. J. & PATTERSON, C. 2009. Engineering a ubiquitin ligase reveals conformational flexibility required for ubiquitin transfer. *The Journal of Biological Chemistry,* 284**,** 26797-802.
QU, M., REN, S. C. & SUN, Y. H. 2014. Current early diagnostic biomarkers of prostate cancer. *The Asian Journal of Andrology,* 16**,** 549-54.
RAFFENETTI, R. C. 1973. General contraction of Gaussian atomic orbitals: Core, valence, polarization, and diffuse basis sets; Molecular integral evaluation. *The Journal of Chemical Physics,* 58**,** 4452-4458.
RAJESH, C., MAJUMDER, C., MIZUSEKI, H. & KAWAZOE, Y. 2009. A theoretical study on the interaction of aromatic amino acids with graphene and single walled carbon nanotube. *The Journal of chemical physics,* 130**,** 124911.

RAMIREZ, M. L., NELSON, E. C. & EVANS, C. P. 2008. Beyond prostate-specific antigen: alternate serum markers. *Prostate Cancer and Prostatic Diseases,* 11**,** 216-29.
RAPPE, A. K., CASEWIT, C. J., COLWELL, K. S., GODDARD, W. A. & SKIFF, W. M. 1992. UFF, a full periodic table force field for molecular mechanics and molecular dynamics simulations. *Journal of the American Chemical Society,* 114**,** 10024-10035.
REITER, R. E., GU, Z., WATABE, T., THOMAS, G., SZIGETI, K., DAVIS, E., WAHL, M., NISITANI, S., YAMASHIRO, J., LE BEAU, M. M., LODA, M. & WITTE, O. N. 1998. Prostate stem cell antigen: a cell surface marker overexpressed in prostate cancer. *Proceedings of the National Academy of Sciences of the USA,* 95**,** 1735-40.
REVANKAR, C. M., CIMINO, D. F., SKLAR, L. A., ARTERBURN, J. B. & PROSSNITZ, E. R. 2005. A Transmembrane Intracellular Estrogen Receptor Mediates Rapid Cell Signaling. *Science,* 307**,** 1625-1630.
RICHTER, M. M. 2004. Electrochemiluminescence (ECL). *Chemical Reviews,* 104**,** 3003-3036.
RITCHIE, D. W. & KEMP, G. J. L. 2000. Protein docking using spherical polar Fourier correlations. *Proteins-Structure Function and Genetics,* 39**,** 178-194.
RITTENHOUSE, H. G., FINLAY, J. A., MIKOLAJCZYK, S. D. & PARTIN, A. W. 1998. Human Kallikrein 2 (hK2) and prostate-specific antigen (PSA): two closely related, but distinct, kallikreins in the prostate. *Critical Reviews in Clinical Laboratory Sciences,* 35**,** 275-368.
ROBERTS, V. A., PIQUE, M. E., TEN EYCK, L. F. & LI, S. 2013. Predicting protein-DNA interactions by full search computational docking. *Proteins-Structure Function and Bioinformatics,* 81**,** 2106-2118.
RODRÍGUEZ-PÉREZ, L., HERRANZ, M. Á. & MARTÍN, N. 2013. The chemistry of pristine graphene. *Chemical Communications,* 49**,** 3721-3735.
ROHS, R., JIN, X., WEST, S. M., JOSHI, R., HONIG, B. & MANN, R. S. 2010. Origins of specificity in protein-DNA recognition. *Annual Review of Biochemistry,* 79**,** 233-69.
RONKAINEN, N. J., HALSALL, H. B. & HEINEMAN, W. R. 2010. Electrochemical biosensors. *Chemical Society Reviews,* 39**,** 1747-1763.
ROOBOL, M. J. & CARLSSON, S. V. 2013. Risk stratification in prostate cancer screening. *Nature Reviews Urology,* 10**,** 38-48.
ROOTHAAN, C. C. J. 1951. New developments in molecular orbital theory. *Reviews of modern physics,* 23**,** 69.
ROSAS, J. J. H., GUTIERREZ, R. E. R., ESCOBEDO-MORALES, A. & ANOTA, E. C. 2011. First principles calculations of the electronic and chemical properties of graphene, graphane, and graphene oxide. *Journal of Molecular Modeling,* 17**,** 1133-1139.
ROSS, J. S., SHEEHAN, C. E., FISHER, H. A., KAUFMAN, R. P., JR., KAUR, P., GRAY, K., WEBB, I., GRAY, G. S., MOSHER, R. & KALLAKURY, B. V. 2003. Correlation of primary tumor prostate-specific membrane antigen expression with disease recurrence in prostate cancer. *Clinical Cancer Research,* 9**,** 6357-62.
RUESS, G. 1947. Über das graphitoxyhydroxyd (graphitoxyd). *Monatshefte für Chemie und verwandte Teile anderer Wissenschaften,* 76**,** 381-417.
SAFAEI, T. S., MOHAMADI, R. M., SARGENT, E. H. & KELLEY, S. O. 2015. In Situ Electrochemical ELISA for Specific Identification of Captured Cancer Cells. *ACS Applied Materials & Interfaces,* 7**,** 14165-9.
SAHA, B., BAURI, K., BAG, A., GHORAI, P. K. & DE, P. 2016. Conventional fluorophore-free dual pH-and thermo-responsive luminescent alternating copolymer. *Polymer Chemistry,* 7**,** 6895-6900.
SAIKIA, N. & DEKA, R. C. 2013a. Ab initio study on the noncovalent adsorption of camptothecin anticancer drug onto graphene, defect modified graphene and graphene oxide. *Journal of Computer-Aided Molecular Design,* 27**,** 807-821.

SAIKIA, N. & DEKA, R. C. 2013b. A comparison of the effect of nanotube chirality and electronic properties on the π–π interaction of single-wall carbon nanotubes with pyrazinamide antitubercular drug. *International Journal of Quantum Chemistry,* 113**,** 1272-1284.
SAIKIA, N. & DEKA, R. C. 2014. Density functional study on noncovalent functionalization of pyrazinamide chemotherapeutic with graphene and its prototypes. *New Journal of Chemistry,* 38**,** 1116-1128.
SAITO, R., HOFMANN, M., DRESSELHAUS, G., JORIO, A. & DRESSELHAUS, M. S. 2011. Raman spectroscopy of graphene and carbon nanotubes. *Advances in Physics,* 60**,** 413-550.
SAMOLETOV, A. A., DETTMANN, C. P. & CHAPLAIN, M. A. 2007. Thermostats for "slow" configurational modes. *Journal of Statistical Physics,* 128**,** 1321-1336.
SARTOR, A. O., HRICAK, H., WHEELER, T. M., COLEMAN, J., PENSON, D. F., CARROLL, P. R., RUBIN, M. A. & SCARDINO, P. T. 2008. Evaluating localized prostate cancer and identifying candidates for focal therapy. *Urology,* 72**,** S12-24.
SAVORY, N., ABE, K., SODE, K. & IKEBUKURO, K. 2010. Selection of DNA aptamer against prostate specific antigen using a genetic algorithm and application to sensing. *Biosensors and Bioelectronics,* 26**,** 1386-1391.
SCHÄFER, A., HORN, H. & AHLRICHS, R. 1992. Fully optimized contracted Gaussian basis sets for atoms Li to Kr. *The Journal of Chemical Physics,* 97**,** 2571-2577.
SCHOLZ, W. & BOEHM, H. 1969. Studies on graphite VI considerations on the structure of graphite. *Zeitschrift fur anorganische und allgemeine Chemie,* 369**,** 327-340.
SCHULZ, W. A., BURCHARDT, M. & CRONAUER, M. V. 2003. Molecular biology of prostate cancer. *Molecular Human Reproduction,* 9**,** 437-48.
SCOTT, A. M., WOLCHOK, J. D. & OLD, L. J. 2012. Antibody therapy of cancer. *Nature Reviews Cancer,* 12**,** 278-87.
SEFAH, K., BAE, K. M., PHILLIPS, J. A., SIEMANN, D. W., SU, Z., MCCLELLAN, S., VIEWEG, J. & TAN, W. 2013. Cell-based selection provides novel molecular probes for cancer stem cells. *The International Journal of Cancer,* 132**,** 2578-88.
SEFAH, K., SHANGGUAN, D., XIONG, X., O'DONOGHUE, M. B. & TAN, W. 2010. Development of DNA aptamers using Cell-SELEX. *Nature Protocols,* 5**,** 1169-85.
SERPE, M. J., KIM, J. & LYON, L. A. 2004. Colloidal hydrogel microlenses. *Advanced Materials,* 16**,** 184-187.
SESSLER, J. L., LAWRENCE, C. M. & JAYAWICKRAMARAJAH, J. 2007. Molecular recognition via base-pairing. *Chemical Society Reviews,* 36**,** 314-325.
SHANGGUAN, D., LI, Y., TANG, Z., CAO, Z. C., CHEN, H. W., MALLIKARATCHY, P., SEFAH, K., YANG, C. J. & TAN, W. 2006. Aptamers evolved from live cells as effective molecular probes for cancer study. *Proceedings of the National Academy of Sciences of the USA,* 103**,** 11838-43.
SHARIAT, S. F., ROEHRBORN, C. G., MCCONNELL, J. D., PARK, S., ALAM, N., WHEELER, T. M. & SLAWIN, K. M. 2007. Association of the circulating levels of the urokinase system of plasminogen activation with the presence of prostate cancer and invasion, progression, and metastasis. *Journal of Clinical Oncology,* 25**,** 349-55.
SHARIAT, S. F., SEMJONOW, A., LILJA, H., SAVAGE, C., VICKERS, A. J. & BJARTELL, A. 2011. Tumor markers in prostate cancer I: blood-based markers. *Acta Oncologica,* 50 Suppl 1**,** 61-75.
SHARMA, A. C., JANA, T., KESAVAMOORTHY, R., SHI, L., VIRJI, M. A., FINEGOLD, D. N. & ASHER, S. A. 2004. A general photonic crystal sensing motif: creatinine in bodily fluids. *Journal of the American Chemical Society,* 126**,** 2971-2977.
SHAW, L. M., RABINOVITZ, I., WANG, H. H.-F., TOKER, A. & MERCURIO, A. M. 1997. Activation of phosphoinositide 3-OH kinase by the α6β4 integrin promotes carcinoma invasion. *Cell,* 91**,** 949-960.

SHEN, M. M. & ABATE-SHEN, C. 2010. Molecular genetics of prostate cancer: new prospects for old challenges. *Genes and Development,* 24**,** 1967-2000.
SHUICHI, N. 1991. Constant temperature molecular dynamics methods. *Progress of Theoretical Physics Supplement,* 103**,** 1-46.
SIEGEL, R. L., MILLER, K. D. & JEMAL, A. 2015. Cancer Statistics, 2015. *Ca-a Cancer Journal for Clinicians,* 65**,** 5-29.
SINHA, R., KIM, G. J., NIE, S. & SHIN, D. M. 2006. Nanotechnology in cancer therapeutics: bioconjugated nanoparticles for drug delivery. *Molecular Cancer Therapeutics,* 5**,** 1909-17.
SIVAKUMARAN, D., MAITLAND, D. & HOARE, T. 2011. Injectable microgel-hydrogel composites for prolonged small-molecule drug delivery. *Biomacromolecules,* 12**,** 4112-4120.
SLATER, J. C. 1930. Atomic shielding constants. *Physical Review,* 36**,** 57.
SMITH, G. R. & STERNBERG, M. J. 2002. Prediction of protein-protein interactions by docking methods. *Current Opinion in Structural Biology,* 12**,** 28-35.
SOHRABI, N., VALIZADEH, A., FARKHANI, S. M. & AKBARZADEH, A. 2016. Basics of DNA biosensors and cancer diagnosis. *Artificial cells, nanomedicine, and biotechnology,* 44**,** 654-663.
SOLDATKIN, A. P., MONTORIOL, J., SANT, W., MARTELET, C. & JAFFREZIC-RENAULT, N. 2003. A novel urea sensitive biosensor with extended dynamic range based on recombinant urease and ISFETs. *Biosensors and Bioelectronics,* 19**,** 131-135.
SOLOMONS, T. W. G., FRYHLE, C. B. & SNYDER, S. A. 2014. *Organic Chemistry, International Student Version,* Singapore, John Wiley & Sons, Inc.
SREEKUMAR, A., LAXMAN, B., RHODES, D. R., BHAGAVATHULA, S., HARWOOD, J., GIACHERIO, D., GHOSH, D., SANDA, M. G., RUBIN, M. A. & CHINNAIYAN, A. M. 2004. Humoral immune response to alpha-methylacyl-CoA racemase and prostate cancer. *Journal of the National Cancer Institute,* 96**,** 834-43.
SREPUSHARAWOOT, P., SCHEICHER, R. H., MOYSÉS ARAÚJO, C., BLOMQVIST, A., PINSOOK, U. & AHUJA, R. 2009. Ab Initio Study of Molecular Hydrogen Adsorption in Covalent Organic Framework-1. *The Journal of Physical Chemistry C,* 113**,** 8498-8504.
STAMEY, T. A., YANG, N., HAY, A. R., MCNEAL, J. E., FREIHA, F. S. & REDWINE, E. 1987. Prostate-specific antigen as a serum marker for adenocarcinoma of the prostate. *The New England Journal of Medicine,* 317**,** 909-16.
STEINHAUSER, M. & HIERMAIER, S. 2009. A Review of Computational Methods in Materials Science: Examples from Shock-Wave and Polymer Physics. *International Journal of Molecular Sciences,* 10**,** 5135.
STERNBERG, M. J., GABB, H. A., JACKSON, R. M. & MOONT, G. 2000. Protein-protein docking: Generation and filtering of complexes. *Protein Structure Prediction: Methods and Protocols***,** 399-415.
STEWART, R. L. & O'CONNOR, K. L. 2015. Clinical significance of the integrin α6β4 in human malignancies. *Laboratory Investigation,* 95**,** 976-986.
STRIMBU, K. & TAVEL, J. A. 2010. What are Biomarkers? *Current opinion in HIV and AIDS,* 5**,** 463-466.
SUN, H. 1998. COMPASS: An ab Initio Force-Field Optimized for Condensed-Phase ApplicationsOverview with Details on Alkane and Benzene Compounds. *The Journal of Physical Chemistry B,* 102**,** 7338-7364.
SUN, H., REN, P. & FRIED, J. R. 1998. The COMPASS force field: parameterization and validation for phosphazenes. *Computational and Theoretical Polymer Science,* 8**,** 229-246.
SUN, W. J., ZHAO, J. H. & DU, Z. 2017. Density-functional-theory-based study of interaction of DNA/RNA nucleobases with hydroxyl- and carboxyl-functionalized armchair (6,6)CNT. *Computational and Theoretical Chemistry,* 1102**,** 60-68.

SUN, X., LIU, Z., WELSHER, K., ROBINSON, J. T., GOODWIN, A., ZARIC, S. & DAI, H. 2008. Nano-Graphene Oxide for Cellular Imaging and Drug Delivery. *Nano Research,* 1**,** 203-212.

SUN, X. T., FENG, Z. W., HOU, T. J. & LI, Y. Y. 2014. Mechanism of Graphene Oxide as an Enzyme Inhibitor from Molecular Dynamics Simulations. *ACS Applied Materials & Interfaces,* 6**,** 7153-7163.

SUN, Y. Y., LEE, K., WANG, L., KIM, Y.-H., CHEN, W., CHEN, Z. & ZHANG, S. B. 2010. Accuracy of density functional theory methods for weakly bonded systems: The case of dihydrogen binding on metal centers. *Physical Review B,* 82**,** 073401.

SZABÓ, T., BERKESI, O., FORGÓ, P., JOSEPOVITS, K., SANAKIS, Y., PETRIDIS, D. & DÉKÁNY, I. 2006. Evolution of surface functional groups in a series of progressively oxidized graphite oxides. *Chemistry of materials,* 18**,** 2740-2749.

TAI, S., SUN, Y., SQUIRES, J. M., ZHANG, H., OH, W. K., LIANG, C.-Z. & HUANG, J. 2011. PC3 Is a Cell Line Characteristic of Prostatic Small Cell Carcinoma. *The Prostate,* 71**,** 1668-1679.

TANG, S. B. & CAO, Z. X. 2011. Adsorption of nitrogen oxides on graphene and graphene oxides: Insights from density functional calculations. *Journal of Chemical Physics,* 134.

TANG, Z., SHANGGUAN, D., WANG, K., SHI, H., SEFAH, K., MALLIKRATCHY, P., CHEN, H. W., LI, Y. & TAN, W. 2007. Selection of aptamers for molecular recognition and characterization of cancer cells. *Analytical Chemistry,* 79**,** 4900-7.

TATIANA DUQUE, M., ANTONIO CARLOS CHAVES, R., HENRIQUE SANTIAGO DE, C., PAULO ALVES DA COSTA, F., HANNAH PAULA MESQUITA, C. & DIOGO LOPES, D. 2013. New Insights on Optical Biosensors: Techniques, Construction and Application.

TAURO, J. R. & GEMEINHART, R. A. 2005. Matrix metalloprotease triggered delivery of cancer chemotherapeutics from hydrogel matrixes. *Bioconjugate chemistry,* 16**,** 1133-1139.

TAYLOR, R. D., JEWSBURY, P. J. & ESSEX, J. W. 2002. A review of protein-small molecule docking methods. *Journal of Computer-Aided Molecular Design,* 16**,** 151-66.

TKATCHENKO, A. & SCHEFFLER, M. 2009. Accurate Molecular Van Der Waals Interactions from Ground-State Electron Density and Free-Atom Reference Data. *Physical Review Letters,* 102.

TOMBELLI, S., MINUNNI, M. & MASCINI, M. 2005. Analytical applications of aptamers. *Biosensors and Bioelectronics,* 20**,** 2424-34.

TORRE, L. A., BRAY, F., SIEGEL, R. L., FERLAY, J., LORTET-TIEULENT, J. & JEMAL, A. 2015. Global cancer statistics, 2012. *CA: A Cancer Journal for Clinicians,* 65**,** 87-108.

TOSOIAN, J. & LOEB, S. 2010. PSA and beyond: the past, present, and future of investigative biomarkers for prostate cancer. *Scientific World Journal,* 10**,** 1919-31.

TOTHILL, I. E. 2009. Biosensors for cancer markers diagnosis. *Seminars in Cell and Developmental Biology,* 20**,** 55-62.

TRICOLI, J. V., SCHOENFELDT, M. & CONLEY, B. A. 2004. Detection of prostate cancer and predicting progression: current and future diagnostic markers. *Clinical Cancer Research,* 10**,** 3943-53.

TSUBOI, Y., NISHINO, M. & KITAMURA, N. 2008. Laser-induced reversible volume phase transition of a poly (N-isopropylacrylamide) gel explored by Raman microspectroscopy. *Polymer journal,* 40**,** 367.

TURNER, A. P. 2013. Biosensors: sense and sensibility. *Chemical Society Reviews,* 42**,** 3184-96.

UETSUKI, H., TSUNEMORI, H., TAOKA, R., HABA, R., ISHIKAWA, M. & KAKEHI, Y. 2005. Expression of a novel biomarker, EPCA, in adenocarcinomas and precancerous lesions in the prostate. *The Journal of Urology,* 174**,** 514-8.

ULIANAS, A., HENG, L. Y., AHMAD, M., LAU, H.-Y., ISHAK, Z. & LING, T. L. 2014. A regenerable screen-printed DNA biosensor based on acrylic microsphere–gold nanoparticle

composite for genetically modified soybean determination. *Sensors and Actuators B: Chemical,* 190**,** 694-701.
VAKSER I , A. 2014. Protein-Protein Docking: From Interaction to Interactome. *Biophysical Journal,* 107**,** 1785-93.
VAKSER, I. A. 1997. Evaluation of GRAMM low-resolution docking methodology on the hemagglutinin-antibody complex. *Proteins-Structure Function and Genetics***,** 226-230.
VARGHESE, N., MOGERA, U., GOVINDARAJ, A., DAS, A., MAITI, P. K., SOOD, A. K. & RAO, C. 2009. Binding of DNA nucleobases and nucleosides with graphene. *ChemPhysChem,* 10**,** 206-210.
VASHIST, S. K. & LUONG, J. H. T. 2015. Recent advances in electrochemical biosensing schemes using graphene and graphene-based nanocomposites. *Carbon,* 84**,** 519-550.
VERLET, L. 1967. Computer" experiments" on classical fluids. I. Thermodynamical properties of Lennard-Jones molecules. *Physical review,* 159**,** 98.
VILARINO, N., FONFRIA, E. S., LOUZAO, M. C. & BOTANA, L. M. 2009. Use of Biosensors as Alternatives to Current Regulatory Methods for Marine Biotoxins. *Sensors,* 9**,** 9414-9443.
VOVUSHA, H. & SANYAL, B. 2015. Adsorption of nucleobases on 2D transition-metal dichalcogenides and graphene sheet: a first principles density functional theory study. *RSC Advances,* 5**,** 67427-67434.
VOVUSHA, H., SANYAL, S. & SANYAL, B. 2013. Interaction of Nucleobases and Aromatic Amino Acids with Graphene Oxide and Graphene Flakes. *Journal of Physical Chemistry Letters,* 4**,** 3710-3718.
WALLACE, P. R. 1947. The Band Theory of Graphite. *Physical Review,* 71**,** 622-634.
WANG, B., YANG, D., ZHANG, J. Z., XI, C. & HU, J. 2011a. Stimuli-responsive polymer covalent functionalization of graphene oxide by Ce (IV)-induced redox polymerization. *The Journal of Physical Chemistry C,* 115**,** 24636-24641.
WANG, H., ZHANG, Q., CHU, X., CHEN, T., GE, J. & YU, R. 2011b. Graphene Oxide–Peptide Conjugate as an Intracellular Protease Sensor for Caspase-3 Activation Imaging in Live Cells. *Angewandte Chemie International Edition,* 50**,** 7065-7069.
WANG, J., SEFAH, K., ALTMAN, M. B., CHEN, T., YOU, M., ZHAO, Z., HUANG, C. Z. & TAN, W. 2013. Aptamer-conjugated nanorods for targeted photothermal therapy of prostate cancer stem cells. *Chemistry, an Asian Journal,* 8**,** 2417-22.
WANG, M. C., VALENZUELA, L. A., MURPHY, G. P. & CHU, T. M. 2002. Purification of a human prostate specific antigen. 1979 [classical article]. *Journal of Urology,* 167**,** 1226-30.
WANG, S., LIU, J. H., DONG, Y. Y., SU, H. J. & TAN, T. W. 2015. Conformational structure-dependent molecular recognition of two aptamers for tetracycline. *RSC Advances,* 5**,** 53796-53801.
WANG, W. 2011. Single cells and intracellular processes studied by a plasmonic-based electrochemical impedance microscopy. *Nature Chemistry*.
WANG, Y.-B. & LIN, Z. 2003. Supramolecular Interactions between Fullerenes and Porphyrins. *Journal of the American Chemical Society,* 125**,** 6072-6073.
WANG, Y., LI, Z., HU, D., LIN, C.-T., LI, J. & LIN, Y. 2010. Aptamer/Graphene Oxide Nanocomplex for in Situ Molecular Probing in Living Cells. *Journal of the American Chemical Society,* 132**,** 9274-9276.
WANG, Y., LUO, Y., BING, T., CHEN, Z., LU, M., ZHANG, N., SHANGGUAN, D. & GAO, X. 2014. DNA aptamer evolved by cell-SELEX for recognition of prostate cancer. *PLoS One,* 9**,** e100243.
WANG, Z. & LU, Y. 2009. Functional DNA directed assembly of nanomaterials for biosensing. *Journal of Materials Chemistry,* 19**,** 1788-1798.
WEINER, L. M., SURANA, R. & WANG, S. 2010. Monoclonal antibodies: versatile platforms for cancer immunotherapy. *Nature Reviews. Immunology* 10**,** 317-327.

WEN, Y. L., PEI, H., SHEN, Y., XI, J. J., LIN, M. H., LU, N., SHEN, X. Z., LI, J. & FAN, C. H. 2012. DNA Nanostructure-based Interfacial engineering for PCR-free ultrasensitive electrochemical analysis of microRNA. *Scientific Reports,* 2.

WESTON, A. & HARRIS, C. C. 2003. Multistage Carcinogenesis. *In:* KUFE DW, POLLOCK RE, WEICHSELBAUM RR & AL., E. (eds.) *Holland-Frei Cancer Medicine.* 6 ed.: BC Decker.

WONG, J. E., GAHARWAR, A. K., MÜLLER-SCHULTE, D., BAHADUR, D. & RICHTERING, W. 2008. Dual-stimuli responsive PNiPAM microgel achieved via layer-by-layer assembly: Magnetic and thermoresponsive. *Journal of colloid and interface science,* 324**,** 47-54.

WU, M., KEMPAIAH, R., HUANG, P.-J. J., MAHESHWARI, V. & LIU, J. 2011. Adsorption and desorption of DNA on graphene oxide studied by fluorescently labeled oligonucleotides. *Langmuir,* 27**,** 2731-2738.

WU, S., HE, Q., TAN, C., WANG, Y. & ZHANG, H. 2013. Graphene-Based Electrochemical Sensors. *Small,* 9**,** 1160-1172.

XIA, L., XIAN, Y. F., WANG, D. N., CHEN, Y. Z., HUANG, X. F., BI, X. J., YU, H., FU, Z., LIU, X. L., LI, S. W., AN, Z. Q., LUO, W. X., ZHAO, Q. J. & XIA, N. S. 2016. A human monoclonal antibody against HPV16 recognizes an immunodominant and neutralizing epitope partially overlapping with that of H16.V5. *Scientific Reports,* 6.

XIAO, H., TAHIR-KHELI, J. & GODDARD, W. A. 2011. Accurate Band Gaps for Semiconductors from Density Functional Theory. *Journal of Physical Chemistry Letters,* 2**,** 212-217.

XIAO, Y., LUBIN, A. A., BAKER, B. R., PLAXCO, K. W. & HEEGER, A. J. 2006. Single-step electronic detection of femtomolar DNA by target-induced strand displacement in an electrode-bound duplex. *Proceedings of the National Academy of Sciences of the United States of America,* 103**,** 16677-16680.

XU, Z., WANG, S., LI, Y., WANG, M., SHI, P. & HUANG, X. 2014. Covalent functionalization of graphene oxide with biocompatible poly(ethylene glycol) for delivery of paclitaxel. *ACS Applied Materials & Interfaces,* 6**,** 17268-76.

YAN, J. A., XIAN, L. D. & CHOU, M. Y. 2009. Structural and Electronic Properties of Oxidized Graphene. *Physical Review Letters,* 103.

YANG, G. H., CAO, J. T., LI, L. L., RANA, R. K. & ZHU, J. J. 2013. Carboxymethyl chitosan-functionalized graphene for label-free electrochemical cytosensing. *Carbon,* 51**,** 124-133.

YANG, H., LI, Z., SHAN, M., LI, C., QI, H., GAO, Q., WANG, J. & ZHANG, C. 2015. Electrogenerated chemiluminescence biosensing for the detection of prostate PC-3 cancer cells incorporating antibody as capture probe and ruthenium complex-labelled wheat germ agglutinin as signal probe. *Analytica Chimica Acta,* 863**,** 1-8.

YANG, X., WANG, Y., HUANG, X., MA, Y., HUANG, Y., YANG, R., DUAN, H. & CHEN, Y. 2011. Multi-functionalized graphene oxide based anticancer drug-carrier with dual-targeting function and pH-sensitivity. *Journal of Materials Chemistry,* 21**,** 3448-3454.

YE, M., HU, J., PENG, M., LIU, J., LIU, J., LIU, H., ZHAO, X. & TAN, W. 2012. Generating aptamers by cell-SELEX for applications in molecular medicine. *International Journal of Molecular Sciences,* 13**,** 3341-53.

YIN, J. A. & GRIMWADE, D. 2002. Minimal residual disease evaluation in acute myeloid leukaemia. *Lancet,* 360**,** 160-2.

YOKOTA, J. 2000. Tumor progression and metastasis. *Carcinogenesis,* 21**,** 497-503.

YOUNG, D. C. 2001. *Computational chemistry : a practical guide for applying techniques to real world problems,* New York, Wiley.

YOUSEF, G. M. & DIAMANDIS, E. P. 2001. The new human tissue kallikrein gene family: structure, function, and association to disease. *Endocrine Reviews* 22**,** 184-204.

ZEIGLER-JOHNSON, C. M., SPANGLER, E., JALLOH, M., GUEYE, S. M., RENNERT, H. & REBBECK, T. R. 2008. Genetic susceptibility to prostate cancer in men of African descent:

implications for global disparities in incidence and outcomes. *The Canadian Journal of Urology,* 15**,** 3872-82.
ZENG, S. W., ZHOU, G. Q., GUO, J. Z., ZHOU, F. & CHEN, J. L. 2016. Molecular simulations of conformation change and aggregation of HIV-1 Vpr13-33 on graphene. *Scientific Reports,* 6.
ZHAO, J., ZHANG, L., CHEN, C., JIANG, J. & YU, R. 2012. A novel sensing platform using aptamer and RNA polymerase-based amplification for detection of cancer cells. *Analytica Chimica Acta,* 745**,** 106-111.
ZHENG, X., GUO, Z. & ZHANG, Z. 2001. Flow-injection electrogenerated chemiluminescence determination of isoniazid using luminol. *Analytical Sciences,* 17**,** 1095-9.
ZHOU, Y., CAO, J., ZHAO, J., XIE, Y., FEI, J. & CAI, Y. 2016. Temperature-responsive amperometric H2O2 biosensor using a composite film consisting of poly(N-isopropylacrylamide)-b-poly (2-acrylamidoethyl benzoate), graphene oxide and hemoglobin. *Microchimica Acta,* 183**,** 2501-2508.
ZHU, X., YANG, J., LIU, M., WU, Y., SHEN, Z. & LI, G. 2013. Sensitive detection of human breast cancer cells based on aptamer–cell–aptamer sandwich architecture. *Analytica Chimica Acta,* 764**,** 59-63.
ZHU, Y., CHANDRA, P. & SHIM, Y.-B. 2012. Ultrasensitive and Selective Electrochemical Diagnosis of Breast Cancer Based on a Hydrazine–Au Nanoparticle–Aptamer Bioconjugate. *Analytical Chemistry,* 85**,** 1058-1064.
ZUKER, M. & JACOBSON, A. B. 1998. Using reliability information to annotate RNA secondary structures. *RNA,* 4**,** 669-679.

APPENDICES

Appendix I: The numbered atoms of the GO/NIPAM (a), GO (b), and NIPAM (c) molecules for DFT calculations.

(a)

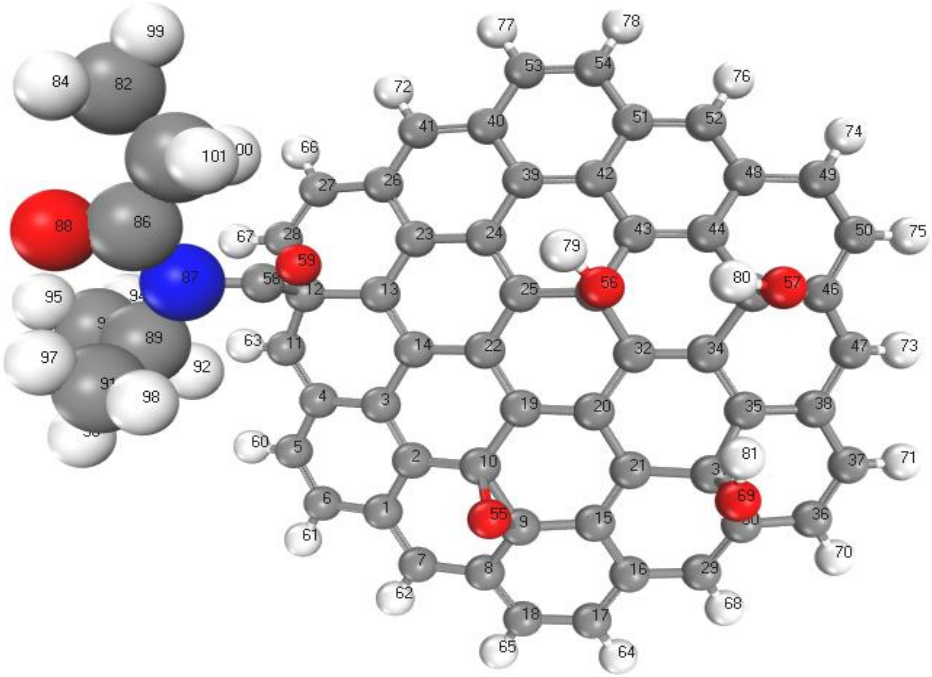

(b)

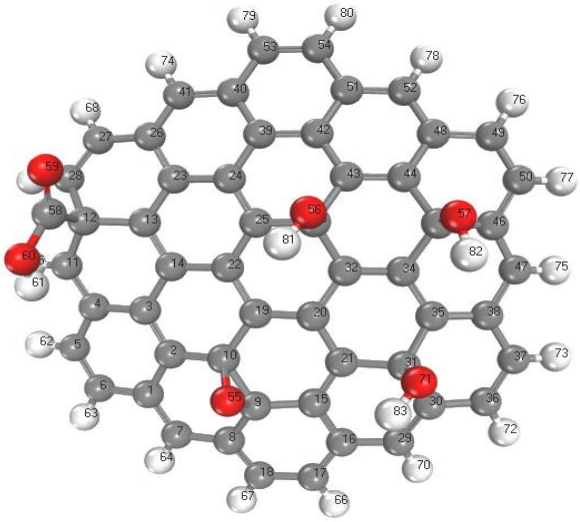

(c)